Crystal growth and nucleation kinetics of diethylenetriammonium hexachlororhodate (III) salt

Dissertation by
Edmund Engelbrecht

In fulfilment of the degree Doctor of Philosophy at the Faculty of Chemical Engineering at the University of Cape Town

Declaration

I, the undersigned, herewith declare that this thesis was produced without assistance from other persons, unless stated otherwise at a specific section.

Engelbrecht, E.	Signed by candidate	12 July 2019
Name	**Signature**	**Date**

Acknowledgement

I wish to thank Anglo Technical Solutions managed by Stephen Woollam for the assistance in terms of required equipment, chemicals and analytical instruments that were available to complete this work. Many thanks to Byron Bezuidenhout for the numerous SEM photographs, Basani Sithole who made up many litres of 6M hydrochloric acid, Sibongile Phajane who assisted with particle size measurement, Grant Summerton and Debbie Craig for helping to get the required equipment as well as the numerous chemical analyses. I also wish to thank Bianca Brits for measuring the metal content in the precipitates. Anglo American Platinum was extremely generous, and I thank the company for the patience with this project.

Many thanks to my wife Ella for the support given throughout this work and the words of encouragement. Without her support, this work would not be complete. I am eternally grateful to my mom Margaret and my dad Leon who have supported me throughout. Lastly, I would like to thank Justin Hagemann and Alison Lewis who always seem to light up the proverbial idea light… Their comments and insights were invaluable in this work.

Distribution:

Mr A. Singh (AP)	**Dr L.R. Nelson (AP)**
Mr F.N. Mashimbye (AP)	**Dr J.P. Hagemann (AA)**
Dr S. Woollam (AP)	**Prof A.E. Lewis (UCT)**
Mrs M. Humphries (AP)	**Mr M. Halhead (AP)**
VTL Technical Library	

AA: Anglo American	AP: Anglo American Platinum
UCT: University of Cape Town	VTL: Anglo American Platinum Virtual Technical Library

Summary

At Anglo American Platinum's Precious Metal Refinery, rhodium separates from a base metal-rich solution by precipitation. Hexachlororhodate (III) ions and cationic protonated diethylenetriamine ions exchange to form diethylenetriammonium hexachlororhodate (III) crystals, a rhodium metal precursor. The objective of this work is to determine nucleation and growth kinetics of diethylenetriammonium hexachlororhodate (III) salt.

Two reactor configurations, namely a transient continuous stirred tank reactor (CSTR) and a t-mixer plug flow reactor (PFR), were used to determine nucleation and growth rates. The objective of the configurations was to eliminate kinetic biases that may be caused by mixing at the mesoscale. Transient saturation in the CSTR ranged up to 43, and in the PFR saturation was varied between 2 and 64. Precipitation kinetic parameters were estimated through data fitting concentration and volume average crystal size profiles to a mass and population balance model.

Temperature dependence of kinetic parameters was found to be universal between reactor configurations. Both growth through interfacial attachment and agglomeration, as defined in this work, were exothermic processes with activation energies of -192.9kJ/mol and -656.1kJ/mol respectively. Nucleation was found to be an endothermic process with an activation energy of 50.9kJ/mol in accord with the observed heat of crystallisation. No evidence of heterogeneous primary nucleation in the form of crystals adhering to the side walls of the reactor or the agitator blades was observed. The experiments were not explicitly designed to distinguish between primary and secondary nucleation mechanisms, therefore excluding one over the other is not justified. However, considering the presence of nucleated crystals in each system combined with the good model fit using a nucleation rate expression typically associated with secondary nucleation, it is likely that the dominating nucleation mechanism is secondary in nature. In the PFR configuration, nucleation and growth occur at a faster rate compared to the CSTR under the experimental conditions in this work. This observation is inferred from the fitted temperature independent kinetic parameters and is linked to a much higher mixing intensity achieved in the PFR relative to the CSTR.

Flow conditions, described by the Reynolds number, can limit conversion in the PFR configuration by a mixing limitation at the micro- or mesoscale. Micro- and mesoscale mixing were represented by a characteristic length scale that was empirically related to temperature for the microscale and fluid velocity for the mesoscale. Under conditions where the Reynolds number is below the point where conversion is independent of the Reynolds number, either micromixing or mesomixing can become a rate limitation. At a sufficiently high Reynolds number neither micromixing nor mesomixing limits conversion and the system equilibrium becomes the limitation. In the CSTR, the system equilibrium limited reaction conversion as the micro- and mesoscale mixing zones were sufficiently small relative to the reactor volume. Parameters related to mixing were found to differ between the configurations, which was caused by different flow patterns within each configuration.

Scanning electron microscopy (SEM) photographs suggest that crystals in the PFR configuration collide both in the radial and axial direction, giving rise to a feathery flat and elongated agglomerated crystal cluster. In contrast, the crystals in the CSTR configuration collide in a chaotic but consistent pattern, giving rise to a desert rose-like agglomerated crystal cluster. The derived model used to describe agglomeration is based on the agglomeration principles proposed by Von Smoluchowski coupled with Fick's law of diffusion and gives a good representation of crystal size. The PFR growth rate supersaturation exponent was 1.13, suggesting a Burton-Cabrera-Frank type growth model, and is indicative of crystal growth from screw dislocations that is limited either through mass transfer to the crystal surface, or surface integration. Thus, in this instance, the rate of aqueous hexachlororhodate (III) conversion to crystal would be responsive to mixing conditions on the micro- or mesoscale, as was experimentally found in the PFR configuration. In comparison, the CSTR growth rate supersaturation exponent was 2.31 and is more in line with polynuclear growth that appears to be limited by interfacial attachment kinetics, as the system equilibrates in the bulk.

Lastly, a key finding of this work is the ability to manipulate the crystal morphology by changing reactor configuration. By creating elongated flat crystal structures in the PFR configuration as opposed to a desert rose crystal structure in the CSTR, it may be possible to reduce impurities within the crystal by entraining less mother liquor.

Key words:

CSTR, Diethylenetriammonium, Hexachlororhodate, MSMPR, PFR, Precipitation, Rhodium

Table of Contents

1. INTRODUCTION

The Anglo American Platinum Precious Metal Refinery, situated on the outskirts of Rustenburg in the North-West province of South Africa, is a primary producer of platinum, palladium, rhodium, iridium and ruthenium. Final purification steps for all the metals produced involve reaction precipitation. The work in this thesis focuses on the nucleation and growth kinetics of the final rhodium purification process.

During the late 1980s and early 1990s a team at the Johnson Matthey Technology Centre in Sonning Common, England, screened several polyamine reagents for application in the precious metal refining flow sheet. This led to the discovery of the precipitation reaction between hexachlororhodate (III) and protonated diethylenetriamine in hydrochloric acid (Burnham et al., 1993). Crozier & Grant (1992) at Johnson Matthey patented the process during the same period.

The group at Johnson Matthey developed a model to predict the equilibrium concentration of hexachlororhodate (III) by way of solubility product. Calculation of the solubility product of the diethylenetriammonium hexachlororhodate (III) salt used the solution concentration of rhodium after 72 hours equilibration at a set temperature. Stability constants accounted for the portion of aquapentachlororhodate (III) (Burnham et al., 1993). The solubility product calculated by this method did not correlate well with temperature.

In addition, concentration prediction was not accurate and was probably because of the solution being non-ideal coupled with poorly defined rhodium speciation. A speciation investigation by Geswindt (2013) has highlighted discrepancies in speciation kinetics reported in literature. This most likely had an impact on the calculated solubility product. However, the project objective was to establish the feasibility of various amine reagents in terms of product yield (Burnham et al., 1993). Further refinement of the model and characterisation of reaction, crystal growth and nucleation kinetics ceased due to poor filterability of the diethylenetriammonium hexachlororhodate (III) salt.

A collaborative research effort between Anglo American Precious Metals Refining Research Group in Germiston, South Africa, and the University of Cape Town sparked interest in the abandoned diethylenetriammonium hexachlororhodate (III) precipitation process during the late 1990s. The objective of this study was to establish factors affecting the crystal size distribution in addition to crystal purity. A response surface experimental design quantified the effects of temperature, degree of stirring, agitator design, reagent addition mode and lastly reagent flow rate on rhodium yield, purity and crystal size distribution (Hagemann et al., 2003). The outcome of the research provided the base to design and build the rhodium production facility at Anglo American Platinum Precious Metal Refinery. The work by Hagemann et al. (2003) identified mesomixing as the controlling step in terms of crystal growth in a semi batch reactor.

Scale-up process parameters obtained from the optimum impurity rejection and yield data within the experimental design of the experiments by Hagemann et al, (2003) provided sufficient information to design the commercial process. Design specifications are therefore empirical in nature and difficult to extrapolate to other conditions. Figure 1.1.1 shows the current rhodium separation flow sheet that originated from the research done to commercialise the rhodium precipitation by protonated diethylenetriamine process.

The process in Figure 1.1.1 shows a double precipitation in series to achieve the desired purity specification. In the crude precipitation circuit, rhodium separates from a feed stream that contains impurities that are mostly base metals. This step rejects virtually all the impurities to the mother liquor. The pure precipitation stage further purifies the salt and separates impurities that occur mainly through entrainment and co-precipitation because of unintended partial oxidation of iridium and ruthenium. After calcination and reduction, the impurity content in the product rhodium metal is less than 200 parts per million by mass (Hagemann et al., 2003).

In both the crude and pure precipitation processes selective oxidation of rhodium through continuous dosing of hydrogen peroxide ensures that it is selectively oxidised from the (II) to the (III) oxidation state whilst ruthenium and iridium remain in the (II) oxidation state. Selectively maintaining redox conditions such that ruthenium and iridium are present as hexachloroirridate(II) and hexachlororuthenate(II) is crucial to effectively reject ruthenium and iridium, present in trace quantities (~100mg/L) in the feed (Hagemann et al., 2003).

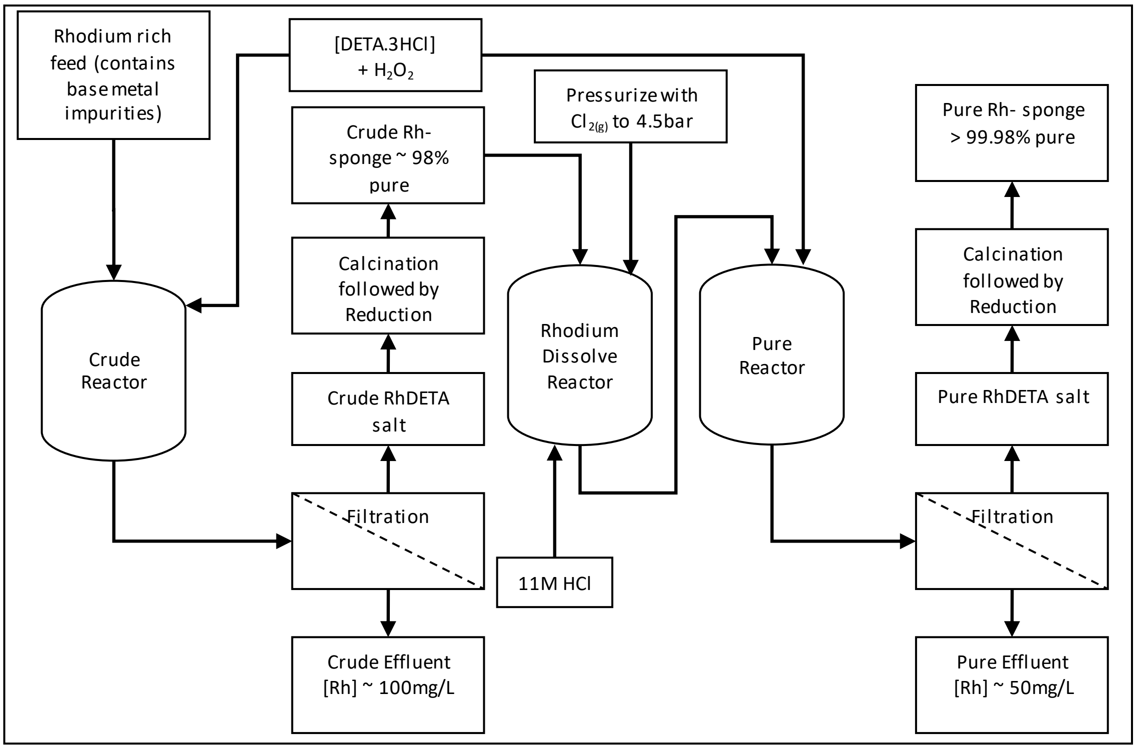

Figure 1.1.1: Rhodium-DETA process flow diagram

According to Cowley (2013), the application of rhodium in auto catalysts makes up approximately 80 per cent of total demand for this metal. The function of rhodium in an auto catalyst is to accelerate the conversion of noxious gas that releases after a combustion cycle in either a diesel or a petrol engine to nitrogen and oxygen. In addition to rhodium's presence in the auto catalyst market, the metal is a catalyst in specialised chemical manufacture of methyl acetate, alcohols, acetic acid and aldehydes (Makaryan et al., 2015).

The stringent gas emission limits governed by Euro 6 legislation coupled with active catalyst application research provide a strong base for maintaining rhodium demand in the future, as outlined by Cowley (2013) and Makaryan et al. (2015). Rhodium is a rare element and intimately linked to minimising damage to the environment from noxious gas emission. It is therefore essential to produce this metal as efficiently as possible.

2. THEORY AND LITERATURE REVIEW

In this section an overview is given of current theory in the field of reaction crystallization that is applicable to the research presented in this thesis. Furthermore, a review of the literature relevant to the system investigated is presented. Keep in mind that the main research objective is to establish the nucleation and growth kinetics of diethylenetriammonium hexachlororhodate (III) crystals. Mersmann (2001) refers to rapid crystallization as precipitation. Throughout this text, crystallization and precipitation are used interchangeably.

2.1. PRECIPITATION AND POPULATION BALANCE THEORY

2.1.1. Crystal nucleation

The onset of the formation of crystals in a system is referred to as nucleation. Literature that covers the theory of nucleation specifies a requirement of supersaturation for nucleation to occur (Bałdyga & Bourne, 1999; Garside, et al., 2002; Jones, 2002; Mersmann, 2001; Myerson, 2002). The definition of supersaturation relevant to a reactive solvent-solute (liquid-solid) system refers to the state where the solvent reactant activities exceed the equilibrium activities. To progress to the mathematical description of supersaturation an arbitrary precipitation reaction is defined in Equation (2.1.1) where aqueous ionic reactants A and B react to form precipitate C.

$$A_{aq} + B_{aq} \rightarrow C_s \qquad \textbf{(2.1.1)}$$

Bałdyga & Bourne (1999) give an approximation of the saturation ratio, for the above reaction stoichiometry in Equation (2.1.1) as the root of the ratio between the product of the reactant activities and the precipitate equilibrium solubility product. This definition is widely used, for example by Jones (2002), Mersmann (2001), and Myerson (2002), and is shown in Equation (2.1.2). Note that activity and solubility product are per thermodynamic definition dimensionless numbers (Atkins, 1997). However, by introducing a mean salt activity coefficient, the solvent activities are written in terms of aqueous concentrations. Garside et al. (2002) warns against careful selection of units when defining supersaturation, as the relationship in Equation (2.1.2) is approximate. The unit of the solubility product is therefore the aqueous concentration unit squared.

$$S = \sqrt{\frac{\gamma_{\pm} C_A C_B}{K_{SP}}} \qquad \textbf{(2.1.2)}$$

Where S = Saturation ratio
C_A = Concentration of reactant A in solution [M]
C_B = Concentration of reactant B in solution [M]
K_{SP} = Solubility product of the precipitate at the system temperature [M^2]
$\gamma_{\pm}$ = Mean activity coefficient of the solvent ionic species

Supersaturation is then defined as the difference between system saturation and the saturation at equilibrium. Saturation at equilibrium is the point where the product between activities, the numerator in Equation (2.1.2), is equal to the solubility product, the denominator in Equation (2.1.2). Thus, the dimensionless supersaturation is mathematically equivalent to $(S - 1)$ to be consistent with the supersaturation approximation in Garside et al. (2002) and Bałdyga & Bourne (1999).

Mersmann (2001), Myerson (2002) and Beckmann (2013) distinguish between two accepted forms of nucleation, namely primary and secondary nucleation. Primary nucleation can further be sub-classified as homogeneous and heterogeneous. Homogeneous nucleation occurs when there is no foreign solid material present in the system that may induce nucleation, whereas heterogeneous nucleation occurs when there is foreign solid material present in the system. Both categories of primary nucleation occur in the absence of crystals formed from the system, thus emphasis is placed on foreign solid material for these two categories. Nucleation is facilitated when the system equilibrates from a non-equilibrium condition. The non-equilibrium condition can be achieved by processes such as evaporation, addition of a drowning out agent or by pairing reactants that form an insoluble product as described by Mersmann (2001). The current view of primary nucleation is that when supersaturation increases to the metastable supersaturation level, nuclei form in accordance with the definition of primary nucleation.

In the presence of solution-own crystals, nuclei form at lower supersaturation levels than the metastable supersaturation level, and this is known as secondary nucleation (Bałdyga & Bourne, 1999; Garside, et al., 2002; Jones, 2002; Mersmann, 2001). Secondary nucleation therefore occurs in the presence of solution-own crystals. Secondary nucleation is further sub-divided into mechanisms related to crystal contact, fluid shear, crystal fracture and crystal attrition or abrasion. Typically, secondary nucleation is driven by system hydrodynamics that cause one or several of the mechanisms mentioned through factors such as mechanical agitation, reagent injection design, pulp density and reactor surface area, as described in texts such as Jones (2002), Mersmann (2001) and Myerson (2002).

Figure 2.1.1 a) illustrates the conceptual relationship between saturation and the various nucleation rates grouped under primary heterogeneous/homogeneous and secondary nucleation. Figure 2.1.1 b) summarises the nucleation categories under constant temperature conditions illustrated within a concentration diagram. Figure 2.1.1 c) illustrates the metastable and nucleation zones in a temperature-concentration phase diagram (Söhnel & Garside, 1992).

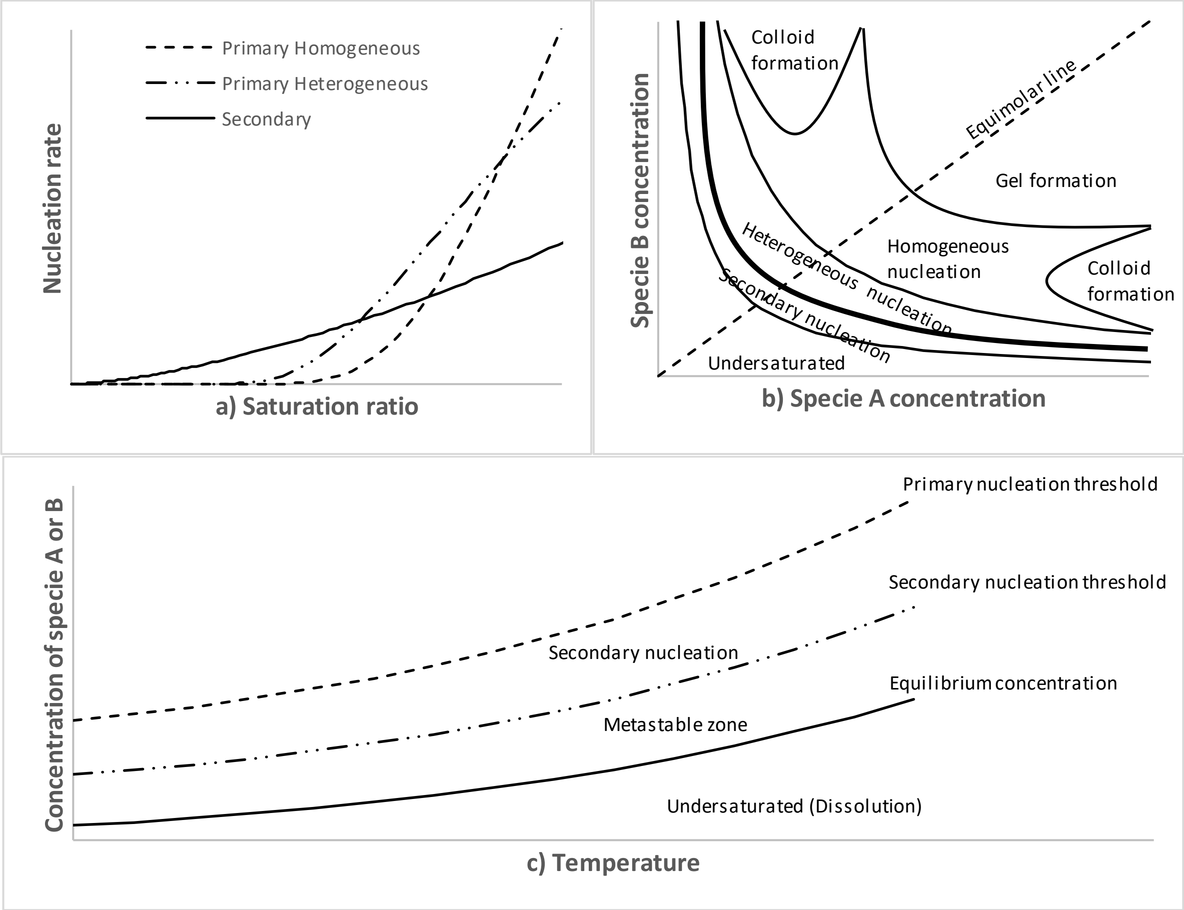

Figure 2.1.1: Conceptual diagrams from Söhnel & Garside (1992) and Beckmann (2013) for a) nucleation rate as a function of saturation ratio for the various categories of nucleation; and b) concentration diagram showing various categories of nucleation and c) temperature-concentration phase diagram

Classic nucleation theory translates to several mathematical expressions that relate homogeneous or heterogeneous primary nucleation rate or surface-induced secondary nucleation rate to saturation ratio and temperature. Garside et al, (2002) summarises primary and secondary nucleation rates into practical relationships given by Equations (2.1.3) and (2.1.4) respectively.

$$R_{n1} = K_{n1} exp\left(-\frac{B_{n1}}{T^3 S^2}\right) \quad \textbf{(2.1.3)}$$

Where R_{n1} = Primary nucleation rate [#/h.dm^3]
K_{n1} = Pre-exponential primary nucleation rate factor [#/h.dm^3]
B_{n1} = Constant related to surface energy [K^3]
T = System temperature [K]

Note that Equation (2.1.3) was simplified by lumping surface energy into the constant B_n. The pre-exponential constant is a function of several physical properties that are concisely defined by Mersmann (2001). Myerson (2002) indicates that the pre-exponential function may also relate to temperature by an Arrhenius function where viscous free energy is a relevant factor in homogeneous nucleation. In Equation (2.1.3) the strong relationship between nucleation rate and saturation is illustrated.

According to Myerson (2002) secondary nucleation is not well understood and a general theory to predict secondary nucleation does not exist. Therefore, it is standard practise to use correlations to describe secondary nucleation. Equation (2.1.4) shows the power law type equation used to describe secondary nucleation by Garside et al. (2002).

$$R_{n2} = K_{n2}(S-1)^{\gamma} \tag{2.1.4}$$

Where R_{n2} = Secondary nucleation rate [#/h.dm^3]
K_{n2} = Secondary nucleation rate constant [#/h.dm^3]
γ = Secondary nucleation supersaturation exponent

The secondary nucleation rate constant K_{n2} can expand as a power law function of pulp density and agitator speed or specific power input to account for interactions due to fluid mechanics (Garside et al., 2002; Myerson, 2002). Myerson (2002) describes a case where the secondary nucleation rate in a fluidized bed and a fixed bed was found to be a function of the Reynolds number. By definition, the Reynolds number is inversely proportional to viscosity, which is generally a strong function of temperature. Therefore, temperature dependence of the rate constant in Equation (2.1.4) is not excluded and is likely caused by viscous effects as with primary nucleation.

2.1.2. Crystal growth rate

Crystal growth refers to the change of some dimension of a crystal over time. In practice, the linear crystal growth rate refers to the change of a characteristic crystal length with time (Jones, 2002; Mersmann, 2001; Myerson, 2002). Like nucleation, growth requires supersaturation as a driving force. Furthermore, the growth rate can be affected by an array of transport and attachment processes both in the solvent phase as well as on the crystal surface or solute phase. Dirksen & Ring (1991) describe the accepted stages required for crystal growth to occur that are typically used to develop growth rate theories from:

i) Transport of the solute from the bulk solution to the crystal surface.
ii) Adsorption of the solute on the crystal surface.
iii) Diffusion of the solute over the crystal surface.
iv) Attachment of the solute to a step on the crystal surface.
v) Diffusion of the solute along a step on the crystal surface.
vi) Integration of the solute into the crystal at a kink site.
vii) Diffusion of coordination shell of solvent molecules away from the crystal surface.
viii) Liberation of heat of crystallization and its transport away from the crystal.

Any one of the mentioned crystal growth stages summarised by Dirksen & Ring (1991) can limit the growth rate of a crystal. Myerson (2002) provides a detailed description of well-known growth theories that are based on the premise that one or more of the above stages limit growth. The models most frequently referred to in the literature that have been developed from these theories are listed below:

- Burton-Cabrera-Frank surface diffusion limited growth model.
- Chernov bulk diffusion limited growth model.
- The diffusion layer model that can either be limited by mass transfer or by interfacial attachment kinetics.

In practice, crystal growth in industrial precipitation reactors is often modelled by way of the power law model. Jones (2002) gives a generic power law relationship that is shown in Equation (2.1.5).

$$G = K_G (S-1)^{\alpha} \tag{2.1.5}$$

Where G = Crystal growth rate by interfacial attachment [µm/h]
K_G = Growth rate constant µm/h]
α = Growth rate supersaturation exponent

The growth rate constant K_G is often related to temperature by an Arrhenius expression (Mersmann, 2001). Jones (2002) relates the value of the growth rate supersaturation exponent to a growth theory discussed above. For α = 1, diffusion-controlled growth is expected, implying that the growth rate is typically limited by a combination of growth stages i) and ii) from the list given by Dirksen & Ring (1991). For 1 < α < 2, growth from screw dislocations can be expected that are limited by interfacial attachment kinetics (surface integration), or mass transfer to the crystal surface that are described by the growth stages i) to vi) in the above list. Lastly, if α > 2, then polynuclear growth is likely and is also limited by stages iii) to vi). However, multiple kinks and steps that originate from secondary nucleation on the crystal surface are available for growth, as described in Dirksen & Ring (1991).

Growth rate is also viewed as the consumption term in the mass balance. Garside, et al., (2002) shows that the change in mass of a crystal is proportional to the product between the surface area (second moment of the population balance) and the crystal linear growth rate. This term is often used to represent reaction rate in the mass balance and essentially links the population and mass balances (Jones, 2002; Mersmann, 2001; Myerson, 2002; Bałdyga & Bourne, 1992). The connection between the mass balance and the population balance through the second moment implies that stages i) and ii) are assumed to be the growth rate limitation based on the list presented by Dirksen & Ring (1991).

2.1.3. The population balance and associated moments for an MSMPR configuration

Randolph & Larson (1971) developed a method to extract nucleation and growth rates from measured population density versus size data. The method is based on a population balance that is in principle comparable to a mass balance. In a population balance, the number of particles is accounted for, whereas a mass balance accounts for component mass. The two balances are linked through saturation as particle nucleation and growth consumes saturation in the same way that chemical reaction in a mass balance consumes reagent components. In a mass transfer limited system, another link between the mass and population balances is the second moment of the population balance. The second moment represents crystal surface area in the rate equation of the mass balance (Jones, 2002).

Firstly, the population density must be defined as this is the intrinsic property that is accounted for in the control volume. Randolph & Larson (1971) and other texts on population balance typically define the population density as the number of particles in an infinitesimal size class per volume of suspension. Population density can also be defined per unit size class volume (Mersmann, 2001). Mathematically, the definition for a crystal size basis is given in Equation (2.1.6).

$$n = \lim_{\Delta L \to 0} \frac{\Delta N}{\Delta L} = \frac{dN}{dL} \tag{2.1.6}$$

Where n = Population density [#/µm.dm^3]
N = Number of particles per volume suspension [#/dm^3]
L = Crystal size [µm]

The transient population balance for a continuous stirred tank reactor, referred to in crystallization texts as a mixed suspension mixed product removal reactor (MSMPR), is given in Equation (2.1.7) (Bałdyga & Bourne, 1999; Garside, et al., 2002; Jones, 2002; Mersmann, 2001; Myerson, 2002; Ramkrishna, 2000; Randolph & Larson, 1971).

$$\frac{\partial n}{\partial t}+\frac{\partial(nG)}{\partial L}+\frac{n}{\tau}=B_{ag}-D_{ag}+B_{dis}-D_{dis} \tag{2.1.7}$$

Where n = Population density [#/µm.dm^3]
G = Crystal growth rate [µm/h]
τ = Reactor residence time = V_r/v [h]
V_r = Reactor operating volume [dm^3]
v = Volumetric flow rate through reactor [dm^3/h]
B_{ag} = Birth rate of particles into a size class due to aggregating processes [#/µm.dm^3.h]
D_{ag} = Death rate of particles into a size class due to aggregating processes [#/µm.dm^3.h]
B_{dis} = Birth rate of particles into a size class due to particle disruption processes [#/ µm.dm^3.h]
D_{dis} = Death rate of particles into a size class due to particle disruption processes [#/µm.dm^3.h]

The hyperbolic partial differential equation above has analytic solutions under specific boundary conditions and assumptions. Ramkrishna (2000) presents several examples of analytic solutions for Equation (2.1.7) and the required boundary conditions. However, in most instances a numeric solution is required through various methods. An elegant method is to convert Equation (2.1.7) into a set of ordinary differential equations through the method of moments (Bałdyga & Bourne, 1999; Garside, et al., 2002; Jones, 2002; Ramkrishna, 2000).

To apply the method of moments, both sides of Equation (2.1.7) must be multiplied by a factor L^i and integrated with respect to crystal size over the interval zero to infinity. The exponent i refers to the particular moment and is equal to 0, 1, 2, 3, 4… The definition of the moments of the population density is given in Equation (2.1.8) (Bałdyga & Bourne, 1999; Garside, et al., 2002; Jones, 2002; Ramkrishna, 2000).

$$M_i=\int_0^\infty nL^i dL \qquad i=0,1,2,3\ldots \tag{2.1.8}$$

Where M_i = ith Population density moment [#.µm^i/ dm^3]

Depending on the relationships on the right-hand side of Equation (2.1.7) different forms of the set of ordinary differential equations of the various moments can be obtained. The set of ordinary differential equations by the method of moments mostly translate to a set of non-linear ordinary differential equations that require numeric solution. The key advantage of the method of moments over full discretization of the population balance is that there is only one independent variable that requires discretization. The disadvantage is that the population density is reduced to a number of moment parameters, and resolution over crystal size is lost.

In an MSMPR configuration, Jones (2002) summarises the various moments of the population balance that enables the calculation of nucleation and growth rates directly from the moments. The population density is first solved after simplifying Equation (2.1.7) through the MSMPR assumption. Jones (2002) lists the requirements for an MSMPR; the resulting simplification and analytic solution is given in Equation (2.1.9).

$$\begin{gathered}\frac{\partial(nG)}{\partial L}+\frac{n}{\tau}=0 \qquad \& \qquad n|_{L=0}=n_0=\frac{R_n}{G}\bigg|_{L=0}\\ \therefore n=n_0 exp\left(-\frac{L}{G\tau}\right)\end{gathered} \tag{2.1.9}$$

In Equation (2.1.9) the initial condition n_0 represents the population density at size zero. The initial condition is defined in literature as the ratio between the nucleation rate and the growth rate at size zero (Bałdyga & Bourne, 1999), (Garside, et al., 2002), (Jones, 2002) and (Ramkrishna, 2000).

The moments of Equation (2.1.9), that are measurable are presented in Equations (2.1.10) to (2.1.12) from Jones (2002) and Mersmann (2001). The Sauter mean and volume average particle sizes (L_{32} and L_{43}) of the population density in Equation (2.1.9) from the definition in Jones (2002) are shown in Equation (2.1.13) and (2.1.14).

$$N_T = M_0 = \int_0^\infty n dL = \int_0^\infty n_0 exp\left(-\frac{L}{G\tau}\right) dL = n_0 G\tau = R_n \tau$$
$$\therefore R_n = \frac{N_T}{\tau} \qquad \textbf{(2.1.10)}$$

Equations (2.1.10) to (2.1.12) illustrates the ability to estimate nucleation and growth rate from measurable variables such as crystal number, crystal surface area, crystal mass, surface and volume shape factors and lastly reactor residence time.

$$A_T = f_s M_2 = f_s \int_0^\infty nL^2 dL = \int_0^\infty n_0 exp\left(-\frac{L}{G\tau}\right) L^2 dL = 2f_s R_n \tau (G\tau)^2$$
$$\therefore G = \sqrt{\frac{A_T}{2f_s R_n \tau^3}} \quad or \quad R_n = \frac{A_T}{2f_s G^2 \tau^3} \qquad \textbf{(2.1.11)}$$

In Equations (2.1.11) and (2.1.12) the surface and volume shape factors are assumed to be independent of crystal size. This is a typical assumption for precipitation systems where the crystal habit does not change with size.

$$M_T = f_v \rho_c M_3 = f_v \rho_c \int_0^\infty nL^3 dL = f_v \rho_c \int_0^\infty n_0 exp\left(-\frac{L}{G\tau}\right) L^3 dL = 6 f_v \rho_c R_n \tau (G\tau)^3$$
$$\therefore G = \left(\frac{M_T}{6 f_v \rho_c R_n \tau^4}\right)^{1/3} \quad or \quad R_n = \frac{M_T}{6 f_v \rho_c G^3 \tau^4} \qquad \textbf{(2.1.12)}$$

Equations (2.1.13) and (2.1.14) give the average size of the crystal size distribution in terms of the Sauter mean (surface area mean size) or volume average (Jones, 2002).

$$L_{32} = \frac{M_3}{M_2} = \frac{\int_0^\infty nL^3 dL}{\int_0^\infty nL^2 dL} = \frac{\int_0^\infty n_0 exp\left(-\frac{L}{G\tau}\right) L^3 dL}{\int_0^\infty n_0 exp\left(-\frac{L}{G\tau}\right) L^2 dL} = 3G\tau$$
$$\therefore G = \frac{L_{32}}{3\tau} \qquad \textbf{(2.1.13)}$$

$$L_{43} = \frac{M_4}{M_3} = \frac{\int_0^\infty nL^4 dL}{\int_0^\infty nL^3 dL} = \frac{\int_0^\infty n_0 exp\left(-\frac{L}{G\tau}\right) L^4 dL}{\int_0^\infty n_0 exp\left(-\frac{L}{G\tau}\right) L^3 dL} = 4G\tau$$
$$\therefore G = \frac{L_{43}}{4\tau} \qquad \textbf{(2.1.14)}$$

Where N_T = Number of crystals per suspension volume [#/dm^3]
A_T = Crystal surface area per suspension volume [m^2/dm^3]
M_T = Crystal mass per suspension volume [kg/dm^3]
R_n = $n_0 G$ = Nucleation rate [#/dm^3.h]
τ = Residence time in MSMPR [h]
f_s = Crystal surface area shape factor [m^2/#.µm^2]
f_v = Crystal volume shape factor [m^3/#.µm^3]
ρ_c = Crystal density [kg/m^3]

Equations (2.1.13) and (2.1.14) suggests that measurement of the Sauter mean crystal size (L_{32}) or the volume average crystal size (L_{43}) permits direct estimation of the growth rate, provided the residence time is known. Thus, an estimation of nucleation and growth rate under MSMPR conditions theoretically only requires measurement of the L_{43} size, total crystal mass or area per suspension volume, volume or area shape factor, and the crystal density as per Equations (2.1.11) to (2.1.14).

2.1.4. Crystal agglomeration

Deviation from ideal MSMPR conditions occurs when any of the mechanisms on the right-hand side of Equation (2.1.7) generates or destroys particles or steady state is not attained (Garside, et al., 2002). For example, when two particles unify during an agglomeration event causing two particles to move out of their respective size classes (death rate, D_{ag}) into a larger size class (birth rate, B_{ag}) the MSMPR assumption is violated. Agglomeration is a common occurrence in precipitation systems and literature provides a wide array of models to describe it.

Mersmann (2001) distinguishes between two main agglomeration types: 1) primary agglomeration due to malgrowth (polycrystals, dendrites and twins); and 2) secondary agglomeration due to crystal-crystal collision in supersaturated solutions. The second category of agglomeration is most often modelled with the number of particles in the system as a key driving force.

Two mechanisms of secondary agglomeration are accepted in the literature: perikinetic agglomeration that is driven by Brownian motion of monodisperse, submicron particles (diffusion controlled) or through orthokinetic agglomeration that is induced through fluid-mechanical forces (shear rate controlled). Von Smoluchowski established that the rate of agglomerating mono sized particles, either through perikinetic or orthokinetic mechanisms, is proportional to the number of particles in the system squared (Mersmann, 2001).

To model agglomeration for a distribution of particle sizes, the observation by von Smoluchowski is used in principle in a discretized version of the classic agglomeration model described in Jones (2002) and Mersmann (2001). The discretized version of the agglomeration model illustrates that the rate of particles disappearing from a size class is proportional to the product between the number of particles in the size class and the number of particles in each size class. The rate of particles entering the size class is proportional to the product between the number of particles in each size class smaller than the size class (Jones, 2002).

Each consumption and generation term has a rate constant, generally referred to as an agglomeration kernel. The agglomeration kernel is typically related to saturation and hydrodynamics in an agitated vessel through some form of agitation power input such as the specific power input, energy dissipation rate ε or the agitator impeller speed (Jones, 2002). Therefore, hydrodynamic behaviour induced through system mixing can have a significant impact on crystal agglomeration within a precipitation system.

2.1.5. Turbulent mixing theory

The theory in sections 2.1.1 to 2.1.3 alludes to hydrodynamics as an important factor affecting secondary nucleation mechanisms, growth mechanisms and agglomeration rate through turbulent mixing of the system. Bałdyga & Bourne (1999) provides a detailed account of the modelling of turbulent mixing in chemical reactors.

The concept of turbulent mixing can be simplified into various mixing scales to enable comparison between systems as well as to establish relevant mixing scales associated with a reactor design. The three major mixing scales are the micro-, meso- and macroscales. The microscale is characterised by mixing near the Kolmogorov or Batchelor scales (mixing on molecular level) and is characterised by molecular diffusion; this is the smallest mixing scale.

Mesoscale mixing occurs on a scale much coarser than the microscale but smaller than the macroscale, and is characterised by dissipation of large eddies that promotes reactant dispersion within the bulk. Macroscale mixing occurs on the scale of the vessel that is used to contain the fluid. Macromixing is characterised by the flow of fluid elements in which meso- and microscale mixing occur through zones of varying turbulence within the vessel and is often compared to the residence time distribution (Bałdyga & Bourne, 1999).

The mixing scale phenomena described above can translate to segregated zones of temperature and specie concentration that deviate substantially from homogeneous behaviour assumed for stirred tank reactors. The localised zones of varying reactant concentration or temperature can lead to unevenly dispersed supersaturation in the case of precipitation, causing a deviation from expected reactor behaviour in terms of conversion, selectivity or crystal size distribution (Bałdyga & Bourne, 1999).

Bałdyga & Bourne (1999) suggest Equation (2.1.15) to estimate the micromixing time. According to Jones (2002), the inverse of the micromixing time can be interpreted as a transfer coefficient for mass transfer by diffusion in a scale-up modelling approach known as the segregated feed model (SFM).

$$\tau_{micro} = 17.24\sqrt{\frac{\eta}{\varepsilon}} \qquad \textbf{(2.1.15)}$$

Where τ_{micro} = Micromixing time [s]
η = Kinematic viscosity [m^2/s]
ε = Local energy dissipation rate [m^2/s^3]

In Equation (2.1.15) the kinematic viscosity is determined from solution viscosity measurements. The local energy dissipation rate is estimated from the empirical relationship in Equation (2.1.16) as used by Vicum (2005).

$$\varepsilon = a\frac{N_p N^3 D_i^5}{V_r} \qquad \textbf{(2.1.16)}$$

Where a = Constant = 2 according to Bałdyga & Bourne (1999).
N_p = Agitator power number = 1.5 according to Nienow (1997) for a pitch blade turbine
N = Agitator angular velocity in revolution per second [1/s]
D_i = Agitator impeller diameter [m]
V_r = Reactor operating volume [m^3]

Torbacke & Rasmuson (2001) estimate the mesomixing time using Equation (2.1.17) for a system where the reagent is injected beneath the surface of the reacting fluid through a dip-tube. It is also useful to conceptualise that meso-mixing occurs at a length scale comparable to the dip-tube diameter. Note that the velocity of the reagent inside the dip-tube is not necessarily equal to velocity of the fluid surrounding the dip-tube, this is illustrated in Equation (2.1.17). According to Jones (2002), the inverse of the mesomixing time can be interpreted as a transfer coefficient for mass transfer by convection when used in the segregated feed model.

$$\tau_{meso} = a\left(\frac{\nu_i}{\pi u \varepsilon}\right)^{1/3} = a\left(\frac{u_p {D_p}^2}{4u\varepsilon}\right)^{1/3} \qquad \textbf{(2.1.17)}$$

Where τ_{meso} = Mesomixing time [s]
a = Constant = 2 according to Bałdyga & Bourne (1999).
ν_i = $\frac{u_p \pi {D_p}^2}{4}$ = ith reactant volumetric flow rate [m^3/s]
u = Fluid local velocity at the dip-tube outlet [m/s]
u_p = Fluid velocity in dip-tube [m/s]
D_p = Dip-tube diameter [m]

A macromixing time estimate by Nienow (1997) is given in Equation (2.1.18).

$$\tau_{macro} = \frac{4V_r}{N_q N D_i^3} \qquad \textbf{(2.1.18)}$$

Where τ_{macro} = Macromixing time constant [s]
N_q = Flow number = 0.73 according to Nienow, (1997) for a pitch blade turbine.

The time constant associated with each mixing scale gives an indication of how fast mixing on each scale occurs. The purpose of identifying the time constant of each mixing scale is to establish whether the time frame of the reaction occurring in the mixed system is shorter than any of the mixing times. All mixing scales with a time constant larger than or close to the reaction time constant is likely to have an influence on the selectivity of the reaction in the case of multiple reactions. In the case of a sparingly soluble precipitation system, conversion of the reactants and the crystal size distribution may be intimately related to any or all of the mixing scales depending on the physical reactor design (Jones, 2002; Mersmann, 2001; Bałdyga & Bourne, 1999).

2.2. LITERATURE REVIEW

The theory presented in section 2.1 indicates that nucleation and growth kinetics are influenced by a myriad of variables. Supersaturation, temperature, the presence of foreign particles and the presence of solution-own crystals are typical variables that can affect both nucleation and growth. Theory highlights that hydrodynamics can affect the distribution of supersaturation and temperature throughout the reactor and can cause localised zones of both temperature and supersaturation. Localised saturation can cause localised zones of nucleation and growth that can cause localised distributions of the population density described in section 2.1.3.

Thus, there is a complex relationship between overall precipitation kinetics and the mixing conditions within the reactor. The variables that determine hydrodynamics or mixing conditions of the system can be simplified into time constants to give a qualitative comparison between different systems. The time constants can provide an indication of relevant mixing scales that may affect the crystal size distribution or conversion, and is therefore useful when analysing experimental data.

In this section, literature is presented that utilises the population density moments to extract nucleation and growth kinetics from experimental measurements. In addition, literature that covers precipitation kinetics under varying hydrodynamics, temperature and supersaturation conditions is reviewed. The objective of this literature review is to derive an experimental and data analysis procedure to determine the growth and nucleation kinetics of diethylenetriammonium hexachlororhodate (III) crystals.

2.2.1. The application of population balance moments to extract crystal growth and nucleation kinetics

Zauner & Jones (2000) studied calcium oxalate precipitation in an MSMPR configuration. They extracted crystal growth rate from the Sauter mean size, defined as the ratio between the third and the second moment of the population balance (see Equation (2.1.13)). The nucleation rate was calculated by the population balance initial condition shown in Equation (2.1.9). The population density at size zero, required in Equation (2.1.19), was estimated from the intercept of $\ln n$ versus L data. By way of modelling, Zauner & Jones (2000) showed that the growth and nucleation kinetics under the assumption of ideal MSMPR conditions is not appreciably affected even with agglomeration and disruption present.

Measurement of crystallization kinetics in steady state crystallizers, like the example above, are widely applied to determine nucleation and growth kinetics (Garside et al., 2002; Jones, 2002; Mersmann, 2001; Myerson, 2002). In contrast to steady state conditions, Timm & Larson (1968) investigated dynamic behaviour of three precipitation systems (potassium aluminium sulphate, ammonium sulphate and sodium chloride). They showed that steady state nucleation and growth kinetics of the three systems investigated adequately described population density dynamic behaviour when a step-change perturbation in crystallizer flow rate was induced.

Similar to the method of Timm & Larson (1968), Sowul & Epstein (1981) produced sucrose growth and nucleation kinetics in an MSMPR configuration during the transient stages of operation. Their kinetics compared well to published kinetics of sucrose crystallization. The researchers tracked the transient behaviour of crystal size distributions in the form of the volume average crystal size, Equation (2.1.14), and fitted growth and nucleation rates through multiple linear regression. Tavare (1986) applied a similar method to extract calcium oxalate precipitation kinetics and recommended that this method be used to independently check parameter estimates obtained from steady state experiments.

Jager et al. (1991) used heat input perturbation to generate a saturation transient in an ammonium sulphate evaporative crystallizer. The purpose of the study was to evaluate four techniques to extract nucleation and growth kinetics from the transient data. The study found that estimation of nucleation and growth rates by way of the moment or Laplace transformation of the population balance is not reliable as the methods rely heavily on the measurement of the number of small crystals beyond the measurement range.

The method of characteristics was found to be susceptible to the same error related to measurements of the number of small crystals (Jager et al., 1991). Laser diffraction was used to measure crystal size distribution in the study by Jager et al. (1991). Beyond the instrument crystal size measurement range, crystal volume fractions become inaccurate and dependent on the method of extrapolation. For this reason, Jager et al. (1991) states that nucleation and growth rates determined by the methods discussed above are susceptible to noise at the crystal size distribution tails.

Jager et al. (1991) recommend a non-linear parameter estimation routine to directly estimate nucleation and growth parameters such as rate constants and supersaturation exponents in Equations (2.1.4) and (2.1.5). The numerical procedure proposed by Jager et al. (1991) is based on the method of lines to solve the transient population balance. The partial differentials with respect to size in Equation (2.1.7) are discretized, which gives an ordinary time differential equation at each size grid point. Pre-defined nucleation and growth parameters are then optimised to give the smallest difference between measured moments or the volume (mass) average size and calculated values from the discretized population balance solution.

2.2.2. Hydrodynamic factors affecting precipitation

Bałdyga et al. (2007) modelled a double feed barium sulphate semi-batch precipitation process by viewing the system as the mixing of three solutions: fresh feed sodium sulphate, fresh feed barium chloride and the bulk that represents a homogeneous mixture. The Reynolds average form of the moment transformation of the population and mass balance was used to model the feed zone by computational fluid dynamics (CFD). Bałdyga et al. (2007) used a parameter, intensity of segregation, as a measure to visualise concentration distribution in the reactor volume. The modelling showed that at the point where barium chloride is injected, a small plume forms that becomes more segregated towards the point where sodium sulphate is injected.

Bałdyga et al. (2007) defined a segregated mixing zone as the volume in the reactor where the intensity of segregation is > 0.01. The volume, defined by the intensity of segregation inequality, was centralised around the reagent injection points that were positioned close to each other and the impeller (Rushton turbine). The segregated mixing zone was comparatively small relative to the remaining volume of the suspension that was considered as the homogeneous bulk.

Bałdyga et al. (2007) used the volume average size as a measured variable to validate the model and found that the model trends agreed with the measurement trends but the crystal size was consistently underpredicted using nucleation and growth kinetics defined by Nielsen (1961). The deviation between modelled L_{43} size and measured L_{43} was attributed to the activity model used for predicting the non-ideal behaviour of the electrolyte. However, four measured relationships were observed in this work: L_{43} size tends to decrease by an increase in either 1) the volume ratio of reagents or 2) the initial concentration of reagents. In contrast the L_{43} size tends to increase by either an increase in 3) the stirrer speed or 4) the feed time of reagents.

The first two relationships reported by Bałdyga et al. (2007) are related to an elevated supersaturation condition near the points of reagent injection that promotes nucleation near the agitator and growth far from the agitator in the bulk. The last two observations are related to supersaturation dilution whereby the volumetric feed rate and the agitator speed determines the rate of dilution between the bulk and the concentrated feed. All these observations strongly relate to mesomixing conditions in the reactor whereby the time required to disperse reagents has a strong influence on the supersaturation profile across the volume of the reactor.

In a continuous MSMPR barium sulphate precipitation system, Vicum (2005) investigated the effects of agitation speed, supersaturation and retention time on the volume average crystal size of the product. In this configuration the sodium sulphate and barium chloride reagent solutions were injected into the reactor through dip-tubes, of which the locations could be varied. Two positions of the dip-tubes were tested: 1) at opposite sides of the reactor and 2) near each other with both positions at an elevation of the agitator impeller. The second dip-tube positioning is similar to the configuration used in the study by Bałdyga et al. (2007) presented above.

Vicum (2005) found no discernible effect on volume average crystal size caused by agitator speed or reagent volumetric flow into the reactor under continuous operation. However, the investigation showed that the volume average crystal size responded markedly to initial reagent concentration and to reagent dip-tube positioning. Vicum (2005) showed that the trends of the above observations were well represented by the multi mixing scale CFD model proposed by Bałdyga (1989).

The multi mixing scale CFD model used by Vicum (2005) showed that the reagent plumes, entering the reactor at opposite sides of the agitator, dispersed rapidly into the bulk. The model highlighted that under the condition of separated reagent injection points, extremely small localised zones of high concentration developed around the feed points in comparison to a homogenised bulk. When reagent injection points were placed near each other, the localised zone of high concentration extended to a much larger volume. This is similar to the results presented by Bałdyga et al. (2007), resulting in the bulk becoming substantially less homogeneous.

It is therefore argued that the factor causing the observation related to agitator speed and retention time (volumetric flow), in the case of separated dip-tubes observed in the work by Vicum (2005) is related to mesoscale mixing. The minimum agitator speed in the continuous tests by Vicum (2005) was at a level where the energy dissipation was large enough to cause the mesomixing time to be close to or smaller than the characteristic time for crystal nucleation and growth. Even under the condition of minimum volumetric flow, where mesomixing time should be at a maximum given a fixed energy dissipation rate, no appreciable effect was observed between agitator speed and particle size.

Thus, within the experimental design chosen by Vicum (2005), the mesomixing time was sufficiently shortened relative to the characteristic nucleation and growth times to cause no observable relationship between residence time (volumetric flow) and crystal size, as the supersaturation in the system was dispersed homogeneously through most of the reactor volume. In comparison, consider the L_{43} size of an ideal MSMPR as calculated by Equation (2.1.14); one would expect a direct relationship between size and residence time at constant growth rate. However, many authors have shown that in an MSMPR, growth rate is typically driven by supersaturation, and supersaturation is typically affected by the residence time (Zauner & Jones, 2000; Garside et al., 2002; Bałdyga et al., 2007; Mersmann, 2001; and Myerson, 2002).

Typically, lower supersaturation in a non-equilibrium system implies longer residence time, therefore growth rate is likely to decline as residence time is increased, as was found by Zauner & Jones (2000). Thus, one could have a condition in the MSMPR whereby the effect of residence time on L_{43} size is counteracted by a decline in growth rate, with reference to Equation (2.1.14). The observations by Vicum (2005) therefore illustrate that the system response was remarkably close to an ideal MSMPR when the reagent dip-tubes were separated. Furthermore, the work by Vicum (2005) illustrates that the crystal size distribution is determined by the history of supersaturation, and is affected by how well mixing in the system distributes the system constituents over the reactor volume. Work by Bałdyga et al. (1995) also highlights this point.

Additionally, the work by Bałdyga et al. (1995) showed variation in barium sulphate morphology based on reagent dip-pipe position in the reactor. Reagent injection at the agitator impeller (elevated mixing intensity) generated crystals that agglomerated flat, plate-like shapes in a star-like fashion. In comparison, highly agglomerated clusters on rectangular shaped crystal structures formed when reagents were injected onto the surface of the suspension (low mixing intensity). The change in morphology is related to a change in mesomixing conditions whereby elevated mixing intensity (energy dissipation rate) causes a reduction in mesomixing time. The morphology of the barium sulphate crystals is therefore inferred to be a strong function of mesomixing conditions in a semi-batch reactor.

In a different study, Hagemann et al. (2003) concluded that mesomixing controls the growth of diethylenetriammonium hexachlororhodate (III) crystals in a semi-batch reactor configuration where the reagents were injected into the suspension through separate dip-tubes. The work further shows that the crystal size distribution after precipitation in a semi batch reactor is typically bimodal. The configurations Hagemann et al. (2003) used to deduce the mesoscale mixing effects was a semi-batch reactor of varying scale and reagent injection protocols (1dm^3 to 10dm^3). An empirical statistical surface response model was used to deduce the relevant effects on crystal size.

Bałdyga et al. (1997) shows that mixing at the micro- and mesoscales can be manipulated through flow rate (Reynolds number) in a plug flow reactor (PFR) configuration using a Sulzer or Kenics mixer. A parallel reaction scheme with one fast and one slow reaction is used to demonstrate that mixing intensity can alter reaction selectivity. The slow, desired reaction is the coupling of 2-naphthol with diazotised sulphanilic acid; the fast (by approximately a factor of 100) unwanted reaction is the coupling of 1-naphthol.

The conversions of both the fast and the slow couplings are strongly influenced by flow rate, whereby the slow coupling conversion increases with decreasing flow rate, and the fast coupling conversion increases with increasing flow rate. Bałdyga et al. (1997) emulate the measured outcomes with a mixing model that incorporates both micro- and mesoscale mixing effects. Mesomixing promotes the conversion of the slow reaction at low flow rates and the fast reaction at high flow rates. Therefore, selectivity of the slow reaction relative to the fast reaction is amplified at long mesomixing times, whereas it is depressed at short mesomixing times.

Bałdyga & Bourne (1999) present a case study whereby barium sulphate is precipitated in a t-mixer followed by a 2m plug flow reactor. The work shows that volume average crystal size weakly relates to volumetric flow (Reynolds number) through the reactor. The measurements indicate that the volume average crystal size decreases by ~15 per cent when the flow is increased fourfold. Furthermore, the volume average crystal size relates to mean concentration of barium chloride in a function that increases from small concentrations up to a peak, then rapidly declines and steadies out at larger concentrations. The relationship is more pronounced relative to flow, as size changes five-fold when concentration is roughly doubled. The measured relationships were well represented by a CFD model coupled with the population balance model. Barium sulphate nucleation, and growth kinetics from Nielsen, (1961) were used to define nucleation and growth. This modelling work also suggests that viscosity of the mixture in the PFR can modify crystal morphology, and is related to altering the micromixing time through Equation (2.1.15).

In a study related to the precipitation of benzoic acid from an ethanol solution using water as an anti-solvent, Ferguson et al. (2013) observed differences in crystal morphology when using different reactor configurations. The study involved precipitation in a semi-batch plug flow with Roughton mixer and MSMPR configuration. Ferguson et al. (2013) highlights that the profile of supersaturation in the three reactor configurations vary substantially as a result of mixing on the mesocale and as a result translate to differences in crystal size distribution and morphology.

Likewise, Jung et al. (2010) show that reactor type influences morphology of calcium carbonate crystals. This study focused on precipitation of calcium carbonate in two reactor types, namely a Couette-Taylor reactor and a CSTR using aqueous calcium hydroxide solution and carbon dioxide gas. It was found that rhombic (cube-like) crystals were produced in both reactor types at low initial calcium hydroxide concentration, whereas spindle-type crystals were formed at high initial concentration. The crystal edges produced from high concentration calcium hydroxide in the Couette-Taylor reactor were rounded and not well defined, as opposed to the CSTR that showed sharp edges.

It is likely that the morphology difference observed in the study by Jung, et al., (2010) is fundamentally related to mixing on the mesoscale that influenced the extent to which carbon dioxide gas was dispersed in the calcium hydroxide solution. To this end, the basis of the experimental procedure by Jung et al. (2010) was to keep the residence time of aqeuous calcium hydroxide constant between the reactors. The Couette-Taylor reactor operating volume was $3dm^3$ compared to $1dm^3$ for the CSTR. Therefore the aqueous reactant injection volumetric rate into the Couette-Taylor reactor was 3 times that of the CSTR. From the theory section, mesomixing time in Equation (2.1.17) is proportional to reagent flow to the power one third, and inversely proportional to fluid velocity near the injection point to the power one third. Thus it is highly likely that the meso mixing time between the reactor configurations was substantially different, causing the observed morphology effect.

2.2.3. Mixing conditions in static or t-type mixers

Fang & Lee (2001) and Fournier et al. (1996) suggest that static mixers or t-mixers can reduce the mixing time constant relative to a continuous stirred tank reactor at the same power input. A method widely used to determine mixing times in a reactor is parallel competitive reaction pathways (Bałdyga & Bourne, 1999). The concept is to add two reagents, A and B, into a reaction volume to form product C. The parallel competitive reaction occurs when product C reacts with B to form D. The reaction rate for the primary reaction (A+B) is typically higher than for the secondary reaction (C+B).

Thus, in an environment where fresh A mixes instantaneously with fresh B, predominantly product C will form. In an environment where mixing is not instantaneous and newly formed C back-mixes with fresh B, then product

D will appear. Thus, product selectivity can be manipulated by changing the mixing conditions within the reaction vessel. There are several parallel reaction schemes available, depending on the mixing time scale under investigation (Bałdyga & Bourne, 1992; Villermaux et al., 1992).

In mixing time studies, mixing times in static mixers between 1 millisecond up to several seconds with Reynolds numbers (based on the reactor diameter) ranging from 10 000 down to 50 have been reported (Lindenberg, et al., 2008; Fang & Lee, 2001). The parallel reaction scheme proposed by Villermaux et al. (1992) was used in a study by Fang & Lee I2001) and the scheme proposed by Bałdyga, et al. (1998) was used in work by Lindenberg et al. (2008). These two studies indicate that a similar mixing time versus Reynolds number relationship can be obtained in different mixer designs using different reaction schemes.

In another study by Lindenberg et al. (2008), a comparison between a Roughton t-mixer and a Y-mixer showed that the Roughton mixing time is 5-10 times faster than the Y-mixer. The work by Lindenberg, et al., (2008) showed that at a Reynolds number of 1000, the mixing time in a Roughton mixer was ~2ms compared to a y-mixer mixing time of ~9ms. In the work by Fang & Lee (2001), the mixing time in a Kenics mixer was ~1ms at a Reynolds number of ~1 000. Thus, two different designs, the Roughton mixer and the Kenics mixer, perform roughly the same at a Reynolds number of 1000.

Furthermore, Fang & Lee (2001) report that the Kenics in-line mixing time was approximately three times faster than in a continuous stirred tank reactor or CSTR at the same power input. This observation emphasises that t-mixers can be more efficient at mixing on the microscale compared to a CSTR. Thus, mixing in a t-type mixer can dampen the effect that mesoscale mixing would have on observed system reaction kinetics, as pointed out in Section 2.2.2.

The reviewed t-mixer studies reveal that mixing time can be manipulated through mixer design as well as the Reynolds number characterised by the diameter of the mixer (macroscale). If the mixing time of the t-mixer is reduced such that it approaches a smaller scale of mixing, then conversion of a reaction that occurs near that time frame can be manipulated. There is also the potential that two different mixer designs at different initial conditions can produce identical mixing times. Furthermore, t-mixers can be more efficient at mixing on sub-macroscales than a CSTR at the same energy dissipation rate.

2.3. THESIS OUTLINE AND OBJECTIVES

The theory and literature reviewed suggests that one can determine precipitation kinetics either through steady state analysis or through transient analysis of a system (Sections 2.1 and 2.2). An apparent advantage of transient over steady state analysis is a reduction in the required raw materials, whilst affording the opportunity to observe the process under a range of supersaturation conditions (Timm & Larson, 1968).

The difficulty with this method is to ensure that nucleation and growth is stalled in the sample from the product stream and that the size distribution is within range of the measurement technique. Typically, the reaction is stalled by adding a diluent, or increasing sample temperature to reduce saturation to near or slightly below equilibrium (Garside, et al., 2002; Sowul & Epstein, 1981). Another method to avoid effects on crystal size distribution and saturation by post-precipitation is to analyse the product and saturation levels online (Jager et al., 1991).

A drawback of transient analysis for either a continuous or semi-batch configuration is the requirement for sophisticated numerical techniques to analyse the data, as was demonstrated by Jager et al. (1991) and modelling by Bałdyga et al. (2007). The data analysis technique chosen may lead to errors in extracted nucleation and growth rate parameters, suggesting that the method should be tested against a wide array of operating conditions and results.

The literature related to hydrodynamic factors covers precipitation of barium sulphate, benzoic acid, calcium carbonate, and diethylenetriammonium hexachlororhodate (III), all of which demonstrate that crystal size distribution and morphology can be controlled by way of manipulating the various mixing scales through methods of reagent injection and reactor design (Vicum, 2005; Bałdyga et al., 1995; Ferguson et al., 2013; Jung et al., 2010). The literature review is biased towards barium sulphate precipitation, as the literature is widely available; and it is considered a proxy for the diethylenetriammonium hexachlororhodate (III) precipitation system based on solubility characteristics.

Initial solubility measurements of diethylenetriammonium hexachlororhodate (III) showed that 0.56g/L to 1.6g/L of the salt dissolves in 6M HCl at 30°C and 80°C respectively. According to Lide (2007), barium sulphate dissolves in water to 0.0029g/L at 30°C. Thus, barium sulphate is approximately ~100 times less soluble than diethylenetriammonium hexachlororhodate (III) in 6M HCl. However, both salts fall within the sparingly soluble class of salts.

Considering the advantages of transient over continuous configurations and noting the ability to manipulate micro- and mesoscale mixing in a PFR configuration, this work will focus on measuring diethylenetriammonium hexachlororhodate (III) precipitation kinetics in two reactor configurations. The first configuration is a transient MSMPR type reactor, and the second is a t-mixer with a PFR in series. The primary motivation for experimentation in the two vastly different reactor configurations is to establish if there are notable mixing scale effects on observed precipitation kinetics and morphology.

The success of the experiments depends on how close each reactor setup is to idealised assumptions of the configuration. To summarise, the work presented in this thesis has the following objectives:

- Derive a mathematical model of the transient precipitation process of diethylenetriammonium hexachlororhodate (III) crystals in a continuous stirred tank reactor configuration.
- Derive a mathematical model of the precipitation process of diethylenetriammonium hexachlororhodate (III) crystals in a t-mixer with a pipe reactor in series configuration.
- Determine if the growth and nucleation kinetics are interchangeable between the two reactor configurations, to establish the extent to which mixing scales may have influenced kinetics.
- Determine if the reactor configuration affects crystal morphology.
- Measure the solubility of diethylenetriammonium hexachlororhodate (III) salt since it is an important thermodynamic property that appears in the definition of saturation.
- Measure the viscosity since it is required to calculate the Reynolds number.

3. RHODIUM DETA PRECIPITATION MODEL DERIVATION

As discussed in Chapter 2, there are varying scales of mixing, most commonly referred to micro-, meso- and macroscale mixing. Hagemann et al. (2003) has concluded that mesomixing controls the growth of diethylenetriammonium hexachlororhodate (III) crystals in a semi-batch reactor configuration. The work further shows that the crystal size distribution after precipitation in a semi-batch reactor is typically bimodal. The literature review also noted that nucleation and growth functions for diethylenetriammonium hexachlororhodate (III) crystals do not exist.

Within this context, concepts from Chapter 2 are used to develop a model of the diethylenetriammonium hexachlororhodate (III) system in two reactor configurations to address the first two objectives in Section 2.3. The framework of the model is such that it allows direct parameter estimation through a non-linear type data fitting routine, as recommended by Jager et al. (1991).

It is logical to start with the most widely used reactor configuration in chemical engineering, namely the continuous stirred tank reactor or CSTR to measure the nucleation and growth kinetics for this system. Literature covering nucleation and growth measurement refer to the CSTR as an MSMPR (Garside et al., 2002; Mersmann, 2001; Myerson, 2002). However, the term CSTR is most frequently used in subsequent sections. The CSTR model is derived in Section 3.1, thereafter a PFR model is derived in Section 3.2.

3.1. CSTR MASS AND POPULATION BALANCE

3.1.1. CSTR Mass balance

Burnham et al. (1993) defined the ion-exchange chemistry that governs diethylenetriammonium hexachlororhodate (III) salt precipitation. Hydronium and chloride are spectator ions in the reaction shown in Equation (3.1.1); acidity therefore remains constant over the course of reaction.

$$\begin{aligned} &H_3RhCl_{6,aq} + C_4N_3H_{16}.3HCl_{aq} \rightarrow [C_4N_3H_{19}][RhCl_6]_s + 3HCl_{aq} \\ &\therefore RhCl^{3-}_{6,aq} + C_4N_3H_{16}.3H^{3+}_{aq} \rightarrow [C_4N_3H_{19}][RhCl_6]_s \end{aligned} \qquad \textbf{(3.1.1)}$$

It is important to keep the free acidity close to 6M as aquated hexachlororhodate (III) species will form at <6M that will impede reaction with protonated diethylenetriamine by way of differences in solubility (Burnham et al., 1993; Hagemann et al., 2003; Geswindt, 2013). Initial experiments in a 2dm^3 reaction vessel showed rapid equilibration of Equation (3.1.1), providing a base to assume a homogeneous bulk volume. Rapid equilibration is common for ion-exchange reactions that have typical reaction times in the order of micro to nano seconds and are generally limited by transport processes affected by various mixing scales rather than reaction kinetics (Perry & Green, 1998; Bałdyga & Bourne, 1999).

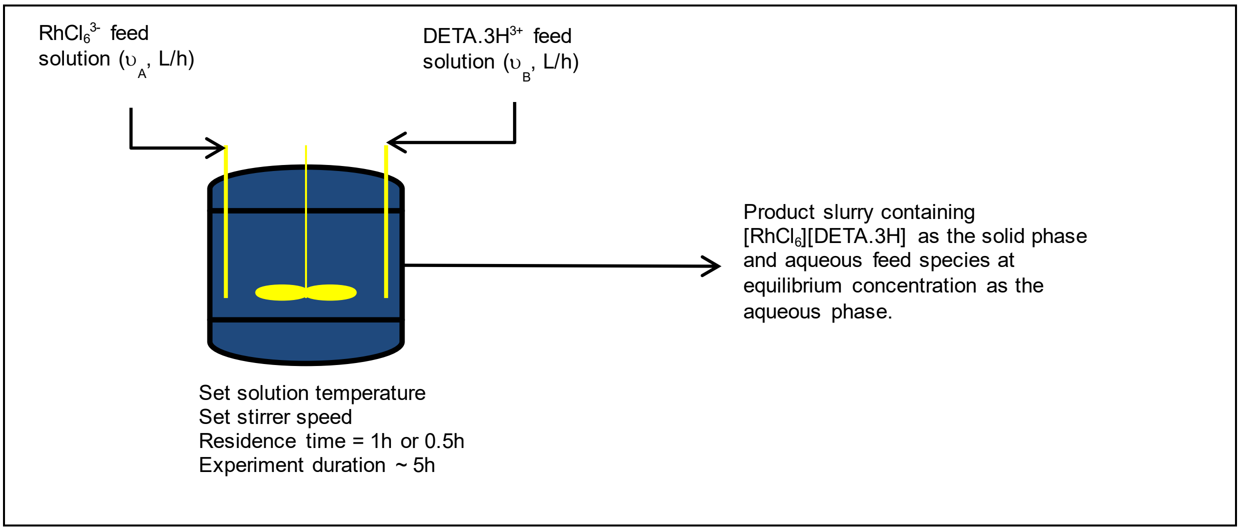

Figure 3.1.1: CSTR flow schematic

Based on the premise that the system rapidly equilibrates, it is reasoned that the localised concentration zones formed at the reagent dip-tubes are negligibly small relative to the bulk volume, similar to the continuous configuration used by Vicum (2005). Under the conditions proposed by Vicum (2005), no effect on crystal size (reaction rate) was observed when residence time and agitation speed was varied, indicating that the operating conditions dampened mesomixing effects to the extent that they were negligible. Thus, a modelling approach like the segregated feed model described in Jones (2002) would result in modelling extremely small localised zones at the reagent injection points.

It is argued that any compartmental modelling approach will not provide any additional information as the reaction proceeds to equilibrium in the bulk. The process is therefore equilibrium-limited. However, saturation is unity at equilibrium conditions implying zero supersaturation that in turn gives zero nucleation and growth. Thus, it is proposed to model the system by referencing saturation to an unreactive mass balance. This, approach creates an artificial supersaturation that is likely to exist only at the point where the reagents are injected, albeit a very small volume as discussed above.

The saturation profile, based on the unreactive and equilibrium concentration profiles, then defines growth and nucleation terms in the population balance. Normally the population balance feeds back to the mass balance through the second moment in a reactive system that is limited by mass transfer, as discussed in Section 2.1.2 of Chapter 2. In this system, where equilibrium occurs in the bulk, mass transfer does not drive reactant conversion. Thus, the mass balance consumption term does not contain the population balance second moment. Figure 3.1.1 shows a schematic of the CSTR configuration used to derive the mass balance.

Initially the reactor contains hexachlororhodate (III) at a concentration of C_{A0} and zero protonated diethylenetriamine. The analytic solutions of the unreactive concentration balance, given the initial conditions, appears in Equations (3.1.2) to (3.1.3). Note that concentration units are defined per unit volume of suspension throughout. The crystal concentration in the suspension is < 0.12M for all experiments implying that the volume contribution due to crystals is < 2.8 per cent by volume and is therefore assumed to be negligible.

$$\begin{gathered}\frac{dC_A}{dt} = \frac{\upsilon_A C_{A0} - \upsilon_{out} C_A}{V_r} \\ \therefore C_A(t) = C_{A0}\frac{\upsilon_A}{\upsilon_{out}}\left(1 - exp\left(-\frac{\upsilon_{out}t}{V_r}\right)\right) + C_{A0}exp\left(-\frac{\upsilon_{out}t}{V_r}\right)\end{gathered} \tag{3.1.2}$$

$$\begin{gathered}\frac{dC_B}{dt} = \frac{\upsilon_B C_{B0} - \upsilon_{out} C_B}{V_r} \\ \therefore C_B(t) = C_{B0}\frac{\upsilon_B}{\upsilon_{out}}\left(1 - exp\left(-\frac{\upsilon_{out}t}{V_r}\right)\right)\end{gathered} \tag{3.1.3}$$

Where C_A = Concentration of $RhCl_6^{3-}$ expressed as mol per unit suspension volume [M]
C_B = Concentration of $DETA.3H^{3+}$ expressed as mol per unit suspension volume [M]
t = Time [h]
V_r = Active reactor volume = Suspension volume in reactor [dm^3]
υ_A = Volumetric flow rate of a feed stream containing $RhCl_6^{3-}$ [dm^3/h]
υ_B = Volumetric flow rate of a feed stream containing $DETA.3H^{3+}$ [dm^3/h]
C_{A0} = Concentration of $RhCl_6^{3-}$ in feed stream and initial concentration in reactor [M]
C_{B0} = Concentration of $DETA.3H^{3+}$ in feed stream [M]
υ_{out} = $\upsilon_A + \upsilon_B$ = Volumetric flow of the exit stream [dm^3/h]

A set of algebraic equilibrium constraints, in Equations (3.1.4) to (3.1.6), describe the equilibrium concentration transient of hexachlororhodate (III), protonated diethylenetriamine and the salt at each time step.

$$V_r C_A(t) - V_r C_{Ae}(t) - R_{eq}(t) = 0 \tag{3.1.4}$$

$$V_r C_B(t) - V_r C_{Be}(t) - R_{eq}(t) = 0 \tag{3.1.5}$$

$$-V_r C_{Ce}(t) + R_{eq}(t) = 0 \tag{3.1.6}$$

Where C_{Ae} = Equilibrium concentration of $RhCl_6^{3-}$ expressed as mol per unit suspension volume [M]
C_{Be} = Equilibrium concentration of $DETA.3H^{3+}$ expressed as mol per unit suspension volume [M]
C_{Ce} = Equilibrium concentration of $[RhCl_6][DETA.3H]$ crystals expressed as mol per unit suspension volume [M]
R_{eq} = Equilibrium amount of $RhCl_6^{3-}$ and $DETA.3H^{3+}$ consumed through Equation (3.1.1) stoichiometry [mol]

The equilibrium condition at any point during the transient must conform to Equation (3.1.7).

$$\gamma_{\pm} C_{Ae} C_{Be} = K_{SP} \quad \textbf{(3.1.7)}$$

Where $\gamma_{\pm}$ = Mean activity coefficient
K_{SP} = Solubility product [M^2]

The mean activity coefficient expression is similar to the activity model defined by Debye-Hückel theory. Regression allowed quantifying the activity coefficient model parameters, this procedure is described in Chapter 5, Section 5.1. Equation (3.1.8) presents the activity coefficient model as determined in this work. Equation (3.1.9) presents the solubility product as determined in this work.

$$\gamma_{\pm} = exp\left(-10.4\sqrt{9C_{Ae} + 9C_{Be} + 12} + 36.01\right) \quad \textbf{(3.1.8)}$$

$$K_{SP} = exp\left(0.976 - \frac{4316}{T}\right) \quad \textbf{(3.1.9)}$$

Where T = System temperature [K]

The numerical procedure requires calculating the unreactive concentration profiles by Equations (3.1.2) and (3.1.3) over a defined period by using the volumetric flow rates and initial conditions as measured in the experiment. The mass balance constraint fixes C_{Be} and is obtained by subtracting Equation (3.1.5) from Equation (3.1.4) to give Equation (3.1.10).

$$\begin{aligned} &C_A(t) - C_{Ae}(t) - C_B(t) + C_{Be}(t) = 0 \\ &\therefore C_{Be}(t) = C_{Ae}(t) + C_B(t) - C_A(t) \end{aligned} \quad \textbf{(3.1.10)}$$

The equilibrium constraint is obtained substituting C_{Be} in Equation (3.1.7) with Equation (3.1.10) and inserting the expressions for the solubility product and the activity coefficient giving Equation (3.1.11).

$$C_{Ae}(t)[C_{Ae}(t) + C_B(t) - C_A(t)] = \frac{exp\left(10.4\sqrt{9\left(2C_{Ae}(t) + C_B(t) - C_A(t)\right) + 12}\right)}{exp\left(\frac{4316}{T} + 36.986\right)} \quad \textbf{(3.1.11)}$$

The objective function is set equal to the difference of the squared right-hand and left-hand sides of Equation (3.1.11) and is shown in Equation (3.1.12).

$$OF = (C_{Ae}(t)[C_{Ae}(t) + C_B(t) - C_A(t)])^2 - \frac{exp\left(20.8\sqrt{9\left(2C_{Ae}(t) + C_B(t) - C_A(t)\right) + 12}\right)}{exp\left(\frac{8632}{T} + 73.972\right)} \quad \textbf{(3.1.12)}$$

At each time step the equilibrium objective function, Equation (3.1.12), is set to zero by adjusting C_{Ae} whilst adhering to the physical constraint that $0 < C_{Ae} < C_A$. To assist with numerical precision the objective function is scaled by 1E6. Solver in Microsoft Excel 2013© is used to determine the equilibrium concentration through constrained non-linear minimisation. The minimisation routine in Solver Excel© uses the generalized reduced gradient algorithm that uses forward differences to estimate the derivative of the objective function.

3.1.2. CSTR Population balance

SEM photographs of crystals formed during initial tests indicated a tendency for the crystals to form agglomerated clusters. Typically, the precipitates formed gave rise to bimodal crystal size distributions by volume. The same bimodal behaviour was observed at similar conditions in a previous semi batch reactor study by Hagemann et al. (2003).

It is postulated that the crystal disruption / breakage process, represented by the terms $B_{dis} - D_{dis}$ in Equation (2.1.7), is the cause for the bimodal behaviour and is further explored through the derived model that follows. Unlike the classic approach in Jones, (2002) and Mersmann, (2001) where each birth and death term is represented by a function representing aggregation or disruption, the approach here lumps these processes into one term.

The aggregation and disruption mechanism in this work is derived on the basis that the steady state population balance solution is bimodal. It is assumed that the agglomeration or disruption rate is the size gradient of the normal growth process and is given in Equation (3.1.13). If the sign of the rate is negative it is a particle generating process, if it is positive it is a particle consuming process. Another description of Equation (3.1.13) is that it is a particle number flux over a crystal surface analogous to Fick's law of diffusion combined with convection as described in Atkins (1997). A justification of the proposed model is given in Section 10.2 in the Appendix. The model is similar to the random fluctuation model that is used to describe growth rate dispersion by Randolph and White (Myerson, 2002).

$$R_{ag} = B_{ag} - D_{ag} + B_{dis} - D_{dis} = \frac{\partial}{\partial L} G_a \tau \left(\frac{n}{\tau} + G \frac{\partial n}{\partial L} \right) \tag{3.1.13}$$

Where R_{ag} = Crystal aggregation or disruption rate [#/µm.dm^3.h]
G_a = Crystal growth rate due to aggregation (agglomeration) when positive and crystal disruption (breakage) rate when negative [µm/h]
τ = Reactor residence time representing the time required to form an averaged sized aggregate or fracture = V_r/υ_{out} [h]
n = Population density [#/µm.dm^3]
L = Crystal characteristic size (largest crystal dimension) [µm]

A combination of Equations (2.1.7) and (3.1.13) gives rise to the transient population balance in Equation (3.1.14), with the aggregation or disruption model proposed in this work.

$$\frac{\partial n}{\partial t} + \frac{\partial (nG)}{\partial L} = -\frac{n}{\tau} + R_{ag} \tag{3.1.14}$$

If growth by interfacial attachment, G, and agglomerative or disruptive/breakage growth, G_a, are independent of size Equation (3.1.14) expands to Equation (3.1.15).

$$\frac{\partial n}{\partial t} + (G - G_a)\frac{\partial n}{\partial L} - G G_a \tau \frac{\partial^2 n}{\partial L^2} + \frac{n}{\tau} = 0 \tag{3.1.15}$$

To give rise to a bimodal population density function and volume fraction distribution the boundary conditions at steady state are as shown in Equation (3.1.16) and is typical from literature, (Jones, 2002; Bałdyga & Bourne, 1999; Garside et al., 2002; Ramkrishna, 2000). Here the boundary conditions confirm to a population density-size relationship that is exponential.

$$\begin{aligned} n(0, t_{ss}) &= n_{01} + n_{02} = constant \\ n(\infty, t_{ss}) &= 0 \end{aligned} \tag{3.1.16}$$

Where n_{0i} = ith Nucleated population density at size zero [#/dm^3.µm]
t_{ss} = Time to attain steady state where $\partial n/\partial t = 0$ [h]

The steady state solution of Equation (3.1.15) using the boundary conditions in Equation (3.1.16) is then given by Equation (3.1.17).

$$n(L,t>t_{ss}) = n_{01}exp\left(-\frac{L}{G\tau}\right) + n_{02}exp\left(\frac{L}{G_a\tau}\right) \qquad \textbf{(3.1.17)}$$

Note that the population density in Equation (3.1.17) is only valid for negative values of G_a considering the upper population density bound that requires the limit of the population density to be zero as size tends to infinity. Therefore, under the requirement that G_a is less than zero it is more appropriate to refer to Equation (3.1.13) as a net disruption or breakage term as it tends to increase the number of particles in the system. It is shown later that if the process is one of agglomeration (reduces the number of particles) then G_a must be greater than zero. When agglomeration is present the boundary condition at size infinity requires n_{02} to be zero otherwise the population density diverges to infinity at increasing size. The steady state population density therefore reduces to the standard exponential distribution when G_a is greater than zero. In Section 3.1.3 this statement is justified by Equation (3.1.29) when the nucleation and growth kinetic expressions are defined.

To illustrate the potential to model a bimodal volume fraction distribution assume the process is one of disruption or breakage. The cumulative volume fraction transformation of Equation (3.1.17) has an analytic solution that is given by Equation (3.1.18). As mentioned earlier, a previous study by Hagemann, et al., (2003) showed bimodal crystal size distributions of diethylenetriammonium hexachlororhodate (III) salt precipitated under various conditions in a semi batch reactor. By inspection Equation (3.1.18) appears to be bimodal as it is a mixed exponential distribution. The form of the population balance in Equation (3.1.15) therefore has the potential to model this system.

$$\begin{aligned}
&\Phi(L) = \frac{\int_0^L nl^3dl}{\int_0^\infty nl^3dl} = 1 - \sum_{i=1}^{2} x_i exp(-B_iL)\left[1 + B_iL + \frac{(B_iL)^2}{2} + \frac{(B_iL)^3}{6}\right] \\
&with \quad x_1 = \frac{n_{01}G^4}{n_{01}G^4 + n_{02}G_a^4} \qquad \& \qquad x_2 = 1 - x_1 \\
&\qquad\quad B_1 = \frac{1}{G\tau} \qquad\qquad\qquad \& \qquad B_2 = \frac{1}{G_a\tau}
\end{aligned} \qquad \textbf{(3.1.18)}$$

A natural conclusion that follows from the above discussion is that under conditions where agglomeration exists the population balance transient never diminishes as the steady state solution diverges to infinity. Now consider the case when breakage or disruption is negligible and aggregation through agglomeration dominates. First the transient population balance is simplified into a set of time dependent ordinary differential equations by the method of moments. The population density moments are defined in Equation (3.1.19) and is a common definition in Garside et al. (2002), Jones (2002), Ramkrishna (2000) and Myerson (2002).

$$M_i = \int_0^\infty nL^i dL \qquad i = 0, 1, 2, 3 \ldots \qquad \textbf{(3.1.19)}$$

Where M_i = ith Population density moment [#.µmⁱ/ dm³]

When the size variable is eliminated from Equation (3.1.15) through the moment conversion in Equation (3.1.19) the moment generating function is obtained, Equation (3.1.20).

$$\begin{aligned}
\frac{dM_i}{dt} &= -(G - G_a)\left(L^i n(L,t)\Big|_{L=0}^{L\to\infty} - iM_{i-1}\right) \\
&\quad + GG_a\tau\left(L^i\frac{\partial n}{\partial L}\Big|_{L=0}^{L\to\infty} - iL^{i-1}n(L,t)\Big|_{L=0}^{L\to\infty} + i(i-1)M_{i-2}\right) - \frac{M_i}{\tau}
\end{aligned} \qquad \textbf{(3.1.20)}$$

Note that all crystal size distributions produced in this work gave rise to lognormal or mixed lognormal size distributions for the cumulative volume fraction. This suggests that the population density can contain elements from the lognormal distribution. The form of the population density under the above conditions is derived in

Section 10.3 in the Appendix. The first size derivative of a lognormal population density distribution gives Equation (3.1.21).

$$
\begin{aligned}
&\frac{\partial n}{\partial L} = -\frac{(-m + 4s^2 + \ln L)}{s^2 L^5} exp\left(-\frac{(\ln L - m)^2}{2s^2}\right) \\
&\therefore \lim_{L\to 0^+} \frac{\partial n}{\partial L} = \lim_{L\to\infty} \frac{\partial n}{\partial L} = 0 \quad \Leftrightarrow \quad m \in \mathbb{R}, s > 0
\end{aligned}
\qquad \textbf{(3.1.21)}
$$

Equation (3.1.21) provides a base to define the boundary conditions of Equation (3.1.20) that are different from the exponential population density boundary conditions in Equation (3.1.16). The boundary conditions for a lognormal type population density is therefore as shown in Equation (3.1.22).

$$
\begin{aligned}
&n(0,t) = n_0(t) \\
&n(\infty,t) = 0 \\
&\left.\frac{\partial n}{\partial L}\right|_{L=0} = \left.\frac{\partial n}{\partial L}\right|_{L\to\infty} = 0
\end{aligned}
\qquad \textbf{(3.1.22)}
$$

The simplified expansion of Equation (3.1.20) given the boundary conditions in Equation (3.1.22) is given in matrix form in Equation (3.1.23). The initial conditions denoted by IC, is zero for all moments.

$$
\begin{bmatrix} \frac{dM_0}{dt} \\ \frac{dM_1}{dt} \\ \frac{dM_2}{dt} \\ \frac{dM_3}{dt} \\ \frac{dM_4}{dt} \end{bmatrix} = \boldsymbol{A} \begin{bmatrix} M_0 \\ M_1 \\ M_2 \\ M_3 \\ M_4 \end{bmatrix} + \begin{bmatrix} (G - G_a)n_0(t) \\ GG_a\tau n_0(t) \\ 0 \\ 0 \\ 0 \end{bmatrix} \quad \& \quad IC\colon \begin{bmatrix} M_0 \\ M_1 \\ M_2 \\ M_3 \\ M_4 \end{bmatrix}_{t=0} = \begin{bmatrix} 0 \\ 0 \\ 0 \\ 0 \\ 0 \end{bmatrix} \qquad \textbf{(3.1.23)}
$$

The connection matrix is given in Equation (3.1.24).

$$
\boldsymbol{A} = \begin{bmatrix}
-\frac{1}{\tau} & 0 & 0 & 0 & 0 \\
(G - G_a) & -\frac{1}{\tau} & 0 & 0 & 0 \\
2GG_a\tau & 2(G - G_a) & -\frac{1}{\tau} & 0 & 0 \\
0 & 6GG_a\tau & 3(G - G_a) & -\frac{1}{\tau} & 0 \\
0 & 0 & 12GG_a\tau & 4(G - G_a) & -\frac{1}{\tau}
\end{bmatrix} \qquad \textbf{(3.1.24)}
$$

Typically, nucleation rate is very sensitive to changes in saturation (Mersmann, 2001). Saturation in a transient reactor changes over time due to chemical reaction. For this reason, nucleation, will tend to be a function that rapidly changes with time giving rise to a system of differential equations that are likely to be stiff. Stiffness in general does not have an exact definition but the effect thereof is usually an unstable numeric solution of a system of differential equations. This is typical of differential equations that model chemically reactive systems (Burden & Faires, 1993). Care was thus taken to select an appropriate numeric solution method.

The numerical method that was most successful to solve the system in Equations (3.1.23) and (3.1.24) was found to be the modified Rosenbrock formula of order two that is programmed as a standard Matlab function '*ode23s*', (Shampine & Reichelt, 1997). The variable step solver, '*ode15s*', that is based on numeric differencing formulas or NDFs by Shampine & Reichelt (1997) and Shampine et al. (1999) also worked but gave less reliable results. The minimum time step in both variable step solvers '*ode23s*' and '*ode15s*' was automatically set by the software and typically ranged between 1E-15h to 1E-18h. Shape preservation was activated for both solvers. The model represented by Equations (3.1.23) and (3.1.24) was coded in Simulink®, available in Matlab version R2009a.

3.1.3. CSTR Nucleation and growth kinetics

The mass balance in Section 3.1.1 highlighted that the reaction rapidly proceeds to equilibrium and poses a challenge to determine the system saturation that drives crystal growth. It should be noted that one could use a segregated feed model (SFM) to describe saturation within each separate feed plume with the assumption that the bulk is at equilibrium in accordance with the modelling work by Zauner & Jones (2002). However, a small reactor that is ideally mixed in terms of the aqueous is likely to have small segregated mixing zones that are potentially negligible or too small to model.

The segregated feed model approach is therefore not considered on the 2dm^3 scale and saturation is estimated from the unreactive concentration profiles of hexachlororhodate (III) in Equation (3.1.2) and protonated diethylenetriamine in Equation (3.1.3). It is assumed that the driving force for crystal growth and nucleation is the difference between the unreactive concentration and the equilibrium concentration at a specific point in time within the CSTR.

It is not uncommon to use activity coefficients to define saturation ratio in particular when the thermodynamics of the system is not ideal, (Bałdyga & Bourne, 1999; Garside et al., 2002; Myerson, 2002; Zauner & Jones, 2002). Given a known activity coefficient model, the saturation ratio in this work is defined in Equation (3.1.25) and is consistent with the definition in the literature for non-ideal solute-solvent mixtures.

$$S = \sqrt{\frac{\gamma_{\pm} C_A C_B}{K_{SP}}} \tag{3.1.25}$$

Where C_A = Concentration of $RhCl_6^{3-}$ from unreactive mass balance, Equation (3.1.2) [M]
C_B = Concentration of DETA.$3H^{3+}$ from unreactive mass balance, Equation (3.1.3) [M]
K_{SP} = Solubility product at the system temperature [M^2]
$\gamma_{\pm}$ = Mean activity coefficient at the system equilibrium concentrations
S = Saturation ratio

Nucleation and growth is assumed to be related to supersaturation ($S - 1$) by power law and is an assumption common to Myerson (2002) and Jones (2002). From the literature, primary nucleation is associated with crystal forming directly from a saturated solution whereas secondary nucleation is induced by physical surfaces present in the system such as the reactor wall, the impeller blades and shaft and also the surfaces of the other crystals in the system, (Garside et al., 2002; Jones, 2002; Myerson, 2002).

In this work the effect of agitation power was not investigated. The agitation power was kept constant at a level to achieve CSTR conditions. No experiments were done to establish a difference between primary and secondary nucleation terms, they were viewed to occur simultaneously at a rate that could be combined. The nucleation rate presented here is a sum of primary and secondary mechanisms and it is assumed that it translates to a boundary condition that follows a power law with supersaturation.

From the population balance texts, the size zero boundary condition is generally accepted to be the ratio of nucleation rate to growth rate at size zero according to Ramkrishna (2000). As both terms are assumed to be a power function of supersaturation it is reasonable to state that the population density at size zero will also be a power function albeit with an exponent that is the difference between the nucleation rate exponent and the growth rate exponent. The expression is given in Equation (3.1.26) where the nucleation rate constant is assumed to be an Arrhenius expression.

$$n_0(t) = K_n(S-1)^{\beta} = A_n exp\left(\frac{B_n}{T}\right)(S-1)^{\beta} \tag{3.1.26}$$

Where $n_0(t)$ = Population density boundary at size zero [#/μm.dm^3]
K_n = Nucleation rate constant [#/μm.dm^3]
A_n = Primary nucleation frequency constant [#/μm.dm^3]
B_n = Primary nucleation activation energy divided by the gas constant [K]
T = Temperature [K]

β = Population density at size zero supersaturation exponent

The growth rate through integration of unit cells into the crystal lattice is assumed to follow a supersaturation power law as suggested in Garside et al. (2002), Jones (2002) and Bałdyga & Bourne (1999). This growth rate represents the transfer of paired ions, a new molecule, from the solution phase to the crystal. The relationship is given in Equation (3.1.27).

$$G = K_g(S-1)^{\alpha} = A_g exp\left(\frac{B_g}{T}\right)(S-1)^{\alpha} \qquad \textbf{(3.1.27)}$$

Where G = Growth rate [µm/h]
K_g = Growth rate constant [µm/h]
A_g = Growth rate frequency constant [µm/h]
B_g = Growth rate activation energy divided by the gas constant [K]
α = Growth rate supersaturation exponent

Crystal agglomeration is believed to occur due to crystal collisions that are induced by the agitation of the mixture, implying orthokinetic agglomeration. During an agglomeration event, it is likely that dissolved crystal in the solution phase is precipitated onto the surface of the contact area between the two crystals that agglomerate, implying that the agglomeration rate is a function of solution saturation. This concept agrees with the finding by Zauner & Jones (2000) that agglomeration of calcium oxalate in an MSMPR configuration is related to supersaturation through a power law. From classic agglomeration theory, the above discussion implies that the agglomeration rate is proportional to the number of crystals squared in the system (Mersmann, 2001; Myerson, 2002); Jones, 2002).

To incorporate the classic agglomeration rate dependency on the number of crystals, it is assumed that the agglomerative growth rate is proportional to the number of crystals in the system squared (zeroth moment) and to system supersaturation. The Arrhenius equation is used to describe the agglomeration rate temperature dependence. From the above, the formulated relationship between agglomerative growth, supersaturation, number of particles and system temperature is shown in Equation (3.1.28).

$$G_a = K_{ag}M_0^2(S-1) = A_{ag} exp\left(\frac{B_{ag}}{T}\right)M_0^2(S-1) \qquad \textbf{(3.1.28)}$$

Where G_a = Agglomerative growth rate [µm/h]
K_{ag} = Agglomeration growth rate constant [µm.dm^3/#.h]
A_{ag} = Agglomerative growth rate frequency constant [µm.dm^3/#.h]
B_{ag} = Agglomerative growth rate activation energy divided by the gas constant [K]
M_0 = Zeroth population density moment, number of crystals per volume [#/dm^3]

If a breakage or disruption mechanism is included into the population balance it would require that another term, like Equation (3.1.13), is added to the population balance in Equation (3.1.14) with the growth term negative in sign. It is likely that the disruption or breakage rate is related to variables that translate to shear stress in the mixture such as agitation rate and pulp density as literature suggests (Zauner & Jones, 2002). However, these variables were not changed in this work therefore it is believed that any disruption or breakage mechanism would be considered part of the agglomerative growth rate frequency constant and it is not further considered.

The definition of the agglomeration growth rate in Equation (3.1.28) permits further discussion on the sign of the agglomeration rate in Equation (3.1.14). To continue the zeroth moment (i = 0) is first determined by inserting the boundary conditions in Equation (3.1.22) into the moment generating function in Equation (3.1.20). Substituting the assumed nucleation, growth and agglomeration rate functions, Equations (3.1.26) to (3.1.28), into the zeroth moment equation then gives Equation (3.1.29).

$$\frac{dM_0}{dt} = K_gK_n(S-1)^{\alpha+\beta} - K_{ag}K_n(S-1)^{1+\beta}M_0^2 - \frac{M_0}{\tau} \qquad \textbf{(3.1.29)}$$

In Equation (3.1.29) the first term on the right-hand side generates new particles and is effectively the nucleation rate driven by both temperature and saturation. The second term consumes particles and is proportional to the number of particles squared in the system as well as supersaturation. This term represents particle disappearing due to agglomeration and is consistent with the work of von Smoluchowski as described in Mersmann (2001). The last term in Equation (3.1.29) represents particles being swept out of the reactor through the discharge stream. If the agglomerative growth term was negative, i.e. $G_a < 0$, it is easy to deduce that the second term in Equation (3.1.29) would be positive implying particles are generated. In terms of agglomeration this is not possible therefore for the case of $G_a < 0$ the term must represent something else such as crystal disruption or breakage.

The moment balance is fully specified by inserting Equations (3.1.2), (3.1.3), (3.1.27) to (3.1.29) into Equation (3.1.23) and specifying the constants K_{SP}, $\gamma_\pm$, α, β, b_s, A_n, B_n, A_g, A_{ag}, B_g and B_{ag}. In addition, the initial reagent concentrations (C_{A0} and C_{B0}) in the feed streams, the feed flows (υ_A and υ_B), the reactor volume V_r, the initial reactor concentrations and lastly the initial reactor moments and concentrations must also be specified to enable moment and concentration profile calculation.

3.1.4. Initial guess for nucleation and growth exponents through steady state equilibrium mass balance

The purpose of this section is to establish an initial guess for the growth and nucleation exponents in Equations (3.1.26) and (3.1.27). Literature suggests that the nucleation saturation ratio exponent is in most cases ≥ 2 for primary nucleation. Growth saturation exponents are typically ≥ 1 but smaller than or equivalent to the nucleation saturation exponent (Myerson, 2002).

For this system, initial growth and nucleation exponents are estimated by assuming steady state and that equilibrium is reached in the bulk. At equilibrium, it is assumed that the crystals nucleate and grow mostly where the bulk is in contact with the reagent dip-pipes, i.e. at a point in the reactor where the reagent concentrations are not at equilibrium values. The transient mass balance for the two reacting components is given in Equations (3.1.30) and (3.1.31).

$$\frac{dC_{Ae}}{dt} = \frac{\upsilon_A C_{A0} - \upsilon_{out} C_{Ae} - R_{eq}}{V_r} \tag{3.1.30}$$

$$\frac{dC_{Be}}{dt} = \frac{\upsilon_B C_{B0} - \upsilon_{out} C_{Be} - R_{eq}}{V_r} \tag{3.1.31}$$

To eliminate the equilibrium quantity reacted, Equation (3.1.30) is subtracted from (3.1.32) to obtain Equation (3.1.32).

$$\frac{dC_{Ae}}{dt} - \frac{dC_{Be}}{dt} = \frac{(\upsilon_A C_{A0} - \upsilon_{out} C_{Ae}) - (\upsilon_B C_{B0} - \upsilon_{out} C_{Be})}{V_r} \tag{3.1.32}$$

The equilibrium condition in differential form is obtained by differentiating Equation (3.1.7) with respect to time. Equation (3.1.33) is obtained after setting the background ionic strength equal to K_1 (sum of hydronium and chloride concentrations divided by two). Note that the solubility product under isothermal conditions remains constant, therefore its differential with respect to time is zero. Furthermore K_1 is assumed constant, therefore its differential with respect to time is also zero.

$$\begin{gathered}\frac{d\gamma_\pm}{dt} C_{Ae} C_{Be} + \frac{dC_{Ae}}{dt} \gamma_\pm C_{Be} + \frac{dC_{Be}}{dt} \gamma_\pm C_{Ae} = 0 \\ \therefore \frac{dC_{Be}}{dt} = -\frac{C_{Be}}{C_{Ae}} \left(\frac{9C_{Ae}A_1 + 4\sqrt{4.5C_{Ae} + 4.5C_{Be} + K_1}}{9C_{Be}A_1 + 4\sqrt{4.5C_{Ae} + 4.5C_{Be} + K_1}} \right) \frac{dC_{Ae}}{dt}\end{gathered} \tag{3.1.33}$$

The goal, as in Section 3.1.1, is to eliminate the unknown quantity of hexachlororhodate (III) reacted at equilibrium, R_{eq}, and back substitute the dC_{Be}/dt term into Equation (3.1.33). The elimination procedure was demonstrated in Equation (3.1.32) that was rearranged to make dC_{Be}/dt the argument. After substitution, Equation (3.1.34) is the result.

$$\frac{dC_{Ae}}{dt} = \frac{v_A C_{A0} - v_B C_{B0} + v_{out}(C_{Be} - C_{Ae})}{V_r\left[1 + \frac{C_{Be}}{C_{Ae}}\left(\frac{9C_{Ae}A_1 + 4\sqrt{4.5C_{Ae} + 4.5C_{Be} + K_1}}{9C_{Be}A_1 + 4\sqrt{4.5C_{Ae} + 4.5C_{Be} + K_1}}\right)\right]} \tag{3.1.34}$$

The protonated diethylenetriamine transient is obtained by rearranging Equation (3.1.7) such that the concentration of protonated diethylenetriamine is the argument (see Equation (3.1.35)).

$$C_{Be} = \frac{K_{SP}}{\gamma_{\pm} C_{Ae}} \tag{3.1.35}$$

Evident from Equations (3.1.34) and (3.1.35) is the occurrence of an algebraic loop. To solve for Equation (3.1.34) one must specify C_{Be}, and that requires the specification of C_{Ae}. Note that the system will only equilibrate to C_{Be} after a sufficient quantity of protonated diethylenetriamine ($v_B C_{B0}$) is added. This is modelled by numerically setting dC_{Ae}/dt equal to zero until sufficient time has passed for Equation (3.1.35) to be valid. The crystal concentration is calculated by making R_{eq} the argument in Equation (3.1.30) and substituting the hexachlororhodate (III) transient with Equation (3.1.34) and then inserting the result into the transient crystal mass balance. Equation (3.1.36) gives the simplified result for the crystal concentration transient.

$$\frac{dC_C}{dt} = \frac{v_A C_{A0} - v_{out}(C_C + C_{Ae})}{V_r} - \frac{v_A C_{A0} - v_B C_{B0} + v_{out}(C_{Be} - C_{Ae})}{V_r\left[1 + \frac{C_{Be}}{C_{Ae}}\left(\frac{9C_{Ae}A_1 + 4\sqrt{4.5C_{Ae} + 4.5C_{Be} + K_1}}{9C_{Be}A_1 + 4\sqrt{4.5C_{Ae} + 4.5C_{Be} + K_1}}\right)\right]} \tag{3.1.36}$$

Equations (3.1.34) to (3.1.36) describe the precipitation behaviour at equilibrium conditions during the transient and yields the same results as the method outlined in Section 3.1.1.

The saturation at the feed is the product between the feed concentration of, for example, specie B and the equilibrium concentration of specie A, or vice versa at feed point of specie A. Equation (3.1.36) was rearranged to make C_C the argument after setting the transient to zero. All the remaining terms were arranged into a saturation term, and the result is shown in Equation (3.1.37).

$$\begin{gathered} C_C = \frac{v_A K_{SP}}{v_{out}\gamma_{\pm}}(S_0^2 - S_A^2) \quad or \quad C_C = \frac{v_A K_{SP}}{v_{out}\gamma_{\pm}}(S_0^2 - S_B^2) \\ S_A = \sqrt{\frac{\gamma_{\pm} C_{A0} C_{Be}}{K_{SP}}} \quad , \quad S_B = \sqrt{\frac{\gamma_{\pm} C_{B0} C_{Ae}}{K_{SP}}} \quad \& \quad S_0 = \sqrt{\frac{\gamma_{\pm} C_{A0} C_{B0}}{K_{SP}}} \end{gathered} \tag{3.1.37}$$

The crystal concentration is related to the population balance through the third moment as described in literature (Garside et al., 2002; Jones, 2002). It is assumed that the volume shape factor is constant and that agglomeration is present. Equation (3.1.38) shows the crystal concentration as derived from the third moment of Equation (3.1.17) with n_{02} set to zero.

$$\begin{aligned} C_C &= \rho_c K_v \int_0^{\infty} nL^3 dL \\ &= \rho_c K_v \int_0^{\infty} n_{01} exp\left(-\frac{L}{G\tau}\right) L^3 dL \\ &= \rho_c K_v 6\tau^4 n_{01} G^4 \end{aligned} \tag{3.1.38}$$

By inspection, the highest power of saturation is 2 in Equation (3.1.37); likewise, the highest power of growth is 4 in Equation (3.1.38). To solve for growth rate as a function of saturation, Equation (3.1.37) is equated to (2.1.39). The highest power of saturation obtained this way is 0.5. It is therefore assumed that a good starting point for α in Equation (3.1.27) is 0.5. Applying the same method to solve for n_{01} it is found that the highest power of saturation is 2, implying that a reasonable starting point for β in Equation (3.1.26) is 2.

3.2. PFR MASS AND POPULATION BALANCE

In the sections that follow an idealised model is proposed for a t-mixer configuration with a plug flow reactor in series. It is assumed that the design of the reactor reduces axial dispersion to the point that it is negligible. Furthermore, it is assumed that the crystal suspension moves through the reactor like a plug and that the feed solutions are perfectly mixed at the point in the t-mixer where the feed solutions meet.

3.2.1. PFR Mass balance

The initial plug flow experiments showed that the extent of the reaction did not always proceed to equilibrium under certain input flow rates. Additionally, the initial experiments indicated that hexachlororhodate (III) conversion to salt was related to the Reynolds number, and beyond a threshold the conversion reached a plateau. From these observations, it is postulated that the reaction rate can become limited by mixing at a scale smaller than the reactor. The finding by Hagemann et al. (2003) suggests that mixing at the mesoscale may be a prominent mechanism limiting reaction rate.

Based on the above discussion it is proposed that the reaction rate is proportional to the difference between bulk concentration and equilibrium concentration of hexachlororhodate (III). This is a common driving force in reaction kinetics, especially if there are mass transfer limitations and the reaction order is one (see Levenspiel, 1999; Perry & Green, 1998). Considering the above points, the proposed reaction rate for this system in the PFR configuration is shown in Equation (3.2.1).

$$r_A = \hat{A}_p h(C_A - C_{Ae}) \qquad \textbf{(3.2.1)}$$

Where r_A = Reaction rate [mol/dm^3.s]
C_A = Hexachlororhodate (III) concentration or $RhCl_6^{3-}$ [mol/dm^3]
C_{Ae} = Equilibrium hexachlororhodate (III) concentration [mol/dm^3]
$\hat{A}_p$ = Specific particle area [m^2/m^3]
h = Mass transfer rate constant [m/s]

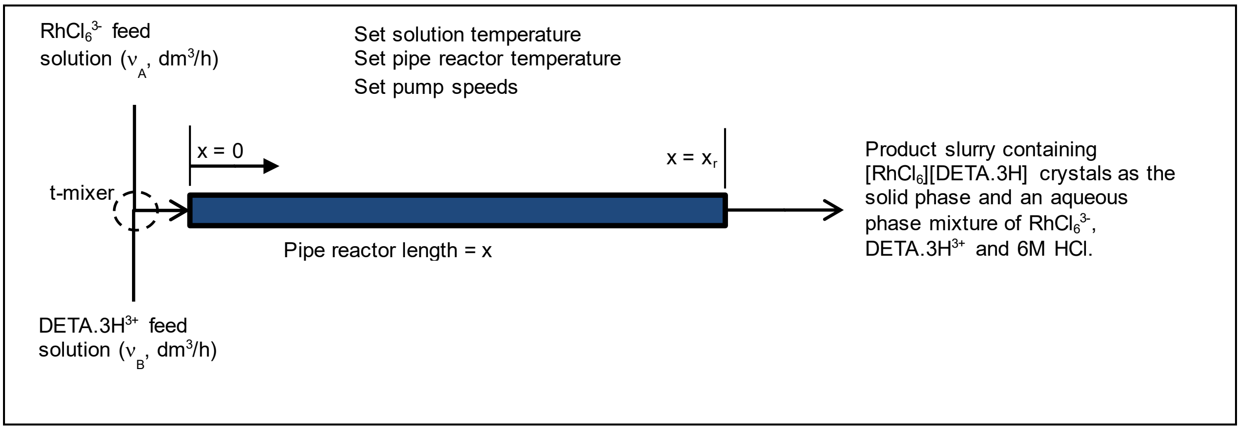

Figure 3.2.1: PFR flow schematic

In the literature, the mass transfer rate constant is typically related to the Sherwood number that in turn is an empirical function of the particle Reynolds and the solution Schmidt numbers as is shown in Equation (3.2.2) (Perry & Green, 1998). Here it is assumed that the characteristic length in the Sherwood number is represented by the diameter of the pipe reactor and the particle Reynolds number is defined based on volume average particle size or L_{43}.

$$\begin{aligned} &h = \frac{ShD_{AB}}{D} \\ &with \quad Sh \propto Re_p^m Sc^n \\ &\therefore h = cRe_p^m Sc^n \frac{D_{AB}}{D} = cReRe_p^{m-1} Sc^n D_{AB} \frac{L_{43}}{D^2} \end{aligned} \qquad \textbf{(3.2.2)}$$

Where Sh = Sherwood number
D_{AB} = Diffusivity of paired $RhCl_6^{3-}$ and $DETA.3H^{3+}$ in 6M hydrochloric acid [m^2/s]
Re_p = Particle Reynolds number = uL_{43}/η
Re = Reactor Reynolds number = uD/η
η = Aqueous phase viscosity [m^2/s]
u = Pulp linear velocity [m/s]
D = Reactor diameter [m]
Sc = Schmidt number = D_{AB}/η
c = Proportionality constant of the correlation, $Sh \propto Re^m Sc^n$

From the definition of the Schmidt number it is obvious to state that it is primarily temperature dependent as it is a function of the diffusivity and the solution viscosity, both being strong functions of temperature (Lide, 2007; Perry & Green, 1998). Furthermore, if Equation (3.2.2) is inserted into Equation (3.2.1) it becomes apparent that the reaction rate is proportional to the reactor Reynolds number. This justifies to an extent the initial plug flow experiment's observation regarding the Reynolds number.

The rate equation in Equation (3.2.1) is simplified by factoring out the Reynolds number and lumping all resulting terms together into a pseudo rate constant, K_r. It is important to stress that the specific particle surface area $\hat{A}_p$ in Equation (3.2.1) is proportional to the second moment of the population balance, as described in Chapter 2. Typically, reaction rate is proportional to the second moment as discussed in Bałdyga & Bourne (1999), Garside et al. (2002), Mersmann (2001) and Myerson (2002). Thus, by lumping the particle surface area into the pseudo rate constant it is inherently assumed that the second moment will have an average constant effect on the rate of reaction over the length of the reactor. This assumption automatically excludes mass transfer across the particle boundary layer as a growth limitation. Equation (3.2.3) presents the mass balance for hexachlororhodate (III) in solution in the PFR flow configuration shown in Figure 3.2.1 by taking into account the simplifying assumptions made above.

$$\begin{aligned} &\frac{dC_A}{dx} = -\frac{A_c}{v_A + v_B} r_A = -\frac{r_A}{u} = -K_r Re(C_A - C_{Ae}) \\ &with \quad K_r = c\hat{A}_p Re_p^{m-1} Sc^n D_{AB} \frac{L_{43}}{uD^2} \end{aligned} \tag{3.2.3}$$

Where K_r = Pseudo rate constant, empirically related to temperature, pulp velocity, reactor diameter, specific particle area and L_{43} size [1/m]
x = Reactor length [m]
A_c = Reactor cross sectional area [m^2]
v_i = Volumetric flow rate of the feed reagents (i = A, B), [m^3/s]

Equation (3.2.4) gives the mass balance for protonated diethylenetriamine and Equation (3.2.5) gives the mass balance for diethylenetriammonium hexachlororhodate salt.

$$\frac{dC_B}{dx} = -\frac{r_A}{u} = -K_r Re(C_A - C_{Ae}) \tag{3.2.4}$$

$$\frac{dC_C}{dx} = \frac{r_A}{u} = K_r Re(C_A - C_{Ae}) \tag{3.2.5}$$

Where C_B = Protonated diethylenetriamine or DETA.3HCl [mol/dm^3]
C_C = Diethylenetriammonium hexachlororhodate crystal concentration or $[RhCl_6][DETA.3H]$ [mol/dm^3]

Equation (3.2.3) is solved analytically with an initial condition C_{A0} and the assumption that specific particle area remains constant along the length of the reactor. The solution is shown in Equation (3.2.6).

$$X_A = X_{Ae}\left(1 - exp(-ReK_r x)\right)$$
$$with\ X_A = 1 - \frac{C_A}{C_{A0}} \quad \&\quad X_{Ae} = 1 - \frac{C_{Ae}}{C_{A0}} \tag{3.2.6}$$

Where X_A = Conversion of $RhCl_6^{3-}$
X_{Ae} = Equilibrium conversion of $RhCl_6^{3-}$

Initial experimental observation suggests that low Reynolds number causes reduced conversion, as implied by Equation (3.2.6). It is thus possible that the limitation is related to the mixing time within the PFR configuration. Various researchers have demonstrated the effect of mixing scales on reaction conversion. Systems of parallel competing reaction schemes are frequently used to illustrate that mixing efficiency on either the micro- or mesoscale can determine reactant conversion and product selectivity (Bałdyga et al., 1998; Falk & Villermaux, 1997; Fang & Lee, 2001).

In the PFR configuration, a low Reynolds number would imply the mixing intensity on the microscale is low as studies by Falk & Villermaux (1997) and Fang & Lee (2001) suggest. The literature review in Chapter 2 presents a case study where reaction conversion is sensitive to mixing on the micro- and mesoscales. At a low Reynolds number where mixing intensity is low, literature suggests that mesoscale mixing factors are more likely to contribute to conversion.

At a high Reynolds number, the mixing intensity is high and the solution plug is completely homogenised. Here the reaction conversion becomes less dependent on Reynolds number as the micromixing and mesomixing times are sufficiently short such that the reaction extent is limited by the system equilibrium. Leading to the transition point where equilibrium limits the reaction extent, microscale mixing is likely a factor that determines conversion.

The conversion effect caused by the Reynolds number can also be achieved through changing the length of the reactor at constant a Reynolds number, according to Equation (3.2.6). However, reaching equilibrium at low Reynolds number and an infinitely long reactor would imply that the mixing is governed by turbulent diffusion processes at the mesoscale.

The work by Hagemann et al. (2003) identified mesomixing as an important factor affecting crystal size distribution in a semi batch configuration. T-mixer studies by Falk & Villermaux (1997) and Fang & Lee (2001) showed the ability to manipulate micromixing efficiency. It is therefore reasoned that the dominating mixing processes affecting conversion in the PFR configuration can change from the microscale to the mesoscale depending on the reactor conditions. Based on the above discussion and considering the units of the pseudo rate constant, it would be more appropriate to refer to the pseudo rate constant, K_r, as an inverse of mixing length scale.

The mass transfer analogy used to derive a relationship for the pseudo rate constant in Equation (3.2.3) implies that this rate constant is related to temperature (through diffusivity and kinematic viscosity), fluid velocity, reactor diameter and volume average particle size. The current form of the pseudo rate constant does not permit separation of the dominant mixing effect. It is therefore proposed to model the interaction between microscale and mesoscale mixing through the classic series reaction modelling technique as described by Levenspiel (1999).

To derive an expression for the pseudo rate constant, the reaction rates associated with micromixing and mesomixing are equated to solve for an intermediate concentration. The intermediate concentration represents the plane of mixing transition, like surface reactions that are limited by either mass transfer or chemical reaction, as described in Levenspiel (1999) and Perry & Green (1998). The intermediate concentration is plugged back into the rate expression to elucidate a combined rate constant that is a function of micromixing and mesomixing. Equation (3.2.7) shows the procedure to identify the intermediate concentration and the expression for the rate constant that follows from the intermediate concentration C_A^*. Thereafter the pseudo rate constant is solved for in terms of micro- and mesomixing length scales.

$$
\begin{aligned}
&r_A' = \frac{r_A}{u} = K_{mi}(C_A - C_A^*) = K_{me}Re(C_A^* - C_{Ae}) \\
&\therefore C_A^* = \frac{K_{mi}C_A + K_{me}ReC_{Ae}}{K_{mi} + K_{me}Re} \\
&=> r_A' = K_{me}Re\left(\frac{K_{mi}C_A + K_{me}ReC_{Ae}}{K_{mi} + K_{me}Re} - C_{Ae}\right) = \frac{K_{mi}K_{me}Re}{K_{mi} + K_{me}Re}(C_A - C_{Ae}) \\
&Let\ \ K_{MI} = \frac{K_{mi}}{Re}\ \ =>\ \ K_r = \frac{K_{MI}K_{me}}{K_{MI} + K_{me}}
\end{aligned}
\tag{3.2.7}
$$

Where K_{me} = Mesomixing length scale inverse [1/m]
K_{mi} = Micromixing length scale inverse [1/m]
K_{MI} = Scaled micromixing length scale inverse [1/m]

It is assumed that the mesomixing length scale simplifies to a velocity correlation shown in Equation (3.2.8). Additionally, it is assumed that the scaled micromixing length scale reduces to a correlation that is only temperature dependent as shown in Equation (3.2.9). The micro- and mesomixing length scales are therefore empirical.

$$K_{me} = exp(\ln A_{m0} + A_{m1}u + A_{m2}u^2) \tag{3.2.8}$$

$$K_{MI} = exp\left(\ln A_{MI} + \frac{B_{MI}}{T}\right) \tag{3.2.9}$$

Where A_{m0} = Mesomixing length scale frequency parameter [1/m]
A_{m1} = Mesomixing length scale 1st order slope parameter [s/m]
A_{m2} = Mesomixing length scale 2nd order slope parameter [s^2/m^2]
A_{MI} = Scaled micromixing length scale frequency number [1/m]
B_{MI} = Scaled micromixing length scale temperature dependence [K]

The equilibrium concentration, used to estimate equilibrium conversion in Equation (3.2.6), is calculated from the activity coefficient and solubility product like the method applied in Section 3.1.1. The method is adapted to a PFR configuration and appears in Equations (3.2.10) to (3.2.12).

$$vC_{A0} - vC_{Ae} - R_{eq} = 0 \tag{3.2.10}$$

$$vC_{B0} - vC_{Be} - R_{eq} = 0 \tag{3.2.11}$$

$$-vC_C + R_{eq} = 0 \tag{3.2.12}$$

Where C_{Ae} = Equilibrium concentration of $RhCl_6^{3-}$ expressed as mol per unit suspension volume [M]
C_{Be} = Equilibrium concentration of DETA.$3H^{3+}$ expressed as mol per unit suspension volume [M]
C_C = Equilibrium concentration of [$RhCl_6$][DETA.3H] crystals expressed as mol per unit suspension volume [M]
R_{eq} = Equilibrium amount of $RhCl_6^{3-}$ or DETA.$3H^{3+}$ consumed by the reaction shown in Equation (3.1.1) [mol]
v = Total volumetric feed rate through the reactor = $v_A + v_B$ [dm^3/h]
C_{A0} = Concentration of $RhCl_6^{3-}$ immediately after mixing point = $C_{Ai}v_A/v$
C_{B0} = Concentration of DETA.$3H^{3+}$ immediately after mixing point = $C_{Bi}v_B/v$

The equilibrium condition at any point along the length of the reactor is given by Equation (3.2.13). The mean activity coefficient and solubility product are the same as in Equations (3.1.8) and (3.1.9) in Section 3.1.1. To solve for the equilibrium concentrations, Equations (3.2.10), (3.2.11) and (3.2.13) must be solved simultaneously.

$$\gamma_{\pm} C_{Ae} C_{Be} = K_{SP} \tag{3.2.13}$$

Where $\gamma_{\pm}$ = Mean activity coefficient
K_{SP} = Solubility product [M^2]

To convert Equations (3.2.10), (3.2.11) and (3.2.13) into an amenable form for numerical solution, Equation (3.2.11) is first subtracted from Equation (3.2.10) to yield (3.2.14). In this equation, C_{Be} is expressed as the argument.

$$\begin{gathered} C_{A0} - C_{Ae} - C_{B0} + C_{Be} = 0 \\ \therefore C_{Be} = C_{B0} - C_{A0} + C_{Ae} \end{gathered} \tag{3.2.14}$$

The equilibrium constraint is obtained by substituting C_{Be} in Equation (3.2.13) with Equation (3.2.14). The solubility product and the activity coefficient are then replaced by the expressions in Equations (3.1.8) and (3.1.9) to give Equation (3.2.15).

$$C_{Ae}[C_{Ae} + C_{B0} - C_{A0}] = \frac{exp\left(10.4\sqrt{9(2C_{Ae} + C_{B0} - C_{A0}) + 12}\right)}{exp\left(\frac{4316}{T} + 36.986\right)} \tag{3.2.15}$$

The objective function is set equal to the difference of the squared right-hand and left-hand sides of Equation (3.2.15) and is shown in Equation (3.2.16).

$$OF = (C_{Ae}[C_{Ae} + C_{B0} - C_{A0}])^2 - \frac{exp\left(20.8\sqrt{9(2C_{Ae} + C_{B0} - C_{A0}) + 12}\right)}{exp\left(\frac{8632}{T} + 73.972\right)} \tag{3.2.16}$$

Equation (3.2.16) is set to zero by adjusting C_{Ae} subject to the constraint $0 < C_{Ae} < C_{A0}$. To assist with numerical precision the objective function was scaled by 1E6. Solver in Microsoft Excel 2013© was used to determine the equilibrium concentration through constrained non-linear minimisation. The minimisation routine in Solver Excel© uses the generalized reduced gradient algorithm that uses forward differences to estimate the derivative of the objective function.

3.2.2. PFR Population balance

The method of moments is used to convert the PFR population balance into a set of ordinary differential equations that is computationally less intensive to solve relative to the full discretization of the population balance. The method of transforming the PFR population balance into the constituent moments is in principle the same as the method followed for the CSTR configuration in Section 3.1.2, aside from a difference in independent variable.

To derive the population balance for the PFR configuration it is argued that the crystals grow along the length of the reactor. The crystals start to move slower relative to the solution due to an increase in surface area that increases the drag force on the crystal, thereby slowing it down. When saturation is consumed up to the point where equilibrium is reached, the crystals cease to grow and maintain the lowered velocity, u_c, until discharged from the reactor. An illustration of the concept is in the diagram in Figure 3.2.2 and the difference between the solution velocity and the crystal velocity is identical to the slip velocity defined in multiphase fluid flow (Byron, 2015).

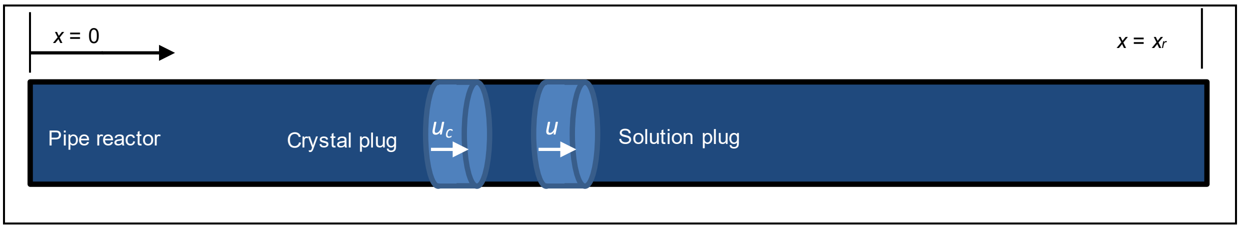

Figure 3.2.2: Crystal plug moving at a slower velocity than the solution plug

The following narrative aims to conceptually visualise how the crystals grow and move along the length of the reactor based on selected references covering multiphase flow. In the fluid field just after nucleation several discreet particles will exist in suspension; this is common in a system where crystals are formed due to the fluid being supersaturated, (Bałdyga & Bourne, 1999).

Consider two nucleated particles, one leading and one trailing in the flow field for the configuration in Figure 3.2.2. The distance separating the two particles is large enough to prevent attraction by mass or electrostatic forces. Provided the leading particle grows to a size that would cause interaction with the fluid, it is reasonable to assume that a trailing wake will form behind the particle, as in experiments by Fortes et al. (1987) and Adekani et al. (2016). When the trailing particle falls within the leading particle wake, it accelerates towards the leading particle by a phenomenon known as drafting (Byron, 2015; Adekani et al., 2016). The trailing particle then collides with the leading particle, which is also known as kissing, and then sticks or tumbles away to one side (Fortes et al., 1987).

According to Fortes et al. (1987) and Adekani et al. (2016), tumbling occurs after two inert spheres have collided whereas sticking is proposed to resemble agglomeration in this work. For the particles to stick, the collision requires sufficient kinetic energy coupled with supersaturation to cement the two particles together (Mersmann, 2001). Not all collisions will translate to two particles sticking together and this is commonly modelled with an agglomeration kernel or agglomeration rate constant that is a function of collision efficiency (Myerson, 2002; Mersmann, 2001; Jones, 2002). Thus, a particle that tumbles away after collision will then fall within the wake of a particle in a neighbouring streamline.

Conceptually, particles that stick will tend to do so along the trajectory of the leading particle. It is therefore logical to deduce that this process will continue until the particles form a rod- or needle-like shape. Direct numeric simulation shows that non-inertia rods preferentially tend to spin around the long axis and align with the vorticity or streamlines (Byron, 2015). The alignment of non-spherical particles with inertia in a flow field is a subject of ongoing research.

Considering this point, a simulation study of oblate particles falling in a stagnant fluid has shown that the particles tend to align with the largest projected surface area perpendicular to acceleration (Adekani et al., 2016). This provides some evidence to infer that as particles become larger they will tend to align such that the largest area is perpendicular to a force causing acceleration in a certain direction. In a turbulent flow field within a pipe the velocity profile over the diameter of the pipe is erratic about the average fluid velocity (Bałdyga & Bourne, 1999). The difference in radial velocity can therefore cause random directional acceleration that can possibly cause the rod-like crystal to vibrate. The vibration can in turn cause collision with neighbouring rod-like crystals to form random links between rods flowing in neighbouring streamlines.

This conceptual process implies that the crystals are likely elongated as opposed to spherical, as was observed in SEM photographs of crystals precipitated under various experimental conditions. The discussion above also implies an assumption that agglomeration is present in the PFR configuration. Therefore, the CSTR agglomeration mechanism as derived in Section 10.2 in the Appendix is applied. Note that the time required for agglomeration in the PFR configuration is the time a crystal plug remains inside the reactor. Stated differently, it is the residence time of the slower moving plug of crystals depicted in Figure 3.2.2. The difference between the crystal velocity and the solution velocity is arguably minimal due to no detectable evidence of accumulation. Therefore, the crystal plug velocity is comparable or equal to the solution plug velocity. Thus, for the PFR configuration the population balance becomes Equation (3.2.17).

$$
\begin{aligned}
&u\frac{\partial n}{\partial x} + (G - G_a)\frac{\partial n}{\partial L} - GG_a\tau_a\frac{\partial^2 n}{\partial L^2} = 0 \\
&with \quad \tau_a = \frac{x_r}{u}
\end{aligned}
\qquad \textbf{(3.2.17)}
$$

The moment transformation of Equation (3.2.17) is like the CSTR population balance moment transformation, with the exception that the convection term is omitted. Equation (3.2.18) gives the moment generating function for the PFR population balance in Equation (3.2.17).

$$\begin{aligned}\frac{dM_i}{dx} &= -\frac{(G-G_a)}{u}\left(L^i n(L,t)\Big|_{L\to 0}^{L\to\infty} - iM_{i-1}\right)\\ &+\frac{GG_a\tau_a}{u}\left(L^i\frac{\partial n}{\partial L}\bigg|_{L\to 0}^{L\to\infty} - iL^{i-1}n(L,t)\Big|_{L\to 0}^{L\to\infty} + i(i-1)M_{i-2}\right)\end{aligned} \tag{3.2.18}$$

The boundary conditions are given in Equation (3.2.19). The population density derivative with respect to size at the boundary is based on the observed mixed lognormal volume crystal size distribution for this system; the reasoning is identical to the CSTR discussion in Chapter 3, Section 3.1.2. Note that the steady state population balance, where $\partial n/\partial x$ is zero, can only occur at equilibrium, thus at the point in the reactor from where saturation ratio is one. For this system there is therefore no analytic steady state solution aside from the conclusion that the population density remains a constant function of size when the system equilibrates.

$$\begin{aligned}&n(0,x) = n_0(x)\\ &n(\infty,x) = 0\\ &\frac{\partial n}{\partial L}\bigg|_{L=0} = \frac{\partial n}{\partial L}\bigg|_{L\to\infty} = 0\end{aligned} \tag{3.2.19}$$

The set of ordinary differential equations obtained by inserting the boundary conditions in Equation (3.2.19) into Equation (3.2.18) is shown in matrix form in Equation (3.2.20) with the connection matrix in Equation (3.2.21).

$$\begin{bmatrix}\frac{dM_0}{dx}\\ \frac{dM_1}{dx}\\ \frac{dM_2}{dx}\\ \frac{dM_3}{dx}\\ \frac{dM_4}{dx}\end{bmatrix} = \boldsymbol{A}\begin{bmatrix}n_0(x)\\ M_0\\ M_1\\ M_2\\ M_3\end{bmatrix} \quad \& \quad IC\colon \begin{bmatrix}M_0\\ M_1\\ M_2\\ M_3\\ M_4\end{bmatrix}_{x=0} = \begin{bmatrix}0\\0\\0\\0\\0\end{bmatrix} \tag{3.2.20}$$

As with the CSTR configuration, nucleation is an integral process in the PFR configuration, thereby rendering the system inherently stiff. Stiffness of a differential equation is discussed in Section 3.1.1.

$$\boldsymbol{A} = \frac{1}{u}\begin{bmatrix}(G-G_a) & 0 & 0 & 0 & 0\\ GG_a\tau_a & (G-G_a) & 0 & 0 & 0\\ 0 & 2GG_a\tau_a & 2(G-G_a) & 0 & 0\\ 0 & 0 & 6GG_a\tau_a & 3(G-G_a) & 0\\ 0 & 0 & 0 & 12GG_a\tau_a & 4(G-G_a)\end{bmatrix} \tag{3.2.21}$$

The numerical method that was most successful to solve the system in Equations (3.2.20) and (3.2.21) was found to be the modified Rosenbrock formula of order two. This method is available as a standard Matlab function '*ode23s*' (Shampine & Reichelt, 1997). The minimum size step in the variable step solver '*ode23s*' was automatically set by the software and ranged between 1E-15m and 1E-18m. Shape preservation was activated. The model represented by Equations (3.2.3) to (3.2.5), (3.2.20) and (3.2.21) was coded using Simulink in Matlab version R2009a.

3.2.3. PFR Growth and nucleation kinetics

The PFR configuration growth and nucleation rate functions are like the functions used for the CSTR configuration in Section 3.1.3, albeit with potentially different parameter values. Before defining the growth and nucleation rate, the saturation in the PFR at a specific distance in the reactor is given in Equation (3.2.22).

$$S = \sqrt{\frac{\gamma_\pm C_A C_B}{K_{SP}}} \tag{3.2.22}$$

Where C_A = Concentration of $RhCl_6^{3-}$ at distance x in the pipe reactor, Equation (3.2.3) [M]
C_B = Concentration of DETA.$3H^{3+}$ at distance x in the piper reactor, Equation (3.2.4) [M]
K_{SP} = Solubility product [M^2]
$\gamma_\pm$ = Mean activity coefficient at distance x in the pipe reactor
S = Saturation ratio at distance x in the pipe reactor

The PFR population density at the size zero boundary is given by Equation (3.2.23).

$$n_0(x) = K_n(S-1)^\beta = A_n exp\left(\frac{B_n}{T}\right)(S-1)^\beta \tag{3.2.23}$$

Where $n_0(x)$ = Population density boundary at size zero at distance x in the piper reactor [#/μm.dm^3]
K_n = Nucleation rate constant [#/μm.dm^3]
A_n = Primary nucleation frequency constant [#/μm.dm^3]
B_n = Primary nucleation activation energy divided by the gas constant [K]
T = Temperature [K]
β = Population density at size zero supersaturation exponent

The average linear crystal growth rate through interfacial attachment is given by Equation (3.2.24)

$$G = K_g(S-1)^\alpha = A_g exp\left(\frac{B_g}{T}\right)(S-1)^\alpha \tag{3.2.24}$$

Where G = Growth rate at distance x in the pipe reactor [μm/s]
K_g = Growth rate constant [μm/s]
A_g = Growth rate frequency constant [μm/s]
B_g = Growth rate activation energy divided by the gas constant [K]
α = Growth rate supersaturation exponent

As with the CSTR configuration, orthokinetic agglomeration is assumed for the PFR configuration. The agglomerative growth rate relationship is shown in Equation (3.2.25).

$$G_a = K_{ag}M_0^2(S-1) = A_{ag} exp\left(\frac{B_{ag}}{T}\right)M_0^2(S-1) \tag{3.2.25}$$

Where G_a = Agglomerative growth rate at distance x in the pipe reactor [μm/s]
K_{ag} = Agglomeration growth rate constant [μm.dm^3/#.s]
A_{ag} = Agglomerative growth rate frequency constant [μm.dm^3/#.s]
B_{ag} = Agglomerative growth rate activation energy divided by the gas constant [K]

Inserting Equations (3.2.22) to (3.2.25) into the moment equations in Equation (3.2.20) and solving the mass balance in Equations (3.2.3) to (3.2.5) fully specifies the problem, provided the constants K_{SP}, $\gamma_\pm$, α, β, A_n, B_n, A_g, A_{ag}, B_g and B_{ag} are specified. In addition, the initial reagent concentrations (C_{A0} and C_{B0}) in the feed streams, the feed flows (υ_A and υ_B), the reactor length (x_r) and lastly the initial reactor moments (all are zero) must also be specified before the mass and population balance can be solved.

4. EXPERIMENTAL DESIGN AND METHODS

In this chapter an overview of the health and safety associated with the chemicals used in this work is firstly given in Section 4.1. The chemicals used are extremely toxic and corrosive thus care must be taken in terms of materials of construction selection as well as safety precautions taken to avoid physical contact. Furthermore, the experimental design and methods associated with required measurements are discussed in detail.

From the theory and literature reviewed in Chapter 2 it was proposed to use two reactor configurations to extract nucleation and growth kinetics. The reasoning was mainly to quantify and possibly mitigate the effects of mixing at scales below the macroscale of the reactor. Thus, the experimental design covers two reactor configurations, namely a CSTR and a PFR.

The CSTR design is presented in Section 4.2 and compared in terms of mixing time constants to the reactor configuration used by Vicum (2005). In addition, Section 4.2 describes the product sampling protocol and the measures taken to ensure accurate product analysis.

Aqueous and solids residence time distribution tests are then applied to the reactor design in Sections 4.3.1 and 4.3.2 to qualify the homogeneity assumption. In Sections 4.3.3 and 4.3.4 a data analysis method is proposed to evaluate the extent that segregation can influence nucleation and growth parameters extracted from a reactor configuration where segregation may be present.

The PFR design is presented in Section 4.4 and uses a simple t-mixer design to mix the reagents at the PFR inlet. Section 4.4 elaborates on the PFR product sampling protocol and highlights measures taken for accurate product analysis. In Section 4.5 the expected error associated with the analytical and particle sizing methods are discussed and quantified.

4.1. HEALTH AND SAFETY

The chemicals required to precipitate diethylenetriammonium hexachlororhodate (III) salt includes 6M hydrochloric acid, diethylenetriamine and hexachlororhodate (III) solution at a free hydrochloric acid content of 6M. These chemicals are hazardous and necessary precautions must be taken to avoid direct human contact.

Normal handling of the chemicals requires appropriate protective clothing and containment measures. Sealed containers should only be opened when a negative pressure atmosphere prevails and the draught is directed away from the person handling the chemicals. Typically, this is achieved by performing the work in a fume cabinet that is connected to a draught system.

The off-gas from the draught system is scrubbed in 3M sodium hydroxide solution before it is emitted to the atmosphere. All experiments in this work were carried out in a ventilated fume cabinet. An acid-resistant laboratory coat, latex gloves and eye protection are required when working with these chemicals to protect the user against unforeseen splashes.

Hydrochloric acid at a concentration of 6M is classified as a severely corrosive substance and human toxic effects are well documented and freely available through the latest material safety data sheet from various manufacturing companies such as NCP Chlorchem (Pty) Ltd, BASF Corporation and Du Pont. Diethylenetriamine is classified as corrosive and is a known skin irritant; the chemical toxicity is well documented and the latest material data sheet is available from DOW chemical company.

A proxy for hexachlororhodate (III) solution is 6M hydrochloric acid in terms of hazard rating. In this work 6M hydrochloric acid is the solvent and makes up more than 97 per cent by mass of the solution. Hazards and toxicity associated with hexachlororhodate (III) mainly exist if the hexachlororhodate (III) ion precipitates from solution as a sodium salt. Sodium hexachlororhodate (III) salt is a known irritant and the latest material safety data sheet is available from Merck (Sigma-Aldrich) chemical company.

4.2. CONTINUOUS STIRRED TANK REACTOR EXPERIMENTAL METHOD LAYOUT, DESIGN AND CALIBRATION

Considering the hydrodynamic effects described in Chapter 2, the CSTR reactor design should cater for homogeneous mixing at the macro length scale. By implication, the design should minimise conversion effects due to mixing on the micro- or mesoscale characterised by localised concentration zones within the reactor. It stands to reason that such a configuration will translate to nucleation and growth kinetics that are least affected by sub-macroscale mixing conditions.

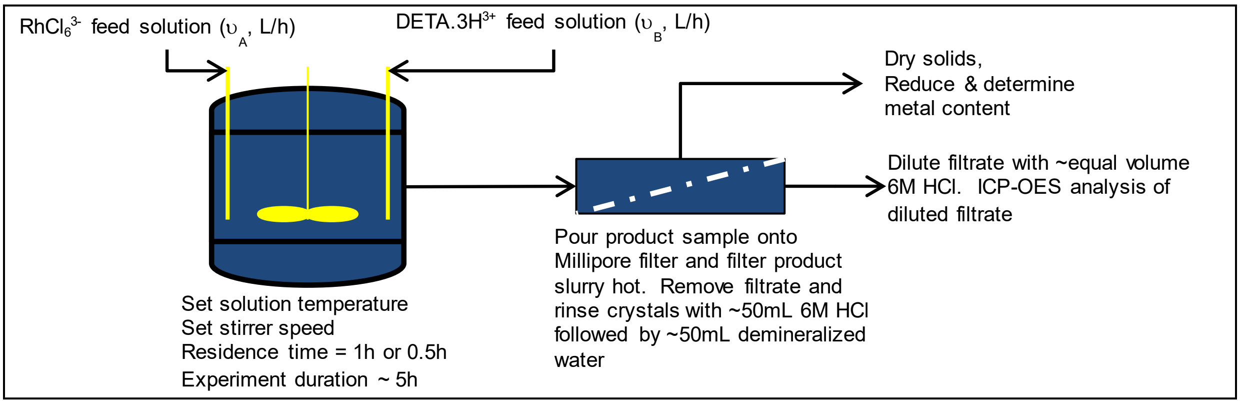

Figure 4.2.1: CSTR experimental flow schematic

The continuous stirred tank reactor flow diagram is shown in Figure 4.2.1 and the physical configuration is shown in Figure 4.2.2. The hexachlororhodate (III) feed solution is injected into the reactor through a dip-tube at the agitator impeller elevation. Likewise, the injection of protonated diethylenetriamine is injected at the opposite side at the same elevation. The purpose of the injection method is to minimise the effects of mesoscale mixing on reaction kinetics as highlighted in Chapter 2.

The product slurry is extracted from the reactor through a third dip-tube, 60mm above the elevation of the reagent dip-tubes. The flow patterns in a stirred tank equipped with a down pumping, axial flow agitator configuration typically show up flow near the reactor boundary (Aubin, et al., 2004). The purpose of the arrangement is to ensure suspension homogeneity before the reactor content is discharged through the outlet dip-tube.

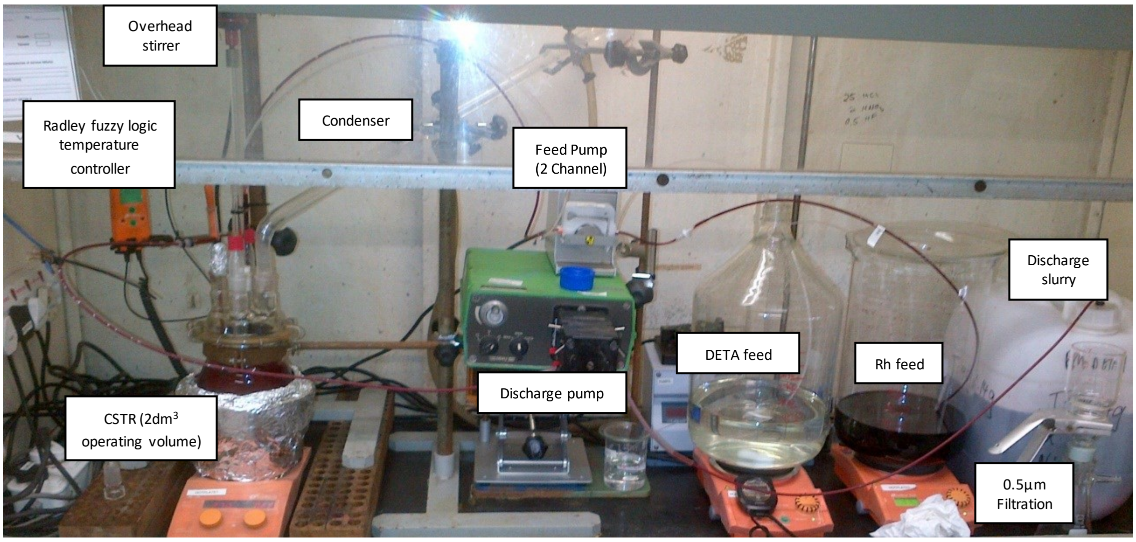

Figure 4.2.2: Reactor setup

The slurry sample is taken directly from the discharge tube and is filtered hot on 0.2μm cellulose filter paper. The filtrate is removed and diluted by roughly an equal volume of 6M HCl to prevent post precipitation of salt due to cooling of the solution. The dilute solution metal concentrations are measured by inductive coupled plasma optical emission spectroscopy (ICP-OES).

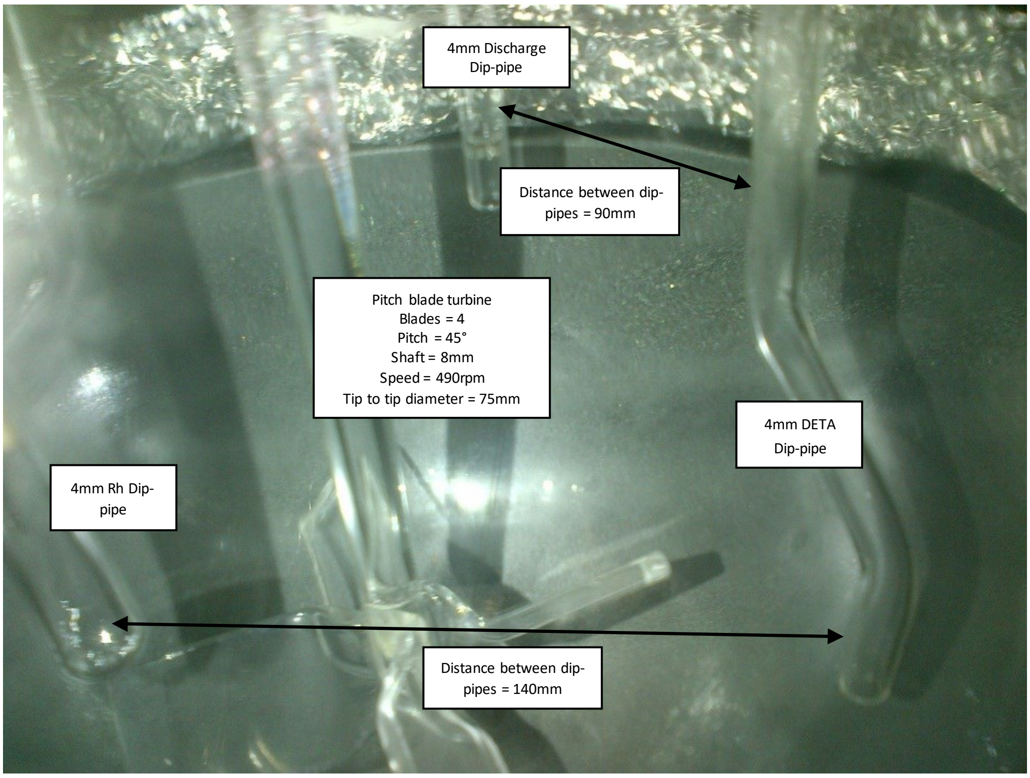

Figure 4.2.3: Reactor internal layout

Figures 4.2.3 and 4.2.4 show the internal layout and dimensions of the reactor and the positioning of the dip-tubes and the agitator. The design objective was to meet the requirements for a CSTR. The experimental conditions are summarised in Table 4.2.1. In Table 4.2.1 the estimated macromixing, mesomixing and micromixing times are estimated from relationships given in Chapter 2, Section 2.1.5.

Table 4.2.1: Experimental operating and initial conditions for the CSTR configuration

Variable	Experiment 1	Experiment 2	Experiment 3	Experiment 4
T, °C	100	80	60	65
τ, h	1.00	1.00	1.00	0.55
V_r, dm^3	2	2	2	2
υ_A, dm^3/h	0.95	0.95	0.95	1.88
υ_B, dm^3/h	1.05	1.05	1.05	1.76
C_{A0}, M	0.250	0.253	0.259	0.262
C_{B0}, M	0.211	0.222	0.216	0.223
Initial C_A, M	0.249	0.256	0.265	0.262
Initial C_B, M	0	0	0	0
Initial C_C, M	0	0	0	0
*$u \approx 4V_r/A_{cr}\tau_{macro}$, m/s	0.21	0.21	0.21	0.21
τ_{micro}, s - Equation (2.1.15)	0.0087	0.0097	0.0109	0.0106
$\tau_{meso,A}$, s - Equation (2.1.17)	0.0121	0.0121	0.0121	0.0152
$\tau_{meso,B}$, s - Equation (2.1.17)	0.0125	0.0125	0.0125	0.0149
τ_{macro}, s - Equation (2.1.18)	3.25	3.25	3.25	3.25

*The fluid velocity near the dip-tube outlet u is estimated by dividing the agitator circulation flow by the cross-sectional area beyond the agitator impeller ~1.257E-5m^2 (from the reactor geometry in Figure 4.2.3). The agitator circulation flow is equal to $4V_r/\tau_{macro}$ as estimated by Nienow (1997).

The temperature of the reactor was controlled and measured with a Radley fuzzy logic temperature control unit, accurate to ~0.5°C. A glass tube was used as protective barrier between the solution and the stainless steel thermocouple. A Heidolph variable speed overhead stirrer was used to drive a 4-blade (pitch 45°) glass agitator. The speed setting was 480rpm for all experiments. A condenser was attached to the reactor vapour space with a cooling capacity of ~30W to ensure total reflux at boiling temperature and to prevent loss of reactor volume through evaporation.

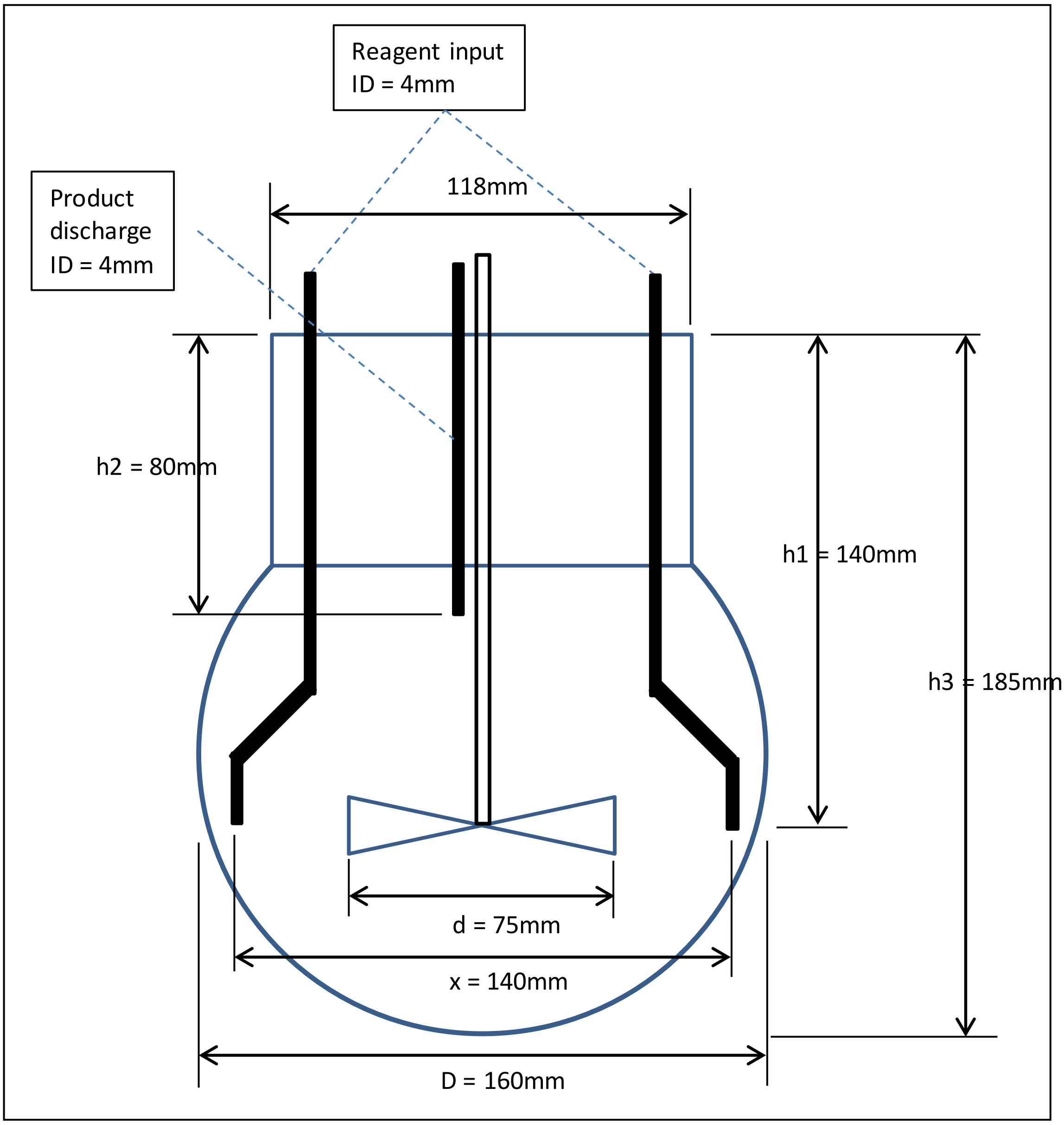

Figure 4.2.4: Reactor internal dimensions (Note: Product discharge dip-pipe is positioned exactly behind the agitator at a spacing indicated on Figure 4.2.3)

Figure 4.2.5 shows the calibration curve for the ISMATEC feed pump (two channels) and the Watson-Marlow discharge pump. Polytetrafluoroethylene (PTFE) tubes of 4.5mm diameter were used to transfer feed and product streams. Tygon tubes of 4.5mm diameter were used inside each pump cassette. The calibration curves in Figures 4.2.5 a) and b) show linear relationships.

The reactor configuration shown above was designed using the configuration of Vicum (2005) as a reference. In the study by Vicum (2005) the reaction volume was 6dm^3 with a continuous total flow ranging between ~0.24 to 12dm^3/h, giving a residence time of ~27 to 29 minutes. The agitator speeds were changed from 200 to 600rpm. Vicum (2005) used a Rushton turbine to agitate the barium sulphate system. The power number of this agitator is 5, as suggested by Nienow (1997). To assess the reactor design by Vicum (2005), the fluid properties of the solution used in this work is applied at 100°C in place of the barium chloride and sodium sulphate solution properties. The mixing time constants defined in Chapter 2, Equations (2.1.15) to (2.1.18), combined with the dimensions mentioned above and the power number translates to a macromixing time of ~11s to 33s, a mesomixing time of ~0.0247 to 0.159s, and a micromixing time of ~0.0079s to 0.0412s.

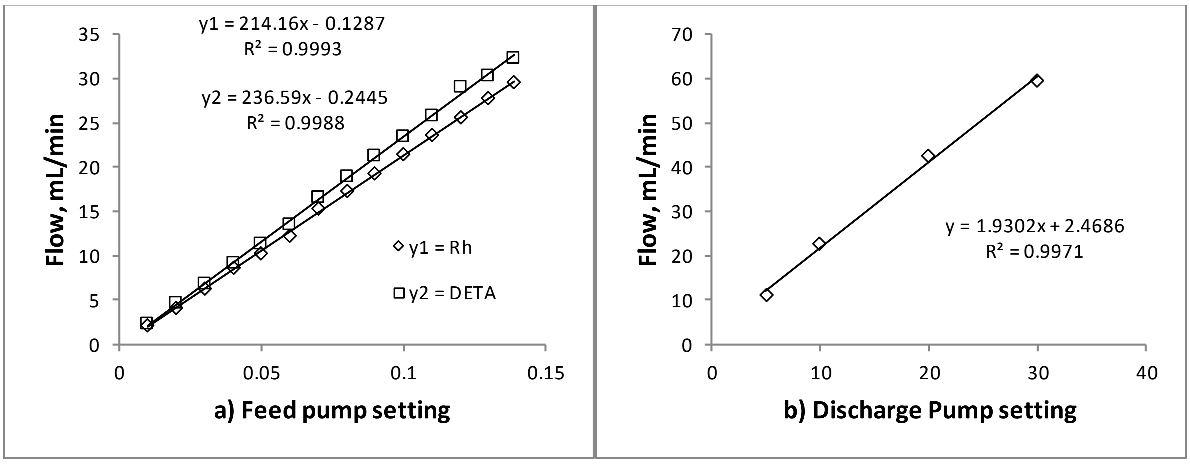

Figure 4.2.5: Calibration curve for a) two channel feed pump (ISMATEC) and b) discharge pump (Watson-Marlow 520D)

The experimental conditions proposed in this work therefore translate to micromixing times in range with the study by Vicum (2005). However, macro- and mesomixing times are substantially shorter relative to the reactor design by Vicum (2005); it is therefore expected that the dispersion of the reactant plumes would be more effective.

Thus, it is highly likely that the mesomixing zones under the proposed conditions in Table 4.2.1 would be substantially smaller than the mesomixing zones described by Vicum (2005). This suggests that the mesomixing zones in the continuous configuration of this work may be negligibly small and that no crystal size distribution effect will be observed at varying agitator speeds as was found by Vicum (2005) in a continuous reactor configuration. Initial experiments showed that the reaction in Equation (3.1.1) proceeds to equilibrium in the bulk, suggesting minimum sub-macroscale effects. In Section 4.3, a residence time distribution test further compares how close the configuration in this work is to an idealised continuous stirred tank reactor.

4.3. CONTINUOUS REACTOR RESIDENCE TIME DISTRIBUTION

Homogeneity for an isothermal CSTR is valid provided that the following criteria are met (Perry & Green, 1998; Levenspiel, 1999):

- The reactor contents must be a homogeneous mixture at any given time.
- Particles may not segregate according to size/density in the discharge line (iso-kinetic sampling).
- The input and output flow rates must be in balance, the reactor volume must remain constant.
- The reactor must be isothermal.

The following tests were used to validate homogeneity of the reactor:

- An aqueous residence time distribution step test was used with aqueous hydrochloric acid ($HCl_{(aq)}$) at pH = 1 ($[H_3O^+] = 0.1M$) as tracer at a flow rate of 1dm^3/h and 2.4dm^3/h respectively.
- A wash out test was used to determine if segregation occurred in the reactor discharge system at an initial solids content of 5 per cent (w/w) and a wash water flow rate of 2dm^3/h.

4.3.1. Aqueous residence time distribution

The reactor was initially filled with demineralised water, heated to 80°C, and agitated at 480rpm. The tracer solution was made up to pH1 by adding 34 per cent (w/w) commercial grade hydrochloric acid from Merck to ultra-pure water at 25°C. Tap water was purified in a SIEMENS LaboStar water purification system. Each sample pH was measured at ambient temperature of 25°C with a Metrohm 914 pH probe with a platinum electrode. The effect of temperature was therefore removed by maintaining a reference temperature for all measurements. The pK_a of hydrochloric acid is -6.3, therefore the acid is completely dissociated at any temperature implying negligible concentration error due to temperature variation (Jolly, 1984).

Figure 4.3.1 a) shows the pH profile of the reactor over time. Time zero represents the starting point when the step tracer was introduced. The concentration (mol/dm^3 or M) was calculated from the pH measurements by the Søren Peder Lauritz Sørensen relationship, Equation (4.3.1).

$$[H_3O^+] = 10^{-pH} \tag{4.3.1}$$

The solid lines in Figure 4.3.1 b) were calculated from an analytic solution of a transient mass balance for when a tracer is continuously added to the reactor. The balance assumes that the vessel is a continuous stirred tank reactor. Equation (4.3.2) shows the differential equation and the analytic solution.

$$\begin{aligned} \frac{dC}{dt} &= \frac{v(C_0 - C)}{V_r} = \frac{(C_0 - C)}{\tau} \\ \therefore C(t) &= C_0\left(1 - exp\left(-\frac{t}{\tau}\right)\right) + C|_{t=0}exp\left(-\frac{t}{\tau}\right) \end{aligned} \tag{4.3.2}$$

Where
$C(t)$ = Hydronium concentration at any given time [M]
C_0 = Hydronium concentration in step solution = 100 [M]
$C|_{t=0}$ = Initial hydronium concentration in reactor = 10^{-5} [M]
t = Time [min]
τ = V_r/v = Reactor residence time [h]
v = Volumetric flow rate of step solution [dm^3/h]
V_r = Reactor working volume [dm^3]

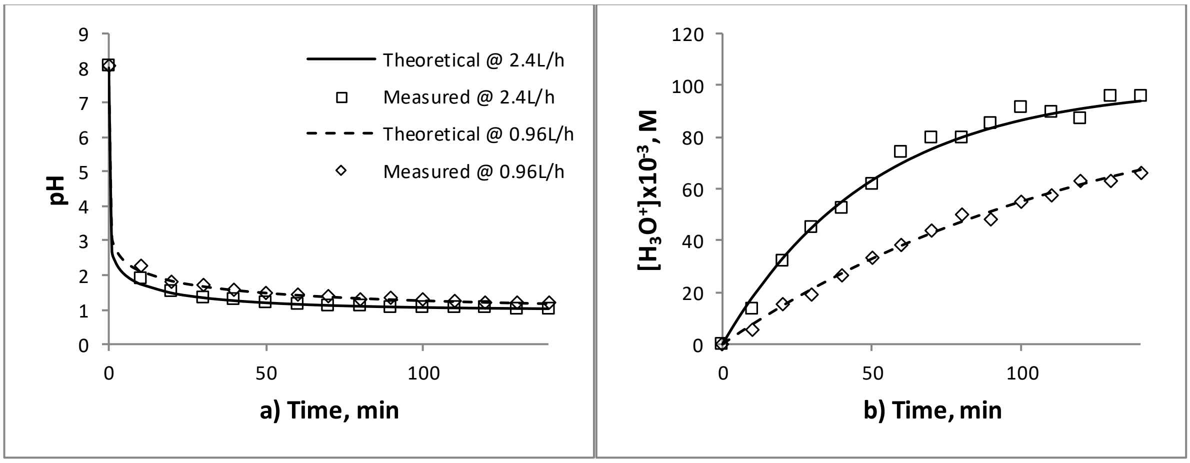

Figure 4.3.1: Reactor residence time distribution: a) pH – time profile and b) concentration-time profile

A tracer step test requires that no tracer is present in the reactor at time zero. In these tests the water contained an initial quantity of hydronium ion which was corrected for by rearranging Equation (4.3.2) into Equation (4.3.3). The manipulation transforms the mass balance solution into the age function of a continuous stirred tank reactor, as described in Perry & Green (1998).

$$F(t_m) = \frac{C_m(t_m) - C|_{t=0}exp\left(-\frac{t_m}{\tau}\right)}{C_0} = 1 - exp\left(-\frac{t_m}{\tau}\right) \tag{4.3.3}$$

Where $F(t)$ = Age function

In Equation (4.3.3) the variable C_m represents the measured hydronium ion concentrations at the measurement time t_m. The R^2 values for the 1dm^3/h (16mL/min) and 2.4dm^3/h (40mL/min) predictions in Figure 4.3.2 are 0.991 and 0.994 respectively. The good data fit illustrates that the reactor can be considered a continuous stirred tank reactor as per the definition in Perry & Green (1998). The aqueous mixture inside the reactor at any given time is therefore homogeneous and confirms the deductions made from the macro- and mesoscale mixing time comparison in Section 4.2.

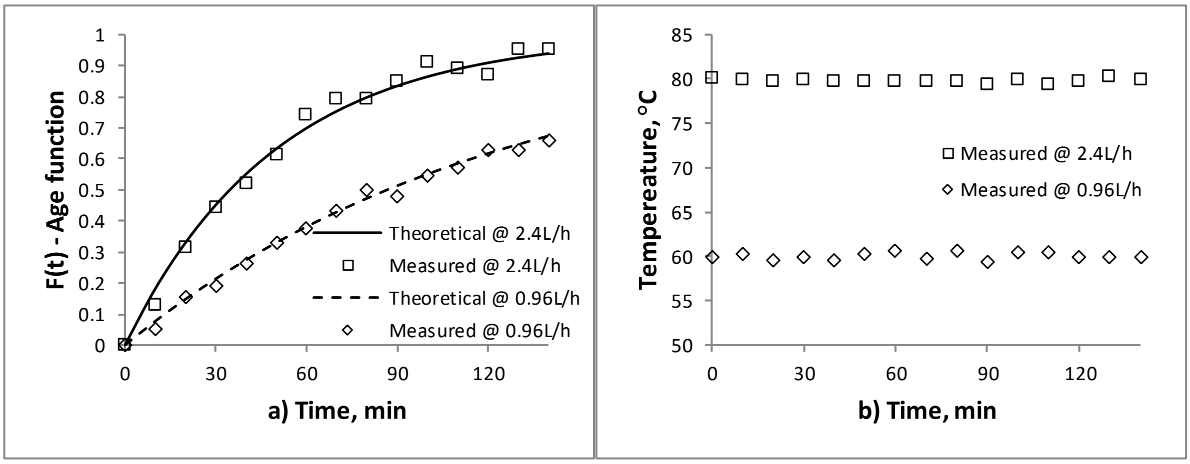

Figure 4.3.2: Reactor a) age function and b) temperature profile

The 95 per cent temperature control confidence limit for both flow experiments were 79.9°C +/-0.4°C and 60.1°C +/-0.8°C respectively. The reactor is therefore isothermal within the confidence limits. It is further observed that the confidence limit narrows as temperature is increased. The increase in accuracy of temperature control is related to approaching the boiling point of the liquid that at any given heat input remains a constant at a constant pressure. Temperature control under boiling conditions is therefore more accurate than at a temperature below boiling point.

4.3.2. CSTR Solids residence time distribution (Wash out test)

The diethylenetriammonium hexachlororhodate (III) crystals, used for the wash out test, were prepared by precipitation. An aqueous solution of 0.26M hexachlororhodate (III) was combined with 0.22M protonated diethylenetriamine at 100°C in a 2dm^3 reaction vessel, both reagents set at a rate of 1dm^3/h respectively. Initially the vessel was filled with 0.24M hexachlororhodate (III) solution and a total of 2dm^3/h was drawn from the discharge dip-tube to maintain a constant level within the reactor.

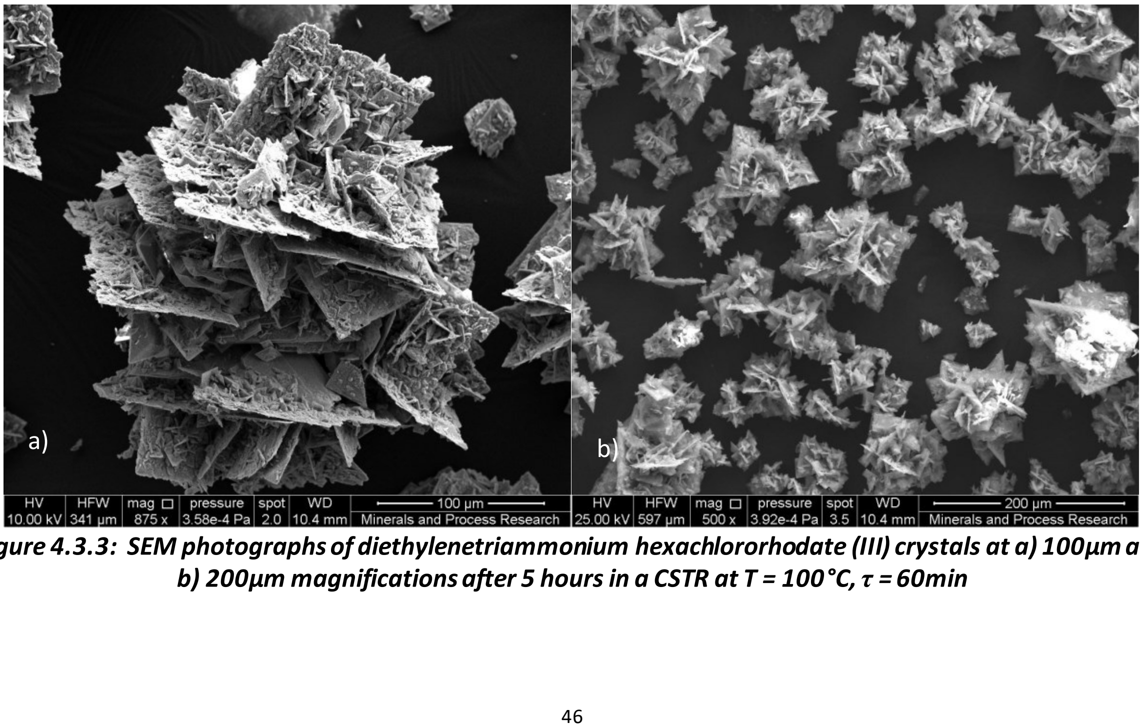

Figure 4.3.3: SEM photographs of diethylenetriammonium hexachlororhodate (III) crystals at a) 100µm and b) 200µm magnifications after 5 hours in a CSTR at T = 100°C, τ = 60min

The reaction was left to proceed for 5 residence times (5 hours). After 5 hours the reactor content was filtered hot on a Buchner filter with 3µm cellulose filter paper. The crystals were washed on the filter paper with approximately 500mL of 6M HCl and the acid remaining in the crystals was rinsed out with approximately 500mL of demineralised water. Scanning electron microscope (SEM) photos showed some fractures and chips on the edges of the clustered crystals that were produced showing minor signs of breakage, see Figure 4.3.3.

To obtain a coarse fraction of the crystals a sample was scooped from the top of the filter cake that remained after filtering the reactor content. The crystals were dried overnight for ~8 hours at ~40°C in a benchtop oven. The low temperature was chosen because the filter paper becomes fragile and brittle at 60°C, which causes sample contamination. The relatively long drying time was chosen as the SEM photograph of the crystals in Figure 4.3.3 showed that the crystals were likely to entrap liquid. Drying is therefore required to enable accurate dry mass measurement. Approximately 0.2g was used to measure crystal size in a Malvern Mastersizer 2000. Demineralised water was used as dispersant in the Malvern Mastersizer 2000.

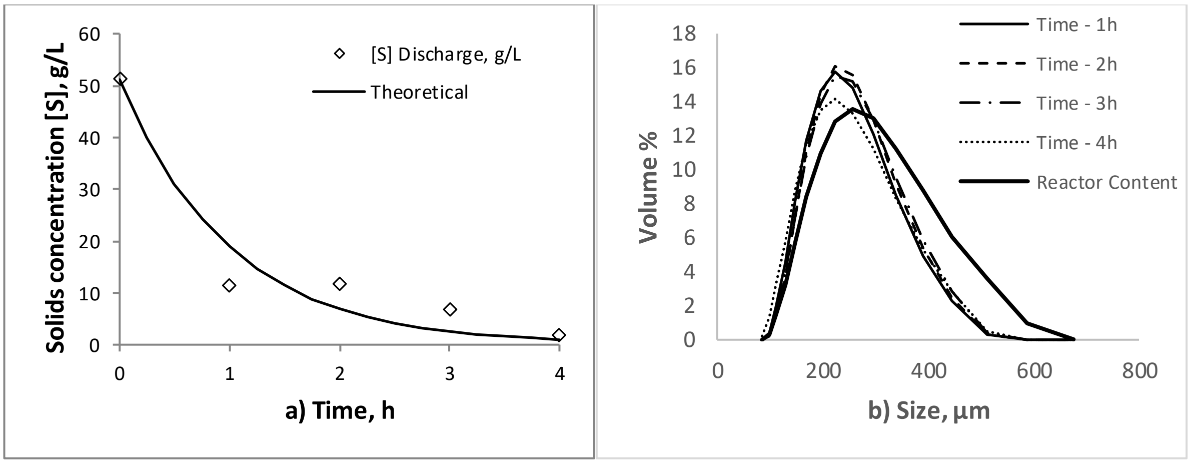

Figure 4.3.4: CSTR wash-out test a) solids concentration profile over time and b) crystal size distribution profile over time

For the wash out test the reactor was initially filled with 100g of diethylenetriammonium hexachlororhodate (III) crystals produced from the method above and 1900g of demineralised water to give a slurry that is 5 per cent solids by weight ~51g/dm^3. The water flow rate through the reactor was set at the minimum test flow of 2dm^3/h or ~1h residence time. During the wash out test the reactor was controlled at 60°C and the agitator speed was set at 480rpm. The reactor operating conditions were chosen to emulate exacerbated segregation conditions at elevated temperature where crystal buoyancy is reduced relative to a lower operating temperature.

In Figure 4.3.4 a) the theoretical solid concentration profile is based on a solution of the transient mass balance equation for decay of non-reacting solids content. The solution is given by Equation (4.3.2) with C_0 = 0g/L and $C|_{t=0}$= 51g/L. The residence time for the wash out test using water as wash medium was 1 hour, as stated above. The data agrees with the theoretical trend with a R^2 value of 0.94.

A lognormal distribution was fitted to each crystal size distribution data set in Figure 4.3.4 b). Figure 4.3.5 a) shows the cumulative lognormal distribution compared to the measured crystal size distributions. The fitted lognormal distribution parameters and L_{43} size of the data is shown later in Table 4.3.1. The R^2 values are all above 0.99 and the parity chart in Figure 4.3.5 b) suggest the data is well represented by the lognormal distribution.

Visually the data in Figure 4.3.4 b) suggests that the reactor content distribution after the test is coarser than the sampled product over time. The small extent of breakage observed in Figure 4.3.3 does not explain the large increase in average crystal size from the discharge distributions over time to the reactor content at the end of the experiment. The reactor content therefore appears to segregate over time, indicating non iso-kinetic conditions at the discharge. To prevent segregation, a smaller discharge tube with a 2.5mm bore was tested but it was found to frequently block at the operating conditions of the tests. Due to the difficulty of meeting homogeneous crystal suspension criteria under the conditions specified above, the extent that segregation affects homogeneity is explored through population balance modelling in section 4.3.3.

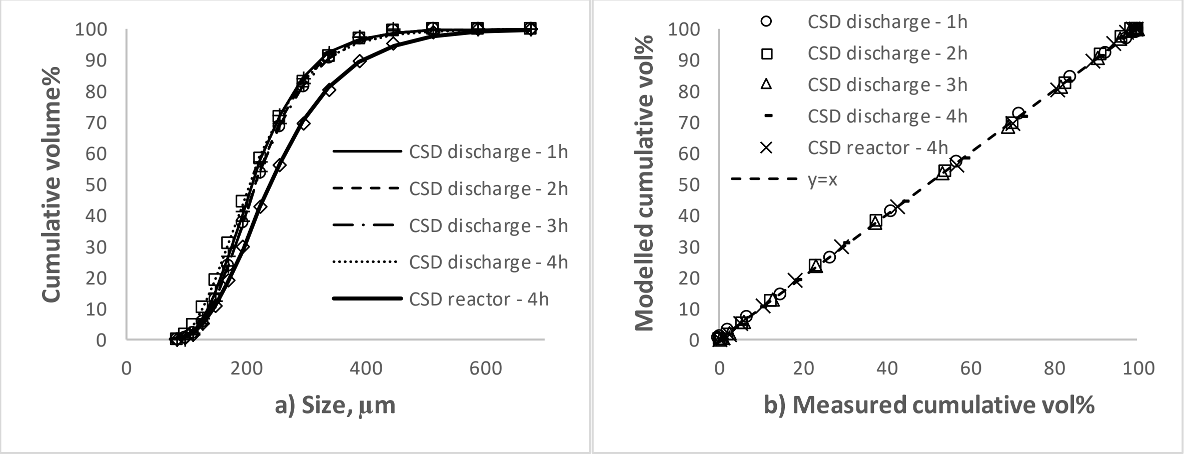

Figure 4.3.5: CSTR wash-out test a) lognormal distribution and b) parity chart of lognormal distribution volume per cent VS measured volume per cent

4.3.3. CSTR solids residence time distribution model by segregation

Given that the volume distributions appear to be lognormal as shown in Figure 4.3.5, it is proposed that the population density would also contain elements of the lognormal distribution. Analytic expressions for the population density moments are therefore not likely as given for an MSMPR in Chapter 2, Section 2.1.3, and will therefore require numeric integration to evaluate.

Considering the numeric integration requirement, the extent that the measured distributions deviate from the exponential distribution is first investigated. Provided that the deviation at the tail end of the distribution is low, the exponential distribution will then be used to determine the minimum upper integration limit when calculating moments of the population density. Note that the minimum upper limit is a proxy for infinity, which is the theoretical upper limit for all moment calculations.

To establish the minimum upper limit, the lognormal distributions in Figure 4.3.5 are approximated by exponential distributions. The L_{43} size is used to conserve the location of each distribution that is approximated by the exponential distribution through the identities that follow. Let $\phi(L)$ in Equation (4.3.4) be the differential form of the volume fraction cumulative distribution, representative of the volume fraction density distribution.

$$\phi(L) = \frac{d}{dL}\left(\frac{\int_0^L nl^3\,dl}{\int_0^\infty nl^3\,dl}\right) = \frac{nL^3}{\int_0^\infty nl^3\,dl} = \frac{nL^3}{M_3} \tag{4.3.4}$$

Where $\phi(L)$ = Volume fraction density distribution as a function of size L [μm^{-1}]
n = Population density function [#/μm.dm^3]
M_3 = Third moment of the population density (volume of particles per volume of suspension) [#.μm^3/dm^3]

The first moment of the differential form of the volume fraction distribution can then be transformed into the L_{43} size as shown in Equation (4.3.5).

$$\int_0^\infty \phi(L)\,L\,dL = \int_0^\infty \frac{nL^3 L}{M_3}\,dL = \frac{1}{M_3}\int_0^\infty nL^4\,dL = \frac{M_4}{M_3} = L_{43} \tag{4.3.5}$$

If $\phi(L)$ is a lognormal distribution, Weisstein (2016) gives the analytic expression for the first moment in Equation (4.3.6).

$$\int_0^\infty \phi(L)\, LdL = L_{43} = exp\left(m + \frac{s^2}{2}\right)$$
$$\& \ \phi(L) = \frac{1}{\sqrt{2\pi}sL} exp\left(-\frac{(\ln L - m)^2}{2s^2}\right) \tag{4.3.6}$$

Where m = Location parameter of lognormal distribution
s = Spread parameter of lognormal distribution
L = Crystal size [μm]
L_{43} = Mean particle size by volume [μm]

To convert the lognormal distribution into the exponential distribution, the lognormal L_{43} is set equal to the exponential distribution L_{43} and the exponential decay constant *B* is solved for. The procedure is illustrated in Equation (4.3.7).

$$L_{43} = \frac{\int_0^\infty Aexp(-BL)\, L^4 dL}{\int_0^\infty Aexp(-BL)\, L^3 dL} = \frac{4}{B} = exp\left(m + \frac{s^2}{2}\right)$$
$$\therefore \ B = 4exp\left(-m - \frac{s^2}{2}\right) \tag{4.3.7}$$

The analytic cumulative volume fraction for the exponential distribution from Garside et al. (2002) is shown in Equation (4.3.8).

$$\Phi(L) = 1 - exp(-BL)\left(1 + BL + \frac{(BL)^2}{2} + \frac{(BL)^3}{6}\right) \tag{4.3.8}$$

Figure 4.3.6 shows the data fit if the population density function is the exponential distribution. The R^2 values for the data fit in Figure 4.3.6 ranged from 0.96 to 0.98 and is lower than the R^2 values for the lognormal fit in Figure 4.3.5.

Table 4.3.1: Distribution statistics for data in Figures 4.3.5 a) and 4.3.6 a)

Sample	s	m	L_{43} μm	B μm^{-1}
1h	0.34	5.35	223	0.018
2h	0.33	5.38	228	0.018
3h	0.34	5.38	230	0.017
4h	0.37	5.33	221	0.018
Reactor at 4h	0.39	5.48	259	0.015

Table 4.3.1 shows the distribution statistics for the data fits in Figures 4.3.5 a) and 4.3.6 a). The L_{43} size indicates that the reactor content becomes coarser over time. The parameter in the last column of Table 4.3.1 represents an exponential distribution decay constant as used in Equations (4.3.7) and (4.3.8).

Figure 4.3.6 b) shows that the tail end towards the higher sizes under predict the cumulative volume per cent passing. This will give rise to a conservative upper size limit to approximate infinity in moment calculations as the exponential distribution decays to zero at a slower rate than the corresponding lognormal distribution. The point is better explained through Equation (4.3.9).

$$\int_0^{L_{max}} exp(-BL)\, L^4 dL \leq 10^{-6}$$
$$\therefore \ \frac{24exp(-BL_{max})}{B^5} g(L_{max}) \leq 10^{-6} \tag{4.3.9}$$

$$\& \; g(L_{max}) \leq \left(1 + BL_{max} + \frac{(BL_{max})^2}{2} + \frac{(BL_{max})^3}{6} + \frac{(BL_{max})^4}{24}\right)$$

To minimise the numerical integration error in moment calculations the following criteria is set for L_{max} based on assuming an exponential distribution at sizes greater than L_{max}. Note that the 4th moment is the highest moment used in this study, therefore it is used to set the limiting upper size as the lower moments will automatically fall within the constraint. L_{max} is chosen such that Equation (4.3.9) holds.

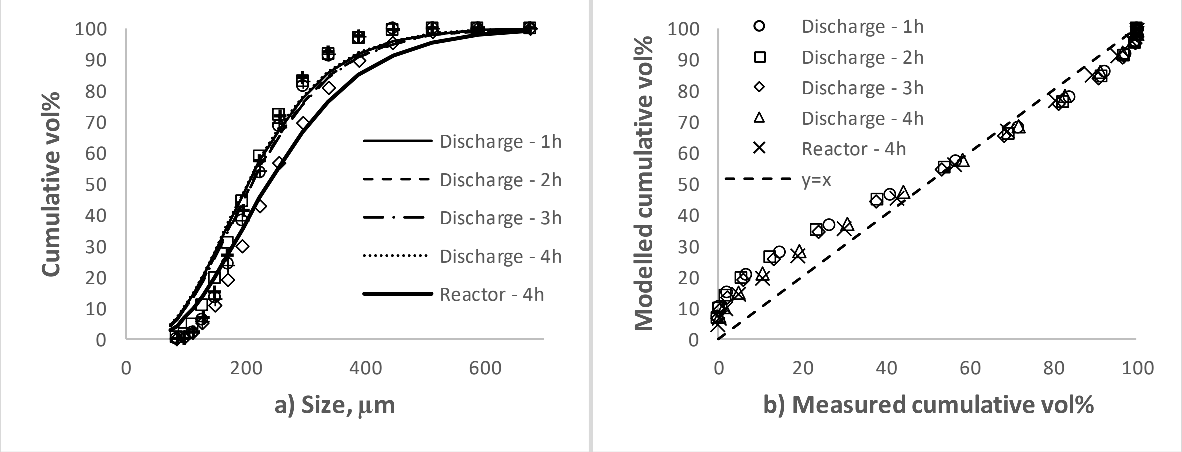

Figure 4.3.6: CSTR wash-out test a) exponential distribution b) parity chart of exponential distribution volume per cent VS measured volume per cent

If B equals 0.018µm^{-1} the constraint requires L_{max} to be greater or equal to 2749µm. An empirical equation that gives the minimum required L_{max} to satisfy the constraint in Equation (4.3.9) is given in Equation (4.3.10).

$$\ln B = -0.9 \ln L_{max} + 3.14 \qquad \textbf{(4.3.10)}$$

Equation (4.3.10) illustrates that at a conservative L_{max} of 10 000µm the decay constant B can be as low as 0.0056 and still satisfy the constraint in Equation (4.3.9). This B value is well below the observed range of B in Table 4.3.1, implying that the upper limit integration error at $L_{max} \geq$ 10 000µm is negligible.

Following from the defined upper limit of integration the next step is to develop a transient population balance for a segregating system with no nucleation or growth processes occurring. The assumptions for the transient population balance are as follows:

- The feed flow into the reactor is constant and does not contain any crystals.
- The discharge stream flow is constant and maintains the reactor volume at a constant level.
- The discharge population density is not equal to the reactor population density.

By applying the above assumption, the transient population balance reduces to Equation (4.3.11).

$$\frac{\partial n(L,t)}{\partial t} = -\frac{\upsilon n_{out}(L,t)}{V_r} = -\frac{n_{out}(L,t)}{\tau} \qquad \textbf{(4.3.11)}$$

Where n = Population density inside reactor [#/µm.dm^3]
t = Time [h]
n_{out} = Population density in the discharge stream [#/µm.dm^3]
υ = Volumetric flow rate of water [dm^3/h]
V_r = Active reactor volume [dm^3]
τ = V_r / υ = Reactor residence time [h]

Given that segregation occurs by size between the reactor and the discharge stream a size dependent function bounded between 0 and 1 is proposed to limit the discharge population density as in Equation (4.3.12).

$$n_{out}(L,t) = f(L)n(L,t) \quad \textbf{(4.3.12)}$$

It is further proposed that $f(L)$ is exponentially distributed over crystal size such that the population density at smaller sizes are preferentially removed from the reactor and removal of larger sizes are less likely. The proposed mathematical expression for $f(L)$ is shown in Equation (4.3.13).

$$f(L) = exp(-b_s L) \quad \textbf{(4.3.13)}$$

Where $f(L)$ = Size segregation function
L = Crystal size [μm]
b_s = Segregation spread [μm^{-1}]

Inserting Equation (4.3.13) into Equation (4.3.12) and then solving (3.3.11) gives Equation (4.3.14).

$$n(L,t) = n(L,0)exp\left[-\frac{t}{\tau}exp(-b_s L)\right] \quad \textbf{(4.3.14)}$$

Where $n(L,0)$ = Population density inside reactor at time zero [#/μm.dm^3]

Figure 4.3.7 illustrates the effect of segregation spread b_s on the population density inside the reactor. An exponential population density distribution at time zero was assumed for the illustration. Equation (4.3.15) shows the expression for the assumed distribution.

$$n(L,0) = 10^{10}exp[-0.018L] \quad \textbf{(4.3.15)}$$

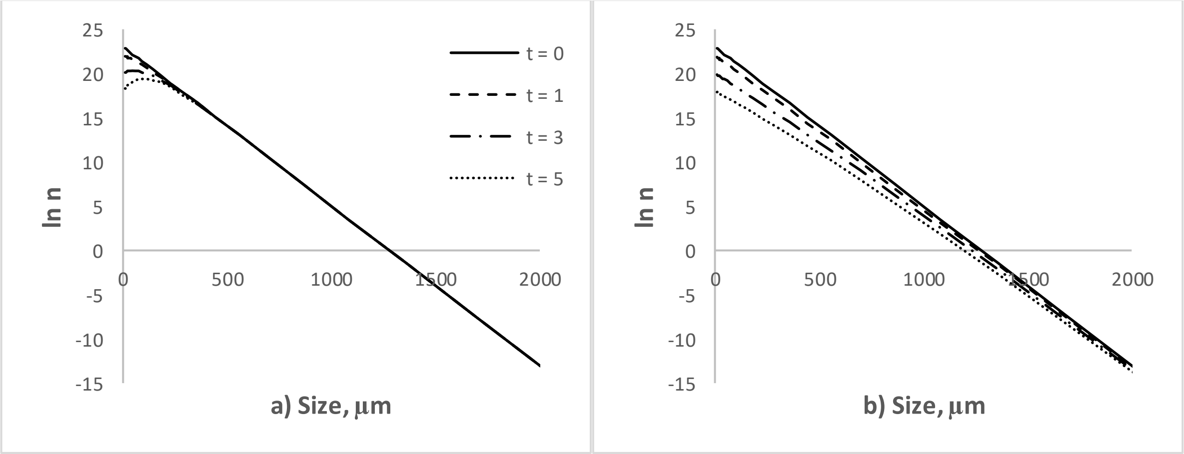

Figure 4.3.7: Population density VS size transient time profile: a) b_s = 0.01μm^{-1}, b) b_s = 0.001μm^{-1}

Figure 4.3.7 a) and b) shows that the segregation spread bends the population density in the reactor downward creating a coarser distribution in the reactor as time passes. If there is no segregation then b_s tends to zero and the population density curves will become parallel as time passes. This indicates that the fraction of particles and the particle length, area and volume in the outlet remains constant over time.

To continue, the derivation of the population density under the assumption that it is lognormal is applied (refer to Section 10.3 in the Appendix). To determine the population density function for a lognormal volume fraction distribution, the population density, n, is made the argument in Equation (10.3.1). Equation (10.3.2) is then inserted into the rearranged Equation (10.3.1) and the result is shown in Equation (4.3.16).

$$n(L,0) = \frac{M_3|_{t=0}}{\sqrt{2\pi}sL^4}exp\left(-\frac{(\ln L - m)^2}{2s^2}\right) \quad \textbf{(4.3.16)}$$

By inserting Equation (4.3.16) into Equation (4.3.14) the population density over time is obtained. The volume fraction under the lognormal assumption is then given by Equation (4.3.17) after applying the identity in Equation (4.3.4).

$$\phi(L,t) = \frac{\frac{1}{L} exp\left(-\frac{(\ln L - m)^2}{2s^2} - \frac{t}{\tau} exp(-b_s L)\right)}{\int_0^\infty \frac{1}{L} exp\left(-\frac{(\ln L - m)^2}{2s^2} - \frac{t}{\tau} exp(-b_s L)\right) dL} \tag{4.3.17}$$

Equation (4.3.17) is converted to the L_{43} size through Equation (4.3.5) to obtain Equation (4.3.18).

$$L_{43} = \frac{\int_0^\infty exp\left(-\frac{(\ln L - m)^2}{2s^2} - \frac{t}{\tau} exp(-b_s L)\right) dL}{\int_0^\infty \frac{1}{L} exp\left(-\frac{(\ln L - m)^2}{2s^2} - \frac{t}{\tau} exp(-b_s L)\right) dL} \tag{4.3.18}$$

The reactor cumulative volume fraction distribution is calculated by integrating the volume fraction density distribution in Equation (4.3.17) up to size L; the result is shown in Equation (4.3.19).

$$\Phi(L,t) = \int_0^L \phi(l,t) dl = \frac{\int_0^L \frac{1}{l} exp\left(-\frac{(\ln l - m)^2}{2s^2} - \frac{t}{\tau} exp(-b_s l)\right) dl}{\int_0^\infty \frac{1}{l} exp\left(-\frac{(\ln l - m)^2}{2s^2} - \frac{t}{\tau} exp(-b_s l)\right) dl} \tag{4.3.19}$$

The advantage of the cumulative distribution is that the third moment value at time zero cancels and the function only has parameters b_s, m and s. Another advantage is that the output of this function is directly comparable with instruments that measure particle volume fraction such as a Malvern Mastersizer that uses laser diffraction to infer particle volume. The outlet stream cumulative volume fraction distribution is calculated by combining Equation (4.3.17) with Equation (4.3.13) as per Equation (4.3.12), and then taking the third moment; the result is shown in Equation (4.3.20).

$$\Phi_{out}(L,t) = \int_0^L \phi_{out}(l,t) dl = \frac{\int_0^L \frac{1}{l} exp\left(-\frac{(\ln l - m)^2}{2s^2} - \frac{t}{\tau} exp(-b_s l) - b_s l\right) dl}{\int_0^\infty \frac{1}{l} exp\left(-\frac{(\ln l - m)^2}{2s^2} - \frac{t}{\tau} exp(-b_s l) - b_s l\right) dl} \tag{4.3.20}$$

The third moment of the population density function is fitted to the measured crystal concentration profile over time, shown in Figure 4.3.4 a) by converting the population density function to crystal concentration as per Equation (4.3.21). According to literature, the third moment of the population density is defined as the crystal volume per pulp volume (Garside et al., 2002; Myerson, 2002; Jones, 2002). The conversion to crystal concentration follows by multiplying particle volume per volume solution with crystal density as in Equation (4.3.21). The SEM photographs in Figure 4.3.3 suggest that volume shape factor is related to size (the larger the crystal the more porous it becomes). It is therefore proposed that the volume shape factor of the crystals, K_v, decays exponentially with size.

$$\begin{aligned} [S]_{out} &= \rho_c \int_0^\infty K_v n(L,t) L^3 dL \\ &= \frac{\rho_c M_3|_{t=0}}{\sqrt{2\pi} s} \int_0^\infty \frac{A_{K_v} exp\left(-b_{K_v} L\right)}{L} exp\left(-\frac{(\ln L - m)^2}{2s^2} - \frac{t}{\tau} exp(-b_s L) - b_s L\right) dL \\ &= K_{M_3} \int_0^\infty \frac{1}{L} exp\left(-\frac{(\ln L - m)^2}{2s^2} - \frac{t}{\tau} exp(-b_s L) - BL\right) dL \end{aligned} \tag{4.3.21}$$

Where $[S]_{out}$ = Concentration of crystals in the reactor discharge [g/dm^3]
ρ_c = Crystal density [g/dm^3]
K_v = Crystal volume shape factor (Actual crystal volume per characteristic length cubed per particle) [µm^3/#.µm^3]

K_{M_3} = $\frac{\rho_c M_3|_{t=0} A_{K_v}}{\sqrt{2\pi}s}$ = Lumped crystal concentration constant [g/dm^3]
B = $b_s + b_{K_v}$ = Lumped decay constant [1/μm]

Trapezoidal integration was used to numerically evaluate the integrals in Equations (4.3.19) to (4.3.21). The upper size limit used as a proxy for infinity was 10 000μm as determined earlier. The parameters b_s, m, s, B and K_{M_3} were fitted by using the non-linear least squares minimisation function, *lsqnonlin*, in Matlab version 2009a (Coleman & Li, 1996; Coleman & Li, 1994). The objective function was the square of the difference between the measurements and the calculated values from the integrals in Equations (4.3.19) to (4.3.21). The crystal size distribution at time 4 hours seemed biased relative to the crystal size distributions at 1-3 hours as it appears finer. The distribution contribution to the objective function was therefore weighted by multiplying its contribution by 0.1. The minimisation routine converged to the following values for a residence time of 1 hour:

m = 5.42895615731341 ≈ 5.429
K_{M_3} = 109.762566394075 ≈ 109.8g/dm^3
B = 0.00302713892418489 ≈ 0.00303μm^{-1}
s = 0.353925621768622 ≈ 0.346
b_s = 0.000493415013878869 ≈ 0.000493μm^{-1}

In Figure 4.3.8 the fitted Equations (4.3.19) to (4.3.21) are represented by lines and the measurements are represented by discrete markers. Note that Equation (4.3.20) represents the discharge stream in Figure 4.3.8 a) and the reactor content is represented by Equation (4.3.19).

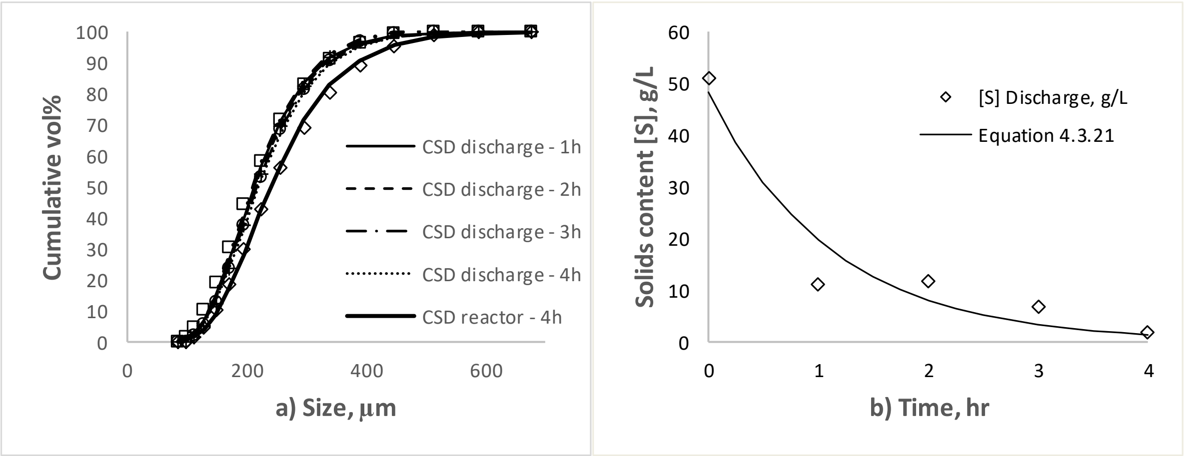

Figure 4.3.8: Population balance model output VS measurements: a) Washout test crystal size distribution over time; b) Crystal concentration profile over time

The total sum of squared errors for the data fit was ~42 resulting in an overall R^2 value of ~0.98 indicating a reasonable fit. The data fit parity chart in Figure 4.3.9 below shows that the CSD at 4 hours produced the worst fit, justifying the low weighting assigned to this data set for the least squares fitting routine.

The initial L_{43} size, calculated by inserting the fitted location and spread parameters m and s into Equation (4.3.7), was 243μm. The parameter K_{M_3} multiplied by 0.44, the integral portion of Equation (4.3.21) at time zero, is equal to the fitted initial solids concentration of ~48g/dm^3. The fitted initial solids concentration is therefore comparable to the measured value of 51g/dm^3; the difference is attributed to experimental error.

The segregation function is ~0.95 at a size of 100μm, confirming that 5 per cent of the population density function at size 100μm remains in the reactor. At a size of 3000μm, the portion of the population density function that remains in the reactor is 77 per cent, indicating that particles > 3000μm have a small chance of entering the discharge stream. The above analysis suggests that segregation should be incorporated into a population balance for this reactor configuration where nucleation and growth is present, as the classic MSMPR assumption relating to segregation is not adhered to. A population balance with nucleation, growth and segregation is presented in Section 4.3.4. The segregated reactor model is then compared to the ideal reactor model to ascertain the validity of segregation in the continuous experimental results.

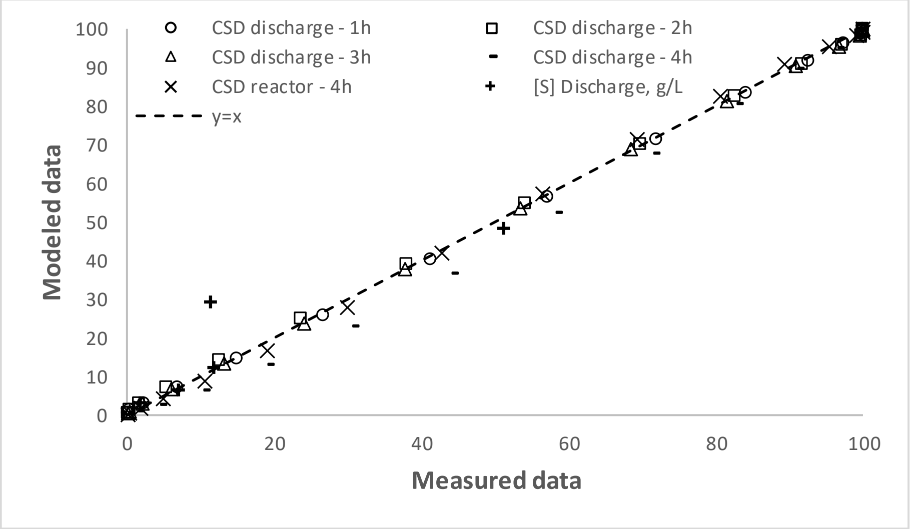

Figure 4.3.9: Modelled VS measured data for washout test

4.3.4. CSTR discharge solids segregation model

In Section 4.3.3 it was shown that discharge segregation influences the crystal size distribution inside the reactor over time, under exacerbated segregation conditions described in Section 4.3.2. Segregation, as defined in Equation (4.3.12), effectively partitions the reactor population density by a function that is bounded between 0 and 1 to form the discharge population density. Thus, the last term in the population balance in Equation (3.1.15) is multiplied by the segregation function $f(L)$. By applying the moment transform to the population balance with segregation, the moment-generating equation is obtained, namely Equation (4.3.22).

$$\begin{aligned}\frac{dM_i}{dt} &= -(G-G_a)\left(L^i n(L,t)\Big|_{L\to 0}^{L\to\infty} - iM_{i-1}\right) \\ &\quad +GG_a\tau\left(L^i\frac{\partial n}{\partial L}\bigg|_{L\to 0}^{L\to\infty} - iL^{i-1}n(L,t)\Big|_{L\to 0}^{L\to\infty} + i(i-1)M_{i-2}\right) - \frac{\psi_i}{\tau}\end{aligned} \qquad \textbf{(4.3.22)}$$

The last term in Equation (4.3.22) represents the *i*th moment of the segregated discharge stream; this term is expanded in Equation (4.3.23).

$$\psi_i = \int_0^\infty exp(-b_s L)n(L,t)L^i dL \qquad i = 0, 1, 2, 3 \ldots \qquad \textbf{(4.3.23)}$$

Equation (4.3.23) can further expand to Equation (4.3.24), an infinite series, by repeatedly integrating by parts.

$$\begin{aligned}\psi_0 &= \frac{n(0,t)}{b_s} + \frac{1}{b_s}\sum_{r=1}^{\infty}\frac{1}{b_s^r}\frac{\partial^r n}{\partial L^r}\bigg|_{L=0} \\ \psi_i &= \frac{i\psi_{i-1}}{b_s} + \frac{1}{b_s^{i+1}}\sum_{r=1}^{\infty}\frac{\prod_{k=0}^{i-1}(r+k)}{b_s^r}\frac{\partial^r n}{\partial L^r}\bigg|_{L=0}\end{aligned} \qquad \textbf{(4.3.24)}$$

Equation (4.3.24) is convergent only if the segregation function decays at a faster rate than the population density function. This is justified by considering the size derivative of the steady state population density in Equation (3.1.17) with negative one factored out of G_a for the case of disruption or breakage. The *r*th partial derivative of Equation (3.1.17) gives rise to Equation (4.3.25).

$$\begin{aligned}n(L, t > t_{ss}) &= n_{01}exp\left(-\frac{L}{G\tau}\right) + n_{02}exp\left(-\frac{L}{G_a\tau}\right) \\ \frac{\partial^r n}{\partial L^r}\bigg|_{L=0} &= \frac{(-1)^r}{\tau^r}\left(\frac{n_{01}}{G^r} + \frac{n_{02}}{G_a^r}\right) \qquad \& \qquad r \in [0, 1, 2, 3 \ldots . \infty)\end{aligned} \qquad \textbf{(4.3.25)}$$

Inserting Equation (4.3.25) into Equation (4.3.24) and considering the first four moments gives the equations in Equation (4.3.26).

$$
\begin{aligned}
\psi_0 &= \frac{1}{b_s}\sum_{r=0}^{\infty}\frac{(-1)^r}{\tau^r b_s^r}\left(\frac{n_{01}}{G^r}+\frac{n_{02}}{G_a^r}\right)\\
\psi_1 &= \frac{\psi_0}{b_s}+\frac{1}{b_s^2}\sum_{r=0}^{\infty}\frac{(-1)^r r}{\tau^r b_s^r}\left(\frac{n_{01}}{G^r}+\frac{n_{02}}{G_a^r}\right)\\
\psi_2 &= \frac{2\psi_1}{b_s}+\frac{1}{b_s^3}\sum_{r=0}^{\infty}\frac{(-1)^r r(r+1)}{\tau^r b_s^r}\left(\frac{n_{01}}{G^r}+\frac{n_{02}}{G_a^r}\right)\\
\psi_3 &= \frac{3\psi_2}{b_s}+\frac{1}{b_s^4}\sum_{r=0}^{\infty}\frac{(-1)^r r(r+1)(r+2)}{\tau^r b_s^r}\left(\frac{n_{01}}{G^r}+\frac{n_{02}}{G_a^r}\right)\\
\psi_4 &= \frac{4\psi_3}{b_s}+\frac{1}{b_s^5}\sum_{r=0}^{\infty}\frac{(-1)^r r(r+1)(r+2)(r+3)}{\tau^r b_s^r}\left(\frac{n_{01}}{G^r}+\frac{n_{02}}{G_a^r}\right)
\end{aligned}
\tag{4.3.26}
$$

The expressions in Equation (4.3.26) converge to Equation (4.3.27) only if $b_s > max(1/G\tau, 1/G_a\tau)$. This criterion justifies, to an extent, the above statement that the segregation function must decay at a faster rate than the population density over size. If the criteria to converge is met, the series reduces to Equation (4.3.27).

The constraint on b_s gives a probable stability condition for the population balance with segregation at steady state if and only if the *rth* size derivative of the population density is comparable to Equation (4.3.25). If the stability condition at steady state can be extended to the transient, it can be stated that the segregation function must decay at a faster rate than the population density function along L, to prevent an unstable solution that does not tend to zero as L approaches infinity, i.e. violates a boundary condition.

$$
\begin{aligned}
\psi_0 &= \tau\left(\frac{n_{01}G}{1+b_sG\tau}+\frac{n_{02}G_a}{1+b_sG_a\tau}\right)\\
\psi_1 &= \frac{\psi_0}{b_s}-\frac{\tau}{b_s}\left(\frac{n_{01}G}{(1+b_sG\tau)^2}+\frac{n_{02}G_a}{(1+b_sG_a\tau)^2}\right)\\
\psi_2 &= \frac{2\psi_1}{b_s}-\frac{2\tau}{b_s^2}\left[\frac{n_{01}G}{(1+b_sG\tau)^2}\left(1-\frac{1}{1+b_sG\tau}\right)+\frac{n_{02}G_a}{(1+b_sG_a\tau)^2}\left(1-\frac{1}{1+b_sG_a\tau}\right)\right]\\
\psi_3 &= \frac{3\psi_2}{b_s}-\frac{6\tau}{b_s^3}\left[\begin{aligned}&\frac{n_{01}G}{(1+b_sG\tau)^2}\left(\frac{1}{(1+b_sG\tau)^2}-\frac{2}{1+b_sG\tau}+1\right)\\ &+\frac{n_{02}G_a}{(1+b_sG_a\tau)^2}\left(\frac{1}{(1+b_sG_a\tau)^2}-\frac{2}{1+b_sG_a\tau}+1\right)\end{aligned}\right]\\
\psi_4 &= \frac{4\psi_3}{b_s}-\frac{24\tau}{b_s^4}\left[\begin{aligned}&\frac{n_{01}G}{(1+b_sG\tau)^2}\left(1-\frac{3}{1+b_sG\tau}+\frac{3}{(1+b_sG\tau)^2}-\frac{1}{(1+b_sG\tau)^3}\right)\\ &+\frac{n_{02}G_a}{(1+b_sG_a\tau)^2}\left(1-\frac{3}{1+b_sG_a\tau}+\frac{3}{(1+b_sG_a\tau)^2}-\frac{1}{(1+b_sG_a\tau)^3}\right)\end{aligned}\right]
\end{aligned}
\tag{4.3.27}
$$

All crystal size distributions produced in this work gave rise to lognormal or mixed lognormal size distributions for the cumulative volume fraction. This suggests that the population density possibly contains elements from the lognormal distribution. A possible form of a lognormal population density distribution is given in the Appendix, Section 10.3. Applying the *rth* derivative to the exponential part of the lognormal population density distribution gives Equation (4.3.28).

$$
\frac{\partial^r n}{\partial L^r}=\frac{(-1)^r}{L^r}exp\left(-\frac{(\ln L-m)^2}{2s^2}\right)\sum_{i=0}^{r}a_i(\ln L-m)
\tag{4.3.28}
$$

Note that the constants a_i in Equation (4.3.28) are only functions of the spread s. The constant a_i for the first four derivatives are shown in Table 4.3.2. Potentially there is a sequence that relates a_i to both s and r in Equation (4.3.28) but that is not the purpose of this study.

Table 4.3.2: Equation (4.3.29) constant a_i for the first four derivatives (r = 1, 2, 3, 4)

r	a_0	a_1	a_2	a_3	a_4	**....**	a_r
1	0	$1/s^2$	0	0	0	....	0
2	$-1/s^2$	$1/s^2$	$1/s^4$	0	0	....	0
3	$-3/s^2$	$2/s^2-3/s^4$	$3/s^4$	$1/s^6$	0	....	0
4	$-11/s^2+3/s^4$	$6/s^2-18/s^4$	$8/s^4-3/s^6$	$6/s^6$	$1/s^8$	....	0
:	:	:	:	:	:	⋱	:
r						....	$1/s^{2r}$

Taking the limit of Equation (4.3.28) as L approaches zero from the right for r = 1, 2, 3 and 4 gives zero. This finding is strong evidence that the limit of Equation (4.3.28) as L approaches zero is zero for all r. Equation (4.3.29) is obtained by inserting the size limit, as discussed above, into Equation (4.3.24), to obtain an expression for the segregated outlet stream of the continuous stirred reactor with a lognormal population density distribution.

$$\psi_i = i!\frac{n(0,t)}{b_s^{i+1}} \qquad \textbf{(4.3.29)}$$

The L_{43} size for the outlet then reduces to Equation (4.3.30).

$$L_{43} = \frac{\psi_4}{\psi_3} = \frac{4}{b_s} \qquad \textbf{(4.3.30)}$$

During the transient stages of precipitation, it was found that the L_{43} size was time dependent, suggesting that the segregation spread b_s in Equation (4.3.30) is likely to be time dependent. Given the possibility of a lognormal population density distribution, the boundary conditions follow from the discussion above and are shown in Equation (4.3.31).

$$\begin{aligned} n(0,t) &= n_0(t) \\ n(\infty,t) &= 0 \\ \left.\frac{\partial^r n}{\partial L^r}\right|_{L\to 0} &= 0 \qquad \& \qquad r \in [0,1,2,\dots,\infty) \\ \left.\frac{\partial^r n}{\partial L^r}\right|_{L\to\infty} &= 0 \end{aligned} \qquad \textbf{(4.3.31)}$$

The moment transformed population balance in Equation (4.3.22) combined with the boundary conditions specified in Equation (4.3.31), and the saturation profile from the mass balance in Section 3.1.1, give a set of non-linear ordinary differential equations. Equation (4.3.32) gives the time dependent set of segregated moment equations in matrix notation.

$$\begin{bmatrix} \frac{dM_0}{dt} \\ \frac{dM_1}{dt} \\ \frac{dM_2}{dt} \\ \frac{dM_3}{dt} \\ \frac{dM_4}{dt} \end{bmatrix} = \boldsymbol{A} \begin{bmatrix} n_0(t) \\ M_0 \\ M_1 \\ M_2 \\ M_3 \end{bmatrix} - \begin{bmatrix} \frac{\psi_0}{\tau} \\ \frac{\psi_1}{\tau} \\ \frac{\psi_2}{\tau} \\ \frac{\psi_3}{\tau} \\ \frac{\psi_4}{\tau} \end{bmatrix} \qquad \& \qquad IC\colon \begin{bmatrix} M_0 \\ M_1 \\ M_2 \\ M_3 \\ M_4 \end{bmatrix}_{t=0} = \begin{bmatrix} 0 \\ 0 \\ 0 \\ 0 \\ 0 \end{bmatrix} \qquad \textbf{(4.3.32)}$$

The segregation outlet terms ψ_i are as shown in Equation (4.3.29). The connection matrix $\boldsymbol{A}$ is a function of time through the terms G and G_a and is given in Equation (4.3.33). This implies that the non-linear set of ordinary differential Equations in (4.3.32) can only be solved numerically.

$$\boldsymbol{A} = \begin{bmatrix} (G-G_a) & 0 & 0 & 0 & 0 \\ GG_a\tau & (G-G_a) & 0 & 0 & 0 \\ 0 & 2GG_a\tau & 2(G-G_a) & 0 & 0 \\ 0 & 0 & 6GG_a\tau & 3(G-G_a) & 0 \\ 0 & 0 & 0 & 12GG_a\tau & 4(G-G_a) \end{bmatrix} \tag{4.3.33}$$

As with the numeric solution of the system without segregation in Section 3.1.2, the numerical method that was most successful to solve the system in Equations (4.3.32) and (4.3.33) was the modified Rosenbrock formula of order two that is programmed as a standard Matlab function '*ode23s*' (Shampine & Reichelt, 1997). The variable step solver, '*ode15s*', that is based on numeric differencing formulas or NDFs by Shampine & Reichelt (1997) and Shampine et al. (1999) also worked but gave less reliable results. The minimum time step in both variable step solvers '*ode23s*' and '*ode15s*' was automatically set by the software and typically ranged between 1E-15h to 1E-18h. Shape preservation was activated for both solvers. The model represented by Equations (4.3.32) and (4.3.33) was coded in Simulink®, available in Matlab version R2009a.

4.4. T-MIXER & PFR - LAYOUT, REACTOR DESIGN AND CALIBRATION

The observations from the literature review in Chapter 2 suggest that one can potentially minimise the effect of mesoscale mixing on observed reaction kinetics by simply combining reactants in a t-mixer. A simple t-mixer design was considered in the experimental procedure to give a mixing time as low as 1ms with the Reynolds number not exceeding 10 000, with the aim of emulating mixing times found in Fang & Lee (2001) and Lindenberg et al. (2008). The proposed t-mixer and PFR configuration flow and test procedure is summarised in Figure 4.4.1.

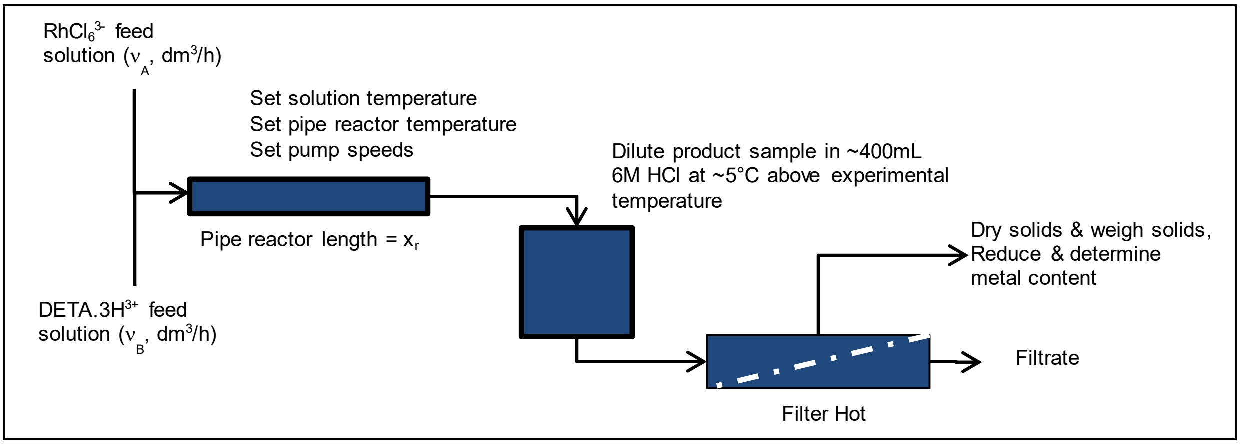

Figure 4.4.1: PFR experimental procedure flow schematic

The designed plug flow reactor setup is shown in Figure 4.4.2. Two different pipe reactor lengths were tested as indicated. A detailed view of the t-mixer and plug flow coil designs are shown as inserts in Figure 4.4.2.

The design in Figure 4.4.2 allows for independent temperature control of the hexachlororhodate (III) solution labelled 'Rh Feed'; the protonated diethylenetriamine solution labelled 'DETA feed'; and the plug flow reactor coil that is submerged in a 5dm^3 water bath. For an experiment, each temperature controller was set to the desired temperature to ensure isothermal conditions. The dilution acid temperature was set to approximately ~5°C above that of the experiment temperature to minimise post precipitation to the point where it is negligible.

Insufficient dilution of the product slurry and cooling during filtration causes severe post nucleation that renders the experiment invalid. Figure 4.4.3 shows examples of optimal and suboptimal filtration conditions. From the simple filtration tests a standard sample handling protocol was adopted that required heating 400-600g of 6M hydrochloric acid at ~5°C above the experimental temperature. Depending on the experimental flow rate, approximately 100-400mL of sample was collected in the dilution sample.

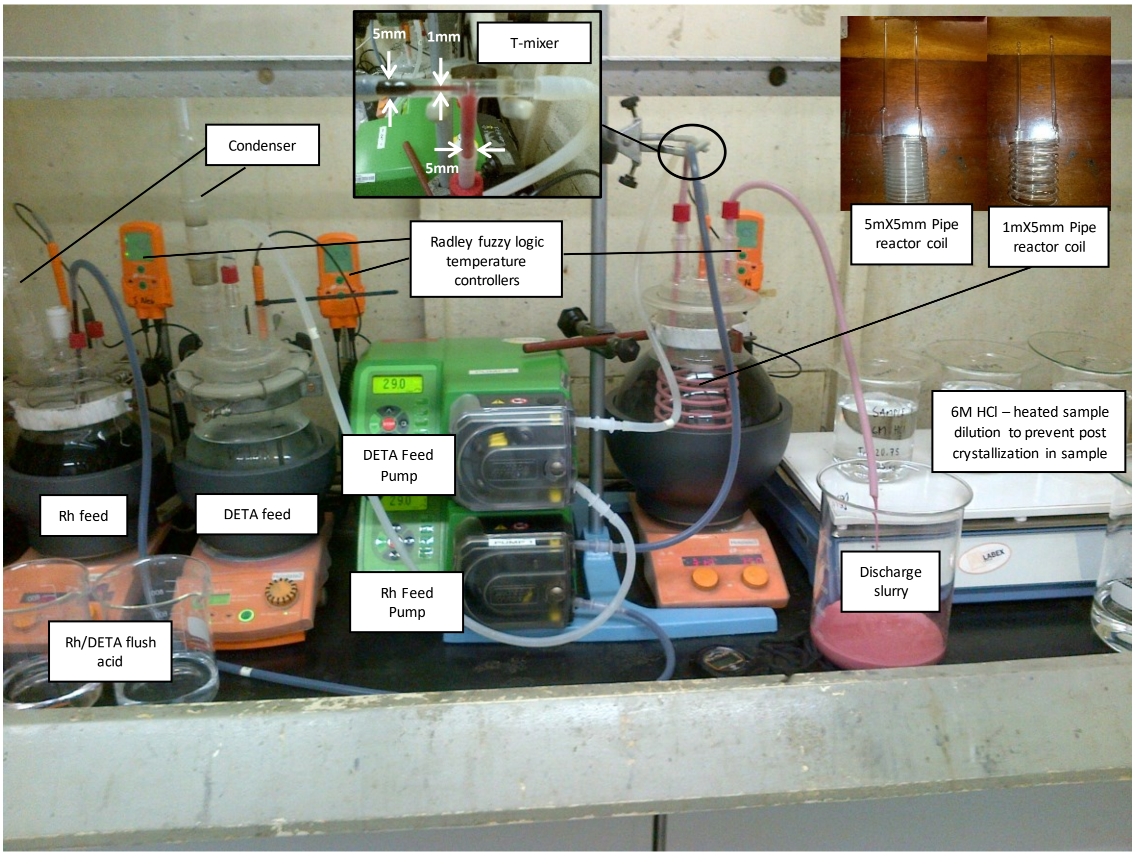

Figure 4.4.2: Plug flow reactor setup

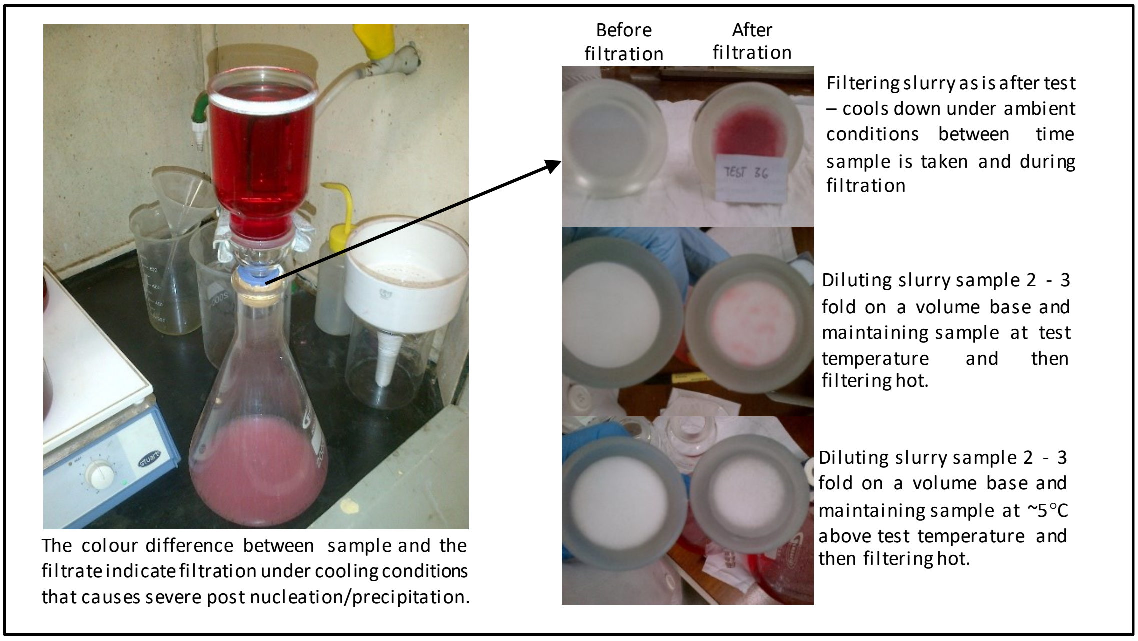

Filtering slurry as is after test – cools down under ambient conditions between time sample is taken and during filtration

Diluting slurry sample 2 - 3 fold on a volume base and maintaining sample at test temperature and then filtering hot.

Diluting slurry sample 2 - 3 fold on a volume base and maintaining sample at ~5°C above test temperature and then filtering hot.

The colour difference between sample and the filtrate indicate filtration under cooling conditions that causes severe post nucleation/precipitation.

Figure 4.4.3: Slurry filtration experimental conditions

The pump calibration curves are shown in Figure 4.4.4 a). The pumps were calibrated independently. The coupling of the two pump deliveries through the t-mixer can cause flow bias if there is a pressure differential between the two lines. To test for bias the independent pump volume flow calibration curves were compared to a measured combined volume flow for each experiment in Figure 4.4.4 b). The regression comparison shows that there is no detectable difference between the two data sets, which suggests the coupled pump delivery lines through the t-mixer do not cause flow bias.

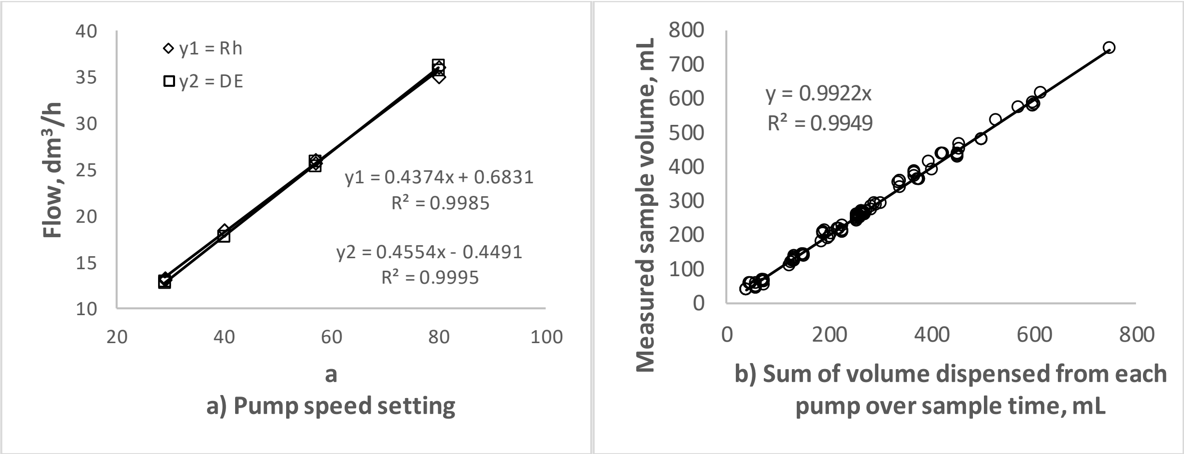

Figure 4.4.4: a) Watson Marlow 520D pump calibration curves and b) test for bias between pump volume dispensed and measured discharge volume

The experimental conditions and calculated equilibrium concentrations, according to the method outlined in Section 3.2.1, for each PFR test are shown in Table 4.4.1.

Table 4.4.1: Plug flow reactor experimental conditions

Test	x, m	T, °C	$C_A\vert_{x=0}$, M	$C_B\vert_{x=0}$, M	v_A, dm³/h	v_B, dm³/h	Re	C_{Ae}, M	C_{Be}, M
1	4.84	30	4.95E-03	2.18E-02	40.9	41.7	5312	1.22E-04	1.38E-01
2	4.84	30	4.95E-03	2.18E-02	40.9	41.7	5312	1.78E-04	1.28E-01
3	4.84	30	4.95E-03	2.18E-02	40.9	41.7	5312	1.84E-04	1.35E-01
4	4.84	30	4.95E-03	2.18E-02	40.9	41.7	5312	1.86E-04	1.36E-01
5	4.84	30	4.97E-03	2.17E-02	18.8	19.0	2429	1.88E-04	1.38E-01
6	4.84	30	4.97E-03	2.17E-02	18.8	19.0	2429	2.66E-04	1.28E-01
7	4.84	30	4.97E-03	2.17E-02	18.8	19.0	2429	2.76E-04	1.35E-01
8	4.84	35	4.99E-03	2.18E-02	18.8	19.0	2617	2.78E-04	1.36E-01
9	4.84	35	4.99E-03	2.18E-02	18.8	19.0	2617	2.81E-04	1.38E-01
10	4.84	35	4.99E-03	2.18E-02	18.8	19.0	2617	3.89E-04	1.28E-01
11	4.84	20	4.97E-03	2.19E-02	40.9	41.7	4541	4.03E-04	1.35E-01
12	4.84	20	4.97E-03	2.19E-02	40.9	41.7	4541	4.07E-04	1.37E-01
13	4.84	20	4.97E-03	2.19E-02	40.9	41.7	4541	4.11E-04	1.38E-01
14	4.84	38	4.99E-03	2.18E-02	18.8	19.0	2734	1.10E-04	1.16E-01
15	4.84	37	4.99E-03	2.18E-02	18.8	19.0	2695	1.15E-04	1.26E-01
16	4.84	38	4.99E-03	2.18E-02	18.8	19.0	2734	1.16E-04	1.28E-01
17	4.84	50	4.99E-03	2.18E-02	18.8	19.0	3228	1.17E-04	1.30E-01
18	4.84	50	4.99E-03	2.18E-02	18.8	19.0	3228	1.69E-04	1.16E-01
19	4.84	50	4.99E-03	2.18E-02	18.8	19.0	3228	1.76E-04	1.26E-01
20	4.84	47	4.94E-03	4.95E-03	18.8	19.0	3101	1.78E-04	1.28E-01
21	4.84	51	4.94E-03	4.95E-03	18.8	19.0	3272	1.80E-04	1.30E-01
22	4.84	52	4.94E-03	4.95E-03	18.8	19.0	3315	2.52E-04	1.17E-01
23	4.84	47	4.92E-03	4.96E-03	29.8	30.3	4940	2.63E-04	1.26E-01
24	4.84	45	4.92E-03	4.96E-03	29.8	30.3	4807	2.66E-04	1.28E-01
25	4.84	45	4.92E-03	4.96E-03	29.8	30.3	4807	2.69E-04	1.30E-01

Test	x, m	T, °C	$C_A\|_{x=0}$, M	$C_B\|_{x=0}$, M	υ_A, dm^3/h	υ_B, dm^3/h	Re	C_{Ae}, M	C_{Be}, M
26	4.84	30	4.92E-03	4.96E-03	29.8	30.3	3871	3.68E-04	1.17E-01
27	4.84	30	4.92E-03	4.96E-03	29.8	30.3	3871	3.85E-04	1.26E-01
28	4.84	30	4.92E-03	4.96E-03	29.8	30.3	3871	3.89E-04	1.28E-01
29	4.84	44	4.92E-03	4.96E-03	29.8	30.3	4741	3.94E-04	1.30E-01
30	4.84	45	4.92E-03	4.96E-03	29.8	30.3	4807	1.22E-04	1.38E-01
31	4.84	43	4.92E-03	4.96E-03	29.8	30.3	4676	1.78E-04	1.28E-01
32	2.95	33	1.47E-01	9.27E-02	16.0	10.2	1759	1.84E-04	1.35E-01
33	2.95	34	1.47E-01	9.27E-02	16.0	10.2	1785	1.86E-04	1.36E-01
34	2.95	34	1.47E-01	9.27E-02	16.0	10.2	1785	1.88E-04	1.38E-01
35	2.95	54	1.47E-01	9.27E-02	16.0	10.2	2356	2.66E-04	1.28E-01
36	2.95	53	1.47E-01	9.27E-02	16.0	10.2	2325	2.76E-04	1.35E-01
37	2.95	54	1.47E-01	9.27E-02	16.0	10.2	2356	2.78E-04	1.36E-01
38	2.95	40	9.27E-02	1.46E-01	6.5	10.3	1247	2.81E-04	1.38E-01
39	2.95	40	9.27E-02	1.46E-01	6.5	10.3	1247	3.89E-04	1.28E-01
40	2.95	40	9.27E-02	1.46E-01	6.5	10.3	1247	4.03E-04	1.35E-01
41	2.95	40	1.18E-01	1.21E-01	25.5	26.2	3854	4.07E-04	1.37E-01
42	2.95	40	1.18E-01	1.21E-01	25.5	26.2	3854	4.11E-04	1.38E-01
43	2.95	40	1.18E-01	1.21E-01	25.5	26.2	3854	1.10E-04	1.16E-01
44	2.95	70	1.21E-01	1.18E-01	10.5	10.3	2282	1.15E-04	1.26E-01
45	2.95	70	1.21E-01	1.18E-01	10.5	10.3	2282	1.16E-04	1.28E-01
46	2.95	70	1.21E-01	1.18E-01	10.5	10.3	2282	1.17E-04	1.30E-01
47	2.95	70	1.18E-01	1.21E-01	25.5	26.2	5687	1.69E-04	1.16E-01
48	2.95	70	1.18E-01	1.21E-01	25.5	26.2	5687	1.76E-04	1.26E-01
49	2.95	70	1.18E-01	1.21E-01	25.5	26.2	5687	1.78E-04	1.28E-01
50	2.95	55	1.21E-01	1.18E-01	10.5	10.3	1896	1.80E-04	1.30E-01
51	2.95	55	1.18E-01	1.21E-01	25.5	26.2	4724	2.52E-04	1.17E-01
52	2.95	65	1.05E-02	9.88E-03	10.5	10.3	2149	2.63E-04	1.26E-01
53	2.95	65	1.05E-02	9.88E-03	10.5	10.3	2149	2.66E-04	1.28E-01
54	2.95	65	1.05E-02	9.88E-03	10.5	10.3	2149	2.69E-04	1.30E-01
55	2.95	30	1.03E-02	1.01E-02	25.5	26.2	3328	3.68E-04	1.17E-01
56	2.95	30	1.03E-02	1.01E-02	25.5	26.2	3328	3.85E-04	1.26E-01
57	2.95	30	1.03E-02	1.01E-02	25.5	26.2	3328	3.89E-04	1.28E-01
58	2.95	30	6.92E-03	1.34E-02	10.5	21.1	2036	3.94E-04	1.30E-01
59	2.95	30	6.92E-03	1.34E-02	10.5	21.1	2036	1.22E-04	1.38E-01
60	2.95	30	6.92E-03	1.34E-02	10.5	21.1	2036	1.78E-04	1.28E-01
61	2.95	50	6.96E-03	1.33E-02	10.7	21.4	2750	1.84E-04	1.35E-01
62	2.95	50	6.96E-03	1.33E-02	10.7	21.4	2750	1.86E-04	1.36E-01
63	2.95	50	6.96E-03	1.33E-02	10.7	21.4	2750	1.88E-04	1.38E-01
64	2.95	30	1.05E-02	1.48E-01	22.6	22.3	2888	2.66E-04	1.28E-01
65	2.95	50	1.06E-02	1.45E-01	13.8	13.2	2311	2.76E-04	1.35E-01
66	2.95	40	1.06E-02	1.45E-01	13.8	13.2	2013	2.78E-04	1.36E-01
67	2.95	40	1.06E-02	1.45E-01	13.8	13.2	2013	2.81E-04	1.38E-01
68	2.95	40	1.06E-02	1.45E-01	13.8	13.2	2013	3.89E-04	1.28E-01
69	2.95	60	1.11E-02	1.39E-01	7.2	6.4	1326	4.03E-04	1.35E-01

Test	x, m	T, °C	$C_A\|_{x=0}$, M	$C_B\|_{x=0}$, M	υ_A, dm^3/h	υ_B, dm^3/h	Re	C_{Ae}, M	C_{Be}, M
70	2.95	60	1.06E-02	1.45E-01	13.8	13.2	2630	4.07E-04	1.37E-01
71	2.95	60	1.05E-02	1.47E-01	18.2	17.8	3499	4.11E-04	1.38E-01
72	2.95	60	1.04E-02	1.48E-01	26.9	26.9	5237	1.10E-04	1.16E-01
73	2.95	40	1.11E-02	1.39E-01	7.2	6.4	1015	1.15E-04	1.26E-01
74	2.95	40	1.06E-02	1.45E-01	13.8	13.2	2013	1.16E-04	1.28E-01
75	2.95	40	1.05E-02	1.47E-01	18.2	17.8	2679	1.17E-04	1.30E-01
76	2.95	40	1.04E-02	1.48E-01	26.9	26.9	4009	1.69E-04	1.16E-01
77	2.95	50	1.11E-02	1.39E-01	7.2	6.4	1165	1.76E-04	1.26E-01
78	2.95	50	1.06E-02	1.45E-01	13.8	13.2	2311	1.78E-04	1.28E-01
79	2.95	50	1.05E-02	1.47E-01	18.2	17.8	3074	1.80E-04	1.30E-01
80	2.95	50	1.04E-02	1.48E-01	26.9	26.9	4601	2.52E-04	1.17E-01
81	2.95	60	1.11E-02	1.39E-01	7.2	6.4	1326	2.63E-04	1.26E-01
82	2.95	60	1.06E-02	1.45E-01	13.8	13.2	2630	2.66E-04	1.28E-01
83	2.95	60	1.05E-02	1.47E-01	18.2	17.8	3499	2.69E-04	1.30E-01
84	2.95	60	1.04E-02	1.48E-01	26.9	26.9	5237	3.68E-04	1.17E-01
85	2.95	70	1.11E-02	1.39E-01	7.2	6.4	1498	3.85E-04	1.26E-01
86	2.95	70	1.06E-02	1.45E-01	13.8	13.2	2971	3.89E-04	1.28E-01
87	2.95	70	1.05E-02	1.47E-01	18.2	17.8	3952	3.94E-04	1.30E-01
88	2.95	70	1.04E-02	1.48E-01	26.9	26.9	5916	1.22E-04	1.38E-01
89	4.84	40	8.65E-03	1.25E-01	6.3	5.1	848	1.78E-04	1.28E-01
90	4.84	40	8.15E-03	1.34E-01	12.6	11.7	1811	1.84E-04	1.35E-01
91	4.84	40	8.03E-03	1.36E-01	16.8	16.1	2453	1.86E-04	1.36E-01
92	4.84	40	7.92E-03	1.38E-01	25.2	24.9	3737	1.88E-04	1.38E-01
93	4.84	50	8.65E-03	1.25E-01	6.3	5.1	973	2.66E-04	1.28E-01
94	4.84	50	8.15E-03	1.34E-01	12.6	11.7	2078	2.76E-04	1.35E-01
95	4.84	50	8.03E-03	1.36E-01	16.8	16.1	2815	2.78E-04	1.36E-01
96	4.84	50	7.92E-03	1.38E-01	25.2	24.9	4289	2.81E-04	1.38E-01
97	4.84	60	8.65E-03	1.25E-01	6.3	5.1	1107	3.89E-04	1.28E-01
98	4.84	60	8.15E-03	1.34E-01	12.6	11.7	2365	4.03E-04	1.35E-01
99	4.84	60	8.03E-03	1.36E-01	16.8	16.1	3204	4.07E-04	1.37E-01
100	4.84	60	7.92E-03	1.38E-01	25.2	24.9	4881	4.11E-04	1.38E-01
101	4.84	70	8.65E-03	1.25E-01	6.3	5.1	1251	1.10E-04	1.16E-01
102	4.84	70	8.15E-03	1.34E-01	12.6	11.7	2672	1.15E-04	1.26E-01
103	4.84	70	8.03E-03	1.36E-01	16.8	16.1	3619	1.16E-04	1.28E-01
104	4.84	70	7.92E-03	1.38E-01	25.2	24.9	5514	1.17E-04	1.30E-01

For test 1 to 72 the crystal size distributions were not accurately measurable due to severe agglomeration during the drying process. The crystals produced were typically agglomerated in a big lump that could only be broken up through hard mechanical impact using a mortar and pestle. These size distributions are therefore excluded from the growth and nucleation kinetic data fitting. For mass balance purpose all the data was used as the crystal weight was not affected by the agglomeration.

The crystal handling, with reference to the drying practise, was changed by lowering the drying temperature from 80°C to 60°C and extending the time in the oven from approximately 8h to 24h. This change made the crystal lumps brittle and easy to break up, eliminating the use of extreme force to break crystal agglomerates formed during the drying process.

4.5. ANALYTICAL METHODS AND EXPECTED ERROR

4.5.1. Aqueous analysis by ICP-OES

Inductively coupled plasma optical emission spectroscopy, or ICP-OES, uses a nebulizer to spray a sample solution into a finely divided mist which is then burnt in a plasma torch. The plasma torch is argon gas superheated to the region of 10 000°C with a radio frequency generator.

When the nebulized sample solution enters the plasma torch, the solution is vaporized and all elements in the solution are ionized. The ionized gas then passes through an electromagnetic field that scatters the ionized elements through a light beam. A detector captures the intensity of the emitted light at various wavelengths. Each element will correspond to a unique set of wavelengths (Boss & Fredeen, 2004).

In practice, multi-component mixtures may contain some elements that emit light at similar wavelengths. This causes error in analysis as the intensity distribution of elements with similar wavelengths overlap or the base line shifts upward. The mentioned sources of error can cause certain elements to appear more concentrated than they actually are. Typically, an interfering 'neighbour' element to the element in question inflates the peak of the wavelength distribution causing the concentration to appear higher than they are (Gaines, 2010).

Table 4.5.1 shows the characteristic wavelengths of the elements expected in the solution and the levels measured for the bulk feed to all experiments. Impurity levels as measured by Hagemann et al. (2003) were typically below 20mg/L and the analysis shown in Table 4.5.1 confirms the low level of impurity. The measurement was performed in a Varian ICP-OES by the Anglo American PGM assay laboratory in Germiston, South-Africa. The element that is of interest in this work is rhodium. In all tests the electrolytes contained less than 20mg/L of all possible impurities listed in Table 4.5.1. Therefore, rhodium analysis error caused by neighbouring elements is most likely negligible in this work.

Table 4.5.1: ICP-OES elemental wavelength and feed assay per experiment defined in Table 4.2.1

Element	Wavelength, nm	Experiment 1, mg/L	Experiment 2, mg/L	Experiment 3, mg/L	Experiment 4, mg/L
As	188.98	0.41185	0.62016	0.59079	0.46938
Au	267.594	0.6249	0.66918	0.66703	0.64337
Co	340.511	0.35062	0.36137	0.37728	0.63116
Cu	327.395	10.793	10.8256	11.2893	11.3037
Fe	259.94	2.55394	2.67923	2.9149	2.34611
Ir	205.116	9.46888	8.83876	14.9995	15.7114
Ni	305.431	3.33525	3.83942	3.55693	1.5092
Pd	340.458	< 0.075	< 0.075	< 0.075	< 0.075
Pt	292.979	1.53115	1.17463	1.78707	1.80212
Rh	343.488	25793.2	26210.8	26591.2	27178.3
Rh	369.236	25627.3	25878.6	26714.4	26843.1
Ru	269.213	6.77808	6.31695	5.16288	6.17916
Sb	217.582	< 0.01	1.29627	0.92909	0.8205
Se	203.985	< 0.001	< 0.001	< 0.001	5.86924
Te	214.282	1.55259	1.21925	1.8885	1.60965

The ICP-OES instrument is calibrated through standard rhodium solutions made up between 1 to 100mg/L. Dilution is required to determine the concentration of rhodium in a sample that exceeds the calibrated concentration range. Three standard dilutions with 6M HCl are performed in a sample of unknown concentration by a factor 10, 100 and a 1000. Whichever dilution falls within the calibration range is used to estimate the rhodium concentration by multiplying the result with the dilution factor.

Rhodium concentration was estimated by the average between the 343.488nm and 369.236nm wavelengths. Note that the samples for Experiment 1 and 2 represents the same bulk sample, likewise for Experiment 3 and 4. An estimate of analysis error, that includes sample dilution, is therefore represented by the standard deviation of Experiment 1 and 2 and Experiment 3 and 4. In the case of rhodium there are 4 points given the two wavelengths. The standard deviation divided by the average for the rhodium concentrations of Experiment 1 and 2 gave 0.95 per cent. The standard deviation divided by the average for the rhodium concentrations of Experiment 3 and 4 gave 0.94 per cent. Worst case analytical error associated with aqueous concentration evaluation is therefore expected to be 0.94 per cent for rhodium.

4.5.2. Diethylenetriamine analysis by titration

The protonation of diethylenetriamine by addition of 6M hydrochloric acid is done by slowly adding diethylenetriamine to the acid. The reaction releases heat; it must therefore be done in a controlled manner.

The determination of protonated diethylenetriamine concentration is performed by titration with 1M sodium hydroxide solution. Sodium hydroxide is added to the protonated diethylenetriamine solution until an inflection point is observed in the redox potential curve, which represents neutralising of the free hydrochloric acid in solution. The second inflection point is associated with stripping off the first protonated site of the diethylenetriamine and the third inflection point represents total neutralisation of the two remaining protonated sites of the diethylenetriamine. This method can only be used to determine diethylenetriamine concentration in made-up feed solutions. No standard method is available to determine diethylenetriamine concentration in electrolytes containing platinum group metals and other heavy metals.

The diethylenetriamine feed samples were submitted to the Anglo American assay laboratory in Germiston, South-Africa, for concentration determination by the titration method discussed above.

4.5.3. Expected experimental error associated with crystal conversion data

Experimental error in this work is defined as the error contributions from the measurements required to define conversion of rhodium from the aqueous phase to the crystal phase. The conversion calculations stem from a mass balance for each configuration and is defined as the mass rate of rhodium in the crystal phase divided by the mass rate of rhodium in the feed stream.

By this definition the required measurements to calculate conversion are the following:

- Aqueous feed stream volumetric rate.
- Concentration of rhodium in the feed stream.
- Crystal mass rate in the product stream.
- Concentration of rhodium in the crystal.

The feed is added to the reactor by ISMATEC peristaltic pumps for the CSTR configuration and withdrawn from the reactor with a Watson Marlow 520D pump. A Watson Marlow 520D pump with a two-channel cassette is used to pump the reagents into the PFR configuration. The calibration charts for the volumetric input to each reactor configuration is in Figures 4.2.5 and 4.4.4, and in both cases the error associated with volumetric flow is less than 1 per cent. The error associated with concentration measurement was estimated at 0.96 per cent in Section 4.5.1.

All crystal masses were measured on a Sartorius micro-balance accurate to 0.0001g. The crystal mass of the various samples for the CSTR and PFR configurations ranged between 0.18g and 10g. The maximum error associated with the minimum mass, thus the standard deviation divided by the average measurement for mass, is estimated by dividing the accuracy of the micro-balance (0.0001g) by the minimum crystal mass (0.18g), giving ~0.056 per cent. Note that this definition excludes error induced through mass loss caused by crystals spilling due to fine dust or manual handling. Careful handling ensured that this error was kept to a minimum, albeit not quantified. Handling error is assumed to be close to the flow error, therefore 1 per cent.

Concentration of rhodium in the crystal was determined by mass loss after calcination under air atmosphere, and reduction under a nitrogen and hydrogen atmosphere. Thus, the error in the rhodium content in the crystal measurement is at worst the accuracy of the micro-balance (0.0001g) divided by the mass left after reduction. Brits (2014) reported rhodium content in a composite sample of all crystals of 24.4 per cent, thus the maximum error for the determination of rhodium content in crystal is ~0.23 per cent.

The measured conversion for each experiment in the PFR configuration is estimated by Equation (4.5.1). The crystal mass is chosen to estimate conversion instead of the aqueous outlet concentration, to avoid additional ICP-OES measurements on the filtrate.

$$X_{Am,PFR} = \frac{M_c x_c}{\Delta t_s F_A C_{A0}} \tag{4.5.1}$$

Where X_{Am} = Measured rhodium conversion from the aqueous phase to the crystal phase
M_c = Measured crystal mass [g]
x_c = Measured rhodium content in the crystal expressed as a mass fraction
Δt_s = Sample time [s]
F_A = Rhodium feed solution volumetric rate [L/s]
C_{A0} = Rhodium concentration in feed solution by ICP-OES [g/L]

A Taylor series expansion of Equation (4.5.1) is used to estimate the error of the measured conversion. The method of the error series expansion is given by Ku (1966) and reduces to the square root of the sum of each variable's squared error defined as the ratio between the standard deviation and the average or expected value. The error contributions from each variable in Equation (4.5.1) is as estimated from the discussion above and translates to an error estimation for conversion of ±1.76 per cent.

Table 4.5.2: Experimental error contributions in the PFR and CSTR configuration

Error source	**PFR**	**CSTR**
Feed flow	1.01%	1.01%
Product flow	-	1.01%
ICP-OES of feed	0.95%	0.95%
ICP-OES of product	-	0.95%
Metal content	0.23%	-
Salt mass	0.056%	-
Handling	1.00%	-
Sample time	0.37%	-
Total error	**1.76%**	**1.96%**

The error associated with conversion calculation for the CSTR configuration is higher than the PFR as the contributing factors are ICP-OES analysis of the feed and the discharge coupled with the volumetric input and output flows. The conversion calculation for the CSTR is shown in Equation (4.5.2).

$$X_{Am,CSTR} = 1 - \frac{F_A C_A}{F C_{A0}} \tag{4.5.2}$$

Where X_{Am} = Measured rhodium conversion from the aqueous phase to the crystal phase in a CSTR
C_A = Rhodium concentration by ICP-OES [g/L]
C_{A0} = Feed rhodium concentration by ICP-OES [g/L]
F = Product solution flow rate [L/s]
F_A = Rhodium feed solution volumetric rate [L/s]

The error estimate for the CSTR conversion calculation in Equation (4.5.2) is estimated at ±1.96 per cent. Note that the CSTR experiments were done before the PFR experiments. The use of crystal mass to define conversion in the PFR configuration is based on the marginal error difference between CSTR and PFR configurations. Table 4.5.2 numerically summarises the discussion.

4.5.4. Particle size characterisation

Crystal size distributions were measured by laser diffraction in a Malvern Mastersizer 2000. Initially test measurements were done to establish a standard size measurement procedure. Data required by the instrument are the refractive indices of the dispersant and the particle, sample agitation time and agitation speed (Malvern Instruments Ltd., 2007).

Deionised water was used as dispersant with a standard refractive index defined in the instrument software of 1.33. Hagemann et al. (2003) used a particle refractive index of 1.52; this parameter was fixed in all measurements. Lide (2007) reports that sodium chlorate has a refractive index of 1.515 at a wave length of 589.3nm, and is close to the refractive index used for the crystals produced in this work. Additionally, Lide (2007) states that the refractive index is a function of the crystal shape.

Interestingly, the growth of a single sodium chlorate crystal has shown that the crystal habit can change from cubic to a tetrahedral shape depending on the conditions of crystallisation (Surender & Rao, 1993). In Chapters 6 and 7, SEM photographs of diethylenetriammonium hexachlororhodate (III) crystals precipitated under various conditions show varying crystal shapes. The shapes in some instances ranged from square planar to octahedral shapes. The unit cell of the diethylenetriammonium hexachlororhodate (III) is not known and further studies are required to determine it. This highlights that the refractive index is possibly not a constant and depends on the shape of the crystal, therefore it is a source of error.

The Malvern Mastersizer 2000 user manual states that the choice of the refractive index can affect the accuracy of the measured crystal size distribution. When the instrument reports a residual above 1 per cent, this indicates that there is error associated with the refractive index of the particles (Malvern Instruments Ltd., 2007).

Given that a single refractive index was defined upfront, it is expected that the refractive index will cause error in the crystal size distribution measurement. All measured size distributions residuals are shown in Figure 4.5.1 a), with the distribution of the residuals in Figure 4.5.1 b). Bear in mind that each sample was analysed in triplicate and the average of the 3 analysed results was reported.

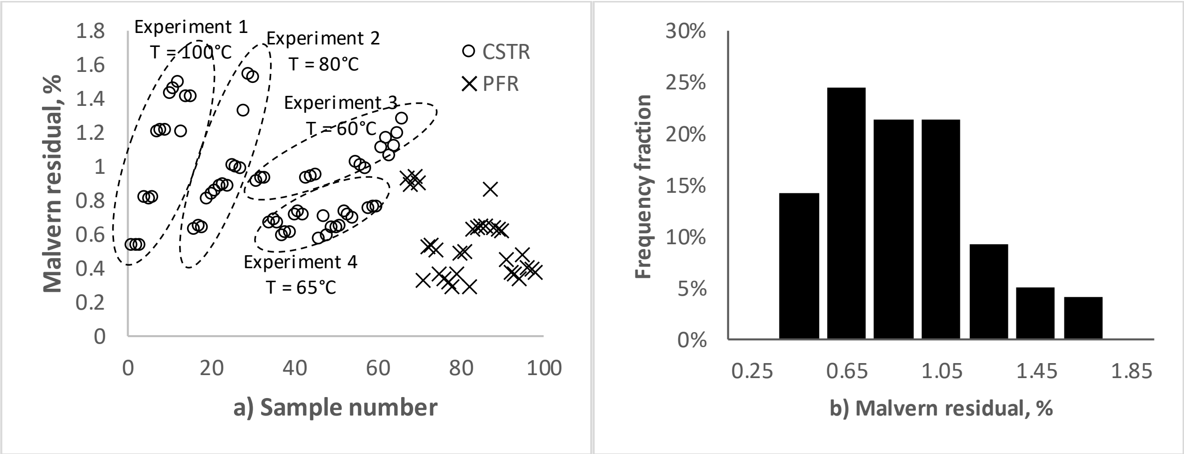

Figure 4.5.1: Malvern Mastersizer 2000 particle size measurement: a) residual per sample and b) residual histogram of all samples

Figure 4.5.1 a) shows that the highest residuals were obtained for the CSTR configuration and Figure 4.5.1 b) shows that approximately 18 per cent of all the sample residuals were above 1 per cent. None of the residuals exceeded 2 per cent. The sample number in Figure 4.5.1 a) follows the chronological order of the experiments. From the residuals it is concluded that the particle shapes produced in the CSTR, particularly as the crystals grow larger at higher temperatures, has the potential to cause an inaccurate crystal size distribution measurement.

To ascertain the accuracy of the Malvern measurement four tests were conducted by varying agitation speed, agitation time, and particle size range.

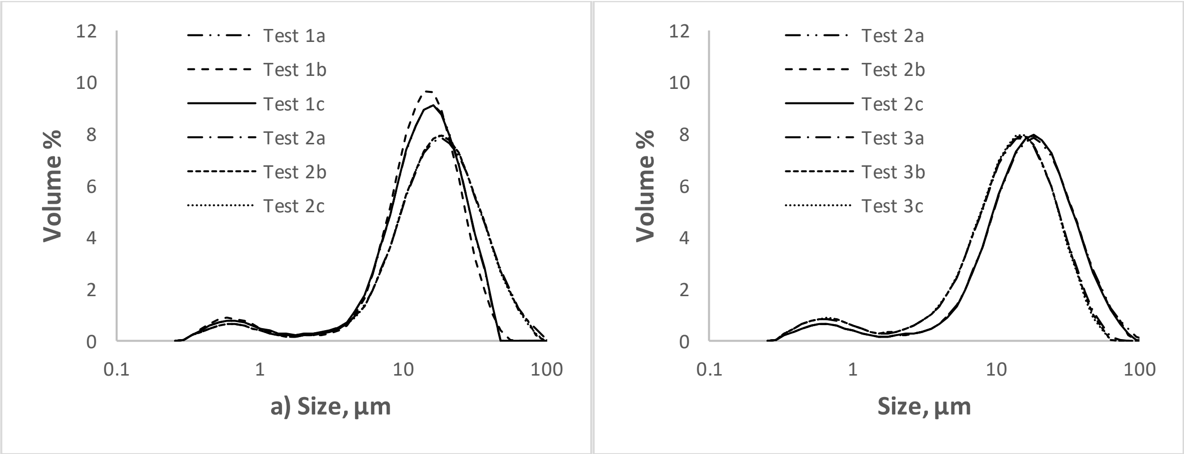

Figure 4.5.2: Malvern Mastersizer 2000 particle size distributions for a fine fraction sample a) agitated at 1500rpm for 1 minute (Test 2) and 3 minutes (Test 1) respectively; and b) agitated for 1 minute at 1500rpmn (Test 2) and 3500rpm (Test 3) respectively

A fine fraction of crystals was obtained under precipitation conditions specified for Experiment 4 in Table 4.2.1, Section 4.2, after 1 hour of precipitation. Approximately 50g of crystal was sampled from the reactor. The sample was filtered and dried as per the procedure given in Section 4.2. A coarse fraction was obtained as per the method used for the wash out test in Section 4.3.2. Each sample was added to the Malvern instrument sample mixer up to a concentration where the laser was obscured by ~15 per cent as prescribed in the user manual (Malvern Instruments Ltd., 2007).

Figure 4.5.2 a) shows the crystal size distributions obtained for agitation speed at 1500rpm and varying agitation times of 1 minute and 3 minutes in the Malvern Hydro 2000S sample mixer respectively. Figure 4.5.2 b) shows the effect of changing agitation speed from 1500rpm to 3500rpm at an agitation time of 1 minute. A mixed lognormal distribution, Equation (10.4.1) as given in Section 10.4 of the Appendix, describes the data in Figure 4.5.2 very well. The distribution parameters, coefficient of determination and the L_{43} size are reported in Table 4.5.3.

Table 4.5.3: Distribution statistics and parameters for data in Figure 4.5.2

Experimental condition	m_1	m_2	s_1	s_2	x_1	L_{43}, µm	σ, µm	R^2
Test 1a: 1500rpm - 3min	-0.14	2.65	0.76	0.54	0.082	15.0	9.0	0.99959
Test 1b: 1500rpm - 3min	-0.36	2.61	0.54	0.52	0.076	14.4	8.2	0.99987
Test 1c: 1500rpm - 3min	-0.15	2.64	0.74	0.54	0.082	15.0	9.0	0.99960
Test 2a: 1500rpm - 1min	-0.32	2.84	0.57	0.65	0.059	20.0	15.0	0.99996
Test 2b: 1500rpm - 1min	-0.29	2.84	0.62	0.64	0.061	19.7	14.5	0.99992
Test 2c: 1500rpm - 1min	-0.28	2.83	0.62	0.64	0.061	19.7	14.4	0.99993
Test 3a: 3500rpm - 1min	-0.12	2.61	0.75	0.62	0.095	15.0	10.7	0.99979
Test 3b: 3500rpm - 1min	-0.08	2.60	0.79	0.61	0.098	14.8	10.4	0.99974
Test 3c: 3500rpm - 1min	-0.06	2.60	0.81	0.60	0.10	14.6	10.2	0.99973

The total standard deviation for the mixed lognormal distribution is calculated by Equation (4.5.3) and is a combination of the location and spread parameters (Weisstein, 2016).

$$\sigma = \sqrt{x_1 exp(2m_1 + s_1^2)(exp(s_1^2) - 1) + (1 - x_1)exp(2m_2 + s_2^2)(exp(s_2^2) - 1)} \qquad \textbf{(4.5.3)}$$

Statistically by the t-test the L_{43} size of Test 2 is larger than for Test 1 and Test 3. No discernible statistical difference was detected between Test 1 and Test 3. The difference in standard deviation σ of all tests was found to be statistically significant by the t-test. Practically, the difference between the standard deviations of Tests 1 and 3 seems marginal compared to Test 2. This implies that the test conditions in Test 1 and Test 3 had a marginal impact on distribution spread.

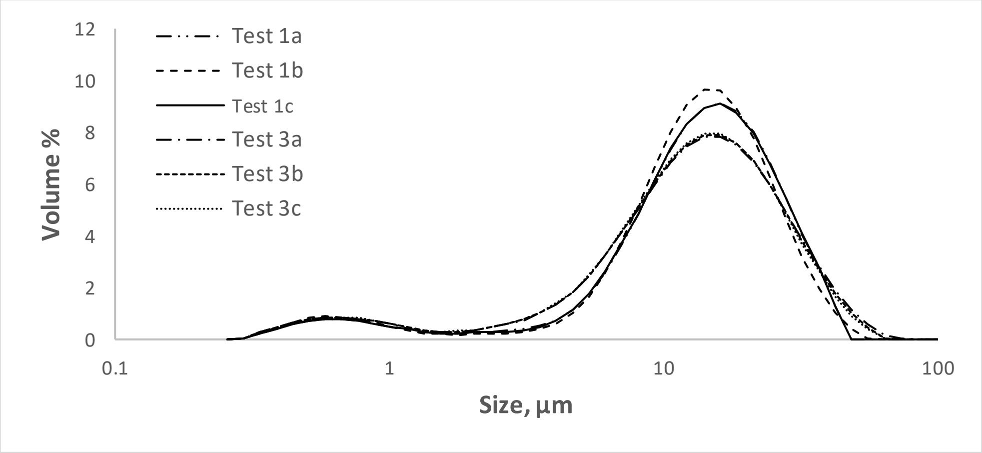

Figure 4.5.3: Malvern Mastersizer 2000 particle size distributions for a fine fraction sample agitated at 1500rpm for 3 minutes (Test 1) and 3500rpm for 1 minute (Test 3)

Visually the distribution spread between Test 2 and 3 seems comparable in Figure 4.5.2 b). However, the difference in the secondary fines distribution, represented by m_1 and s_1, causes the observed calculated difference in Table 4.5.3. In Figure 4.5.3 the secondary fines distributions between Test 1 and 3 are visually comparable. Furthermore, the L_{43} size in Table 4.5.3 indicates that the location of Test 1 and 3 distributions are equal, therefore the standard deviation shows minimal difference. Repeats between tests labelled a, b, and c highlight that the precision associated with L_{43} size was 2.4, 1.0 and 1.3 per cent for Test 1, 2 and 3 respectively. The coarse fraction test results are summarised in Figure 4.5.4 and Table 4.5.4.

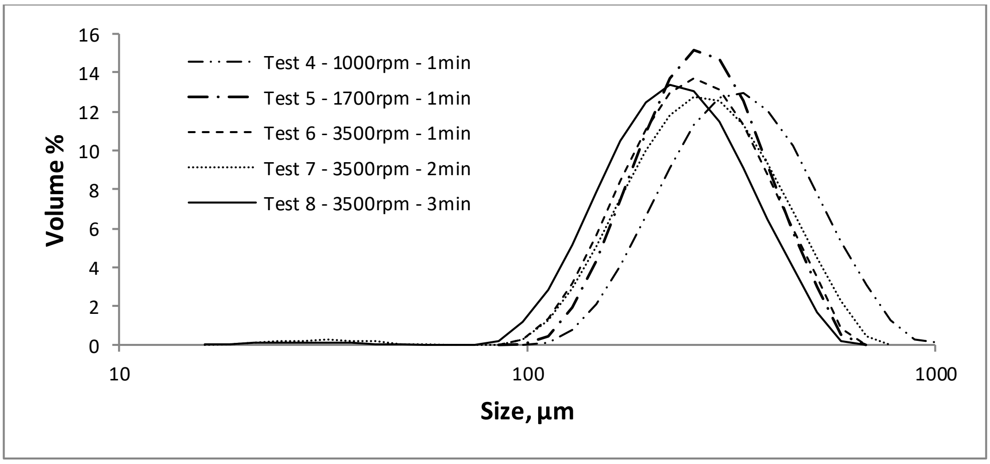

Figure 4.5.4: Malvern Mastersizer 2000 particle size distributions for a coarse fraction sample agitated under various conditions

The distributions in Figure 4.5.4 indicate that Test 5, 6 and 7 are visually comparable. Assuming a precision of 1.55 per cent for L_{43} size (average for the data in Table 4.5.3) no detectable difference between Test 5, 6, 7 and 8 is observed as the 95 per cent confidence intervals overlap.

To summarise, the Malvern tests show that a higher agitation speed at constant agitation time can break up loosely bonded aggregates to an extent that the distribution is shifted from a larger size to a smaller size (Test 2 compared to Test 3). The tests further indicate that increased agitation time at a constant agitation speed can have the same size distribution shift effect (Test 1 compared to Test 2); however, this was not observed for the coarse fraction in Tests 6 to 8. Tests 1 to 3 showed that repeatability is good between sampling, as the average precision between the 3 repeats per test was 1.55 per cent.

Table 4.5.4: Distribution statistics and parameters for data in Figure 4.5.4

Experimental condition	m_1	m_2	s_1	s_2	x_1	L_{43}, µm	σ, µm	R^2
Test 4: 1000rpm - 1min	5.47	5.97	0.30	0.31	0.496	330	107	0.99982
Test 5: 1700rpm - 1min	5.38	5.81	0.29	0.23	0.703	261	72	0.99997
Test 6: 3500rpm - 1min	5.34	5.82	0.32	0.24	0.702	257	76	0.99995
Test 7: 3500rpm - 2min	3.31	5.52	0.19	0.41	0.009	270	115	0.99999
Test 8: 3500rpm - 3min	5.42	5.90	0.36	0.23	0.829	264	89	0.99993

The coarse sample tests showed no detectable effect on L_{43} size when agitation speed was increased from 1700rpm to 3500rpm. It is therefore concluded that agitation at 3500rpm for 1 minute is sufficient to break up loosely bonded aggregates that are not cemented by supersaturation. The error associated with the L_{43} size is estimated using the peak value for Test 1 of 2.4 per cent. The error associated with refractive index was not quantified and further study is required to understand the impact thereof in systems where particle shape changes over time. Thus, particle size measurement accuracy is reasonable in this work, but bias may exist for crystal size distributions of particles with complex shapes.

5. PHYSICAL PROPERTY MEASUREMENT – SOLUBILITY PRODUCT AND VISCOSITY

By definition, saturation in a precipitation system refers to a state that is referenced to an equilibrium state, as discussed in Chapter 2. Since the solubility product represents the equilibrium reference point, it is an important physical property that must be defined initially. Likewise, turbulence in a system can be characterised by the Reynolds number. Since the kinematic viscosity is used in the Reynolds number calculation, it is an important physical property that must be measured.

Therefore, this chapter deals with the measurement of diethylenetriammonium hexachlororhodate (III) salt solubility product and the associated liquid phase kinematic viscosity. The measured properties are used in the derived models presented in Chapter 3 to determine nucleation and growth kinetics in Chapters 6 and 7.

5.1. SOLUBILITY PRODUCT OF DIETHYLENETRIAMMONIUM HEXACHLORORHODATE (III)

The experimental configuration for the solubility experiments in this work is shown in Figure 5.1.1. Experimental time was minimised by utilising three identical configurations to do experiments in parallel. The equilibration time for each experiment was 48 hours at a desired temperature set point. For this method of solubility, the literature suggests 4 – 6 hours of equilibration time (Myerson, 2002). However, based on previous observed dissolution rates, a period of 48h was selected to ensure equilibrium is achieved for this system. Approximately 2.7g of diethylenetriammonium hexachlororhodate (III) salt, the solute, was added to 300 – 350mL of 6M hydrochloric acid, the solvent, and heated to temperature whilst stirring with a magnetic stirrer. The masses of both solute and solvent were measured on a laboratory Sartorius semi-micro balance accurate to 0.0001g.

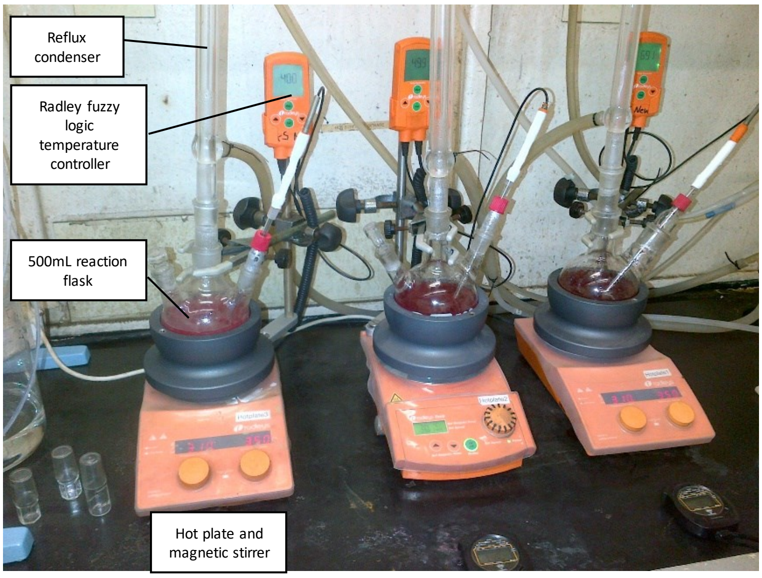

Figure 5.1.1: Solubility measurement experimental setup

The volume of the solvent was estimated using the density of the solvent. The solute is highly insoluble and negligible changes in physical properties of the solvent are expected after the dissolution process. The volume of the solution after equilibration is therefore estimated by using the density of the solvent and the mass of the solvent, as an insignificant volume contribution is expected from the dissolved solute. After filtering the equilibrated mixture, the remaining solute is removed by filtration and then dried at 60°C overnight. The mass loss is determined by weighing the dried salt and subtracting it from the initial mass. The concentration is determined by dividing the solvent volume into the dissolved salt mass. The method is consistent with the method described in Myerson (2002). Solubility measurements have been performed by other researchers but the data was limited. This work therefore expands and unifies previous measurements with the current measurements.

In contrast to the method stated above, researchers at Johnson-Matthey Technology Centre (JMTC) equilibrated protonated diethylenetriamine with hexachlororhodate (III) solution at an acidity of ~6M and various temperatures and stoichiometries over 72 hours (Burnham et al., 1993). The hexachlororhodate (III) solution was initially prepared by dissolving sodium hexachlororhodate (III) salt (Na_3RhCl_6) in 6M hydrochloric acid. The solution was then heated to reflux temperature (~105 °C) whilst adding hydrogen peroxide to oxidise the solution.

The experimental conditions do not specify the extent of oxidation but under reflux conditions with excess hydrogen peroxide added, the redox of a hexachlororhodate (III) solution would typically stabilise out at between 400mV to 600mV. Portions of the prepared solution were then used in the various tests at specified temperatures and initial reagent stoichiometries. The equilibrated concentration of rhodium in the aqueous was measured by Inductive Coupled Plasma Optical Emission Spectroscopy (ICP-OES) (Burnham et al., 1993).

In Figure 5.1.2 a) the concentration product of the data from the experiments by Burnham et al. (1993) is expressed as a function of the inverse of temperature. The plot suggests that an Arrhenius relationship with a constant activation energy (the slope) can potentially describe the data. Furthermore, the frequency constant, represented by the intercept, is potentially a function of other variables such as the reagent concentrations through ionic strength.

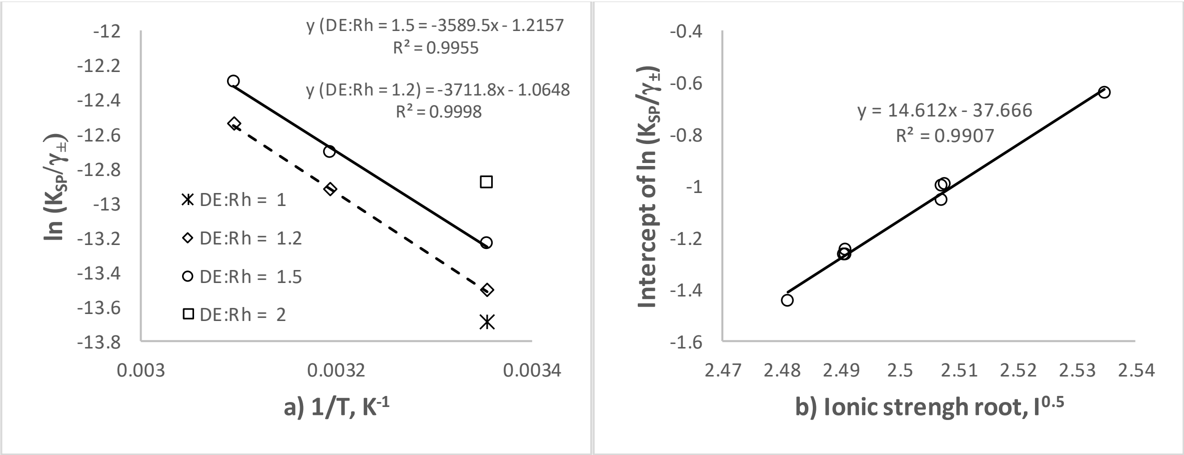

Figure 5.1.2: a) Concentration product versus temperature and b) the intercept of the concentration product versus temperature plot as a function of ionic strength

Figure 5.1.2 b) shows the intercept of the data in Figure 5.1.2 a) as a function of ionic strength. The intercept is calculated for each data point based on a slope of -3651K that is the average of the stated slopes in Figure 5.1.2 a). This observation supports the notion that the activity coefficient is not constant. Table 5.1.1 shows the raw data used to construct the graphs in Figure 5.1.2. The equilibrium concentration of protonated diethylenetriamine was not measured but calculated from a mass balance from the known reaction stoichiometry, as determined by Burnham et al. (1993), Equation (5.1.1).

Table 5.1.1: Diethylenetriammonium hexachlororhodate solubility data from Burnham et al. (1993)

Temperature	$\alpha = DE{:}Rh$	$[Rh]_0$	$[DE]_0$	$[Rh]_{eq}$	$*[DE]_{eq}$
°C	***mol/mol***	***M***	***M***	***M***	***M***
25	1	0.05053	1.411	0.001065	0.001065
25	1.2	0.05053	1.411	0.000138	0.009828
40	1.2	0.04988	1.411	0.000248	0.009818
50	1.2	0.04988	1.411	0.000359	0.009929
25	1.5	0.05053	1.411	0.000074	0.02405
40	1.5	0.04988	1.411	0.000126	0.02381
50	1.5	0.04988	1.411	0.000190	0.02388
25	2	0.05053	1.411	0.000053	0.04721

*Calculated by mass balance, Equation (5.1.1). Rh => hexachlororhodate (III) anion, DE => protonated diethylenetriamine cation

$$[DE]_{eq} = \frac{[Rh]_0(\alpha - 1)}{1 + \alpha \frac{[Rh]_0}{[DE]_0}} + [Rh]_{eq} \qquad \textbf{(5.1.1)}$$

Where $[Rh]_0$ = Concentration of rhodium in solution prior to mixing with protonated diethylenetriamine [M]
$[DE]_0$ = Concentration of protonated diethylenetriamine ($C_4N_3H_{16}Cl_3$) in a separate solution prior to mixing the two reagents [M]
α = Initial ratio of protonated diethylenetriamine to rhodium in solution [mol/mol]
$[Rh]_{eq}$ = Concentration of rhodium in solution after the mixture has equilibrated at the set temperature for a period of 72 hours [M]
$[DE]_{eq}$ = Concentration of protonated diethylenetriamine in solution after the mixture has equilibrated at the set temperature for a period of 72 hours [M]

As a start the correlation slopes in Figure 5.1.2 a) are averaged and this value is used to estimate intercepts for all other measurements. The average slope was found to be -3651K as stated earlier. Table 5.1.2 shows the calculated values of the intercepts for all experiments using a constant slope assumption for the natural logarithm of the concentration product $K_{SP}/\gamma_\pm$ versus the inverse of temperature.

Table 5.1.2: Concentration product VS Arrhenius plot intercept values in Figure 5.1.2

Temperature **°C**	$\alpha = DE{:}Rh$ ***mol/mol***	$K_{SP}/\gamma_\pm$ ***M²***	$\ln K_{SP}/\gamma_\pm$	***Ionic Strength, I***	****Intercept ln(M²)***
25	1	1.13E-06	-13.69	6.156	-1.445
25	1.2	1.36E-06	-13.51	6.205	-1.267
40	1.2	2.43E-06	-12.93	6.203	-1.269
50	1.2	3.56E-06	-12.55	6.204	-1.249
25	1.5	1.78E-06	-13.24	6.288	-0.997
40	1.5	3.01E-06	-12.71	6.285	-1.057
50	1.5	4.55E-06	-12.30	6.286	-1.004
25	2	2.52E-06	-12.89	6.425	-0.646

*Intercept = ln $K_{SP}/\gamma_\pm$ – Slope/T (where temperature T is in kelvin units)

The concentration product in Table 5.1.2 depicted by the ratio of the solubility product by the mean dissolved salt activity coefficient can also be viewed as the reaction quotient as defined in Atkins (1997). Strictly speaking, the reaction quotient is a dimensionless number; however, the concentration units are used throughout in this work (see Equation (5.1.2) for the mathematical description).

$$\frac{K_{SP}}{\gamma_\pm} = [Rh]_{eq}[DE]_{eq} \qquad \textbf{(5.1.2)}$$

Where K_{SP} = Solubility product [M²]
$\gamma_\pm$ = Mean dissolve salt activity coefficient

To define the ionic strength of each system the ions present in the electrolyte at equilibrium are first listed through the known reaction stoichiometries. The precipitation reaction stoichiometry of diethylenetriammonium hexachlororhodate, as determined by researchers at JMTC, is given in Equation (5.1.3) (Burnham et al., 1993).

$$[RhCl_6]^{3-}_{aq} + [H_3NC_2H_4NH_2C_2H_4NH_3]^{3+}_{aq} \rightarrow [H_3NC_2H_4NH_2C_2H_4NH_3][RhCl_6]_S \qquad \textbf{(5.1.3)}$$

The protonation of diethylenetriamine in hydrochloric acid is given by Equation (5.1.4) (Burnham et al., 1993).

$$H_2NC_2H_4NHC_2H_4NH_{2,l} + 3HCl_{aq} \rightarrow [H_3NC_2H_4NH_2C_2H_4NH_3]^{3+}_{aq} + 3Cl^-_{aq} \qquad \textbf{(5.1.4)}$$

The dissolution of sodium hexachlororhodate (III) salt in hydrochloric acid is given by Equation (5.1.5) from Burnham et al. (1993).

$$Na_3RhCl_6 \rightarrow 3Na^{+}_{aq} + [RhCl_6]^{3-}_{aq} \tag{5.1.5}$$

For calculation, reactions in Equations (5.1.4) and (5.1.5) are assumed to proceed to completion in 6M hydrochloric acid. In practise, the reactions would proceed to some equilibrium; however, it is assumed that the extent is sufficiently large such that minimal ionic strength calculation error is made, particularly considering the strong hydrochloric acid background. The ionic strength as defined in Atkins (1997) is given in Equation (5.1.6).

$$I = \frac{1}{2}\sum_{i=1}^{n} z_i^2 \frac{C_i}{C_i^{ref}} \tag{5.1.6}$$

Where I = Electrolyte ionic strength
z_i = Charge of the ith ion
C_i = Concentration of the ith ion [M]
C_i^{ref} = Reference concentration of the ith ion = 1 [M]

Table 5.1.3: Various ions contributing to ionic strength reported in Table 5.1.2 through Equation (5.1.6)

Temperature °C	$\alpha = DE{:}Rh$ *mol/mol*	$[RhCl_6]^{3-}_{aq}$ *M (z = -3)*	$[C_4H_{16}N_3]^{3+}_{aq}$ *M (z = 3)*	*$[Na]^{+}_{aq}$ *M (z = 1)*	*$[Cl]^{-}_{aq}$ *M (z = -1)*	*$[H]^{+}_{aq}$ *M (z = 1)*
25	1	0.00107	0.00107	0.146	6.146	6
25	1.2	0.00014	0.00983	0.145	6.174	6
40	1.2	0.00025	0.00982	0.144	6.172	6
50	1.2	0.00036	0.00993	0.144	6.172	6
25	1.5	0.00007	0.02405	0.144	6.216	6
40	1.5	0.00013	0.02381	0.142	6.213	6
50	1.5	0.00019	0.02388	0.142	6.213	6
25	2	0.00005	0.04721	0.141	6.283	6

*Calculated values based on stoichiometry from reactions in Equations (5.1.4) and (5.1.5) combined with total dissociation of hydrochloric acid to proton and chloride.

Table 5.1.3 gives the ionic concentrations that were used to estimate the ionic strength reported in Table 5.1.2 of the various experimental electrolytes referred to in Table 5.1.1. The empirical relationship that best fits the data in Figure 5.1.2 b) is a straight line. Equation (5.1.7) is obtained when the linear relationship found in Figure 5.1.2 b) is substituted for the intercept of the Arrhenius expression used for the concentration product in Figure 5.1.2 a).

$$\ln\frac{K_{SP}}{\gamma_{\pm}} = \frac{B_{SP}}{T} + \ln A_Q = \frac{B_{SP}}{T} + \ln A_0 + A_1\sqrt{I} \tag{5.1.7}$$

Where B_{SP} = Solubility product activation energy divided by the gas constant [K]
$\ln A_Q$ = Intercept of the concentration product versus temperature plot in Figure 5.1.2 a)
T = Temperature [K]
$\ln A_0$ = Figure 2.1.2 b) intercept
A_1 = Figure 2.1.2 b) slope

The relationship in Equation (5.1.7) is in a form that is amenable to multiple linear regression. The temperature and ionic strength data in Table 5.1.2 was transformed to the forms presented in Equation (5.1.7) and regressed against the concentration product. The regression coefficient of determination, *R^2*, was 0.998, and the overall standard error was 0.025 for the 8 observations, indicating that Equation (5.1.7) fits the data well.

Statistical analysis of the regression is presented in Tables 5.1.4 and 5.1.5. The regression source of error statistically separates from the residual error in Table 5.1.4 by the F-test as the p-value << 0.05. This indicates that Equation (5.1.7) explains virtually all the variance in the measured concentration product data, as *SS (regression)* is practically equal to *SS (total)*.

All parameters in Table 5.1.5 are statistically significant as the respective p-values << 0.05. The upper and lower confidence limits do not overlap zero, which further supports the result. Equation (5.1.7) therefore illustrates that the concentration product, represented by a ratio of the solubility product and the mean salt activity coefficient, has a temperature and ionic strength dependency that is statistically significant.

Table 5.1.4: Equation (5.1.7) regression analysis of variance (ANOVA), raw data from Table 5.1.2

ANOVA parameter	*df*	*SS*	*MS*	*F*	*p-value*
SS (Regression)	2	1.58	0.79	1261	1.74E-07
SS (Residual)	5	0.0031	0.00063		
SS (Total)	7	1.58			

df = degrees of freedom, SS = squared sum of errors, MS = SS/df, F = MS (Regression)/MS (Residual), p-value = F-distribution evaluated at the calculated F value => probability that MS (regression) is equal to MS (residual). For details on multiple linear regression the reader is referred to Vining (1998).

Literature on activity coefficient models suggest that the activity coefficient is most likely a function of ionic strength, whereas the solubility product is more likely to be temperature dependent. In fact, this is a common feature of activity coefficient models derived from Debye-Hückel theory and Pitzer's expansion of free energy (Wright, 2007) and (Pitzer, 1993). The model here is therefore consistent with literature.

Table 5.1.5: Equation (5.1.7) regression parameters, raw data from Table 5.1.2

Parameter	*Value*	*SE*	*t Stat*	*p-value*	*L CL 95%*	*U CL 95%*
$\ln A_0$	-37.60	1.41	-26.6	1.4E-06	-41.23	-33.96
B_{SP}	-3741	80.8	-46.3	8.9E-08	-3949	-3533
A_1	14.70	0.57	25.8	1.6E-06	13.24	16.17

SE = standard error, t-stat = Student's t-distribution estimate from the parameter value and SE, p-value = t-distribution evaluated at the calculated t-stat value, L/U CL = lower/upper confidence limit at a significance level of 0.025. For details on multiple linear regression the reader is referred to Vining (1998).

It is difficult to separate the constant term $\ln A_0$ in Equation (5.1.7) into a part that contributes to the solubility product $\ln A_{0,SP}$ and a part that contributes to the activity coefficient $\ln A_{0,AC}$ as there is insufficient information. The only basis is to reference the activity coefficient to 1 at the solvent ionic strength, i.e. when no other ions except dissociated hydrochloric acid is in solution. In other words, at an ionic strength of 6 (6M HCl) the activity coefficient is 1. Using this as a reference splits up $\ln A_0$ such that -36.01 contributes to activity coefficient intercept, $\ln A_{0,AC}$, and -1.58 contributes to solubility product intercept, $\ln A_{0,SP}$. The separated equations for solubility product and activity coefficient by this method is given by Equations (5.1.8) and (5.1.9).

$$\ln K_{SP} = \frac{B_{SP}}{T} + \ln A_{0,SP} \tag{5.1.8}$$

$$\ln \gamma_{\pm} = -A_1\sqrt{I} - \ln A_{0,AC} \tag{5.1.9}$$

To recover $\ln A_0$ as given in Equation (5.1.7) one must subtract Equation (5.1.9) from Equation (5.1.8). The difference must be equated to Equation (5.1.7) to cancel equivalent terms that eventually gives Equation (5.1.10).

$$\ln A_0 = \ln A_{0,AC} + \ln A_{0,SP} = \ln\left(A_{0,AC} A_{0,SP}\right) \tag{5.1.10}$$

The solubility product as a function of temperature and the activity coefficient as a function of ionic strength for diethylenetriammonium hexachlororhodate (III) salt under oxidising conditions is shown in Figure 5.1.3. As stated earlier the solubility measurements in this work were done by dissolving diethylenetriammonium hexachlororhodate (III) salt into 6M hydrochloric acid at various temperatures over an equilibration period of 48 hours. This method is different to the method used by JMTC in two ways, namely the electrolyte does not contain sodium, nor is it oxidised. Therefore, it is expected that the electrolytes differ in terms of ionic strength and redox potential, giving rise to differences in solubility.

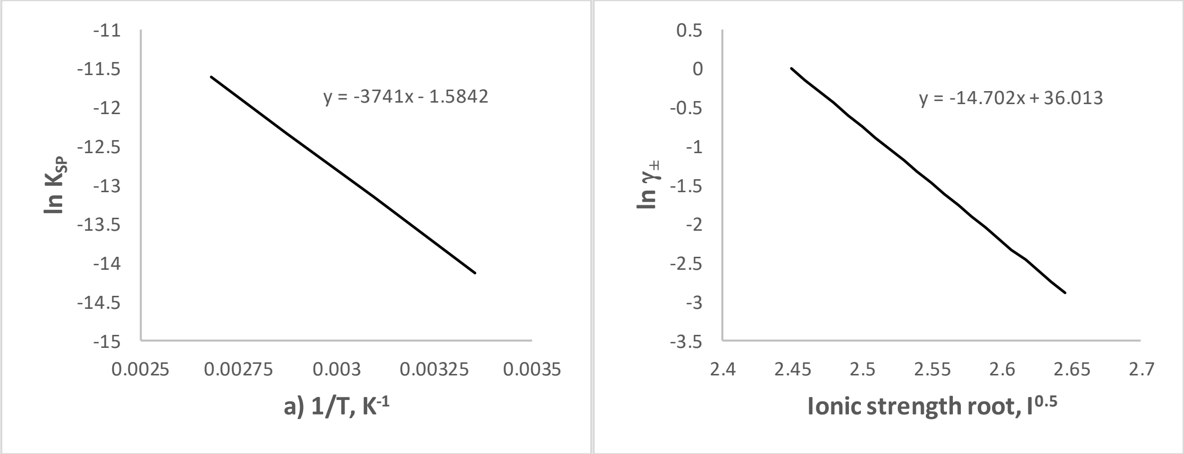

Figure 5.1.3: a) Solubility product versus inverse of temperature under oxidising conditions and b) activity coefficient versus the root of the ionic strength

Prior to the measurements, the salt stoichiometry was determined by way of metal content analysis (calcination and reduction of the salt to pure metal). The measured rhodium metal content of the salt used in solubility measurement tests was 24.40 per cent, which compares well to the metal content by molecular weight of 24.396 per cent (Brits, 2014). In these equilibrium tests the equilibration time was 48 hours, double that of a previous study that suggested equilibration within 24 hours (Hagemann et al., 2003). The results are presented in Figure 5.1.4 and the data in Table 5.1.6.

In Figure 5.1.4 a) the extrapolated line to 100°C from the concentration product measurements made in this work approximately intersects a data point from a previous study. The study by Hagemann et al. (2003) used 5.5M hydrochloric acid to dissolve the salt, whereas this study used 6M. The data is given in Table 5.1.6.

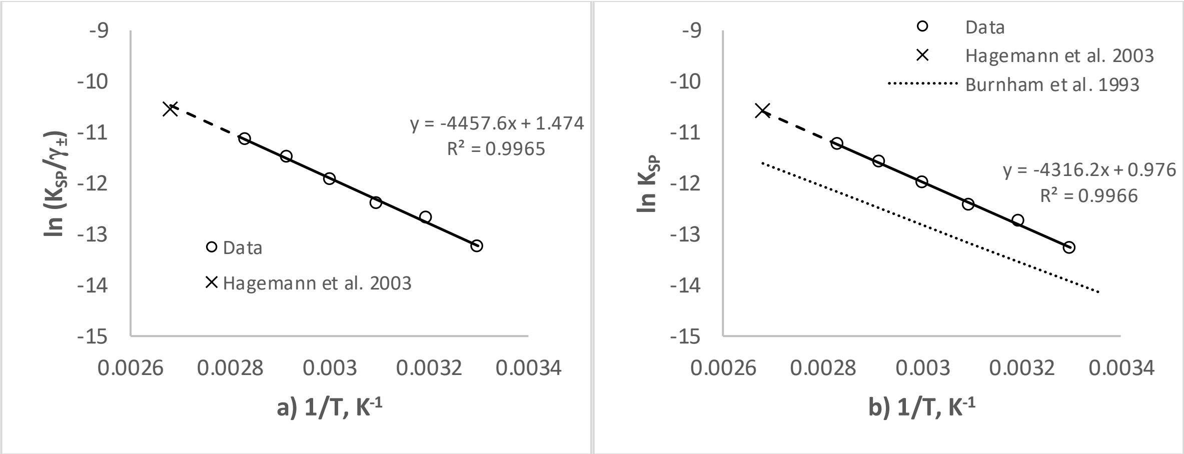

Figure 5.1.4: a) Arrhenius plot of concentration product measured by salt dissolution in 6M hydrochloric acid (data from Hagemann et al, (2003) was at 5.5M HCl; b) Solubility product assuming the activity coefficient model in Equation 4.1.9 is valid

Figure 5.1.4 b) is generated by assuming that the activity coefficient model in Figure 5.1.3 b) is valid for the measurements. If the solubility product for the extrapolated data point in Figure 5.1.4 b) is used with the corresponding concentration product data point in Figure 5.1.4 a), the calculated activity coefficient for the Hagemann et al. (2003) data is ~0.944. Equation (5.1.9) with A_1 = 14.702, $\ln A_{0,AC}$= - 36.013 and the ionic strength for the Hagemann et al, (2003) data in Table 5.1.6 gives an activity coefficient of 4.006. This discrepancy may indicate that the reference electrolyte, or starting ionic strength, has an influence on the mean salt activity coefficient relationship. This observation was not further investigated as all experiments later in this work were done at an acidity of 6M hydrochloric acid.

A difference in solubility product relationships between the data from Burnham et al. (1993) under oxidising conditions and the measurements presented here is apparent in Figure 5.1.4 b). The decrease in solubility over the 25°C to 100°C temperature range in an oxidising environment suggests that the addition of an oxidant such as hydrogen peroxide reduces salt solubility.

Table 5.1.6: Diethylenetriammonium hexachlororhodate (III) salt solubility in hydrochloric acid

Temperature °C	$[RhCl_6]^{3-}_{aq}$ *M* *(z = -3)*	$[C_4H_{16}N_3]^{3+}_{aq}$ *M* *(z = 3)*	$[Cl]^{-}_{aq}$ *M* *(z = -1)*	$[H]^{+}_{aq}$ *M* *(z = 1)*	*Ionic strength* *I*	$\frac{K_{SP}}{\gamma_{\pm}}$ *M²*
30	0.001331	0.001331	6	6	6.012	1.771E-06
40	0.001757	0.001757	6	6	6.016	3.088E-06
50	0.002043	0.002043	6	6	6.018	4.174E-06
60	0.002570	0.002570	6	6	6.023	6.602E-06
70	0.003182	0.003182	6	6	6.029	1.013E-05
80	0.003821	0.003821	6	6	6.034	1.460E-05
100*	0.005161	0.005161	5.5*	5.5*	5.546	2.664E-05

*Data from Hagemann et al. (2003)

Considering the observations above, the reference electrolyte in all subsequent growth tests is 6M hydrochloric acid without redox manipulation through hydrogen peroxide addition. It is therefore assumed that the activity coefficient model derived here combined with the solubility product in Figure 5.1.4 b) remains valid for calculating saturation.

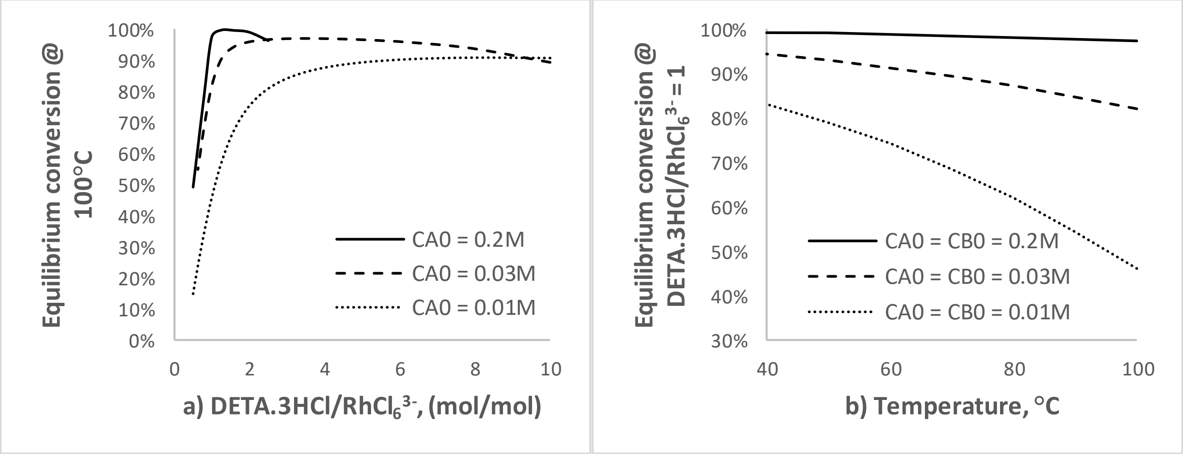

Figure 5.1.5: a) Equilibrium conversion at 100°C and varying initial hexachlororhodate (III) concentration, C_{A0}, and varying mol ratio of protonated diethylenetriamine to hexachlororhodate (III); b) Equilibrium conversion as a function of temperature and initial hexachlororhodate (III) concentration at a mol ratio = 1

The maximum conversion of rhodium from solution to salt form is limited by the equilibrium of hexachlororhodate (III) and diethylenetriammonium hexachlororhodate salt as measured above. Figure 5.1.5 a) illustrates the conversion as a function of mol ratio variation and initial feed concentration of hexachlororhodate (III) at fixed temperature. Figure 5.1.5 b) shows the effect of varying temperature and initial concentration at a fixed mol ratio.

Figure 5.1.5 a) highlights that adding protonated diethylenetriamine in excess beyond the point where the conversion curve peaks will decrease conversion. This counterintuitive result is due to the activity coefficient dependency on ionic strength that decreases when ionic strength is increased. The decrease in activity coefficient then increases the concentration product at equilibrium. Figure 5.1.5 b) shows that the salt becomes more soluble at higher temperature and that conversion is increased by increasing initial concentration at a reagent mol ratio of 1.

Figure 5.1.6 a) shows a contour plot of the equilibrium concentration of hexachlororhodate (III) at various initial mol ratios and temperatures. The plot shows that equilibrium concentration increases as temperature is increased at a mol ratio > 1, i.e. the diethylenetriammonium hexachlororhodate salt becomes more soluble. The contour plot illustrates interaction between temperature and mol ratio when the mol ratio is > 1, as indicated by the curvature in the contour. Figure 5.1.6 a) further illustrates that when protonated diethylenetriamine is not in excess (mol ratio is < 1) the salt solubility is virtually independent of temperature. This is purely due to the sparingly soluble nature of the salt, as demonstrated by the small solubility product.

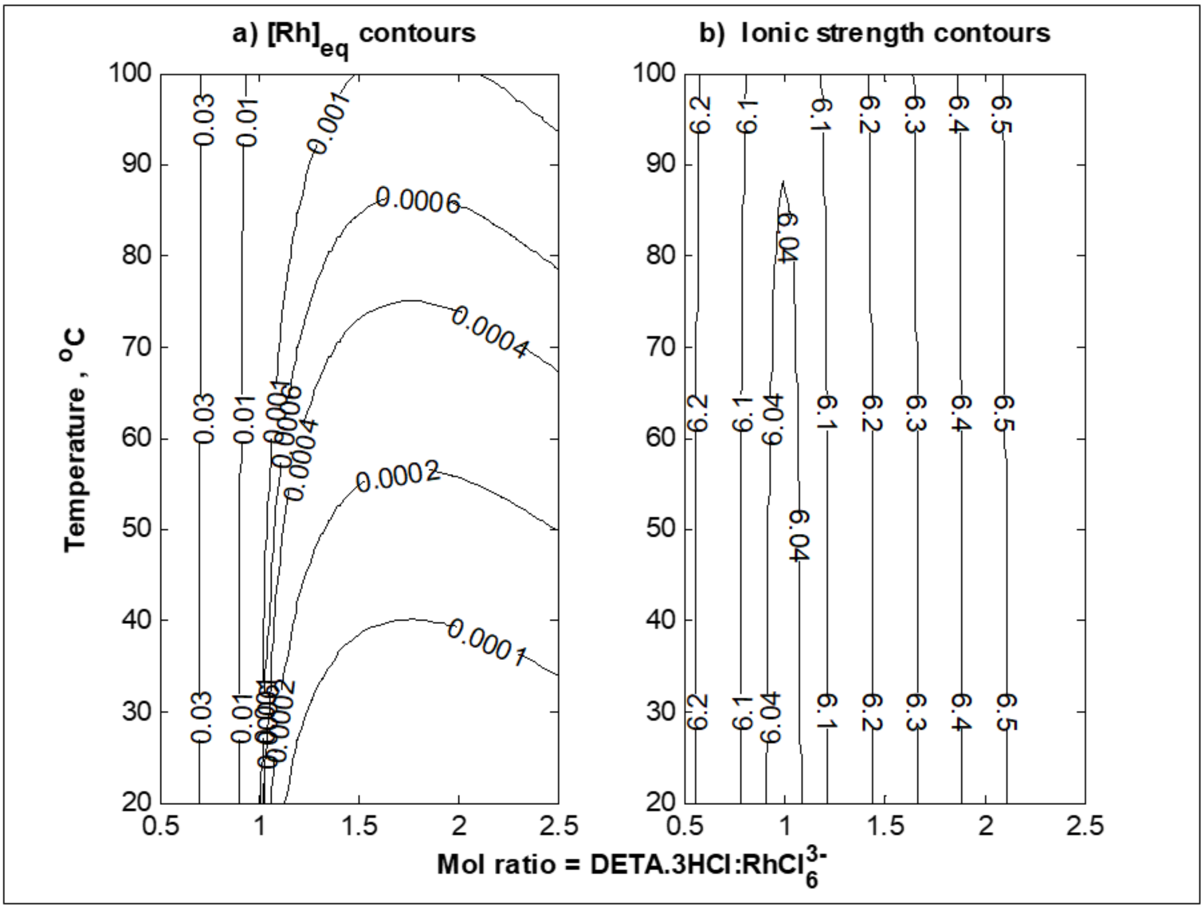

Figure 5.1.6: a) Equilibrium hexachlororhodate (III) concentration and b) ionic strength as a function of mol ratio and temperature at an initial hexachlororhodate (III) concentration of 0.1M

The initial hexachlororhodate (III) concentration used to generate Figures 5.1.6 a) and b) was limited to 0.1M to maintain the ionic strength close to the measured range shown in Figure 5.1.3 b). The higher the initial concentration, the higher the ionic strength at equilibrium up to the point where it significantly exceeds the measured maximum, causing extrapolation errors in activity coefficient calculation.

5.2. VISCOSITY MEASUREMENT OF HEXACHLRORHODATE (III) AND PROTONATED DIETHYLENETRIAMINE SOLUTIONS IN 6M HYDROCHLORIC ACID

Plug flow reactor precipitation experiments were designed at various Reynolds numbers. Viscosity of the feed solution is therefore a required physical property to estimate the Reynolds number at a specific experimental condition. The kinematic viscosity of each feed solution was measured in a capillary tube viscometer. The viscometer containing the sample was left to equilibrate in a thermostat water bath over 24 hours. The plug of the viscometer was then removed and the time for the solution to pass through the capillary tube was measured. Two types of viscometers that had different viscosity-time conversion factors were used. The conversion factors for the type of viscometer used for the hexachlororhodate (III) feed solution and the protonated diethylenetriamine solution were 3.6613E-9m^2/s^2 and 3.7744E-9m^2/s^2 respectively. Table 5.2.1 shows the measured viscosity data at various temperatures and concentrations.

$$\ln \eta = \sum_{i=i}^{2} y_i \ln \eta_i \qquad \textbf{(5.2.1)}$$

Where η = Kinematic viscosity of mixture [m^2/s]

η_i = Kinematic viscosity of the ith stream (i = 1 => $[RhCl_6]^{3-}_{aq}$ solution, i = 2 => $[C_4H_{16}N_3]^{3+}_{aq}$ solution) [m^2/s]

y_i = Volume fraction of the ith stream

The data in Table 5.2.1 follows an Arrhenius relationship with temperature as illustrated in Figure 5.2.1. The viscosity calculation for the combined stream in the pipe reactor is estimated from a simple mixing law as outlined in literature (Perry & Green, 1998). The viscosity mixing relationship is given in Equation (5.2.1).

Table 5.2.1: Kinematic viscosity data for protonated diethylenetriamine and hexachlororhodate (III) solution in 6M hydrochloric acid

Temperature *°C*	$[RhCl_6]^{3-}_{aq}$ *M*	$[C_4H_{16}N_3]^{3+}_{aq}$ *M*	*Time Rh* *s*	*Time DE* *s*	*Rh solution* *m²/s*	*DE solution* *m²/s*
26	0.01	0.01	320.56	311.53	1.174E-06	1.176E-06
26	0.23	0.01	319.91	309.81	1.171E-06	1.169E-06
26	0.26	0.22	320.53	309.56	1.174E-06	1.168E-06
32	0.01	0.01	290.28	281.53	1.063E-06	1.063E-06
40	0.01	0.01	257.34	251.07	9.422E-07	9.476E-07
50	0.01	0.01	225.62	218.57	8.261E-07	8.250E-07
60	0.01	0.01	197.97	191.75	7.248E-07	7.237E-07
70	0.01	0.01	176.97	171.31	6.479E-07	6.466E-07

Rh => [RhCl6]$^{3-}$ solution, and DETA => [C4H16N3]$^{3+}$ solution

The data at 26°C in Table 5.2.1 suggest that within the range of experimental concentrations both hexachlororhodate (III) and protonated diethylenetriamine species in 6M hydrochloric acid do not affect the solution viscosity significantly. Figure 5.2.1 graphically shows that both solutions have very similar viscosity measurements. It is most likely the high hydrochloric acid background concentration that causes negligible viscosity effects from other species in solution.

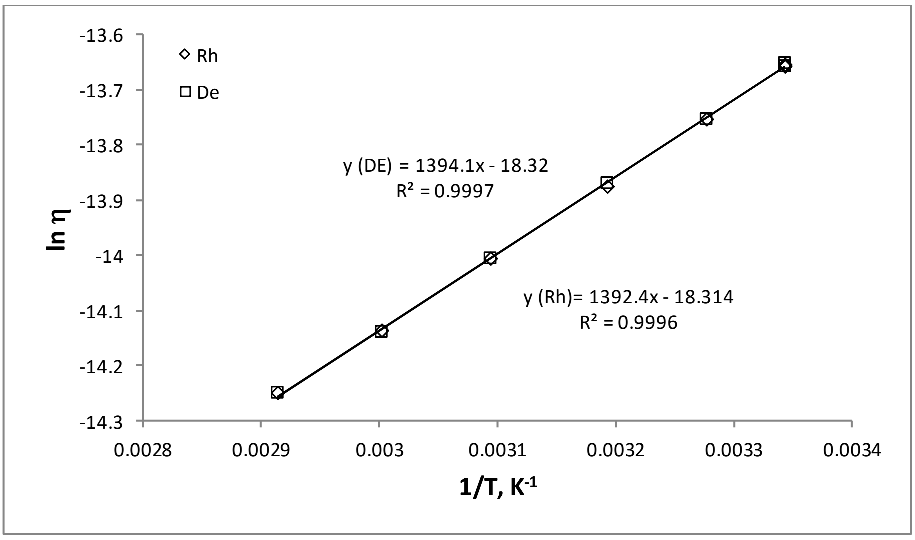

Figure 5.2.1: Kinematic viscosity of 0.25M hexachlororhodate (III) solution and protonated diethylenetriamine solution in 6M hydrochloric acid

6. PFR MODEL REGRESSION: DIETHYLENETRIAMMONIUM HEXACHLORHODATE (III) PRECIPITATION

In this Chapter the models developed in Chapter 3, Section 3.2, are fitted to measurements of conversion and volume average particle size. Section 6.1 deals with estimating the pseudo reaction rate constant introduced in Section 3.2.1 from the system Reynolds number, the measured conversion and the equilibrium conversion. Parameters from the micro- and mesomixing correlations proposed in Section 3.2.1 are then fitted by way of non-linear least squares regression with the pseudo reaction rate constant as the dependent variable and temperature and fluid velocity as the independent variables. Statistical significance of the parameters is evaluated by way of the bootstrap method.

An important assumption in Chapter 3, Section 3.2, is that the second moment of the population balance can be considered part of the pseudo reaction rate constant. This assumption allows for the decoupling of the mass and population balance that allows for independent estimation of firstly the mass balance parameters and secondly the population balance parameters once the saturation profiles are defined. It is therefore inherently assumed that the crystal growth process is limited by either surface integration or mixing scale effects larger than the boundary layer around the particle. Mass transfer by way of diffusion across the crystal surface boundary layer is therefore assumed to have negligible impact on growth rate.

The model parameters are then used to generate saturation and average volume particle size profiles from artificial PFR feed conditions to elucidate general trends in terms of temperature and Reynolds number. The temperature and Reynolds number trends are then compared to actual measured trends in terms of the volume average particle size to validate the proposed model.

Lastly this Chapter presents SEM photographs and population density versus size curves of the crystals that were produced under varying temperature and Reynolds number to validate the mechanisms proposed for agglomeration and growth in Chapter 3, Section 3.2.

6.1. PFR MASS BALANCE PARAMETER ESTIMATION

In the PFR mass balance model, the key unknown driving the reaction extent is the pseudo reaction rate constant K_r. To proceed to data fitting, the correlation between K_r and the process conditions as proposed in Chapter 3, Section 3.2, is further unpacked. To estimate the pseudo reaction rate constant based on experimental measurement, Equation (3.2.6) was re-arranged such that K_r is the argument and is shown in Equation (6.1.1).

$$K_r = -\frac{1}{x_r Re}\ln\left(1 - \frac{X_{Am}}{X_{Ae}}\right) \tag{6.1.1}$$

The length along the reactor x was replaced by the reactor length x_r in Equation (6.1.1). From the relationship in Equation (6.1.1) the reaction rate is not defined when $X_{Am} > X_{Ae}$ as the natural logarithm of a negative number is not defined (the subscript 'm' refers to measured value). For this reason, only data where $X_{Am} < X_{Ae}$ was considered in the calculation. Experimental error caused some of the measurements to be excluded on the above criteria as the reaction extent in those cases was very close to equilibrium.

To estimate the pseudo rate constant from the mixing scale perspective, Equation (3.2.7) was combined with Equations (3.2.8) and (3.2.9); the result is shown in Equation (6.1.2).

$$K_r = \frac{1}{exp\left(-\ln A_{MI} - \frac{B_{MI}}{T}\right) + exp(-\ln A_{m0} - A_{m1}u - A_{m2}u^2)} \tag{6.1.2}$$

Where A_{m0} = Mesomixing length scale frequency parameter [1/m]
A_{m1} = Mesomixing length scale 1st order slope parameter [s/m]
A_{m2} = Mesomixing length scale 2nd order slope parameter [s^2/m^2]
A_{MI} = Scaled micromixing length scale frequency number [1/m]

B_{MI} = Scaled micromixing length scale temperature dependence [K]

The parameters of Equation (6.1.2) were estimated by non-linear regression. The objective function, defined as the difference between natural logarithms of Equations (6.1.1) and (6.1.2) squared, was minimised by a simplex minimisation algorithm that adjusts $\ln A_{m0}$, A_{m1}, A_{m2}, $\ln A_{MI}$ and B_{MI}. The simplex algorithm is programmed as a standard function, '*fminsearch*', in Matlab 2009a (Lagarias et al., 1998). The best data fit parity chart is shown in Figure 6.1.1 with an R^2 value of 0.928.

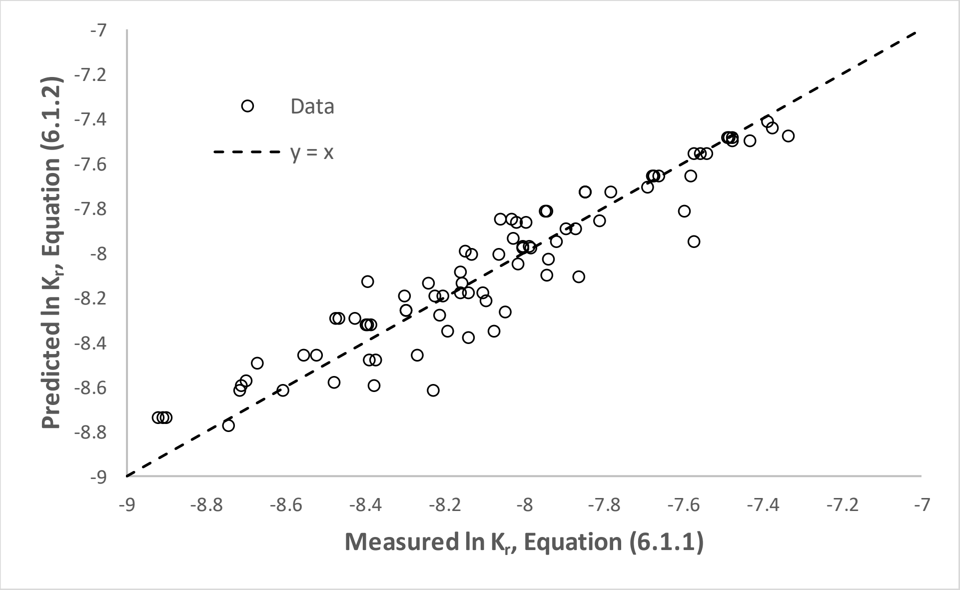

Figure 6.1.1: Parity chart for factored rate constant data fit

To evaluate statistical significance of the parameters the bootstrap method was applied through the standard function '*bootstrp*' available in Matlab 2009a statistical toolbox. A total of 500 bootstrap samples was taken from the original $\ln K_r^*$ versus u, u^2 and $1/T$ data sets. The parameters in Equation (6.1.2) were estimated as described above for each bootstrap sample, giving rise to the bootstrapped parameter distributions in Figures 6.1.2 a) to f). Statistically, a parameter is significant if the bootstrap distribution of the parameter does not overlap zero (Wilcox, 2003).

Table 6.1.1 gives the bootstrap sample 95 per cent confidence intervals for all the parameters in Figure 6.1.2 in addition to the best fit parameter values. The temperature dependence of the micromixing length scale inverse, K_{MI}, suggests an endothermic mixing process, as the best fit value of B_{MI} is 3439K or 28.59kJ/mol (when multiplied by the universal gas constant of 8.314J/mol.K).

Table 6.1.1: Rate constant parameter 95 per cent confidence interval by bootstrap and best fit values

Parameter	$\ln A_{m0}$	A_{m1}	A_{m2}	B_{MI}	$\ln A_{MI}$	R^2
Best fit	-4.84	-5.05	1.25	3439	-18.22	0.928
95% UCL	-3.78	-2.55	2.39	4521	-16.70	0.927
95% LCL	-6.09	-7.27	-0.057	2918	-21.51	0.918

Figure 6.1.2 c) illustrates that ~3.2 per cent of the parameter A_{m2} distribution is less than zero and 96.8 per cent of the distribution is greater than zero. The statistical significance of A_{m2} is therefore inconclusive, thus the parameter may potentially be redundant. However, this parameter is kept in the model purely to prevent a reduction in R^2. The best parameter fit is associated with the maximum R^2 value. Therefore, the best fit parameter set will not necessarily align with the average of each distribution in Figure 6.1.2.

None of the other fitted parameter distributions, including the R^2 distribution in Figure 6.1.2 f), overlap zero. The model for the pseudo rate constant in Equation (6.1.2) is therefore deemed statistically significant. Table 6.1.2 shows the data displayed in Figure 6.1.1 in addition to the predicted conversion from the best fit parameters in Table 6.1.1 and the experimental conditions from Tables 4.4.1 and 10.1.1.

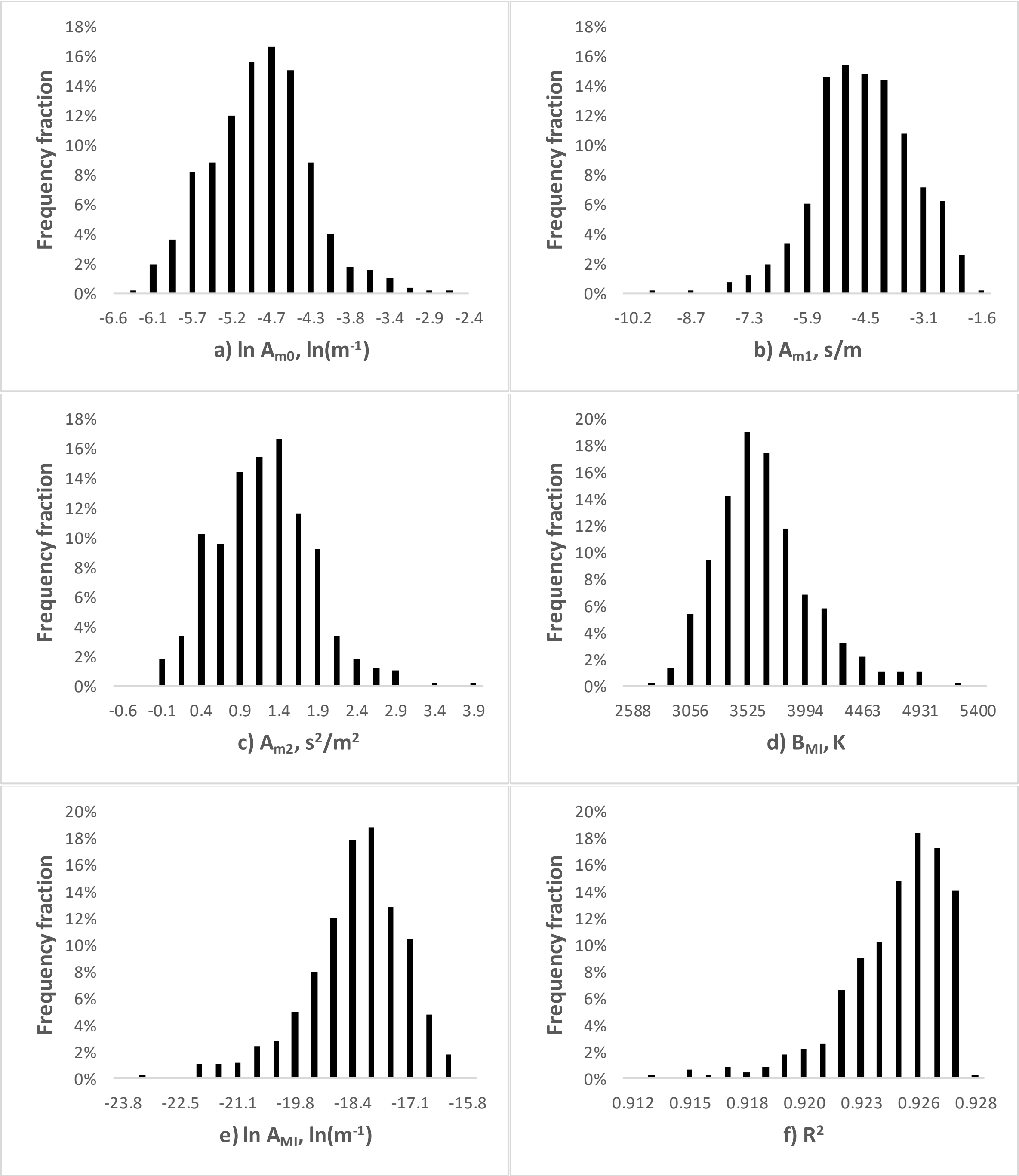

Figure 6.1.2: Non-linear least squares parameter bootstrap distributions

A parity chart of the measured hexachlororhodate (III) conversion and concentration compared to the predicted values, as listed in Table 6.1.2, is shown in Figure 6.1.3. The overall R^2 for the data in Figure 6.1.3 a) is 0.98 and for Figure 6.1.3 b) it is 0.99, indicating a good fit. Interestingly the conversion data in Figure 6.1.3 a) shows less scatter than the rate constant data in Figure 6.1.1. This observation is related to the exponential relationship of conversion and K_r as shown in Equation (3.2.6).

Figure 6.1.3 b) suggests that the accuracy in concentration prediction reduces at smaller concentrations as the scatter seems to increase at the smaller scales below 0.001M. The loss of accuracy is caused by the measured concentration that exceeds the equilibrium concentration as indicated in Table 6.1.2. The outlying points in Figure 6.1.3 b) are associated with the data where $X_{Am} > X_{Ae}$ and is likely caused by the components that make up total experimental error detailed in Chapter 4, Section 4.5.3.

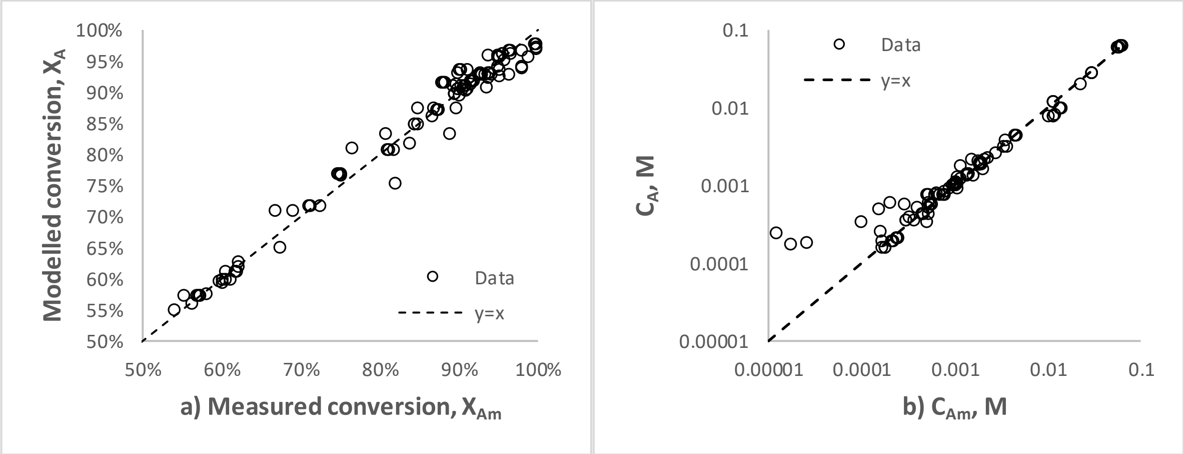

Figure 6.1.3: Parity chart of hexachlororhodate (III) a) conversion and b) concentration at the PFR outlet

Table 6.1.2: Predicted rate constant and conversion using inputs from Table 5.2.1 (X_A estimated from the Best fit values in Table 6.1.1 and input conditions from Table 4.4.1)

Run	u, m/s	Equilibrium $RhCl_6^{3-}$ conversion, X_{Ae}	Predicted $RhCl_6^{3-}$ conversion X_A	Measured $RhCl_6^{3-}$ conversion X_{Am}	$\ln K_r$ from Equation (6.1.1)	$\ln K_r$ from Equation (6.1.2)
1	1.168	97.4%	91.1%	90.3%	-9.190	-9.147
2	1.168	97.4%	91.1%	90.8%	-9.164	-9.147
3	1.168	97.4%	91.1%	91.0%	-9.152	-9.147
4	1.168	97.4%	91.1%	89.4%	-9.239	-9.147
5	0.534	97.4%	96.8%	96.6%	-7.846	-7.735
6	0.534	97.4%	96.8%	96.4%	-7.846	-7.735
7	0.534	97.4%	96.8%	96.3%	-7.846	-7.735
8	0.534	96.7%	96.1%	95.6%	-7.946	-7.817
9	0.534	96.7%	96.1%	95.7%	-7.940	-7.817
10	0.534	96.7%	96.1%	96.6%	-7.594	-7.817
11	1.168	98.4%	89.7%	89.5%	-9.121	-9.113
12	1.168	98.4%	89.7%	89.5%	-9.123	-9.113
13	1.168	98.4%	89.7%	89.4%	-9.125	-9.113
14	0.534	96.3%	95.7%	95.0%	-8.016	-7.869
15	0.534	96.4%	95.8%	95.0%	-8.030	-7.852
16	0.534	96.3%	95.7%	95.2%	-7.994	-7.869
17	0.534	93.8%	93.0%	93.9%	$X_{Am} > X_{Ae}$	-8.094
18	0.534	93.8%	93.0%	93.8%	$X_{Am} > X_{Ae}$	-8.094
19	0.534	93.8%	93.0%	92.7%	-8.160	-8.094
20	0.534	60.1%	59.6%	59.8%	-7.936	-8.036
21	0.534	56.5%	56.0%	56.4%	-7.861	-8.114
22	0.534	55.6%	55.1%	54.1%	-8.392	-8.134
23	0.851	60.2%	59.4%	60.1%	-8.229	-8.621
24	0.851	62.0%	61.1%	62.0%	$X_{Am} > X_{Ae}$	-8.600
25	0.851	62.0%	61.1%	60.6%	-8.710	-8.600
26	0.851	73.1%	71.7%	71.4%	-8.521	-8.464
27	0.851	73.1%	71.7%	72.5%	-8.266	-8.464

Run	u, m/s	Equilibrium $RhCl_6^{3-}$ conversion, X_{Ae}	Predicted $RhCl_6^{3-}$ conversion X_A	Measured $RhCl_6^{3-}$ conversion X_{Am}	$\ln K_r$ from Equation (6.1.1)	$\ln K_r$ from Equation (6.1.2)
28	0.851	73.1%	71.7%	71.1%	-8.555	-8.464
29	0.851	62.8%	61.9%	62.3%	-8.475	-8.589
30	0.851	62.0%	61.1%	61.7%	-8.378	-8.600
31	0.851	63.6%	62.7%	62.1%	-8.700	-8.579
32	0.370	63.2%	59.9%	61.1%	-7.332	-7.482
33	0.370	63.2%	59.8%	60.1%	-7.473	-7.504
34	0.370	63.2%	59.8%	60.5%	-7.429	-7.504
35	0.370	63.2%	57.3%	57.0%	-8.000	-7.980
36	0.370	63.2%	57.5%	58.0%	-7.916	-7.955
37	0.370	63.2%	57.3%	57.3%	-7.985	-7.980
38	0.237	99.9%	87.2%	87.5%	-7.475	-7.487
39	0.237	99.9%	87.2%	87.2%	-7.485	-7.487
40	0.237	99.9%	87.2%	87.3%	-7.484	-7.487
41	0.732	99.3%	93.5%	90.3%	-8.463	-8.296
42	0.732	99.3%	93.5%	91.1%	-8.424	-8.296
43	0.732	99.3%	93.5%	90.1%	-8.474	-8.296
44	0.294	95.7%	76.9%	75.2%	-8.384	-8.329
45	0.294	95.7%	76.9%	74.8%	-8.397	-8.329
46	0.294	95.7%	76.9%	75.0%	-8.391	-8.329
47	0.732	98.2%	91.5%	88.1%	-8.907	-8.741
48	0.732	98.2%	91.5%	87.8%	-8.922	-8.741
49	0.732	98.2%	91.5%	88.3%	-8.901	-8.741
50	0.294	96.3%	83.2%	80.9%	-8.025	-7.939
51	0.732	98.8%	93.1%	89.9%	-8.669	-8.500
52	0.294	69.5%	57.4%	56.9%	-8.222	-8.200
53	0.294	69.5%	57.4%	55.2%	-8.299	-8.200
54	0.294	69.5%	57.4%	57.3%	-8.202	-8.200
55	0.732	86.2%	80.6%	81.8%	-8.101	-8.184
56	0.732	86.2%	80.6%	81.0%	-8.158	-8.184
57	0.732	86.2%	80.6%	81.3%	-8.140	-8.184
58	0.448	95.9%	91.7%	92.0%	-7.540	-7.558
59	0.448	95.9%	91.7%	91.6%	-7.572	-7.558
60	0.448	95.9%	91.7%	91.8%	-7.556	-7.558
61	0.455	90.5%	84.8%	84.8%	-7.983	-7.983
62	0.455	90.5%	84.8%	84.5%	-8.001	-7.983
63	0.455	90.5%	84.8%	84.5%	-8.001	-7.983
64	0.635	99.3%	94.2%	98.0%	-7.572	-7.959
65	0.382	98.3%	90.5%	90.6%	-7.894	-7.896
66	0.382	98.9%	92.9%	92.9%	-7.660	-7.660
67	0.382	98.9%	92.9%	92.7%	-7.670	-7.660
68	0.382	98.9%	92.9%	92.6%	-7.674	-7.660
69	0.193	97.6%	71.0%	69.1%	-8.064	-8.011
70	0.382	97.4%	87.3%	86.9%	-8.155	-8.138

Run	u, m/s	Equilibrium $RhCl_6^{3-}$ conversion, X_{Ae}	Predicted $RhCl_6^{3-}$ conversion X_A	Measured $RhCl_6^{3-}$ conversion X_{Am}	$\ln K_r$ from Equation (6.1.1)	$\ln K_r$ from Equation (6.1.2)
71	0.509	97.4%	90.5%	90.0%	-8.295	-8.267
72	0.761	97.3%	91.3%	91.5%	-8.607	-8.625
73	0.193	99.0%	81.8%	83.8%	-7.376	-7.447
74	0.382	98.9%	92.9%	94.2%	-7.578	-7.660
75	0.509	98.8%	94.2%	94.9%	-7.807	-7.860
76	0.761	98.8%	92.7%	95.1%	-8.192	-8.358
77	0.193	98.4%	76.7%	75.1%	-7.779	-7.731
78	0.382	98.3%	90.5%	91.1%	-7.868	-7.896
79	0.509	98.2%	92.7%	93.4%	-8.014	-8.057
80	0.761	98.2%	92.3%	93.7%	-8.389	-8.483
81	0.193	97.6%	71.0%	66.8%	-8.129	-8.011
82	0.382	97.4%	87.3%	84.9%	-8.238	-8.138
83	0.509	97.4%	90.5%	90.0%	-8.297	-8.267
84	0.761	97.3%	91.3%	89.6%	-8.714	-8.625
85	0.193	96.5%	64.9%	67.5%	-8.211	-8.284
86	0.382	96.2%	83.3%	88.8%	-8.138	-8.382
87	0.509	96.1%	87.5%	89.7%	-8.370	-8.484
88	0.761	96.1%	89.5%	90.2%	-8.743	-8.781
89	0.161	98.7%	90.3%	91.0%	-7.386	-7.421
90	0.344	98.6%	97.3%	99.9%	$X_{Am} > X_{Ae}$	-7.608
91	0.466	98.6%	97.8%	99.8%	$X_{Am} > X_{Ae}$	-7.787
92	0.709	98.5%	97.6%	99.7%	$X_{Am} > X_{Ae}$	-8.250
93	0.161	98.1%	86.1%	86.7%	-7.689	-7.712
94	0.344	97.8%	95.9%	93.8%	-8.057	-7.855
95	0.466	97.8%	96.8%	98.0%	$X_{Am} > X_{Ae}$	-7.997
96	0.709	97.7%	96.9%	99.8%	$X_{Am} > X_{Ae}$	-8.387
97	0.161	97.1%	81.1%	76.6%	-8.145	-7.997
98	0.344	96.8%	93.7%	95.1%	-7.942	-8.106
99	0.466	96.7%	95.2%	95.8%	-8.095	-8.219
100	0.709	96.6%	95.6%	98.7%	$X_{Am} > X_{Ae}$	-8.542
101	0.161	95.7%	75.3%	82.0%	-8.045	-8.273
102	0.344	95.3%	90.7%	93.6%	-8.073	-8.357
103	0.466	95.2%	92.9%	96.3%	$X_{Am} > X_{Ae}$	-8.446
104	0.709	95.0%	93.9%	98.0%	$X_{Am} > X_{Ae}$	-8.712

6.2. PFR NUCLEATION AND GROWTH KINETIC PARAMETER ESTIMATION USING POPULATION DENSITY MOMENT TRANSFORMATIONS

In this section the models derived in Chapter 3, Section 3.2.2, are fitted to measurements at varying input conditions. The t-mixer with PFR in series configuration is chosen as the primary data set used to extract crystal growth and nucleation kinetics dependency on temperature as the range of temperature was widest for this configuration.

The model presented in Equations (3.2.20) and (3.2.21) coupled with the concentration profiles from the mass balance, Equations (3.2.3) to (3.2.5), and the defined expressions for the saturation, growth and nucleation in

Equations (3.2.22) to (3.2.25) was used to extract the parameters A_g, B_g, A_{ag}, B_{ag}, A_n, B_n, α, and β from the L_{43} size. The L_{43} size was estimated from the measured crystal size distributions in the Appendix, Section 10.4, by Equation (10.4.2). The L_{43} calculation procedure from all the measured crystal size volume fraction distributions is outlined in the Appendix, Section 10.4. The modelled L_{43} size was estimated by the ratio of the fourth and third moments that were estimated from Equation (3.2.20), originating from the PFR population balance.

The parameters were estimated using a simplex search routine in Matlab that is available as a standard function '*fminsearch*' (Lagarias et al., 1998). The objective function that was passed through '*fminsearch*' was the weighted sum of squared differences between the measured and modelled values. The objective function is given in Equation (6.2.1) that sums over the *i^th^* experiment.

$$WSSE = \sum_{i=73}^{104} \frac{\left(x_{i,measured} - x_{i,modelled}\right)^2}{SD^2} \qquad \textbf{(6.2.1)}$$

Initial guesses for the parameters were arbitrary and based on initially having the least stiff system (all parameters equal to zero). Note that when the solution became too stiff and the solver remained stuck in a time step, the parameters were manually adjusted between iteration steps. In short, the initial best fit parameter set was determined through trial and error with the aim of reducing the stiffness of the solution. The best fit parameters from the arbitrary initial parameter selection were then used as average values in normal distributions with set precisions of 10 per cent. The distributions were then randomly sampled to get a set of randomized initial parameter guesses that were then passed through the regression routine mentioned above to emulate a Monte Carlo simulation of the data fitting routine. The parameters at the minimum value of the objective function values from the Monte Carlo simulation was then deemed the best data fit.

The procedure is like the bootstrap method used in Section 6.1 but the purpose here is to highlight the effect of initial parameter values on the best fit values for this system. It is emphasised that the system of differential equations is stiff. ODE stiffness is influenced by parameter values that in some instances render the system too stiff to obtain an accurate numeric solution, or the parameter values can dampen or eliminate stiffness as is known for the oscillations described by the Van der Pol differential equation. Due to the influence the parameters have on the stiffness of the system, the initial values can influence the path of minimisation such that the parameter fit moves along the wrong path due to system stiffness.

Bear in mind that the minimisation procedure in '*fminsearch*' is computationally expensive, especially considering that each fitting routine can result in a maximum of 250 000 function evaluations. The number of function evaluations are dictated by the maximum number of iterations and function evaluations per iteration, and was set to 500 respectively. The minimum step size of the variable step ODE solving routing varied between 1E-15m and 1E-18m because of the stiff set of ODEs.

The small minimum step size (stiffness) causes substantial computation time as each function evaluation requires the ODE solver '*ode23s*' in Matlab 2009a to converge to a solution. To summarise, it is possible for the objective function minimisation routine to converge to a solution that is not a global minimum due to the simplex search algorithm moving along a path of least stiffness, resulting in erroneous parameters. However, the Monte Carlo simulation aims to mitigate the risk of following the wrong minimisation path by randomising the initial parameter guesses, as explained above.

Figure 6.2.1 a) shows a parity chart of the data fit and Figure 6.2.1 b) shows the $WSSE$ sorted in descending order as a function of the number of Monte Carlo simulation samples. The overall R^2 value for the data in Figure 6.2.1 a) was 0.82 indicating variance that is most likely related to experimental error combined with numeric computation error. The latter error component is difficult to quantify; a description of how it manifests itself in the output is given later when different feed conditions are simulated in Section 6.3.

However, from a statistical view the data fit appears to be significant. The largest contributor to experimental error is due to the relatively small crystal size distributions produced in the PFR configuration relative to the CSTR configuration that cause fines losses and difficulty with representative sampling. In addition, the elevated dilution temperature used to stall the precipitation prior to filtration is potentially a cause of a separate nucleation process during filtration, resulting in bimodal size distributions that cause inaccurate L_{43} calculation.

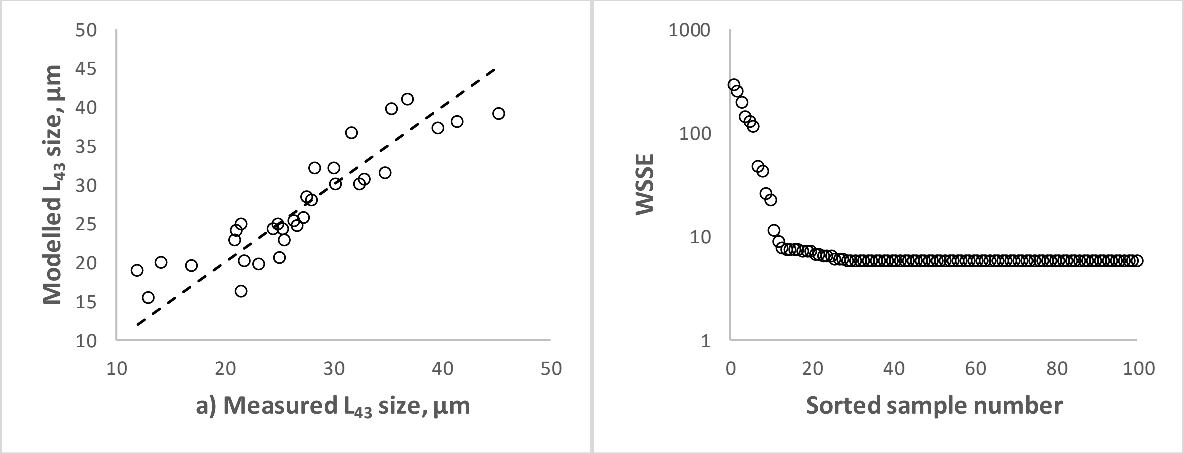

Figure 6.2.1: a) L_{43} size parity chart and b) WSSE sorted in descending order versus Monte Carlo sample number

The raw data in the plot in Figure 6.2.1 a) is tabulated in Table 6.2.1. The SD row in Table 6.2.1 refers to the standard deviation of the data above it. This value is used in the objective function to weight the L_{43} size such that the units become dimensionless during the data fitting optimisation routine (see Equation (6.2.1)).

The simplex search routine applied to the objective function in Equation (6.2.1) given arbitrary parameters as discussed above converged to a set of initial best fit parameters that are shown in Table 6.2.2. The fitted parameters after an iteration was used as an initial guess in the subsequent iteration.

Table 6.2.1: Measured and modelled PFR configuration crystal L_{43} size

Run	***Measured L_{43}, µm***	***Predicted L_{43}, µm***
73	17	19
74	14	20
75	12	19
76	13	15
77	27	25
78	25	24
79	25	24
80	25	25
81	35	31
82	33	31
83	32	30
84	30	30
85	35	40
86	45	39
87	41	38
88	40	37
89	23	20
90	25	20
91	22	20
92	22	16
93	22	25

Run	Measured L_{43}, μm	Predicted L_{43}, μm
94	26	23
95	21	23
96	21	24
97	28	32
98	28	28
99	27	26
100	26	25
101	37	41
102	32	36
103	30	32
104	28	28
SD	7.9	7.1
R^2	0.82	

Iteration 8 in Table 6.2.2 was used as the average values in the constructed normal parameter distributions for the Monte Carlo simulation. The standard deviation of each parameter distribution was chosen as 10 per cent of the average. The parameter distributions were randomly sampled 100 times using the '*rand*' function in Matlab 2009a. Each random initial parameter sample set was first passed through the minimisation routine that gave a converged set of parameter values for the sample. The converged parameter sets were then passed through the routine for a second time and were then reported as the final converged parameter set for the sample.

Figure 6.2.2 a) show the trajectories of the temperature dependent parameters in the Arrhenius expressions along the descending path of the $WSSE$ in Figure 6.2.1 b). In Figure 6.2.2 b) the frequency number of the growth and nucleation rate constants are shown along the path of descending $WSSE$ and in Figure 6.2.2 c) the growth and nucleation exponents are shown.

Table 6.2.2: Arbitrary initial parameter estimates

Parameter	B_g, K	B_{ag}, K	B_n, K	$\ln A_g$	$\ln A_{ag}$	$\ln A_n$	α	β	$WSSE$
Initial guess	0	0	0	0.0	0.0	0.0	1.00	1.00	380.38
Iteration 1	2	2	0	1.3	-1.5	-0.6	0.01	0.39	101.62
Iteration 2	5	-10	0	9.9	-13.3	8.5	1.04	0.79	8.80
Iteration 3	-500	-500	0	9.9	-13.3	8.5	1.04	0.79	9.00
Iteration 4	-1642	1574	-4	15.0	-11.1	5.8	1.09	0.26	7.56
Iteration 5	-10744	-49707	19538	10.0	10.0	2.8	1.16	1.13	409.73
Iteration 6	-4409	-60314	27289	15.5	10.5	0.9	1.17	1.13	10.69
Iteration 7	-29552	-70350	22829	93.7	46.4	14.3	1.18	0.01	6.15
Iteration 8	-29406	-71758	22721	93.2	51.1	13.8	1.13	0.41	5.73

All the trajectory paths show that the final converged value appears to be related to the chosen initial parameter set, as every initial parameter set does not converge to a consistent set. It is furthermore apparent that as the $WSSE$ approaches the minimum value, the parameters tend to converge. However there remains some variation in all the parameters between sample numbers 90 to 100, indicating that the parameters affect the stiffness of the ODE system. Table 6.2.3 shows the best fit parameter set obtained from the Monte Carlo simulation.

Table 6.2.3: Monte Carlo best fit parameter set

Parameter	B_g, K	B_{ag}, K	B_n, K	$\ln A_g$	$\ln A_{ag}$	$\ln A_n$	α	β	$WSSE$
Best fit	-23203	-78921	29322	73.44	29.16	15.00	1.13	0.51	5.65

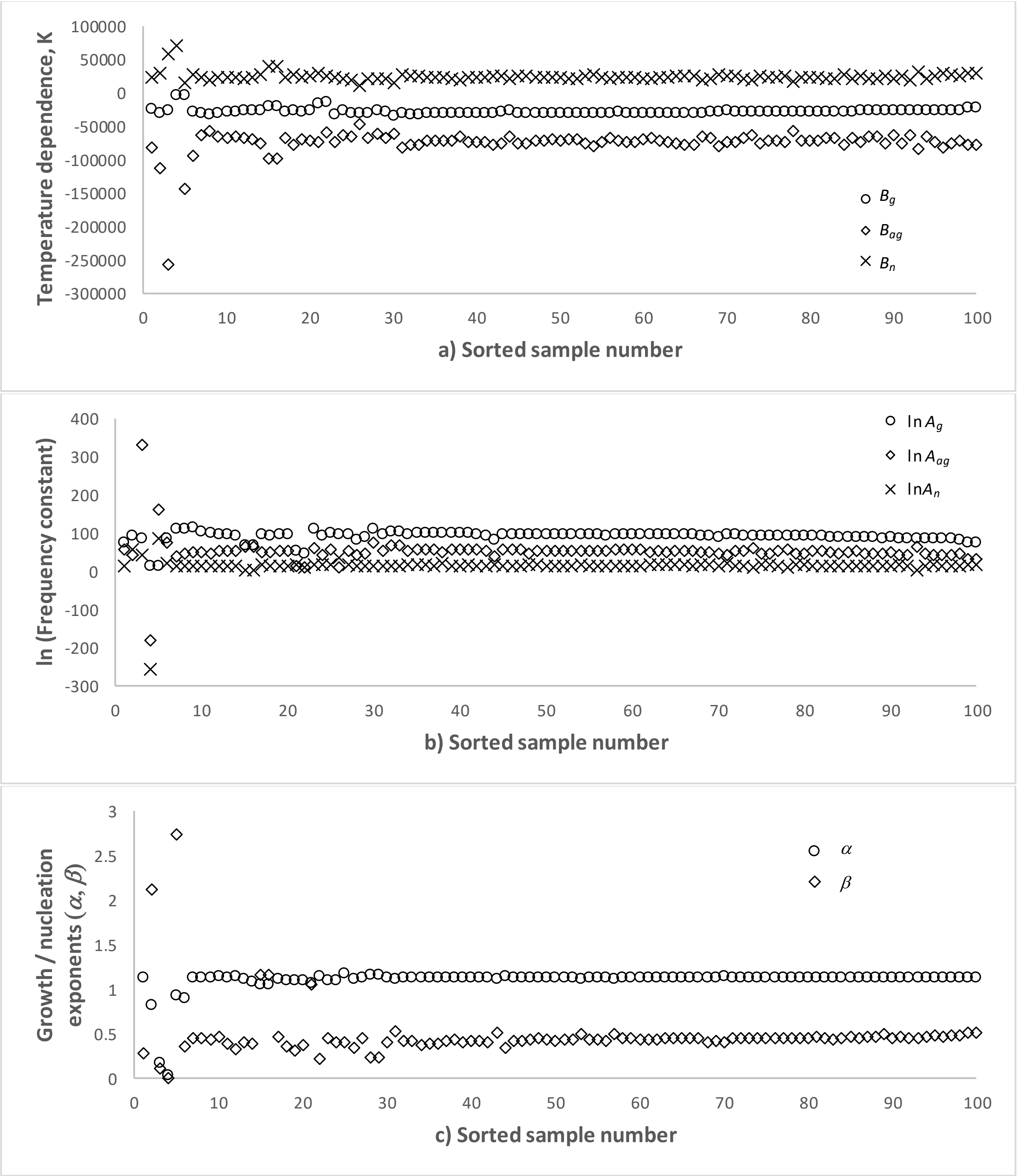

Figure 6.2.2: Monte Carlo parameter trajectories along the path of descending WSSE a) B_g, B_{ag} and B_n, b) logarithm of A_g, A_{ag} and A_n and c) growth and nucleation exponents

The L_{43} size was inferred through a volume size distribution and represents a ratio of the fourth moment over the third moment of an experiment. Keep in mind that the data-fitting routine converged to a parameter set that is likely to be associated with the least stiff solution.

The absolute values of the moments are coupled to the parameter A_n as well as the parameter A_{ag}, noting that these parameters are scaled through data fitting. Equation (6.2.2) shows the derivation of the scale factor based on the premise that the third moment must reconcile with the salt concentration, which is referred to as moment closure in Bałdyga & Bourne (1999). The volume shape factor is assumed to be size independent. The scaling factor is introduced to ensure the third moment reconciles with the crystal concentration.

$$
\begin{aligned}
C_C &= \frac{\rho_c \int_0^\infty K_v n L^3 dL}{MW_c} X10^{-15} = \frac{\rho_c K_v M_3}{MW_c} X10^{-15} = \frac{\rho_c K_v \varepsilon M_3'}{MW_c} X10^{-15} \\
\therefore \varepsilon &= \frac{C_C MW_c}{\rho_c K_v M_3'} X10^{15}
\end{aligned}
\qquad \textbf{(6.2.2)}
$$

Where C_C = Crystal concentration [mol/dm^3]
ρ_c = 1798 = Crystal density [g/dm^3]
K_v = Crystal volume shape factor [m^3/#.m^3]
MW_c = 428.81 = Crystal molecular weight [g/mol]
ε = Moment scale factor
M_3' = Scaled third moment [#.µm^3/dm^3]

If the scale factor is equal to one then the moments are not scaled; otherwise the moments are scaled. The 10^{-15} term in Equation (6.2.2) represents the conversion of the units of the scaled third moment from µm^3/dm^3 to m^3/m^3. Here it is assumed that the volume unit of the scaled third moment is in litre (dm^3). As the third moment was not explicitly measured, it is uncertain what the unit of the denominator is. The 10^{-15} term can therefore be any number above zero depending on the volume unit in which the moment was measured. In this work no moment was explicitly measured, thus it is not possible to know the volume units of the denominator of each moment. The nucleation and growth parameters were estimated by data fitting the moment equations to L_{43} measurements. The volume units cancel out in the L_{43} calculation, therefore certain data fitted parameters are susceptible to the scale factor.

The following expansions of the moment balance aim to clarify the effect of scaling on the fitted nucleation and growth parameters. The influence is determined by replacing the moments in Equation (3.2.20) by the respective scaled moments. Before continuing, Equation (6.2.3) illustrates the concept of a scaled moment.

$$
\begin{aligned}
&M_i = \varepsilon M_i' \\
&\therefore \frac{dM_i}{dz} = \frac{d(\varepsilon M_i')}{dz} = \varepsilon \frac{dM_i}{dz} \quad where\ z = x\ or\ t
\end{aligned}
\qquad \textbf{(6.2.3)}
$$

The scaled moment expansion of the set of differential equations in Equation (3.2.20) is given in Equation (6.2.4).

$$
\begin{aligned}
\varepsilon \frac{dM_0'}{dx} &= \frac{\left(G - K_{ag}\varepsilon^2 M_0'^2 (S-1)\right)}{u} K_n (S-1)^{\beta} \\
\varepsilon \frac{dM_1'}{dx} &= \frac{\left(G - K_{ag}\varepsilon^2 M_0'^2 (S-1)\right)}{u} \varepsilon M_0' + \frac{G K_{ag}\varepsilon^2 M_0'^2 \tau_a}{u} K_n (S-1)^{1+\beta} \\
\varepsilon \frac{dM_2'}{dx} &= \frac{2\left(G - K_{ag}\varepsilon^2 M_0'^2 (S-1)\right)}{u} \varepsilon M_1' + \frac{2G K_{ag}\varepsilon^2 M_0'^2 (S-1)\tau_a}{u} \varepsilon M_0' \\
\varepsilon \frac{dM_3'}{dx} &= \frac{3\left(G - K_{ag}\varepsilon^2 M_0'^2 (S-1)\right)}{u} \varepsilon M_2' + \frac{6G K_{ag}\varepsilon^2 M_0'^2 (S-1)\tau_a}{u} \varepsilon M_1' \\
\varepsilon \frac{dM_4'}{dx} &= \frac{4\left(G - K_{ag}\varepsilon^2 M_0'^2 (S-1)\right)}{u} \varepsilon M_3' + \frac{12G K_{ag}\varepsilon^2 M_0'^2 (S-1)\tau_a}{u} \varepsilon M_2'
\end{aligned}
\qquad \textbf{(6.2.4)}
$$

Let K_n' and K_{ag}' represent the scaled rate constants (determined through data fitting). Equation (6.2.4) illustrates that the scale factor cancels out such that K_n is equal to $K_n'\varepsilon$ and K_{ag} is equal to K_{ag}'/ε^2. Therefore, in Equations (3.2.23) to (3.2.25) the only parameters affected by scaling are A_n and A_{ag}. The same argument holds for the CSTR configuration.

6.3. MOMENT AND CONCENTRATION PROFILES AS A FUNCTION OF PFR LENGTH GIVEN SPECIFIED INPUT CONDITIONS

The purpose of this section is to elucidate PFR configuration trends given a change in operating conditions. Table 6.3.1 gives a variety of input conditions that particularly target changes in temperature and Reynolds number.

Table 6.3.1: Plug flow reactor model input conditions with reactor diameter = 5mm

Input	T, °C	$C_A\|_{x=0}$, M	$C_B\|_{x=0}$, M	v_A, dm^3/h	v_B, dm^3/h	Reynolds number	$*C_{Ae}$, M	$*C_{Be}$, M
1	40	0.01	0.13	0.671	0.671	100	0.0001117	0.1201
2	40	0.01	0.13	3.355	3.355	500	0.0001117	0.1201
3	40	0.01	0.13	6.710	6.710	1000	0.0001117	0.1201
4	40	0.01	0.13	10.065	10.065	1500	0.0001117	0.1201
5	40	0.01	0.13	13.420	13.420	2000	0.0001117	0.1201
6	50	0.01	0.13	0.585	0.585	100	0.0001713	0.1202
7	50	0.01	0.13	2.923	2.923	500	0.0001713	0.1202
8	50	0.01	0.13	5.847	5.847	1000	0.0001713	0.1202
9	50	0.01	0.13	8.770	8.770	1500	0.0001713	0.1202
10	50	0.01	0.13	11.694	11.694	2000	0.0001713	0.1202
11	60	0.01	0.13	0.514	0.514	100	0.0002562	0.1203
12	60	0.01	0.13	2.569	2.569	500	0.0002562	0.1203
13	60	0.01	0.13	5.137	5.137	1000	0.0002562	0.1203
14	60	0.01	0.13	7.706	7.706	1500	0.0002562	0.1203
15	60	0.01	0.13	10.274	10.274	2000	0.0002562	0.1203
16	70	0.01	0.13	0.455	0.455	100	0.0003746	0.1204
17	70	0.01	0.13	2.274	2.274	500	0.0003746	0.1204
18	70	0.01	0.13	4.548	4.548	1000	0.0003746	0.1204
19	70	0.01	0.13	6.822	6.822	1500	0.0003746	0.1204
20	70	0.01	0.13	9.095	9.095	2000	0.0003746	0.1204

*Calculated by the method described in Chapter 3, Section 3.2.1, Equations (3.2.13) to (3.2.16)

A typical concentration versus reactor length profile is shown in Figure 6.3.1 for two Reynolds number input conditions at fixed temperature. The trend suggests that higher Reynolds number results in the chemistry equilibrating at a shorter distance in the reactor.

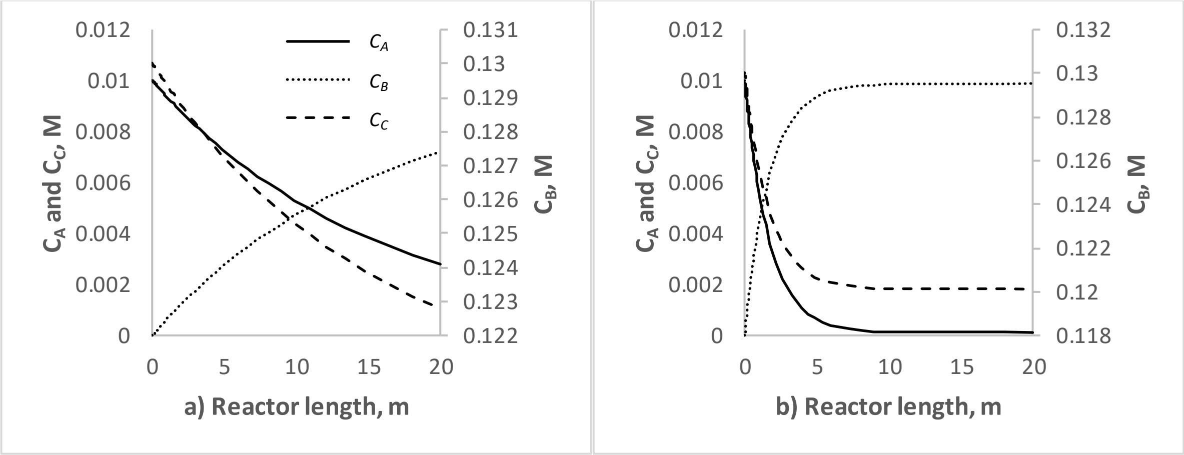

Figure 6.3.1: Reagent and crystal concentration profiles at T = 40°C for a) Re = 100 (Input 1 in Table 6.3.1) and b) Re = 1000 (Input 3 in Table 6.3.1)

The moment profiles associated with the concentration profiles in Figure 6.3.1 are shown in Figure 6.3.2. Here each moment is normalised to the maximum value of the moment calculated over the length of the reactor. Therefore, each moment is bounded between 0 and 1 in Figure 6.3.2.

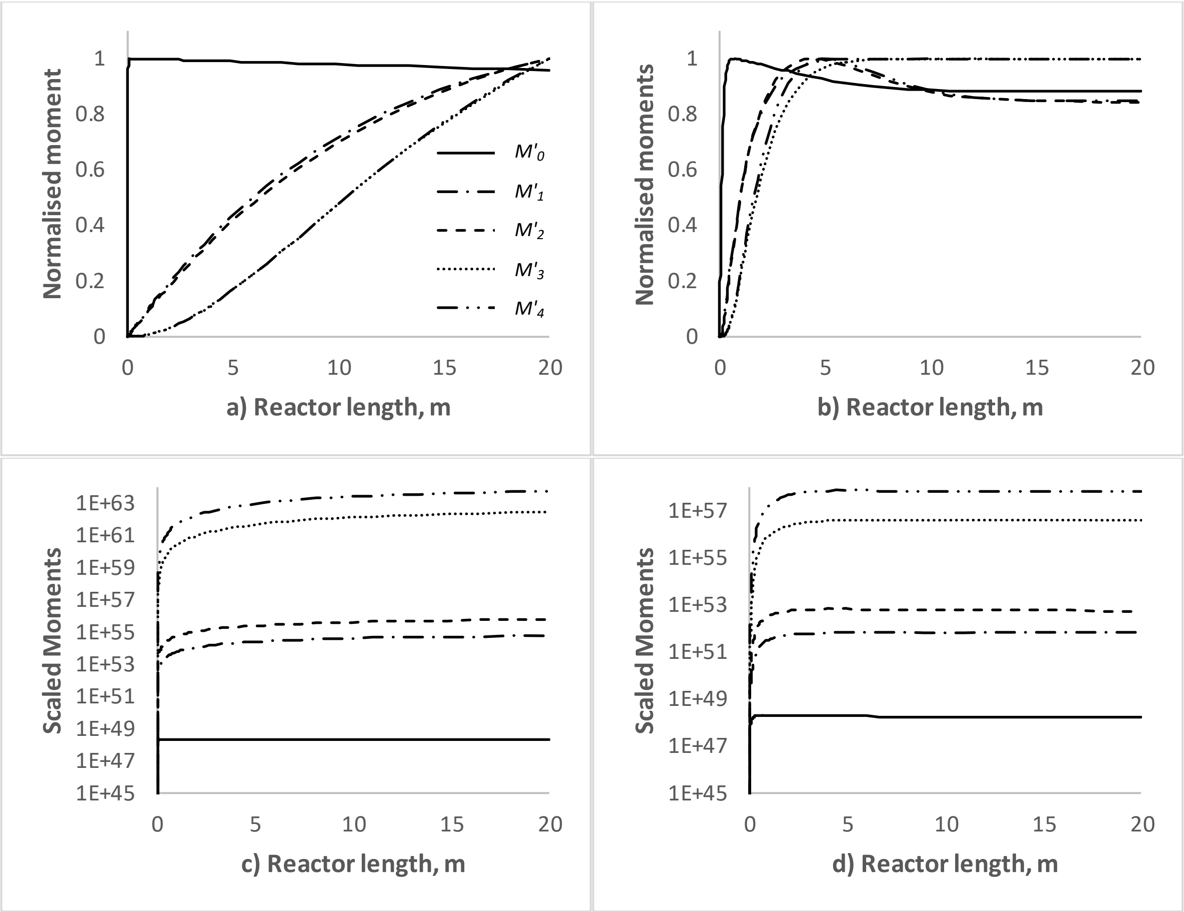

Figure 6.3.2: Normalised moment profiles at T = 40°C for a) Re = 100 (Input 1 in Table 6.3.1) and b) Re = 1000 (Input 3 in Table 6.3.1). Logarithmic scale moment profiles c) Re = 100 (Input 1 in Table 6.3.1) and d) Re = 1000 (Input 3 in Table 6.3.1)

The trends observed on the normalised scale in Figure 6.3.2 a) and b) are not as readily visible when the scaled moments are not normalised, as illustrated through a semi-logarithmic plot in Figure 6.3.2 c) and d). The latter trends are used to illustrate that the relative values of the moments are highest for the fourth moment and lowest for zeroth moment.

Figure 6.3.2 b) relative to a) illustrates that the moments stabilise over a shorter distance in the reactor when increasing the Reynolds number. The zeroth moment in Figure 6.3.2 a) rapidly peaks within the first 0.06m of the reactor and then steadily declines over the remaining length of the reactor due to agglomeration. The convex shape of the higher order moments in Figure 6.3.2 a) is due to agglomeration that tends to decrease the respective moment to reactor length gradient. All the higher moments steadily increase over the whole reactor length due to saturation that is not completely consumed as highlighted in the concentration profile in Figure 6.3.1 a). The system in Figure 6.3.1 a) is therefore still in a transient phase with respect to the processes that govern growth, nucleation and agglomeration. Considering the second moment in Figure 6.3.2, it is shown that the moment changes of the length of the reactor.

In Figure 6.3.2 b) the zeroth moment or number of particles increase from the point of reagent injection, reaches a maximum after approximately 1 metre, declines until approximately 12 metres, and finally steadies out over the remaining reactor length. This observation is related to particle agglomeration that tends to decrease the number of particles in the system. A comparison of the zeroth moment trends in Figures 6.3.2 a) and b) reveals that at a higher Reynolds number, nucleation diminishes and agglomeration dominates over a longer distance in the reactor relative to lower Reynolds numbers, as in Figure 6.3.2 a). This observation is caused by the saturation profile that is rapidly depleted at high Reynolds numbers compared to low Reynolds numbers (see Figure 6.3.1). At high saturation (low Reynolds number) nucleation dominates; in comparison a lower saturation (high Reynolds number and $(S-1)<1$) agglomeration and growth tend to dominate.

To explain the peculiar trends of the normalised first, second, third and fourth moments in Figure 6.3.2 b), first consider the hypothetical case where two cubes that have equal side lengths, a, combine to form a cuboid that has eight side lengths equal to a, and four side lengths equal to $2a$. In other words, the two cubes are joined back to back. The back to back length of the longest side of the two separate cubes ($a + a = 2a$) is equal to the longest side of the joined cubes ($2a$), thus length is conserved, or the first moment is constant before and after the two cubes are joined. The exposed surface area after the two cubes are joined ($4a2a + 2a^2 = 10a^2$) is less than the sum of the individual exposed surface area ($6a^2 + 6a^2 = 12a^2$) of the two cubes, hence the second moment is decreased after the two cubes are joined. The volume of the cubes remains conserved after they are combined ($2a^3$), therefore the third moment remains constant after the two cubes are joined.

The fourth moment is an abstract concept and does not relate to physical space. It is a mathematical calculation that gives the average size of the volume size distribution when divided by the third moment, as described in Equation (3.2.5). However, if the fourth moment is thought of as the product of the area between two planes that are either adjacent to each other or perpendicular to each other, it can be estimated for the hypothetical system above. The total for the two cubes is $2a^4$ and for the combined cuboid it can either be a^4, $2a^4$ or $4a^4$. Therefore, the fourth moment of the cuboid can either be smaller than, equal to, or greater than the fourth moment of the separate cubes. Conceptually, the fourth moment after agglomeration can therefore either be smaller than or greater than before agglomeration.

In Figure 6.3.2 b) it is seen that the first and third moments appear to increase during the first 5 metres of the reactor and then flattens off and stays constant when agglomeration dominates (decreasing zeroth moment). In contrast the second and fourth moment increase to a peak within the first 5 metres, then decreases whilst agglomeration dominates until saturation is consumed and then flattens out, see Figure 6.3.3 b). The observation of a declining second and fourth moment at a constant first and third moment is consistent with the hypothetical example given above. The second order type response for moments was observed in the work by Vicum, (2005) through the average particle size measurement of a continuous stirred tank reactor over a transient period.

A comparison between Figure 6.3.3 a) and b) reveals that a higher Reynolds number has a reducing effect on the L_{43} size as saturation is depleted along the reactor length. When saturation falls roughly below 5 in Figure 6.3.3 b) the L_{43} size starts to decrease until approximately 13 metres and then stabilises. This observation is primarily due to the profile of the third and fourth moments in Figure 6.3.2 b). The declining fourth moment at a constant third moment is because of agglomeration as discussed above.

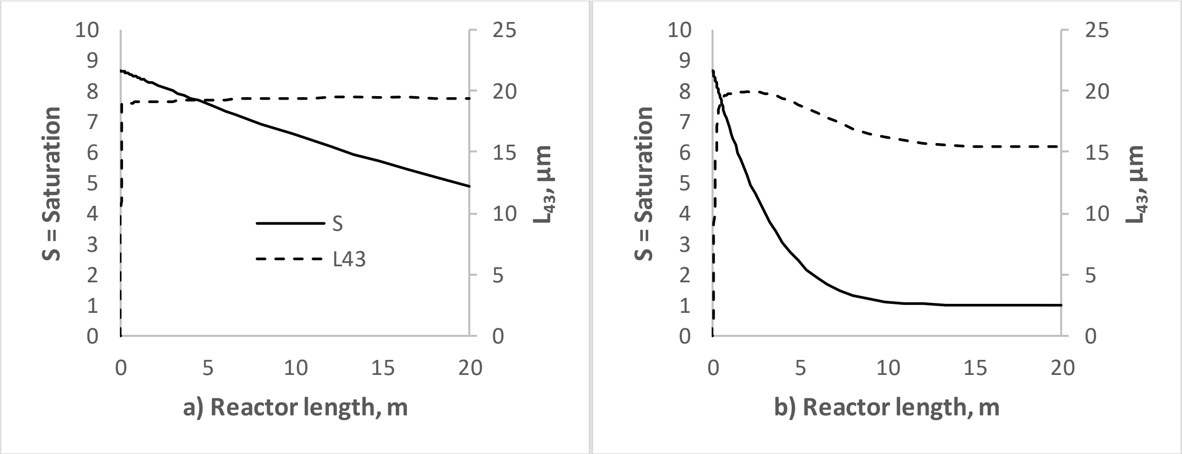

Figure 6.3.3: Saturation and L_{43} profiles at T = 40°C for a) Re = 100 (Input 1 in Table 6.3.1) and b) Re = 1000 (Input 3 in Table 6.3.1)

The effect of temperature on L_{43} at varying Reynolds numbers is illustrated in Figure 6.3.4. From the trends it appears as if the L_{43} size increases with temperature. However, the effect of Reynolds number on the agglomerative process can cause the L_{43} size to decrease further down the PFR, as shown in Figure 6.3.3 b). This observation is also evident to a lesser extent in Figure 6.3.4 b).

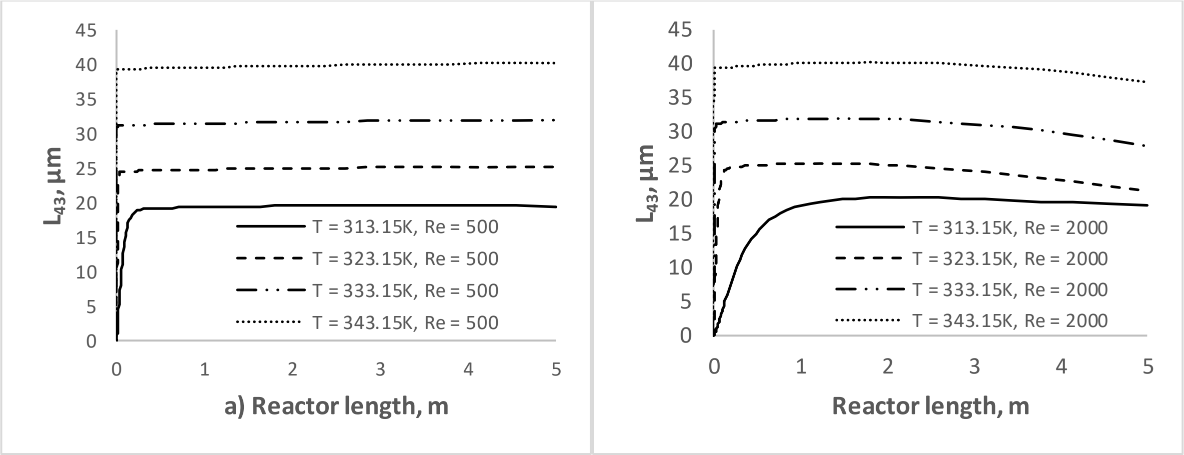

Figure 6.3.4: L_{43} size versus reactor length and varying temperature at a) Re = 500 and b) Re = 2000

The modelled L_{43} sizes at varying Reynolds number and temperature are shown in Figure 6.3.5. The data shows that the L_{43} size at a reactor length of 5 metres has a linear correlation with temperature (see Figure 6.3.5 a)). In Figure 6.3.5 b) the effect of Reynolds number on the L_{43} size is not statistically discernible due to the peak of the L_{43} size being near 5 metres along the reactor length. Multiple linear regression on the modelled results confirms that temperature is the most significant effect at a reactor length of 5 metres, while the effect of Reynolds number on L_{43} size is not statistically detectable (refer to Tables 6.3.2 and 6.3.3).

Table 6.3.2: Regression analysis of variance (ANOVA) for the data in Figure 6.3.5

ANOVA parameter	***df***	***SS***	***MS***	***F***	***p-value***
SS (Regression)	2	673.9	336.9	114.7	3.9E-07
SS (Residual)	9	26.4	2.9		
SS (Total)	11	700.3			

df = degrees of freedom, *SS* = squared sum of errors, *MS* = *SS*/*df*, *F* = *MS* (Regression)/*MS* (Residual), *p-value* = F-distribution evaluated at the calculated F value => probability that MS (regression) is equal to MS (residual). For details on multiple linear regression the reader is referred to Vining (1998).

The R^2 for the modelled correlation showed in Figure 6.3.5 was 0.96. The analysis of variance for the regression is shown in Table 6.3.2, which indicates that the correlation is statistically significant by the F-test as the p-value is << 0.05.

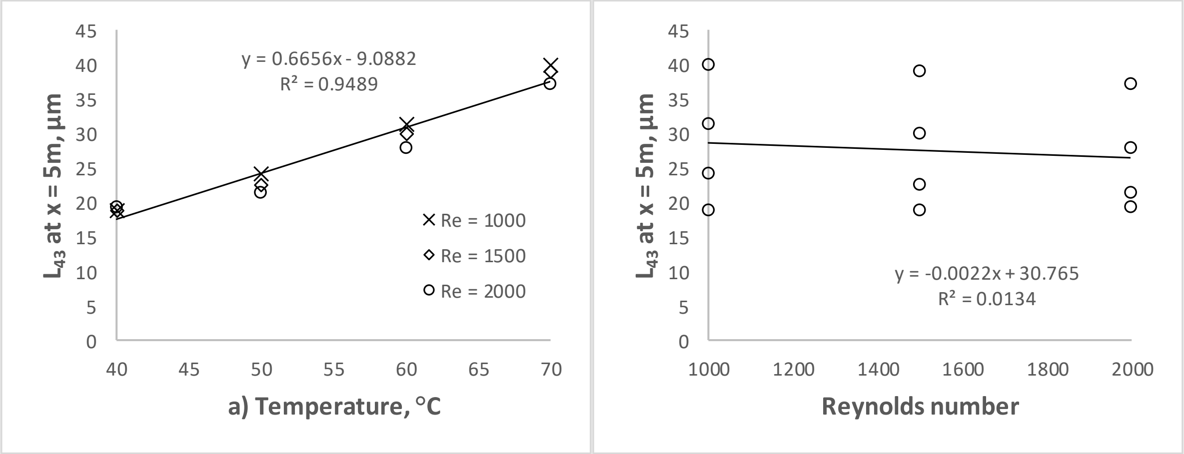

Figure 6.3.5: Modelled effect of a) temperature and b) Reynolds number on L_{43} size at the maximum experimental reactor length

The regression parameter hypothesis test results are given in Table 6.3.3. The data here shows that the temperature is statistically significant as the p-value << 0.05, but the Reynolds number is not at a p-value > 0.05. The effect of Reynolds number is masked due to the saturation not reaching equilibrium at a reactor length of 5 metres for all the modelled runs in Table 6.3.1.

Table 6.3.3: Regression parameters and hypothesis test results for the data in Figure 6.3.5

Parameter	*Value*	*SE*	*t Stat*	*p-value*	*L CL 95%*	*U CL 95%*
Intercept	-5.84	3.08	-1.90	0.09	-12.80	1.12
Re slope	-0.0022	0.0012	-1.79	0.11	-0.0049	0.00058
T slope	0.67	0.04	15.04	0.00	0.57	0.77

Figure 6.3.6 shows the measurements associated with the input data in Table 5.2.1 (runs 73 to 104) expressed as a function of temperature and Reynolds number. The general trend is consistent with the modelled trend in Figure 6.3.5. Multiple linear regression on the measured data set confirms that temperature is the most significant variable and that Reynolds number does not significantly affect L_{43}.

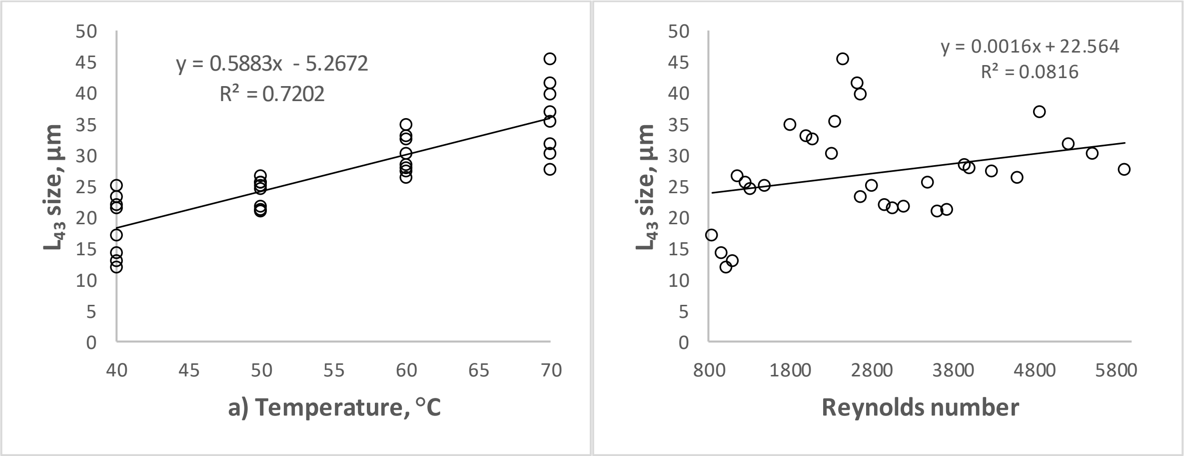

Figure 6.3.6: Experimental L_{43} size versus a) temperature and b) Reynolds number

The relationships between temperature and particle size in Figures 6.3.5 a) and 6.3.6 a) is consistent with previous work by Hagemann et al. (2003). As with the modelled case it is inferred that the effect of the Reynolds number on particle size is masked by the system not equilibrating for all tests in Table 5.2.1. The multiple linear regression results for the data in Figure 6.3.6 with an R^2 value of 0.73 are shown in Tables 6.3.4 and 6.3.5. The measured data regression parameter hypothesis test results are given in Table 6.3.5. Here temperature is statistically significant (p-value << 0.05) but the Reynolds number is not (p-value > 0.05).

Table 6.3.4: Regression analysis of variance (ANOVA) for the data in Figure 6.3.6

ANOVA parameter	*df*	*SS*	*MS*	*F*	*p-value*
SS (Regression)	2	1409	704.3	39.8	4.9E-09
SS (Residual)	29	514	17.7		
SS (Total)	31	1922			

df = degrees of freedom, *SS* = squared sum of errors, *MS* = *SS*/*df*, *F* = *MS* (Regression)/*MS* (Residual), *p-value* = F-distribution evaluated at the calculated F value => probability that MS (regression) is equal to MS (residual). For details on multiple linear regression the reader is referred to Vining (1998).

Table 6.3.5: Regression parameters and hypothesis test results for the data in Figure 6.3.6

Parameter	*Value*	*SE*	*t Stat*	*p-value*	*L CL 95%*	*U CL 95%*
Intercept	-4.72	3.76	-1.26	0.22	-12.42	2.97
Re slope	-0.00065	0.00056	-1.17	0.25	-0.0018	0.00049
T slope	0.61	0.070	8.79	1.1E-09	0.47	0.75

The effect of Reynolds number and reactor length on hexachlororhodate (III) conversion is illustrated in Figure 6.3.7. With reference to Figure 5.1.4, it is observed that an increase in temperature lowers the conversion due to the increased salt solubility at elevated temperature. It is further observed that conversion increases at higher Reynolds number up to the point where it plateaus off.

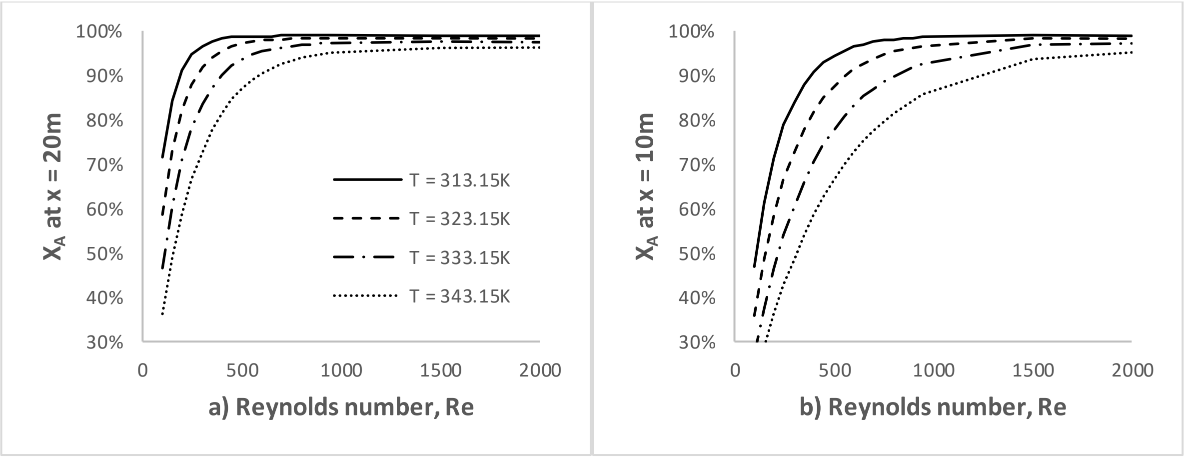

Figure 6.3.7: Conversion versus Reynolds number for a reactor length of a) 20m and b) 10m

The relationship between Reynolds number and conversion therefore suggests that beyond a critical Reynolds number, depending on temperature, the reaction becomes equilibrium-limited whereas below the critical value it is mass transfer limited through micro- or mesomixing effects described by Equation (3.2.7). Reduced reactor length shifts the conversion curves in Figure 6.3.7 a) to the right-hand side as shown in Figure 6.3.7 b). One would therefore require a higher Reynolds number to achieve the same conversion in a short reactor relative to a longer reactor at a fixed temperature.

6.4. PFR CRYSTAL MORPHOLOGY AND SIZE DISTRIBUTION

In this section the crystal surfaces produced in the PFR configuration are examined at varying Reynolds number and saturation (temperature) through SEM photographs. The population density and respective crystal size distributions are also presented. Figure 6.4.1 shows diethylenetriammonium hexachlororhodate (III) salt produced at a temperature of 40°C and a Reynolds number of 848. The crystals appear elongated and agglomeration is evident.

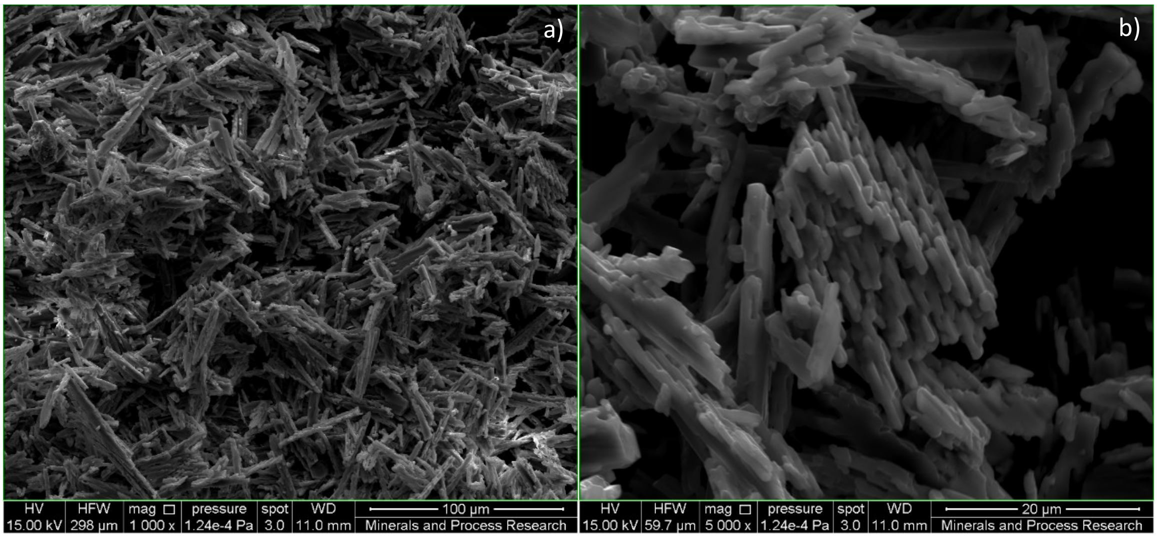

Figure 6.4.1: SEM photographs of Test 89 (T = 40°C, Re = 848) crystals. Test conditions are in Table 4.4.1.

The elongated shape in Figure 6.4.1 a) is probably related to the crystals moving in one direction through the plug flow reactor. It is therefore possible that the crystal growth process occurs as suggested in Chapter 3, Section 3.2.2. The crystal size distribution in Figure 6.4.2 a) indicates bimodal behaviour. The CSD further indicates that particle size by volume fraction at 40°C is insensitive to Reynolds number with an average L_{43} size of 23µm ±3.6µm (99 per cent confidence interval) (refer to the data in Table 6.4.1). The same conclusion was drawn from the L_{43} versus Reynolds number plots in Section 6.3, Figures 6.3.5 and 6.3.6.

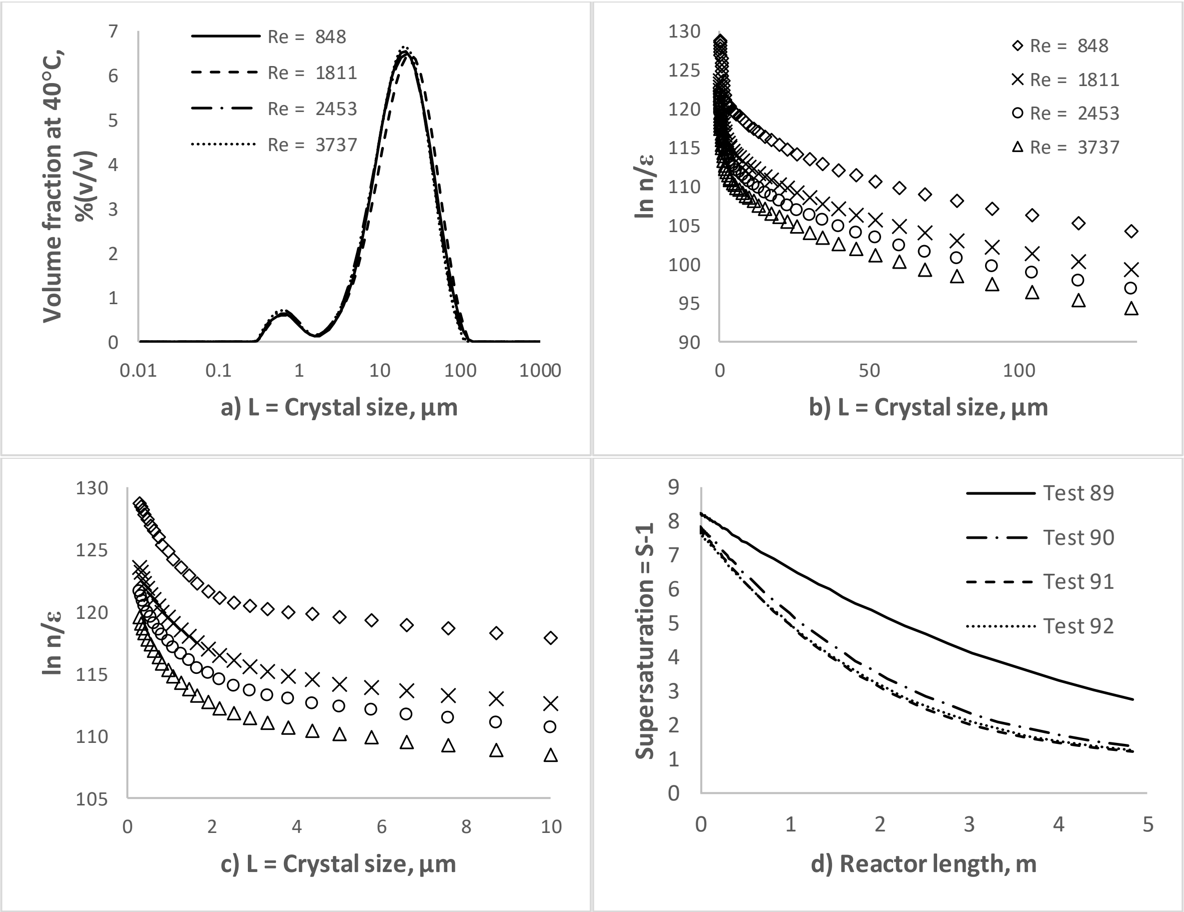

Figure 6.4.2: Size distributions at 40°C and varying Reynolds number (Test 89 to 92 in Table 4.4.1) for a) crystal volume per cent size distribution, b) population density size distribution, c) zoomed in population density size distribution with $L \in [0, 10]$ and d) supersaturation profile

The mixed cumulative lognormal distribution represents the measured cumulative volume per cent distributions of the data in Figure 6.4.2 a) as indicated by the respective R^2 values (>0.99 for all the data fits). Therefore, the volume density distribution of each test is fully described by the lognormal location and spread parameters in Table 6.4.1 within the measured size range. The scaled third moment of the population balance in Equation (3.2.20) combined with the lognormal distribution was used to estimate the scaled population density plots in Figures 6.4.2 b) and c) by the method given in the Appendix, Section 10.3.

Table 6.4.1: Non-linear least squares mixed lognormal parameter estimation results, L_{43} size and scaled third moment at the reactor outlet (Test 89 – 92, Table 4.4.1), T = 40°C

	Test 89	***Test 90***	***Test 91***	***Test 92***
Parameter	***Re = 848*** $S\|_{x=0}$ **= 9.1**	***Re = 1811*** $S\|_{x=0}$ **= 8.7**	***Re = 2453*** $S\|_{x=0}$ **= 8.6**	***Re = 3737*** $S\|_{x=0}$ **= 8.4**
m_1	-0.251	0.809	0.387	0.430
m_2	2.902	3.039	2.902	2.901
s_1	0.708	1.390	1.226	1.275
s_2	0.770	0.740	0.742	0.723
x_1	0.058	0.112	0.099	0.103
R^2	0.9980	0.9979	0.9980	0.9979
L_{43}, μm	23	25	22	22
$M'_3 = M_3/\varepsilon$	4.22E+55	2.46E+53	3.13E+52	3.48E+51

The absolute position of the population density versus size curve on the y-axis is dependent on the moment scale factor that was introduced during data fitting in Section 6.2 through the parameters A_n and A_{ag}. The scale factor is a constant for all the PFR experiments, therefore the relative positions are an indication of relative nucleation rates. The logarithm of population density versus size curves in Figure 6.4.2 shows an overall convex shape and is indicative of agglomeration as described by Myerson (2002). This finding supports agglomeration as a mechanism driving particle size alongside growth through interfacial attachment. The relative separation between the population density curves in Figure 6.4.2 b) and c) is sensitive to Reynolds number and saturation. The supersaturation profiles in Figure 6.4.2 d) show that profiles for Tests 90 to 92 are in closer proximity to one another compared to the profile of Test 89. From Figure 6.4.2 and the data Table 6.4.1, the separation in population density for Tests 90 to 92 is therefore predominantly caused by Reynolds number whereby increased Reynolds number shifts the population density downward on the y-axis.

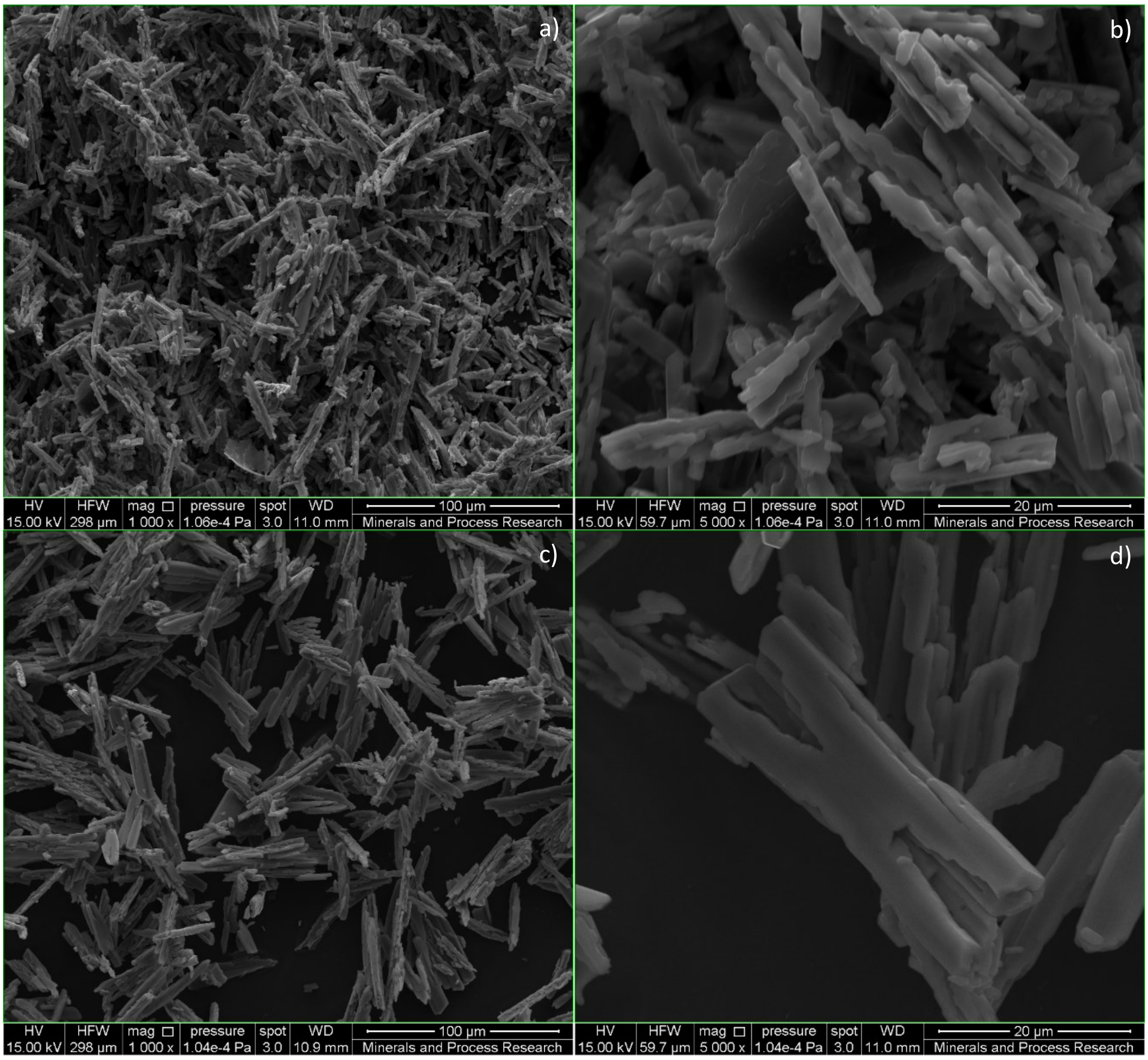

Figure 6.4.3: SEM photographs of Test 94 (T = 50°C, Re = 2078) crystals are shown in a) and b), and crystals from Test 96 (T = 50°C, Re = 4289) are shown in c) and d). Test conditions given in Table 4.4.1.

In contrast, higher supersaturation shifts the population density upwards on the y-axis when comparing the data between Test 89 and 90. The data here would therefore suggest that an increase in Reynolds number attenuates nucleation rate whereas an increase in supersaturation amplifies nucleation rate. The effect of supersaturation conforms to the classic power law relationship between supersaturation and nucleation rate as described in Jones (2002) and Myerson (2002). The supersaturation exponent for growth rate α in Equation (3.2.24) converged to 1.13 and the population density at size zero supersaturation exponent β in Equation (3.2.23) converged to 0.51, as shown in Table 6.2.3. Thus, the nucleation rate $(n(0,x)G)$ is proportional to supersaturation to a power $\gamma = \alpha + \beta$ = 1.64, further validating the observation of upward shift in population density as saturation is increased.

The SEM photographs for the experiments at 50°C are presented in Figure 6.4.3. The crystal size distributions of the crystals are shown in Figure 6.4.4. The crystal size distribution by volume appears bimodal and insensitive to changes in Reynolds number with an average L_{43} size of 22μm ±5.0μm (99 per cent confidence interval) (see Table 6.4.2).

A comparison between Figures 6.4.3 a) and c) does not reveal a significant difference in crystal morphology as the crystal shapes appear to be similar, albeit with a difference in extent of agglomeration. Comparing Figure 6.4.1 to Figure 6.4.3 gives the same result, indicating that temperature within the defined sample space does not affect crystal morphology significantly. Likewise, morphology appears to be insensitive to Reynolds number, aside from some anomalies observed in terms of twinned crystals. Figure 6.4.3 d) shows a classic twinned crystal as described by Jones (2002). This suggests that twinning is a potential agglomeration mechanism.

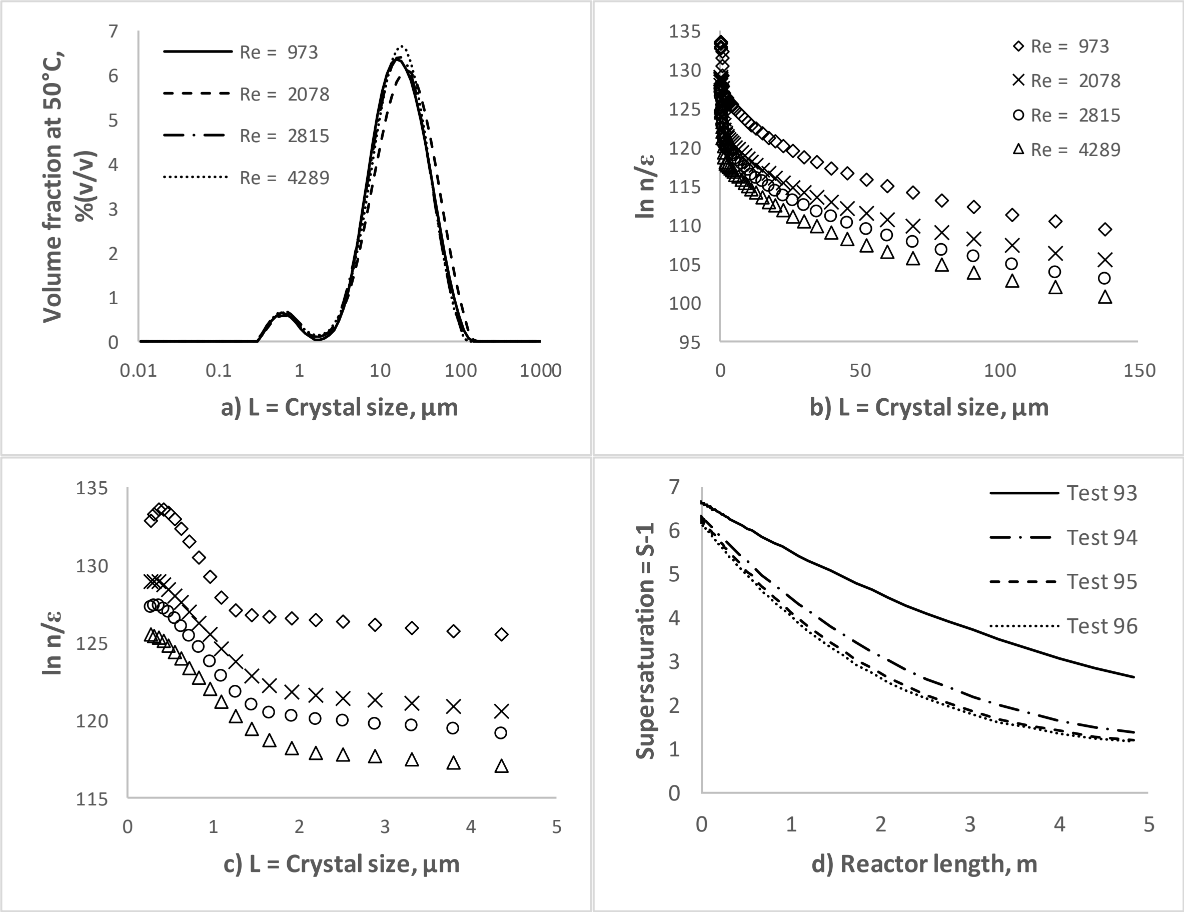

Figure 6.4.4: Size distributions at 50°C and varying Reynolds number (Test 93 to 96 in Table 4.4.1) for a) crystal volume % size distribution, b) population density size distribution, c) zoomed in population density size distribution with L ∈ [0, 5] and d) supersaturation profile

The shape of the population density versus size curves in Figures 6.4.4 b) and c) corresponds to the shape of the plots in Figures 6.4.2 b) and c). Agglomeration is therefore a prominent feature of this system as is demonstrated by the SEM photograph in Figure 6.4.3. At elevated temperature there appears to be a kink in the population density curve within the size range less than 1μm in Figure 6.4.4 c). This is different from the shape in Figure 6.4.2 c) within the same size range. In halide precipitation studies, a similar kink in the population density curve is observed at submicron size range (Leubner, 2009). This observation may possibly be related to disruption or breakage of crystals. However, no clear evidence of fractured crystals is observed.

As with the data displayed in Figure 6.4.2 b) it is observed that Reynolds number and supersaturation affects the separation between population density curves in Figure 6.4.4. The data suggests that an increase in Reynolds number can shift the dominant saturation consumption mechanism from nucleation to most likely growth. The observed behaviour related to population density, supersaturation and Reynolds number for the crystals shown in Figures 6.4.1 and 6.4.3 persisted for all tests discussed in this section.

The volume crystal size distribution in Figure 6.4.4 a) appears bimodal and insensitive to changes in Reynolds number with an average L_{43} size over all Reynolds numbers of 28µm ±2.0µm (see Table 6.4.3). The L_{43} size range in Table 6.4.3 is larger than observed in Figures 6.4.2 and 6.4.4 (Tables 6.4.1 and 6.4.2), emphasising that elevated temperature increases average crystal size.

Table 6.4.2: Non-linear least squares mixed lognormal parameter estimation results, L_{43} size and scaled third moment at the reactor outlet (Test 93 – 96, Table 4.4.1), T = 50°C

	Test 93	***Test 94***	***Test 95***	***Test 96***
Parameter	***Re = 973*** $S\|_{x=0}$ **= 7.3**	***Re = 2078*** $S\|_{x=0}$ **= 7.0**	***Re = 2815*** $S\|_{x=0}$ **= 6.9**	***Re = 4289*** $S\|_{x=0}$ **= 6.8**
m_1	-0.58	-0.44	-0.48	-0.42
m_2	2.79	2.94	2.78	2.81
s_1	0.297	0.429	0.390	0.462
s_2	0.797	0.828	0.785	0.763
x_1	0.039	0.046	0.051	0.053
R^2	0.9982	0.9980	0.9982	0.9981
L_{43}, µm	22	26	21	21
$M_3' = M_3/\varepsilon$	9.68E+57	9.67E+55	1.76E+55	2.45E+54

At elevated temperature, the supersaturation component in Equation (3.2.24) decreases due to the solubility product increasing as per Equation (3.1.9). The temperature effect on L_{43} therefore suggests that elevated temperature increases the growth rate through the temperature dependent rate constant K_g in Equation (3.2.24) such that the effect of decreased supersaturation is masked.

Figure 6.4.5 shows the same crystal shapes as seen in Figures 6.4.1 and 6.4.3. The crystal size distribution statistics and test conditions are summarised in Table 6.4.3. The crystal size distributions and supersaturation profile are shown in Figure 6.4.6. Crystal growth through agglomeration is illustrated in all SEM photographs supporting the agglomeration rate model in Equation (3.1.13). All the population density size curves in this section show a convex shape that roughly appear to consist of two linear lines with different slopes. This shape is representative of an MSMPR configuration with fines removal from the discharge as described by Mersmann (2001). This shape of the population density curve is also reported to imply back mixing that causes segregation (Myerson, 2002).

In the PFR configuration back mixing is not likely and one does not expect this design to segregate. The minimum Reynolds number (848) and fluid velocity (0.16m/s), combined with the maximum kinematic viscosity (1.29E-6m^2/s) for all PFR experiments, translate to a maximum laminar sublayer thickness or viscous wall length scale ($5\eta\sqrt{Re/8u^2}$) of ~0.41mm (Massey, 1970). When the sublayer thickness is substantially smaller than the pipe diameter (5mm) back mixing is unlikely. It is therefore concluded that the mechanism causing the convex shape of the population density curves is most likely agglomeration, as affirmed by SEM photographs of the crystals.

As pointed out in Chapter 2, growth from a screw dislocation that is limited by interfacial attachment kinetics is likely if the supersaturation exponent is between 1 and 2 (Myerson, 2002; Jones, 2002). The growth supersaturation exponent determined by data fitting in Section 6.2 was found to be 1.13. Crystal growth in the PFR configuration therefore appears to conform to BCF growth theory with interfacial attachment kinetics limiting the growth rate.

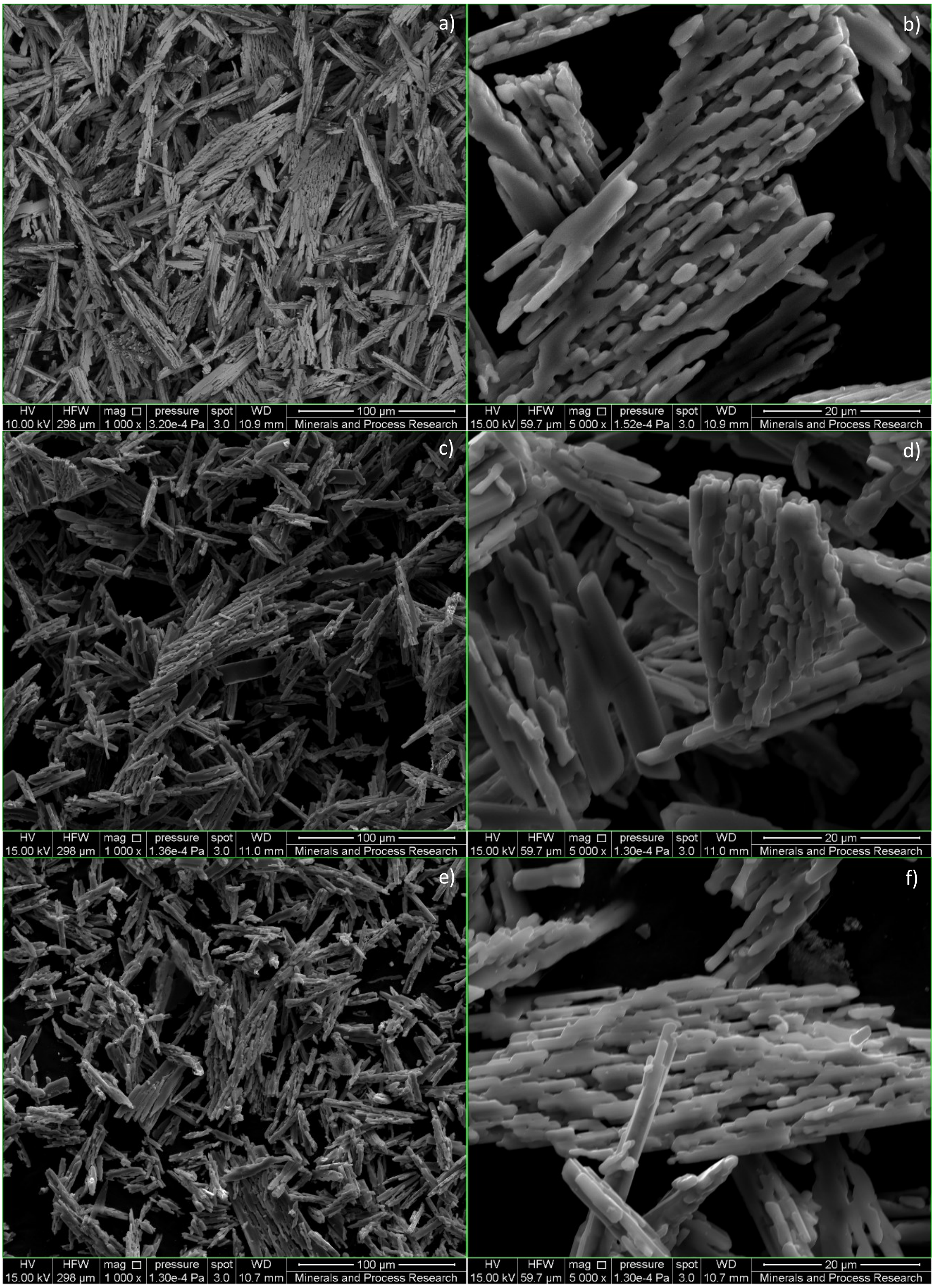

Figure 6.4.5: SEM photographs of Test 97 (T = 60°C, Re = 1107) crystals are in a) and b), crystals from Test 99 (T = 60°C, Re = 3204) are in c) and d), and crystals from Test 100 (T = 60°C, Re = 4881) are in e) and f). Test conditions are given in Table 4.4.1.

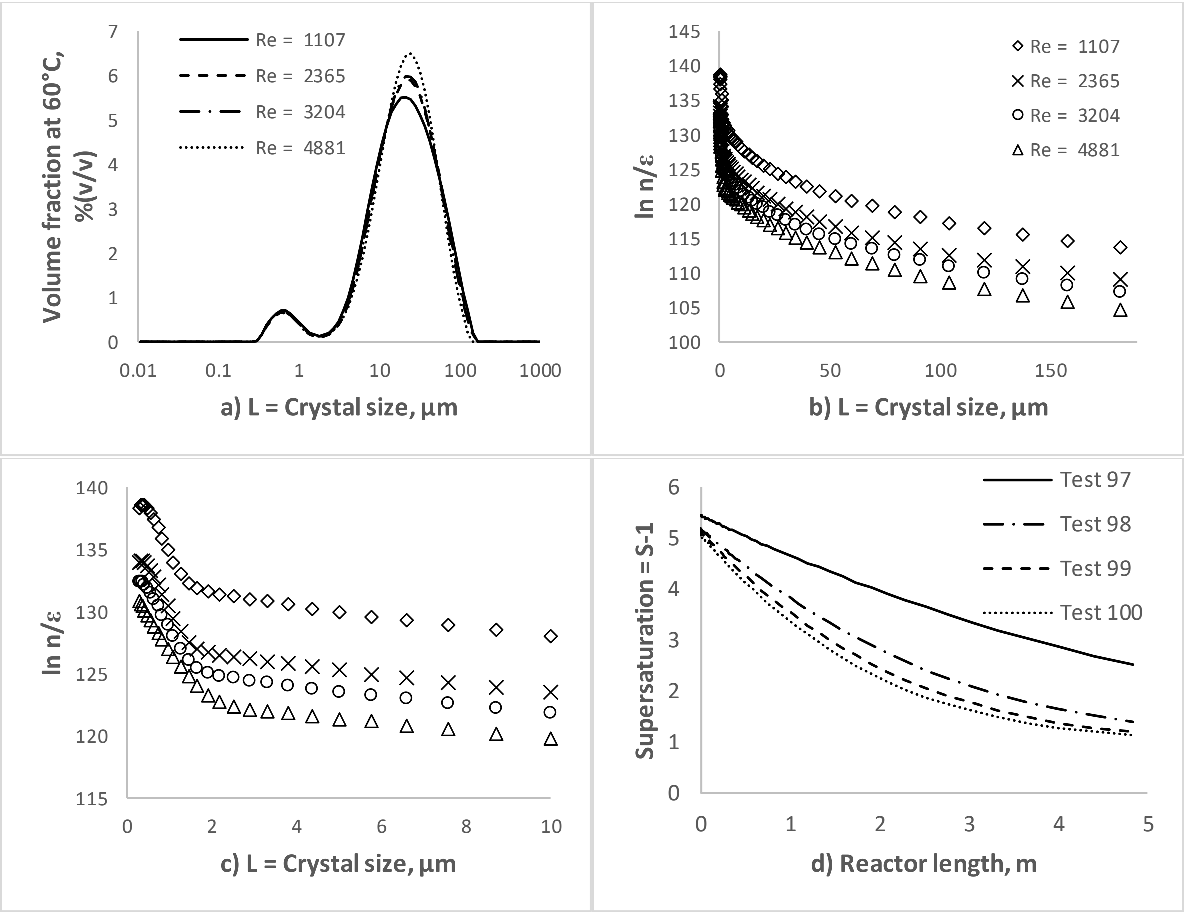

Figure 6.4.6: Size distributions at 60°C and varying Reynolds number (Tests 97 to 100 in Table 4.4.1) for a) crystal volume % size distribution, b) population density size distribution, c) zoomed in population density size distribution with L ∈ [0, 10] and d) supersaturation profile

The mass balance further shows that an increase in Reynolds number tends to drive the system to equilibrium within a fixed PFR length (Figure 6.3.7). Interpreted differently, higher Reynolds number dampens the mass transfer limitation imposed on a scale larger than the crystal boundary layer through either micro- or mesomixing. It is therefore deduced that at higher Reynolds number, saturation is preferentially consumed through crystal growth from screw dislocations and agglomeration as opposed to nucleation.

Table 6.4.3: Non-linear least squares mixed lognormal parameter estimation results, L_{43} size and scaled third moment at the reactor outlet (Test 97 – 100, Table 4.4.1), T = 60°C

	Test 97	***Test 98***	***Test 99***	***Test 100***
Parameter	***Re = 1107*** $S\vert_{x=0}$ **= 6.0**	***Re = 2365*** $S\vert_{x=0}$ **= 5.7**	***Re = 3204*** $S\vert_{x=0}$ **= 5.6**	***Re = 4881*** $S\vert_{x=0}$ **= 5.6**
m_1	-0.50	-0.49	-0.46	-0.36
m_2	2.99	3.02	3.01	3.03
s_1	0.364	0.387	0.418	0.565
s_2	0.896	0.849	0.837	0.777
x_1	0.050	0.048	0.052	0.058
R^2	0.9980	0.9980	0.9980	0.9979
L_{43}, μm	28	28	27	26
$M_3' = M_3/\varepsilon$	1.32E+60	1.39E+58	2.56E+57	3.51E+56

Furthermore, the population density curves here show that the number of crystals in the system is linked to the Reynolds number. Essentially, a more turbulent flow regime (high Reynolds number) translates to more crystal-

crystal collisions, thereby reducing the number of crystals in suspension through agglomeration. The two mechanisms, agglomeration and growth through interfacial attachment would therefore appear to simultaneously promote crystal enlargement. However, the dominant mechanism appears to be agglomeration based on the convex shape of the population density curves in Figures 6.4.2, 6.4.4 and 6.4.6.

To elaborate on the factors affecting the volume shape factor of the crystals in the system, the effect of saturation and Reynolds number on the third moment (crystal volume) is further investigated by multiple non-linear regression. The data presented in Tables 6.4.1 to 6.4.3 gave an empirical relationship between saturation, Reynolds number and the scaled third moment; the relationship is shown in Equation (6.4.1). The regression statistics are shown in Tables 6.4.4 and 6.4.5.

$$\begin{aligned} \ln M_3' &= 173.5 + 203exp(-0.423S|_{x=0}) + 7.3\ln Re \\ \therefore M_3' &= \frac{exp\big(173.5 + 203exp(-0.423S|_{x=0})\big)}{Re^{7.3}} \end{aligned} \qquad \textbf{(6.4.1)}$$

The R^2 for the data fit was 0.99 and the regression is significant by the F-test in Table 6.4.4. All the parameters in Table 6.4.5 are statistically significant by the t-test, therefore the empirical relationship is a reasonable model of the data (Reynolds number and saturation versus scaled third moment) presented in Tables 6.4.1 to 6.4.3.

Table 6.4.4: Regression analysis of variance (ANOVA) for the data from Tables 6.4.1 to 6.4.3 (Re and S VS M_3')

ANOVA parameter	*df*	*SS*	*MS*	*F*	*p-value*
SS (Regression)	3	1.60E+120	5.3E+119	579.79	0.000
SS (Residual)	8	3.27E+116	4.0835E+115		
SS (Total)	11	1.60E+120			

df = degrees of freedom, *SS* = squared sum of errors, *MS* = *SS*/*df*, *F* = *MS* (Regression)/*MS* (Residual), *p-value* = F-distribution evaluated at the calculated F value => probability that MS (regression) is equal to MS (residual). For details on multiple linear regression the reader is referred to Vining (1998).

Table 6.4.5: Parameters and hypothesis test results for the data from Tables 6.4.1 to 6.4.3 (Re and S VS M_3')

Parameter	*Value*	*SE*	*t Stat*	*p-value*	*L CL 95%*	*U CL 95%*
Intercept	173.5	4.38	39.7	0.000	163.4	183.6
$\ln Re$	-7.3	0.59	-12.4	0.000	-8.7	-5.9
$exp(-0.423S\|_{x=0})$	203.0	12.51	16.2	0.000	174.2	231.9

Note that the length of the reactor associated with the data in Tables 6.4.1 to 6.4.3 was 4.84m as given by the experimental method described in Section 4.4. Thus, Equation (6.4.1) is only valid at the mentioned reactor length. This point is relevant as it specifies the length that can be used in the relationship between conversion and Reynolds number in Equation (3.2.6). The purpose is to compare the scaled third moment, an indication of crystal volume, and the crystal concentration, calculated from conversion in Equation (3.2.6). Equation (6.4.2) presents the third moment identity to determine crystal concentration from the third moment as given in literature (Myerson, 2002). However, in this work the third moment is scaled as per the argument presented for Equation (6.2.3) in Section 6.2.

To determine the volume shape factor, first consider the form of Equation (6.4.2) rearranged to make the volume shape factor the argument. Based on this equation the volume shape factor reduces to a ratio of the crystal concentration and the scaled third moment. Bear in mind that the scale factor is not known.

$$\begin{aligned} C_c &= \frac{\rho_c}{MW_c}\int_0^\infty K_v n(L,x)L^3 dL = \frac{\rho_c K_v}{MW_c}M_3 = \frac{\rho_c K_v}{MW_c}\varepsilon M_3' \\ \therefore K_v &= \frac{C_c MW_c}{\rho_c \varepsilon M_3'} \end{aligned} \qquad \textbf{(6.4.2)}$$

Where C_c = Concentration of crystals in the reactor discharge [mol/dm^3]
ρ_c = Crystal density [g/dm^3]

K_v = Crystal volume shape factor (Actual crystal volume per characteristic length cubed per particle) [μm^3/#.μm^3]
MW_c = 428.81 = Crystal molecular weight [g/mol]

Now consider Figure 6.4.7 that shows the relationships between crystal concentration from Equation (3.2.6), the scaled third moment from Equation (6.4.1), and Reynolds number. As Reynolds number increases, the crystal concentration increases but the scaled third moment decreases. The volume shape factor is expected to be a constant if the crystal concentration and the scaled third moment profiles have parallel shapes, as Equation (6.4.2) suggests. Because of the non-parallel shapes between crystal concentration and scaled third moment, it is concluded that the volume shape factor will tend to increase with an increase in Reynolds number.

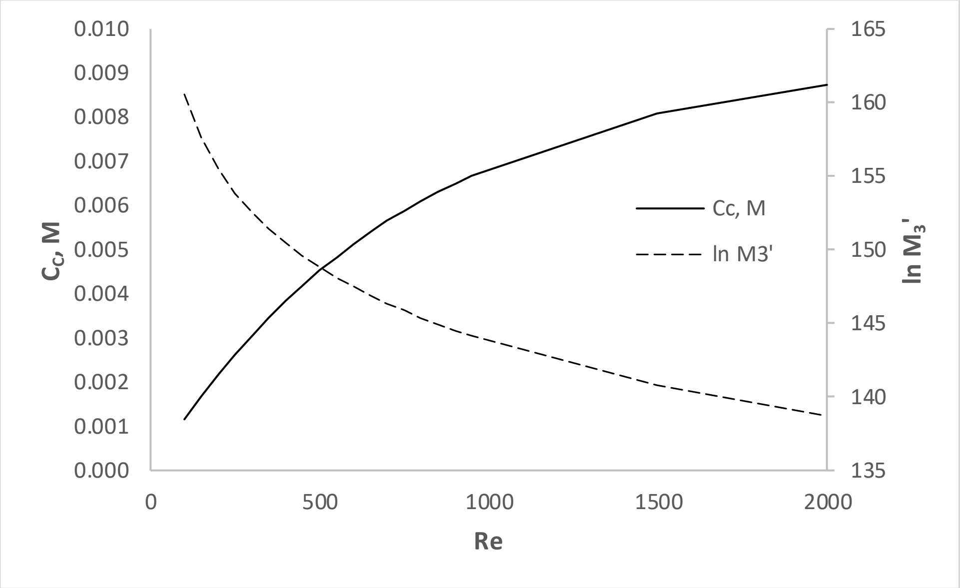

Figure 6.4.7: Modelled crystal concentration and scaled third moment as a function of Reynolds number (C_{A0} = 0.01M, C_{B0} = 0.13M, T = 70°C, $S|_{x=0}$=5.4)

It is difficult to confirm the inference regarding volume shape factor and Reynolds number with the SEM photographs in Figures 6.4.1, 6.4.3 and 6.4.5, as all these crystals were produced at varying initial saturation. However, there is some evidence to suggest that crystals become more solid as Reynolds number increases, especially evident in Figures 6.4.3 d) and 6.4.5 d). More tests are however required to confirm this inference.

7. CSTR MODEL REGRESSION: DIETHYLENETRIAMMONIUM HEXACHLORHODATE (III) PRECIPITATION

The CSTR mass balance utilises the equilibrium assumption discussed in Chapter 3, Section 3.1, to illustrate that the reaction bulk proceeds to equilibrium during the reactor transient. Each CSTR experiment starts off with 2dm^3 of unreacted ~0.25M hexachlororhodate (III) solution at a pre-defined experimental temperature. Hexachlororhodate (III) and protonated diethylenetriamine feed solutions are then injected into the reactor through separate dip-tubes, and at the same time the reactor level is controlled by withdrawing product solution in a separate dip-tube.

The aqueous concentration of the product stream is modelled by the equilibrium model proposed in Chapter 3, Section 3.1, using the operating conditions combined with the activity coefficient and solubility product parameters determined in Chapter 5. No data fitting was applied, aside from the independent activity coefficient and solubility product data fitting in Chapter 5.

To overcome the issue of defining saturation relative to a bulk that is at equilibrium, a transient unreactive concentration profile is used to define saturation for use in the nucleation and growth functions that are used in the population balance. Inherently this assumes that there is no mixing limitation on the micro- or meso scale as suggested by the mixing time constants discussion in Chapter 4, Section 4.2. This assumption decouples the mass balance from the population balance, therefore an inherent assumption is that crystal surface area does not appreciably alter the reaction rate within this system. Therefore, crystal growth is assumed to be limited by interfacial attachment kinetics only.

The volume average crystal size is used to fit nucleation and growth kinetic parameters directly through non-linear least squares as recommended by Jager et al. (1991). To test whether discharge segregation has an appreciable impact on the nucleation and growth kinetics, the fitted parameters are used within the segregation model as derived in Chapter 4, Section 4.3.4. The segregation model prediction of the reactor content volume average crystal size is then compared to the measured discharge volume average crystal size to ascertain if there is a statistical difference.

Lastly, crystal morphology is discussed based on SEM photographs of the crystal formed under the transient of experiment at 60°C. In addition, population density versus size plots are presented to affirm nucleation, growth and agglomeration mechanisms proposed in Chapter 3.

7.1. CSTR MASS BALANCE

The CSTR mass balance is solved by specifying the initial and operating conditions, given in Table 4.2.1. In addition, the activity coefficient and solubility product must be known to solve the mass balance. The activity coefficient and solubility product was determined in Chapter 5, Section 5.1, and is given by Equations (3.1.8) and (3.1.9).

The concentration profiles of Experiment 1 to 4 in Figure 7.1.1 shows that measured hexachlororhodate (III) concentration compares well to the predicted concentration by the transient equilibrium balance derived in Chapter 3, Section 3.1.1. The model fits the data with an overall R^2 value of 0.971, using only the solubility product and activity coefficient parameters combined with the flow into the reactor, reactor volume and reactor initial conditions. No data fitting routine was applied to generate the profiles in Figure 7.1.1.

Figure 7.1.2 shows the parity chart for the hexachlororhodate (III) concentration profiles in Figure 7.1.1. The minor scatter is attributed to experimental error related to sample dilution and analytical determination of the metal concentration through ICP-OES, as described in Chapter 4, Section 4.5.3.

The excellent model agreement further supports the notion that the reaction extent is equilibrium-controlled in this reactor configuration. The system saturation in Figure 7.1.3 a) is therefore specified from the unreactive concentration profiles depicted by C_A and C_B in Figure 7.1.1, and stems from Equations (3.1.2) and (3.1.3). The precipitated diethylenetriammonium hexachlororhodate (III) salt concentration is shown in Figure 7.1.3 b).

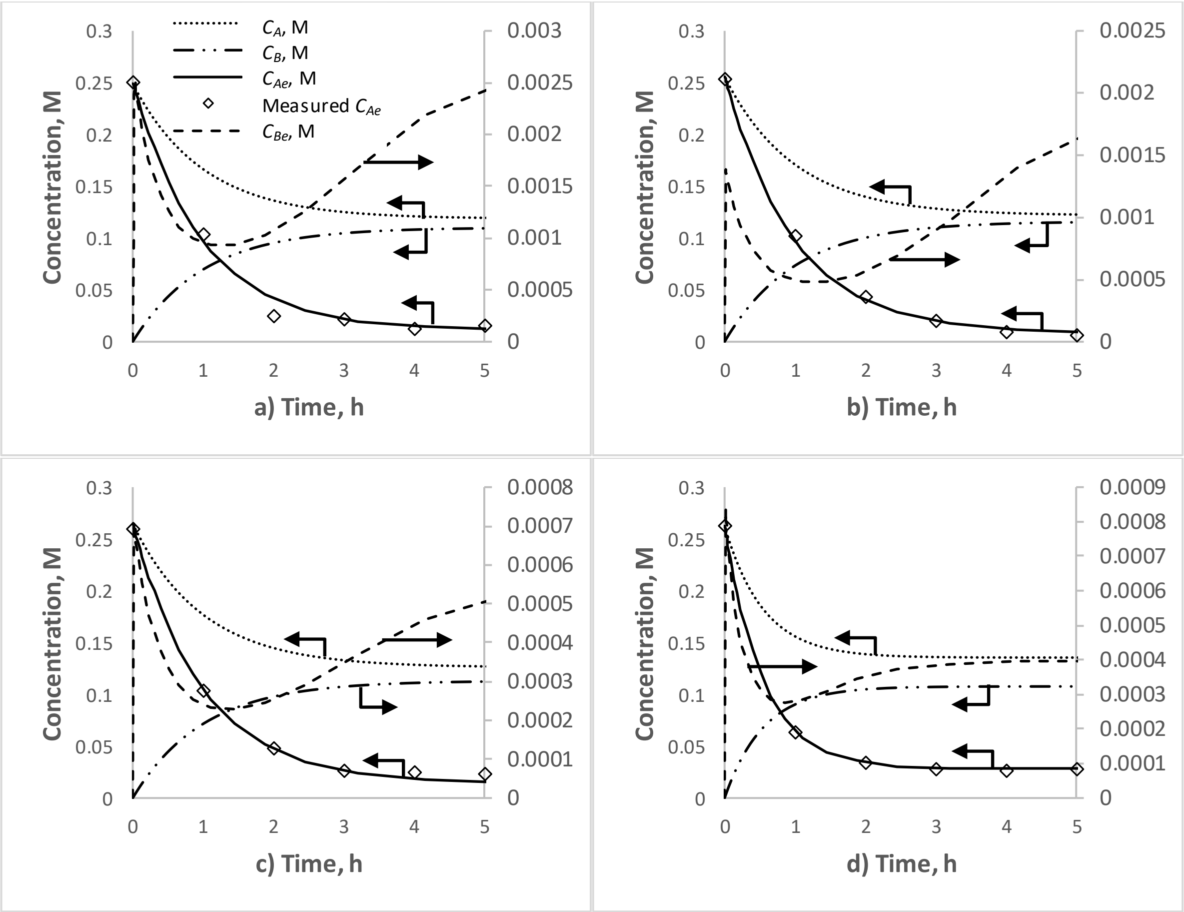

Figure 7.1.1: Unreactive and equilibrium concentration profiles for a) Experiment 1, b) Experiment 2, c) Experiment 3 and d) Experiment 4 (Subscripts A = $[RhCl_6]^{3-}$ and B = DETA.3HCl)

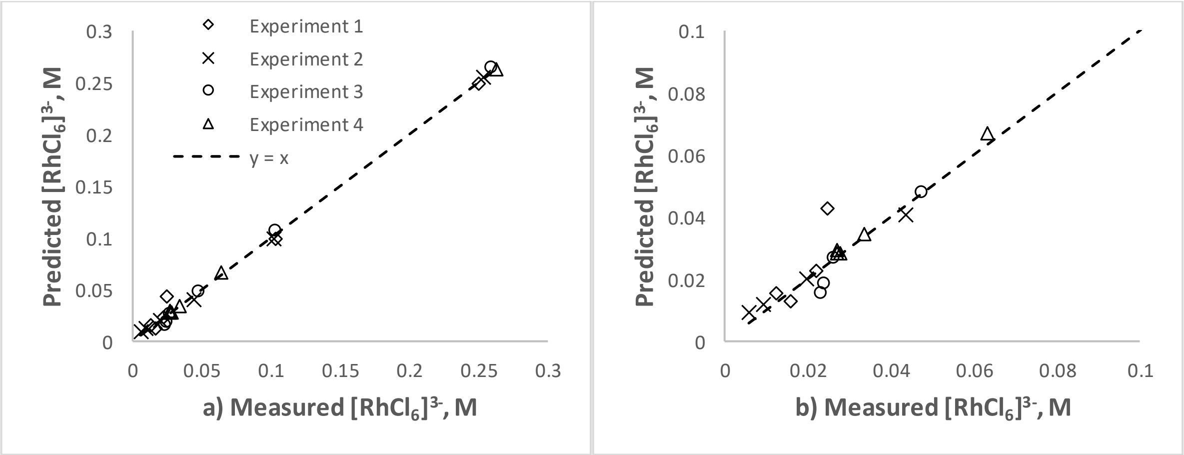

Figure 7.1.2: Parity chart of measured hexachlororhodate (III) concentration values versus predicted values a) normal scale and b) zoomed in scale

Figure 7.1.3 a) suggests that depending on the flow and concentration conditions between 5 to 10 hours of operating time is required for the concentration transient to diminish to achieve steady state in terms of saturation profiles, which is in agreement with the steady state definition for precipitation systems by Randolph & Larson (1971). It is further noted in Figure 7.1.3 a) that the steady state saturation is strongly affected by temperature as is expected from literature (Garside et al., 2002; Mersmann, 2001; Myerson, 2002).

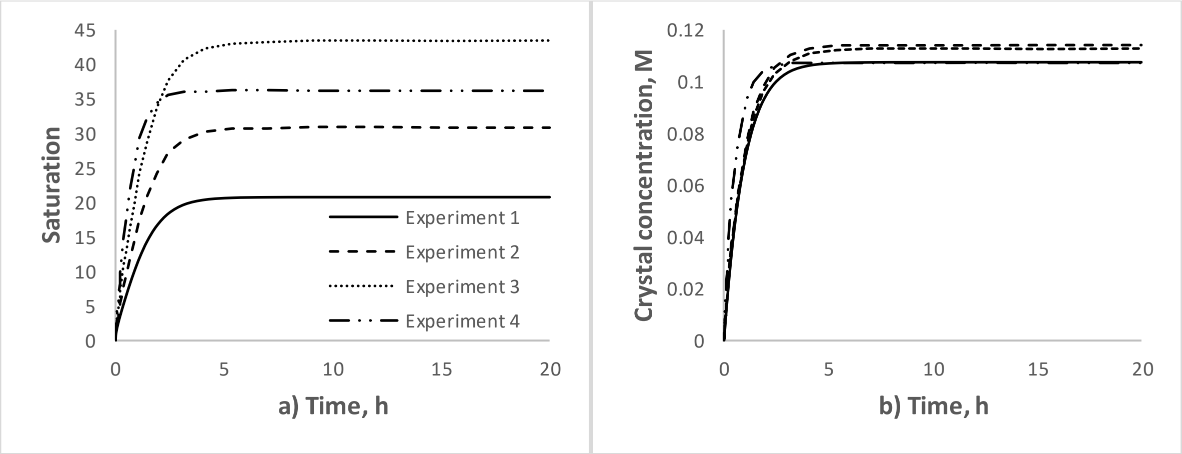

Figure 7.1.3: a) Saturation and b) crystal concentration profiles over 20h at variable temperature 100°C, 80°C, 60°C and 65°C (Experiment 1, 2, 3 and 4)

The effect of residence time on steady state saturation is not clear in Figure 7.1.3 a), aside from the observation that the profile reaches steady state sooner at short residence time (Experiment 4) as opposed to longer residence times (Experiments 1 to 3). A simulation of Experiment 4 conditions at a residence time of 1 hour (υ_A = 1.03dm^3/h and υ_B = 0.97dm^3/h) yields a steady state saturation of ~36 compared to ~36 at a residence time of 0.5h, indicating no effect of residence time on steady state saturation.

This is different from non-equilibrium systems as found by Zauner & Jones (2000). Given that this system proceeds to equilibrium, as demonstrated in Figure 7.1.1, it is a reasonable expectation that the residence time will have no effect on steady state concentrations. Likewise, residence time in a system that proceeds to equilibrium should have no effect on steady state saturation, as suggested above.

7.2. CSTR NUCLEATION AND GROWTH KINETIC PARAMETER ESTIMATION WITHOUT DISCHARGE SEGREGATION

The data fitted temperature dependence of K_g, K_{ag} and K_n from the PFR data in Chapter 6.2 was used as constants in the fitting routine that follows. The frequency constants, nucleation and growth supersaturation exponents were fitted. The parameter extraction method is based on the premise that crystal or molecular collision causing agglomeration, crystal growth and nucleation will be different between the configurations, although the activation energy required for each process will be a constant.

The reasoning for this assumption stems from the expectation that the local Reynolds number as well as the flow patterns between the two reactor configurations are different. Simulation through computational fluid dynamics and flow tracer experiments suggest that the flow patterns between a stirred vessel (CSTR) and direct injection (t-mixer, PFR) are markedly different (Falk & Villermaux, 1997; Javed et al., 2006; Ghanem et al., 2014; Lindenberg et al., 2008). Lindenberg et al. (2008) show linear path lines post a y-mixer mixing zone that has a similar design to the t-mixer in this work. In other words, the extrinsic properties of the molecule or crystal due to its environment are different in a CSTR relative to a PFR. As temperature determines solubility and internal molecular vibration, it is assumed to affect only intrinsic properties of either a molecule or a crystal. Temperature dependence of the various rate constants is therefore assumed to be a constant between reactor configurations.

The population density moments for the CSTR system, assuming no segregation, is used to data fit the growth and nucleation rate parameters in Equations (3.1.26) to (3.1.28). The model presented in Equation (3.1.23) and (2.1.25) was used to extract the growth parameters A_g, A_{ag}, A_n, α and β from the transient L_{43} size measurements. The modelled L_{43} size was calculated by dividing the third moment into the fourth. As stated above, the temperature-dependent parameters in the rate constants were assumed to be equal to the PFR parameter estimates B_g, B_{ag} and B_n.

Bear in mind that Chapter 4, Section 4.3.2, highlighted that the CSTR configuration has a possibility of inducing segregation between the reactor content and the discharge stream under the right conditions. Therefore, the option of segregation was explored mathematically in Chapter 4.3.3. The mathematical analysis suggests that in a system where segregation is present and the volume fraction size distribution is lognormal, one can expect the discharge stream moments to be decoupled from the reactor content moments through the segregation function $f(L)$.

This poses a dilemma as the discharge stream is supposed to represent the reactor content, and with an unrepresentative discharge stream it is not possible to measure the reactor content at a given time. For this reason, the growth and nucleation parameters are first estimated by assuming no segregation. The assumption that the growth and nucleation kinetics are not affected by segregation is tested later in Section 7.3.

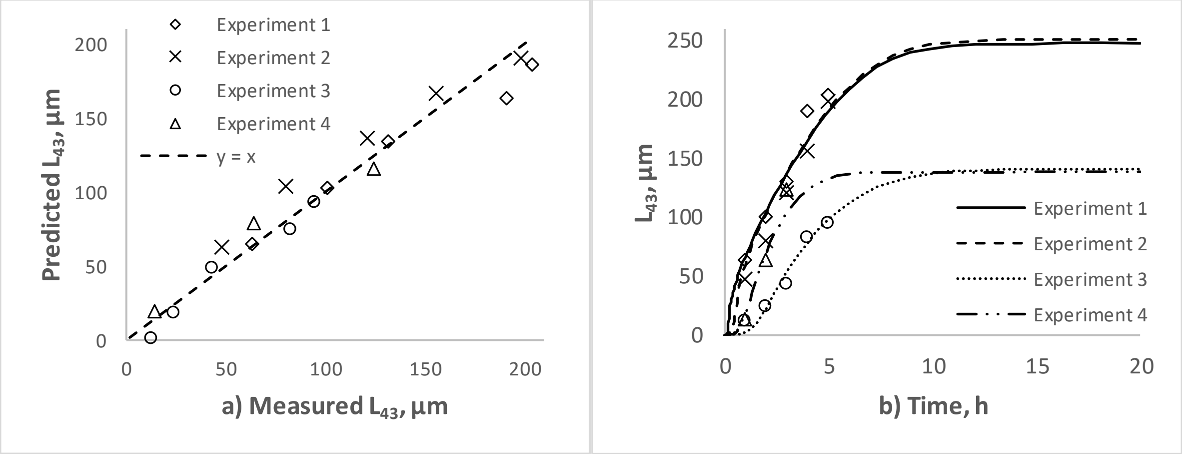

Figure 7.2.1: a) L_{43} size parity chart and b) L_{43} time profile with no segregation

Figure 7.2.1 a) shows a parity chart of the L_{43} size, assuming no segregation. Figure 7.2.1 b) shows the L_{43} size time profile where the markers are the measurements and the lines are the model. The overall R^2 value for the data in Figure 7.2.1 b) was 0.96, indicating a fair fit that is representative of the trend observed in the data. The model therefore accounts for 96 per cent of the variation in the L_{43} size.

Table 7.2.1 lists the raw data displayed in Figure 7.2.1. The SD row in Table 7.2.1 refers to the standard deviation of the data above it. This value is used in the objective function to weight each respective data set such that the units become dimensionless during the data fitting routine; and to weight experimental data relative to the measurement variance.

Table 7.2.1: Measured and modelled crystal L_{43} over time

Time, h	Experiment 1		Experiment 2		Experiment 3		Experiment 4	
	L_{43}, µm	Model L_{43}, µm	L_{43}, µm	Model L_{43}, µm	L_{43}, µm	Model L_{43}, µm	L_{43}, µm	Model L_{43}, µm
1	64	66	48	60	12	2	14	18
2	101	105	80	104	24	22	64	70
3	131	137	121	137	43	53	124	103
4	191	166	156	167	83	79		
5	204	189	198	190	95	97		
SD	60	-	60	-	36	-	55	-
R^2	0.934	-	0.920	-	0.959	-	0.919	-

Table 7.2.1 highlights that Experiment 4 data prediction is the least accurate with an R^2 of 0.919. The overall R^2 is 0.956, which indicates that the model cannot account for approximately 4 per cent of the variance. Experimental error is believed to be the cause of the unexplained variance combined with Experiment 4 that has the least number of data points due to insufficient crystals for Malvern sizing. Additional experimental error is

believed to be induced by small particle sizes that cause errors in terms of solids handling as well as reducing the chance of obtaining a representative sample when sampling the dry crystals.

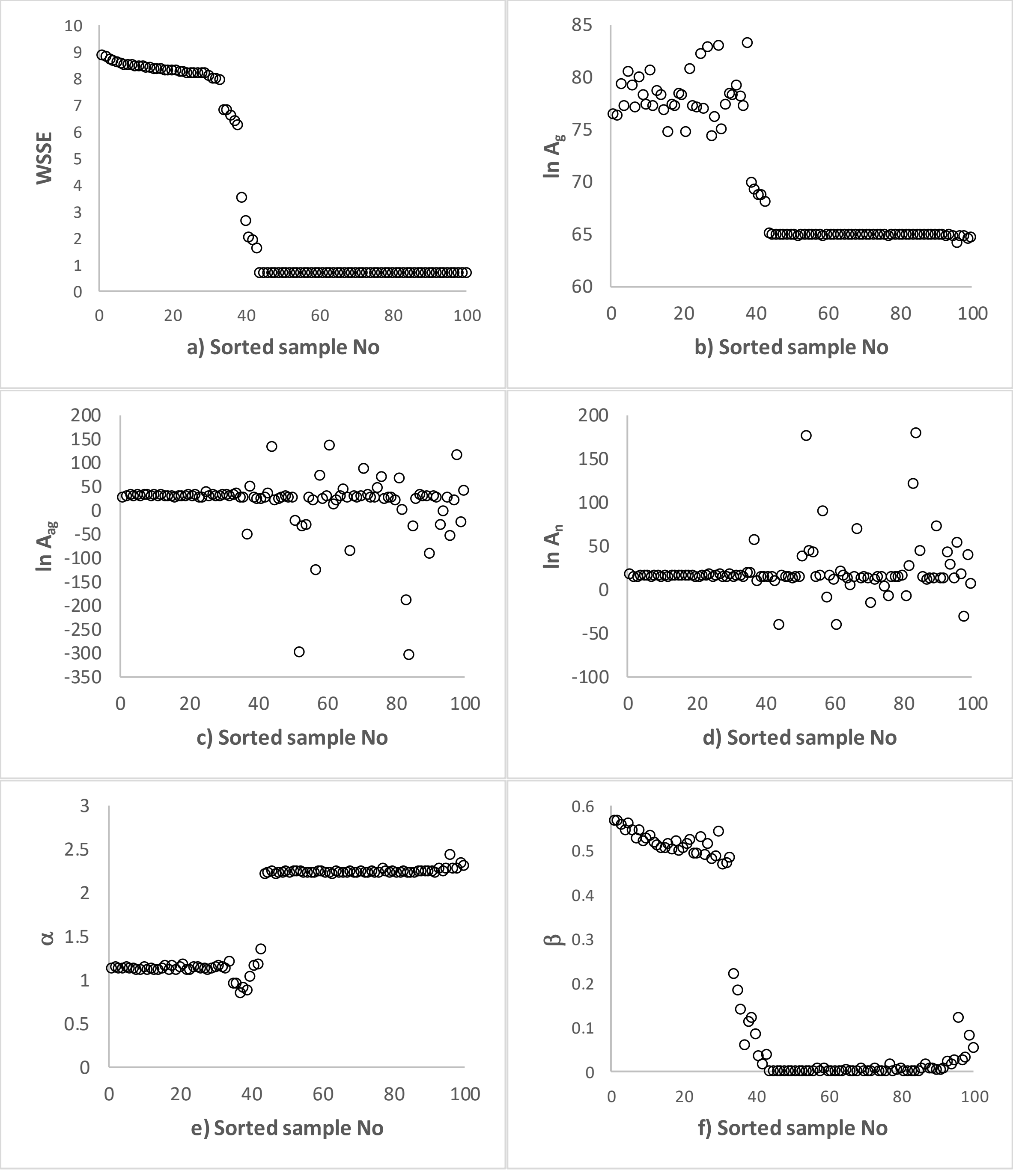

Figure 7.2.2: Monte Carlo data fitting routine results sorted in descending WSSE order a) WSSE b) ln A_g, c) ln A_{ag}, d) ln A_n, e) α and f) β

The model parameters were estimated using a simplex search routine in Matlab that is available as a standard function '*fminsearch*' (Lagarias et al., 1998). The objective function that was passed through '*fminsearch*' was the weighted sum of squared differences between the measured and modelled values. The objective function is given in Equation (7.2.1) that sums over the i^{th} measurement for the k^{th} experiment. This form of the objective function causes the data fitting routine to resolve the unknown parameters around the smallest size measurements, as it has the smallest standard deviation.

$$WSSE = \sum_{k=1}^{4} \sum_{i=1}^{5} \frac{\left(x_{i,measured} - x_{i,modelled}\right)^2}{SD_k^2} \qquad \textbf{(7.2.1)}$$

As mentioned earlier it is assumed that the activation energy terms in the CSTR rate constants are equivalent to the PFR activation energy terms in the respective rate constants K_g, K_{ag} and K_n. Therefore, the parameters B_g, B_{ag} and B_n for the CSTR data fitting routine are taken to be equal to the values in Table 6.2.3. The remaining parameters A_g, A_{ag}, A_n, α and β are fitted by the Monte Carlo method described in Chapter 6.2 using the respective parameter values in Table 6.2.3 as the initial parameter set distribution averages.

Of the 100 sets of initial conditions used in the Monte Carlo data fitting routine, the best fit associated with the lowest $WSSE$ in Figure 7.2.2 a) is presented in Table 7.2.2. Each Monte Carlo sample number in Figure 7.2.2 represents up to 1000 function evaluations and up to 1000 simplex iterations. The procedure is therefore computationally strenuous, with a total time of data fitting approaching almost 20h.

Figures 7.2.2 b) to f) show the path each fitted parameter followed along the path of descending $WSSE$. As with the PFR Monte Carlo data fitting routine in Chapter 6.2, the variation in converged parameter value as a function of sample number indicates that the converged parameter set is related to the initial parameter guesses. Of all the parameters, A_g appears to be most stable when the $WSSE$ approaches the minimum.

All the other parameters show scatter over the range where $WSSE$ approaches the minimum. It is possible that this observation is linked to the effect these variables have on system stiffness. Following from this argument, it would therefore seem likely that the parameter A_g does not affect the stiffness of the set of differential equations to the same degree as A_{ag}, A_n, α and β. This observation was not evident for the estimated parameters in the PFR configuration in Figures 6.2.2 a) to c), as all the parameters appeared to steady out as the $WSSE$ approached the minimum. The parameters representing the best fit are shown at sample number 100 in Figure 7.2.2, and are tabulated in Table 7.2.2 below.

Table 7.2.2: Best fit CSTR nucleation and growth parameters from Monte Carlo data fit

Parameter	$\ln A_g$	$\ln A_{ag}$	$\ln A_n$	α	β	$WSSE$
Best fit	64.70	41.69	6.35	2.31	0.05	0.68

It is appropriate to discuss Equation (3.1.29) to enable physical interpretation of the rate constants. In Equation (3.1.29) the product between K_g, K_n and supersaturation to the power $\alpha + \beta$ determine how many crystals are generated in the system per unit of time. The product between K_{ag}, K_n and supersaturation to the power $1 + \beta$ govern the number of crystals disappearing due to agglomeration.

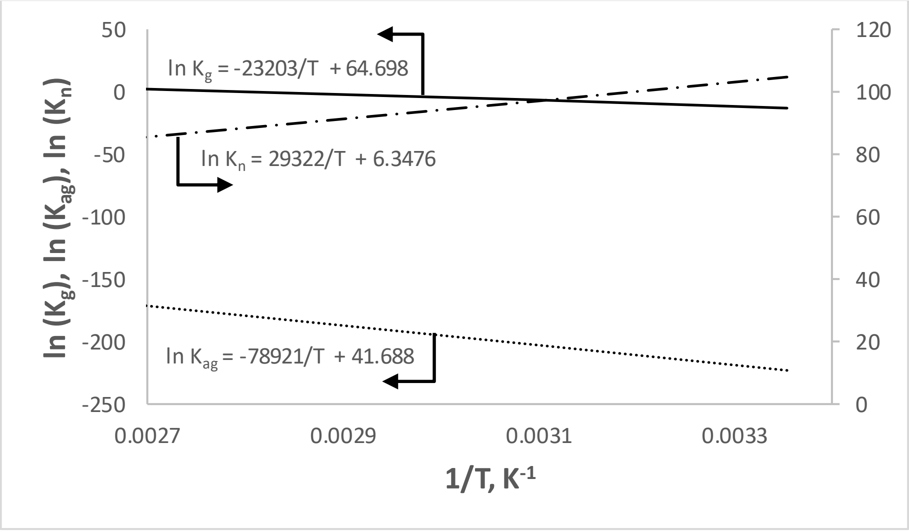

Figure 7.2.3: Growth and nucleation rate constants versus temperature

From Figure 7.2.3 it is evident that the temperature dependence of the product between the parameters K_g and K_n gives a positive inverse temperature dependence of 6119K, implying that as the temperature is increased, the number of crystals generated due to nucleation reduces. The product between K_{ag} and K_n gives a negative inverse temperature dependence of - 49599K, which implies that the rate at which the number of particles disappears is due to agglomeration increases as temperature is increased.

Furthermore, the nucleation rate constant represented by K_n/K_g suggests that nucleation is an endothermic process with an activation energy $\left(E_n + E_g\right)/R = B_n + B_g$ of 6119K or 51kJ/mol. From the negative gradients of K_g and K_{ag} the growth and agglomeration processes are deemed exothermic, with activations energies E_g and E_{ag} of -193kJ/mol and -656kJ/mol respectively. Note that these activation energies were obtained from the PFR data fitting routine and were not fitted to the CSTR data set. The activation energy discussion above therefore applies to the PFR configuration as well. Given the good agreement between measured and predicted L_{43} sizes in Figure 7.2.1, it is deduced that the activation energies are universal between reactor configurations.

The PFR discussion regarding parameter scaling through data fitting also applies to the CSTR data fitting. To summarise, Equation (6.2.4) shows that the only parameters affected by scaling are A_n and A_{ag}; the other parameters are not affected by scaling. Bear in mind that it is not possible to determine the scaling constant as no moment was measured explicitly. However, this will only affect modelling if one is interested in the absolute value of the moments; relative comparison remains valid.

7.3. SEGREGATED CSTR DISCHARGE MODELLING

The segregation spread and all other nucleation and growth parameters must be specified to solve the segregated discharge model presented in Chapter 4, Section 4.3.4. Equation (4.3.31) suggests that the segregation spread b_s can be determined through transient L_{43} measurements of the discharge stream. To extract nucleation and growth kinetic parameters through non-linear data fitting of Equations (4.3.33) and (4.3.34) an accurate measurement of L_{43} or associated moments is required of the reactor content. Thus, for a system with segregation and no accurate measurement of reactor content one can only deduce the segregation spread parameter b_s.

The objective of the study is to determine the nucleation and growth kinetics. Under the segregation condition this is not possible unless a representative sample of the reactor content is also measured. Considering this dilemma, the fitted nucleation and growth parameters under the perfectly mixed CSTR assumption in Section 7.2 is used in the segregation model, and the spread parameter is determined through transient L_{43} measurements. The output of the segregation model is then used to deduce if significant error is made by the initial assumption that segregation is insignificant during the sampled transient stages of the experiments in Table 4.2.1.

Therefore, the objective of this section is to validate the assumption that the nucleation and growth kinetics can be derived from this system when segregation is deemed negligible. The assumption is tested against the discharge segregation model as presented in Equations (4.3.33) and (4.3.34), with growth and nucleation kinetics as determined in Section 7.2. Therefore, the null hypothesis is that there exists a difference between the L_{43} size of the reactor content and the discharge stream. The hypothesis is tested by comparison of the model output of the reactor content and the discharge L_{43} size.

Before continuing to the comparison, the segregation spread is estimated empirically as follows. For each experiment in Table 4.2.1 it was observed that L_{43} increased over time. The assumed relationship for L_{43} variation over time based on the measured trends is shown in Equation (7.3.1).

$$L_{43} = D_p[1 + exp(-K_{bs}t)] \qquad \textbf{(7.3.1)}$$

Where D_p = Diameter of the discharge pipe = 4000 [μm]
K_{bs} = L_{43} decay constant [1/h]
t = Time, h

For each experiment a decay constant, K_{bs}, was fitted through non-linear least squares. Equation (7.3.1) gives a reasonable data fit to the measured data as observed in Figure 7.3.1.

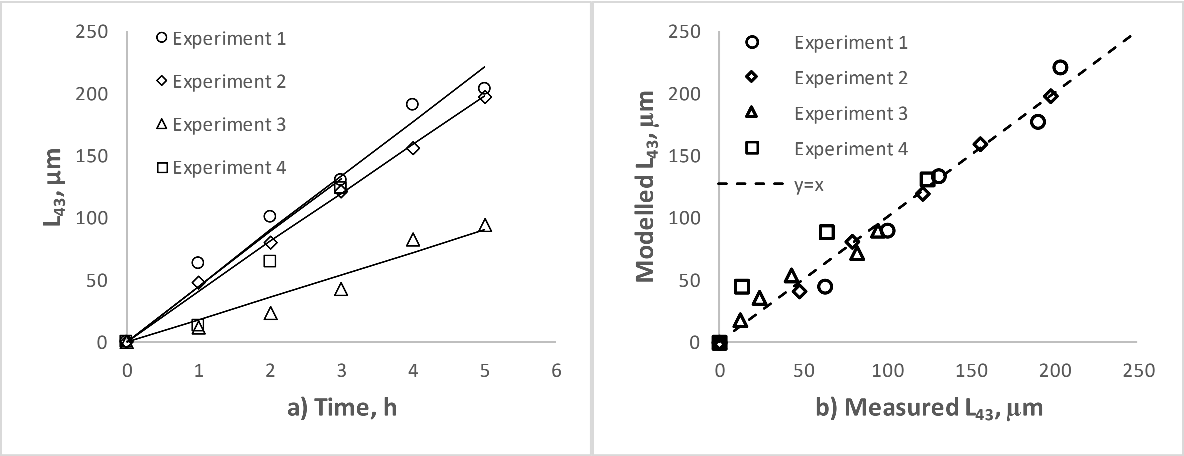

Figure 7.3.1: a) L_{43} time profile, markers represent measurements and the lines represent Equation (7.3.1); b) Parity chart of L_{43} measurements VS modelled data

The fitted K_{bs} values are given in Table 7.3.1 with the sum of squared errors and the coefficient of determination, R^2, per experiment. The R^2 values indicate a reasonable fit as is visually confirmed in Figure 7.3.1. It is crudely proposed that K_{bs} correlates to temperature and residence time.

Table 7.3.1: CSTR L_{43} data fit results

Experiment	*T*, °C	*τ*, h	K_{bs}, h^{-1}	*SSE*	R^2
1	100	1	0.0114	918.4	0.969
2	80	1	0.0101	66.7	0.997
3	60	1	0.0046	445.6	0.940
4	65	0.55	0.0111	1840.9	0.957

A potential correlation was found by trial and error, which is given in Equation (7.3.2) below, and is graphically represented in Figure 7.3.2.

$$K_{bs} = A_{bs}\left[1 + erf\left(\frac{T - m_{bs}\tau}{s_{bs}\tau}\right)\right] \tag{7.3.2}$$

Where A_{bs} = K_{bs} scale constant [1/h]
m_{bs} = K_{bs} location parameter [K/h]
s_{bs} = K_{bs} spread parameter [K/h]

Substituting K_{bs} in Equation (7.3.1) with the expression given by Equation (7.3.2), inserting the result into Equation (4.3.31) and re-arranging such that b_s is the argument, gives Equation (7.3.3).

$$b_s = \frac{1}{1000\left[1 - exp\left(-0.00563\left[1 + erf\left(\frac{T - 336\tau}{13\sqrt{2}\tau}\right)\right]t\right)\right]} \tag{7.3.3}$$

It is immediately apparent that b_s tends to infinity at time zero. The limit of the segregation function $f(L)$, as b_s tends to infinity and L tends to zero, is 1. This implies that the population density formed at size zero through nucleation has a 100 per cent chance of being removed through the outlet stream. Furthermore, the relationship in Equation (7.3.3) does not cause a violation of the initial and boundary conditions imposed on the population density, especially the limit, as size tends to infinity. The relationship indicates that the segregation spread becomes smaller over time (within the measured sample space) and eventually settles out at 1/1000µm^{-1}. This suggests that segregation becomes worse as time passes or as particles grow larger.

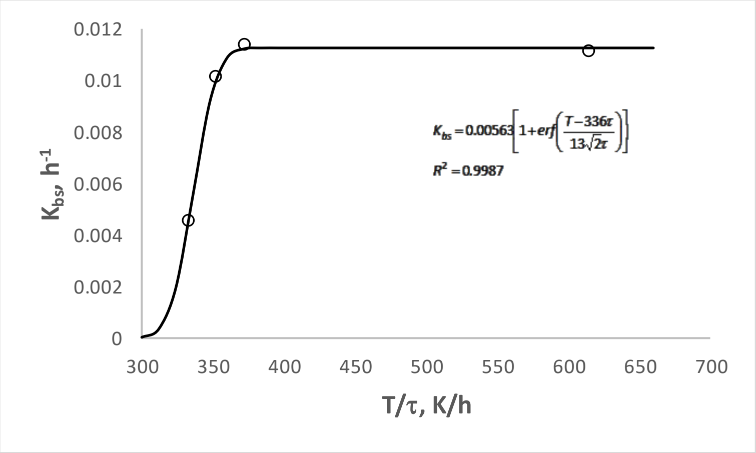

Figure 7.3.2: L_{43} decay constant correlation with residence time and temperature

With the segregation spread b_s defined, the moment balance with segregation is fully specified assuming that the growth and nucleation kinetics determined in Section 7.2 is a fair representation of the true kinetics. The initial and operating conditions of the CSTR are identical to the conditions listed in Table 4.2.1 for the various experiments combined with the initial condition for all moments of zero. To give a comprehensive comparison, the zeroth to the fourth moments are shown in Figures 7.3.3 to 7.3.7.

To gain insight into the shapes of the moments displayed the zeroth moment differential equation for the case of segregation is given in Equation (7.3.4). Equation (4.3.30) is combined with (4.3.33), (4.3.34), (3.2.23), (3.2.24), (3.2.25) and (7.3.1) to form the zeroth moment time differential equation shown in Equation (7.3.4).

$$\begin{aligned}\frac{dM_0}{dt} &= (G - G_a)n(0,t) - \frac{\psi_0}{\tau} = (G - G_a)n(0,t) - \frac{n(0,t)}{b_s\tau} = n(0,t)\left(G - G_a - \frac{L_{43}}{4\tau}\right) \\ &= K_n(S-1)^{\beta}\left(\begin{matrix} K_g(S-1)^{\alpha} - K_{ag}(S-1)M_0^2 \\ -\dfrac{D_p\left[1 - exp\left(-0.00563\left[1 + erf\left(\dfrac{T-336\tau}{13\sqrt{2}\tau}\right)\right]t\right)\right]}{4\tau}\end{matrix}\right)\end{aligned} \tag{7.3.4}$$

The zeroth moment of Experiments 1 and 2 in Figure 7.3.3 a) show that the zeroth moment increases up to a peak then steadily decays over time. The model output trend for Experiment 3 and 4 in Figure 7.3.3 a) indicates that the zeroth moment increases to a peak then rapidly decays to zero. These trends are explained by inspection of Equation (7.3.4) that is used to model the zeroth moment under segregating conditions.

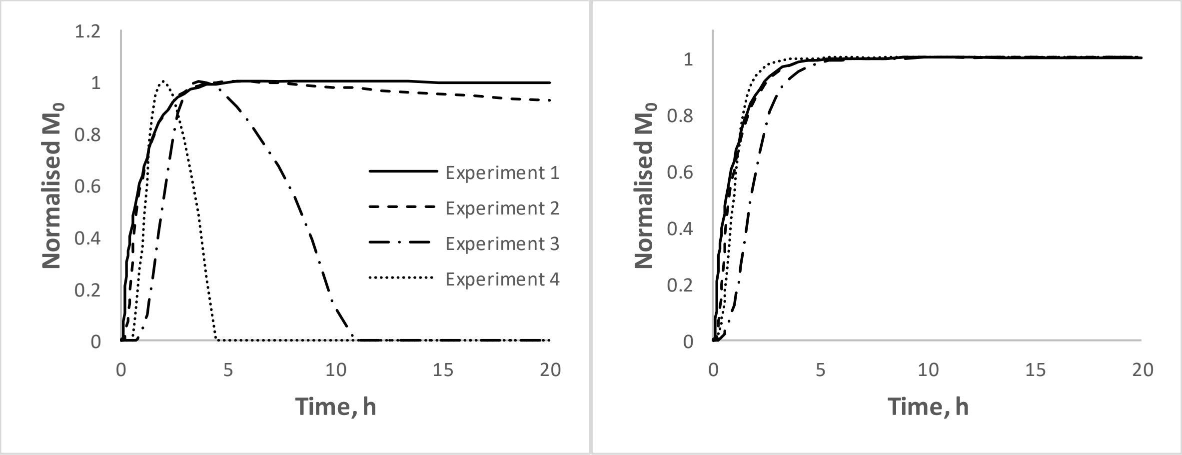

Figure 7.3.3: Normalised zeroth moment a) with segregation and b) without segregation for Experiment 1-4 in Table 6.1.1

First consider the case where the system reaches a steady saturation point and the segregating term (third term in brackets on the right-hand side of Equation (7.3.4)) has progressed to the point where it is equal to the limiting value of $4000/4\tau$ or $D_p/4\tau$. At this limiting point in time, Equation (7.3.4) can then be simplified to Equation (7.3.5).

$$\frac{dM_0}{dt} = K_1(K_2 - M_0^2)$$
$$with\ K_1 = K_n K_{ag}(S-1)^{1+\beta} \qquad \& \qquad K_2 = \frac{K_g(S-1)^\alpha - D_p/4\tau}{K_{ag}(S-1)} = \frac{G - D_p/4\tau}{K_{ag}(S-1)} \tag{7.3.5}$$

The ODE in Equation (7.3.5) has a solution in the real domain provided K_2 is positive, thus $G > D_p/4\tau$. For the case where $G < D_p/4\tau$ the ODE has a solution in the imaginary plane that has no physical interpretation, aside from the conclusion that segregation will not occur under these circumstances.

Physically this provides a constraint in terms of when a precipitation system, starting with no crystals, will segregate given the crystal growth rate, CSTR discharge pipe diameter and the residence time. Therefore, if $G < D_p/4\tau$ then the particles in the system are not likely to segregate. The analytic solution of Equation (7.3.5) given an initial condition of M_{0i} is given in Equation (7.3.6).

$$M_0 = \sqrt{K_2}\frac{M_{0i} + \sqrt{K_2} + \left(M_{0i} - \sqrt{K_2}\right)exp\left(-K_1\sqrt{K_2}t\right)}{M_{0i} + \sqrt{K_2} - \left(M_{0i} - \sqrt{K_2}\right)exp\left(-K_1\sqrt{K_2}t\right)} \tag{7.3.6}$$

As time increases to infinity in Equation (7.3.6) M_0 approaches the limit of $\sqrt{K_2}$. The exponential term in Equation (7.3.6) shows that the rate of this process under the conditions described above is governed by the product of K_1 and $\sqrt{K_2}$. Furthermore if K_2 is equal to M_{0i}^2 then M_0 remains constant at M_{0i} for all time. The zeroth moment M_0 increases over time until it reaches $\sqrt{K_2}$ if $K_2 > M_{0i}^2$. Likewise, if $K_2 < M_{0i}^2$ then M_0 decreases over time until it reaches $\sqrt{K_2}$.

From the discussion above it is noted that the zeroth moment of a precipitation system with segregation in the discharge, after saturation has stabilised, can increase or decrease over time and then approach a constant value. The numeric solutions in Figure 7.3.3 a) shows that Experiment 1 and 2 are likely to represent the case where $\sqrt{K_2}$ is less than the peak zeroth moment as the data tends to decrease over time after reaching a peak.

Note that the decay of the zeroth moment over time at constant saturation in Figure 7.3.3 a) for Experiment 1 and 2 is representative of agglomeration reducing the number of particles in the system. When agglomeration dominates, the denominator in K_2 is >> than the numerator, or $K_{ag}(S-1) \gg K_g(S-1)^\alpha - 1000/\tau$. The rapid decay of the zeroth moment for Experiment 3 and 4 in Figure 7.3.3 a) is because of the growth rate that is smaller than the pipe diameter divided by the residence time, $G < D_p/4\tau$, implying that segregation is not likely for Experiment 3 and 4.

Numerically this condition causes K_2 in Equation (7.3.5) to be negative, which causes the zeroth moment to decay to zero. Note that the numeric solution of the moments is capped at zero, therefore a numeric solution will always be equal to or greater than zero. Figure 7.3.3 b) shows that when segregation is not present, the zeroth moment increases up to a peak value and then stabilises at steady state. Further comparisons ignore Experiments 3 and 4 for the case of segregation as the zeroth moment for these experiments suggests that segregation was not likely.

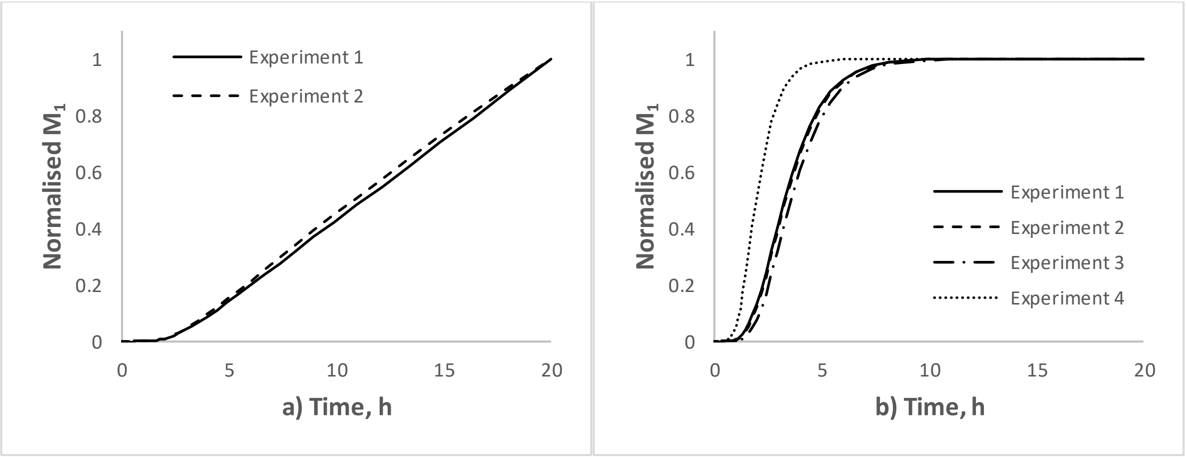

Figure 7.3.4: Normalised first moment a) with segregation for Experiment 1-2 and b) without segregation for Experiment 1-4

Figure 7.3.4 shows the scaled first moment for both systems with and without segregation. For the case of segregation in Figure 7.3.4 a) the trend suggests a diverging moment that is primarily related to particles that accumulate and agglomerate in the reactor as time passes. In Figure 7.3.4 b) a perfectly mixed system is illustrated where the first moment increases and then plateaus over time.

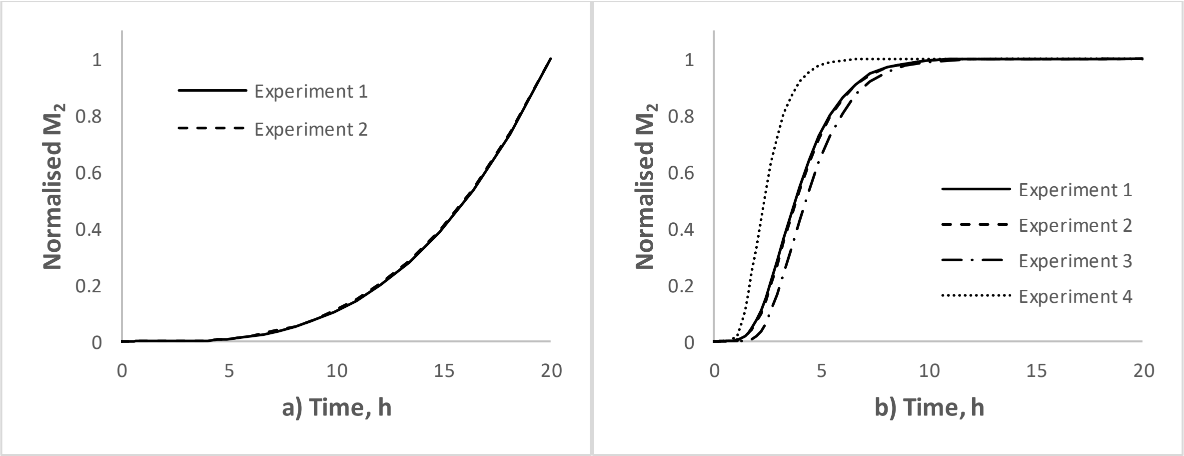

Figure 7.3.5: Normalised second moment a) with segregation for Experiment 1-2 and b) without segregation for Experiment 1-4

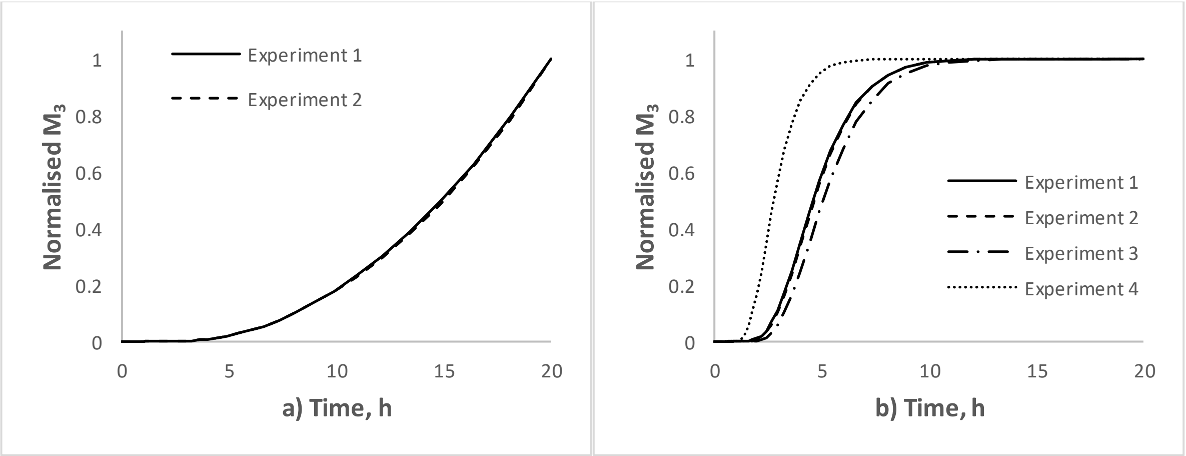

Figure 7.3.6: Normalised third moment a) with segregation for Experiment 1-2 and b) without segregation for Experiment 1-4

The second moment in Figure 7.3.5 shows the same trend as for the lower moments albeit slightly lagged over time. The lagging of higher moments relative to lower moments is due to the functionality of M_i to M_{i-1} and M_{i-2} as in the moment-generating function Equation (4.3.23). The third and fourth moments in Figures 7.3.6 and 7.3.7 show similar lagged trends to the lower moments. This is caused by the moment dependency on the lower moments as mentioned above.

Note that the absolute values of the moments are scaled due to the scaling introduced through data fitting as discussed in Chapter 6.2. The scaled moment value in descending order is $M_4 > M_3 > M_2 > M_1 > M_0$ therefore M_4 numerically has the largest value and M_0 the smallest value.

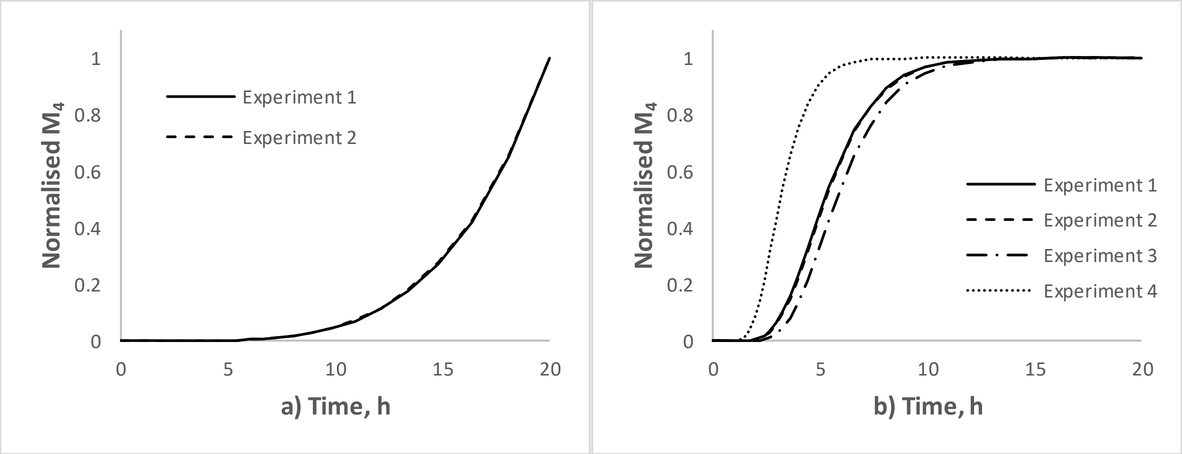

Figure 7.3.7: Normalised fourth moment a) with segregation for Experiment 1-2 and b) without segregation for Experiment 1-4

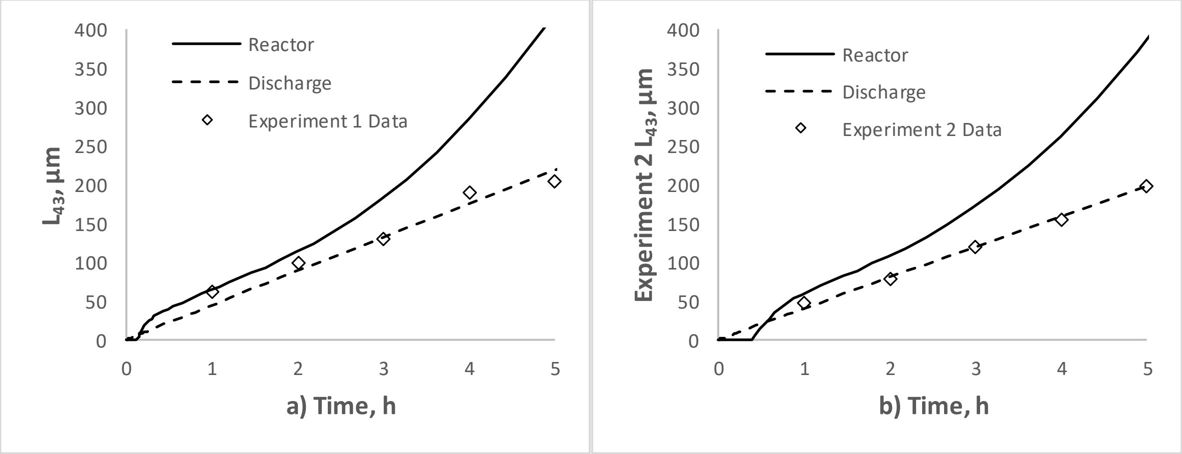

Figure 7.3.8: Reactor and discharge stream L_{43} size with segregation a) Experiment 1 and b) Experiment 2

Figure 7.3.8 shows the L_{43} reactor content and discharge comparison for the system with segregation. Graphically it appears as if the reactor content L_{43} size diverges from the discharge values. In Table 7.3.2 the statistical significance of the separation in Figure 7.3.8 is tested by the two-tailed paired t-test at the various sample times.

From Table 7.3.2 it is noted that the p-values are greater than the typical significance cut-off for hypothesis tests at 0.05. This observation suggests no detectable difference between the discharge and the reactor content size distribution at the sample times for Experiments 1 and 2. Thus, from a statistical view it cannot be stated with absolute certainty that the reactor content and discharge L_{43} sizes are identical.

The finding is not conclusive as one cannot say with certainty that segregation is negligible due to the p-values being marginally greater than 0.05. However, it does provide evidence to suggest that the error associated with the growth and nucleation kinetics under the ideal mixing assumption for the experiments listed in Table 4.2.1 is small.

Table 7.3.2: Comparison of modelled reactor content and discharge stream L_{43} size with segregation

	Experiment 1		Experiment 2	
Time, h	Discharge L_{43}, µm	Reactor L_{43}, µm	Discharge L_{43}, µm	Reactor L_{43}, µm
1	44	64	40	59
2	88	113	80	108
3	132	181	119	170
4	176	284	159	263
5	216	412	196	378
p-value		0.074		0.065

7.4. CSTR TRANSIENT CRYSTAL MORPHOLOGY

In this section the crystal morphology and crystal size distributions at hourly intervals are shown to illustrate how the crystal shapes and size distributions change over time during the transient stages in the CSTR configuration. The SEM photographs represent crystals formed under the precipitation conditions described by Experiment 3 in Table 4.2.1.

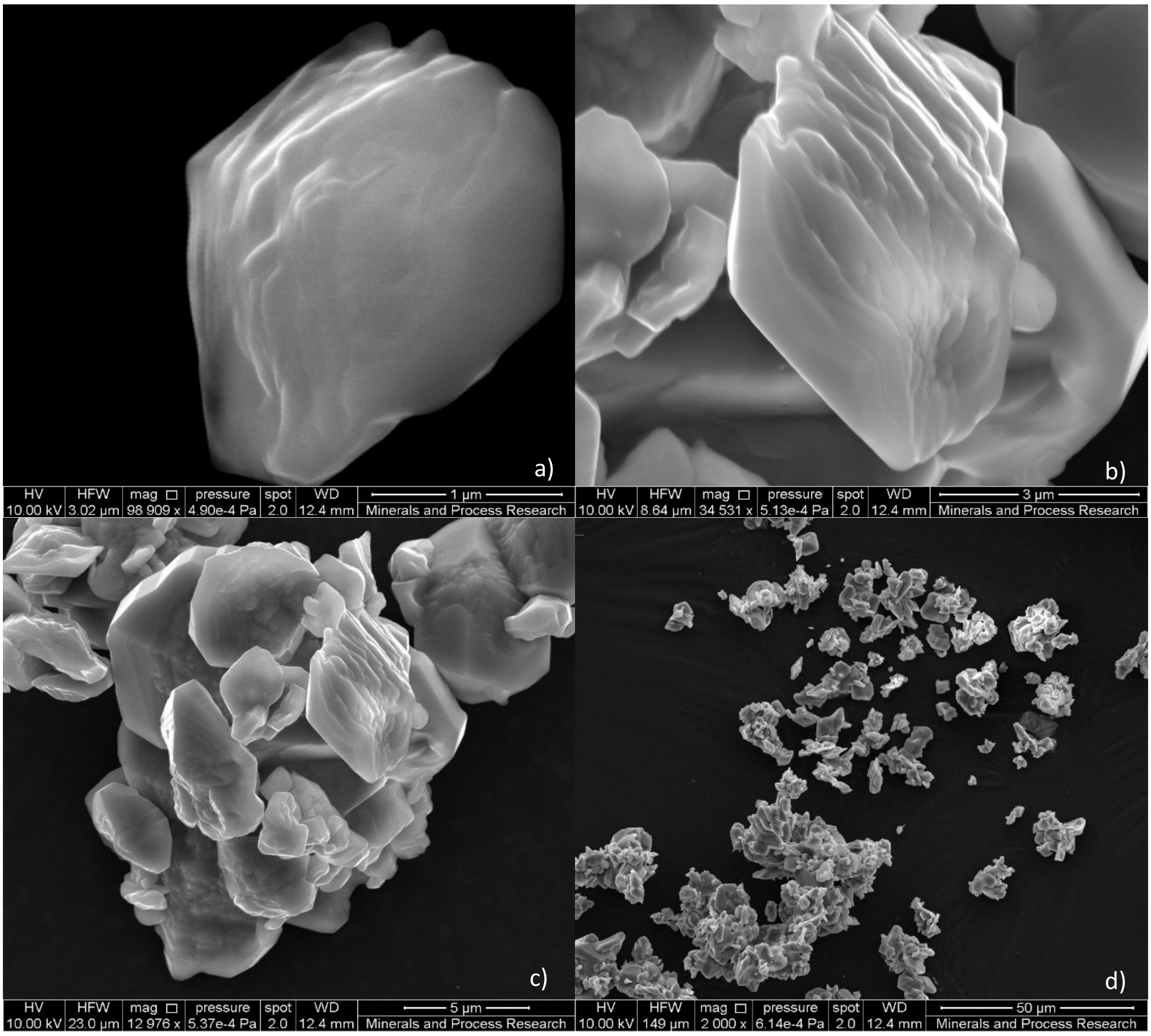

Figure 7.4.1: a) to d) SEM photographs (scales ranging from 1, 3, 5 and 50µm) of diethylenetriammonium hexachlororhodate crystals after 1 hour. Experimental conditions described by Experiment 3 in Table 4.2.1

After 1 hour of precipitation the crystals have grown to an L_{43} size of 12µm and are shown in Figure 7.4.1. Figure 7.4.1 a) shows a single crystal that appears to have a layered structure that is to an extent square planar. Figure 7.4.1 b) shows a different crystal with similar features as observed in Figure 7.4.1 a). Figure 7.4.1 c) shows an agglomerate emphasising that agglomeration is present in this system. Some of the crystals in Figure 7.4.1 c) exhibit an octahedral shape. In Figure 7.4.1 d) several agglomerates are present with scattered single crystals providing some evidence to support the measured bimodal volume size distribution in Figure 7.4.2 a).

The population density versus size plot is constructed from the mixed lognormal parameters in Table 7.4.1, determined from the data in Figure 7.4.2 a) using the identity in Equation (10.3.2) (refer to Section 10.3 in the Appendix). The third moment in Equation (10.3.2) is obtained from the model output data for Experiment 3. The scaled third moment used in the calculation is given in Table 7.4.1 and is defined in Section 6.2 of Chapter 6. Only the parameters A_n and A_{ag} are affected by scaling and these parameters shift the population density curve intercept on the y-axis. Therefore, nucleation rate divided by the growth rate (represented by the y-axis intercept) inferred from the population density versus size plots below, should be viewed in a relative sense.

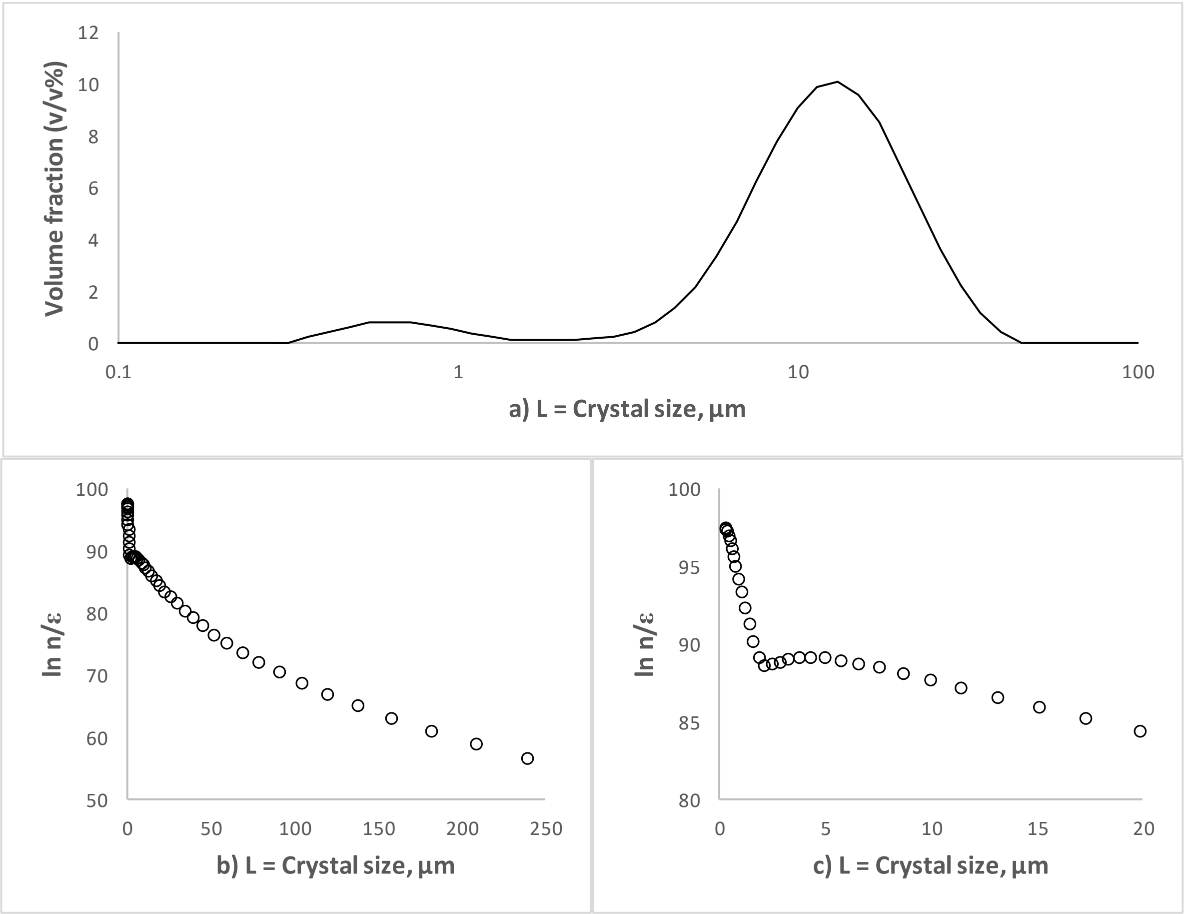

Figure 7.4.2: Experiment 3 in Table 4.2.1 after 1 hour: a) CSD and population density versus size; b) normal scale c) zoomed scale L ∈ [0, 20]

Accommodating the analogy of an idealised mixed suspension mixed product removal system or MSMPR provides a reference to assess potential growth and disruption mechanisms that govern this system. The overall convex shape of the population density in Figure 7.4.2 b) is indicative of agglomeration as literature in Jones (2002) and Mersmann (2001) suggest. A concave shape of the population density versus size suggests disruption or breakage as Figure 7.4.2 c) suggests for size within the range 2µm to 10µm.

Mersmann (2001) and Myerson (2002) additionally illustrate that if the population density versus size curve is convex a possibility exists for the system to dissolve fines, or there may be segregation in the reactor discharge. From the SEM photographs in Figure 7.4.1 it is not clear if significant dissolution occurs as one would expect rounded edges of the crystals; breakage would likewise indicate fractures. In Section 7.3 the potential of segregation was argued as unlikely by comparing modelled crystal size in the reactor to the discharge.

Agglomeration is therefore deemed a key mechanism causing the overall convex population density curve in Figure 7.4.2 b). Visually Figures 7.4.1 c) and d) indicate that the sample comprises separate agglomerates, providing some justification to the aforementioned argument.

SEM photographs of the crystals after 2 hours in the CSTR are shown in Figure 7.4.3. The crystals, at this stage in the precipitation transient, have grown to an *L*$_{43}$ size of 24µm and the crystal volume size distribution is shown in Figure 7.4.4 a). The volume average crystal size has approximately doubled after 2 hours into the CSTR transient compared to after 1 hour.

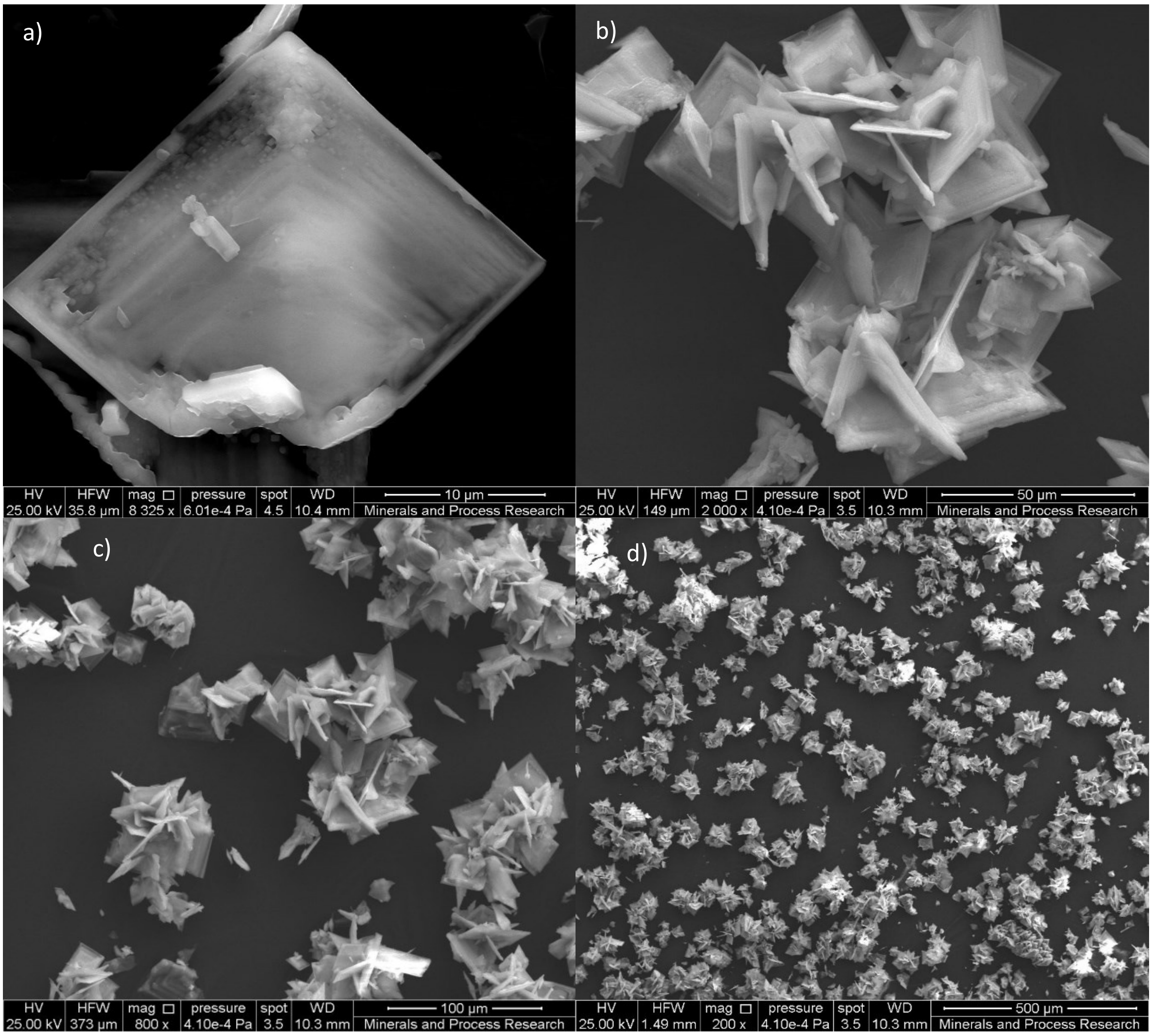

Figure 7.4.3: a) to d) SEM photographs (scales ranging from 10, 50, 100 and 500µm) of diethylenetriammonium hexachlororhodate crystals after 2 hours. Experimental conditions described by Experiment 3 in Table 4.2.1

Figure 7.4.3 a) shows a single crystal at a scale of 10µm that appears to have grown larger relative to the crystals shown in Figure 7.4.1, supporting an increase in the average volume crystal size calculated from the data in Figure 7.4.4 a). The layered structure observed in Figure 7.4.1 is visible in Figure 7.4.3, but the crystal shape has become octahedral and appears square planar at lower magnifications. Crystal agglomeration is evident in Figures 7.4.3 b) to d).

The low magnification SEM photograph at a scale of 500µm in Figure 7.4.3 d) shows single crystals and agglomerates validating to an extent the measured bimodal volume size distribution shown in Figure 7.4.4 a). Figure 7.4.3 a) shows jagged crystal edges that indicate the presence of breakage. Potential locations where crystals can break in this system are firstly inside the reactor, due to collision induced by agitation, and secondly inside the discharge pump, due to crystal-crystal abrasion inside the tubing that passes through the pump cassette. The work here did not explicitly differentiate between these mechanisms as the right-hand side of the population balance in Equation (2.1.7) was combined into one expression. The effect of disruption or breakage mechanisms is therefore mathematically integrated into the agglomeration rate constant through the parameter A_{ag} in Equation (3.1.28).

In Figure 7.4.4 b) the population density versus size graph is a similar shape at a crystal size above 20µm compared to Figure 7.4.2 b), suggesting that the dominant mechanism of crystal growth remains the same moving 2 hours into the precipitation transient. The upward turn of the population density at the smaller sizes in Figure 7.4.4 c) is dampened relative to Figure 7.4.2 c), which may be an indication that crystal disruption (possibly attrition) becomes less prominent as time passes and the crystals grow larger.

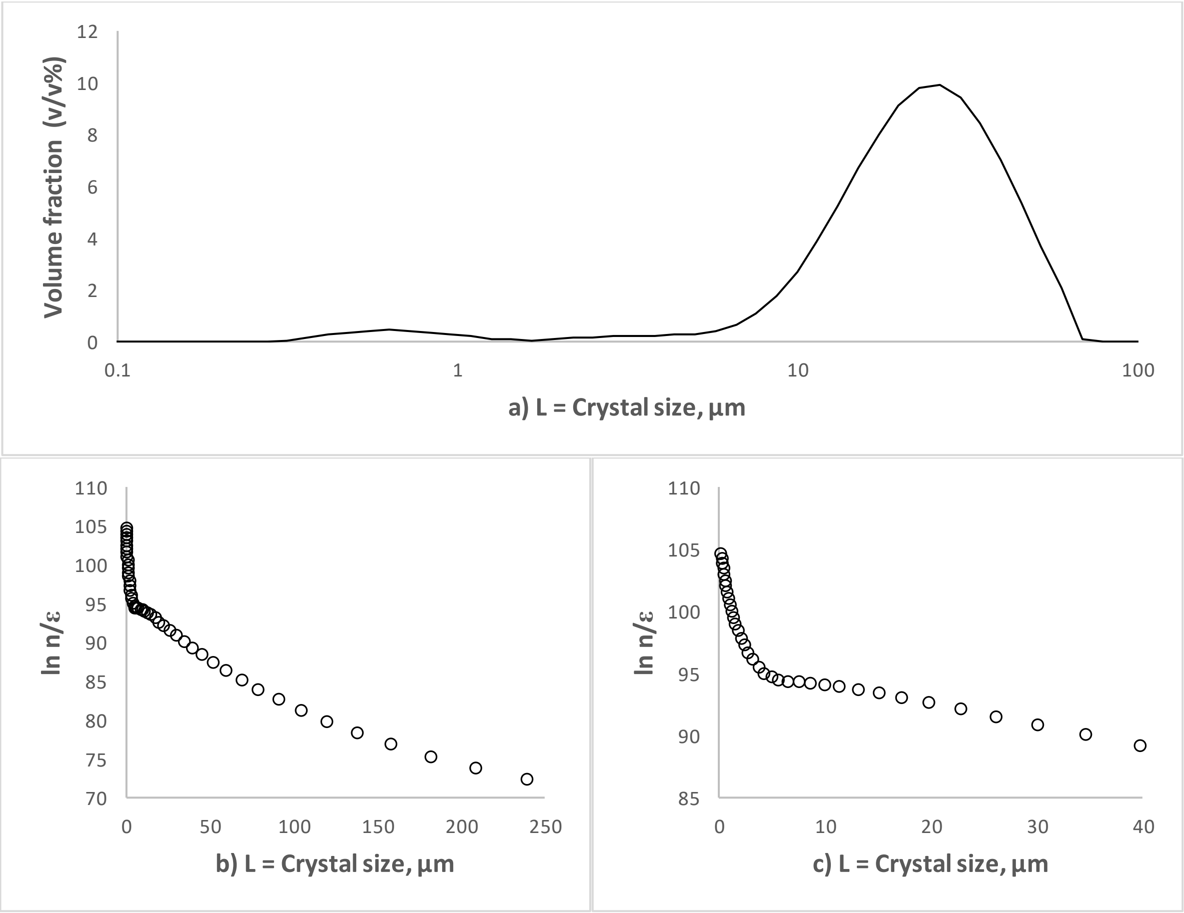

Figure 7.4.4: Experiment 3 in Table 4.2.1 after 2 hours a) CSD and population density versus size b) normal scale c) zoomed scale L ∈ [0, 40]

After 3 hours of precipitation the crystals have grown to an L_{43} size of 43µm approximately 1.8 times larger than the crystals at 2 hours in Figure 7.4.3. SEM photographs of the crystals and the associated volume crystal size distribution are presented in Figure 7.4.5. Figure 7.4.5 a) shows a single crystal highlighting the octahedral shape and jagged edges due to breakage. The crystal edges of one agglomerate in Figure 7.4.5 c) are shown under high magnification in Figure 7.4.5 b). Layers are still visible at the crystal edges but the octahedral shape seems to have collapsed into a planar shape for some of the crystals that form part of the agglomerate. It is possible that as the crystals become more agglomerated and grow bigger, the inner part of the agglomerate is starved of saturated solution and the outer edges then catch up to form a crystal that appears to be square planar. The rounded crystal edges in Figure 7.4.5 a) suggests dissolution but this is believed to be an artefact of sample handling. During washing of the crystals, a loss of vacuum on the filter prolonged the wash cycle, which potentially caused the crystals to partially dissolve on the filter. The rounded edges are not observed for any of the other SEM photographs taken at earlier and later stages in the precipitation, suggesting that it is an anomaly associated with only this sample. Figure 7.4.5 e) shows the associated volume per cent crystal size distribution; the population density size versus size curve is depicted in Figure 7.4.6.

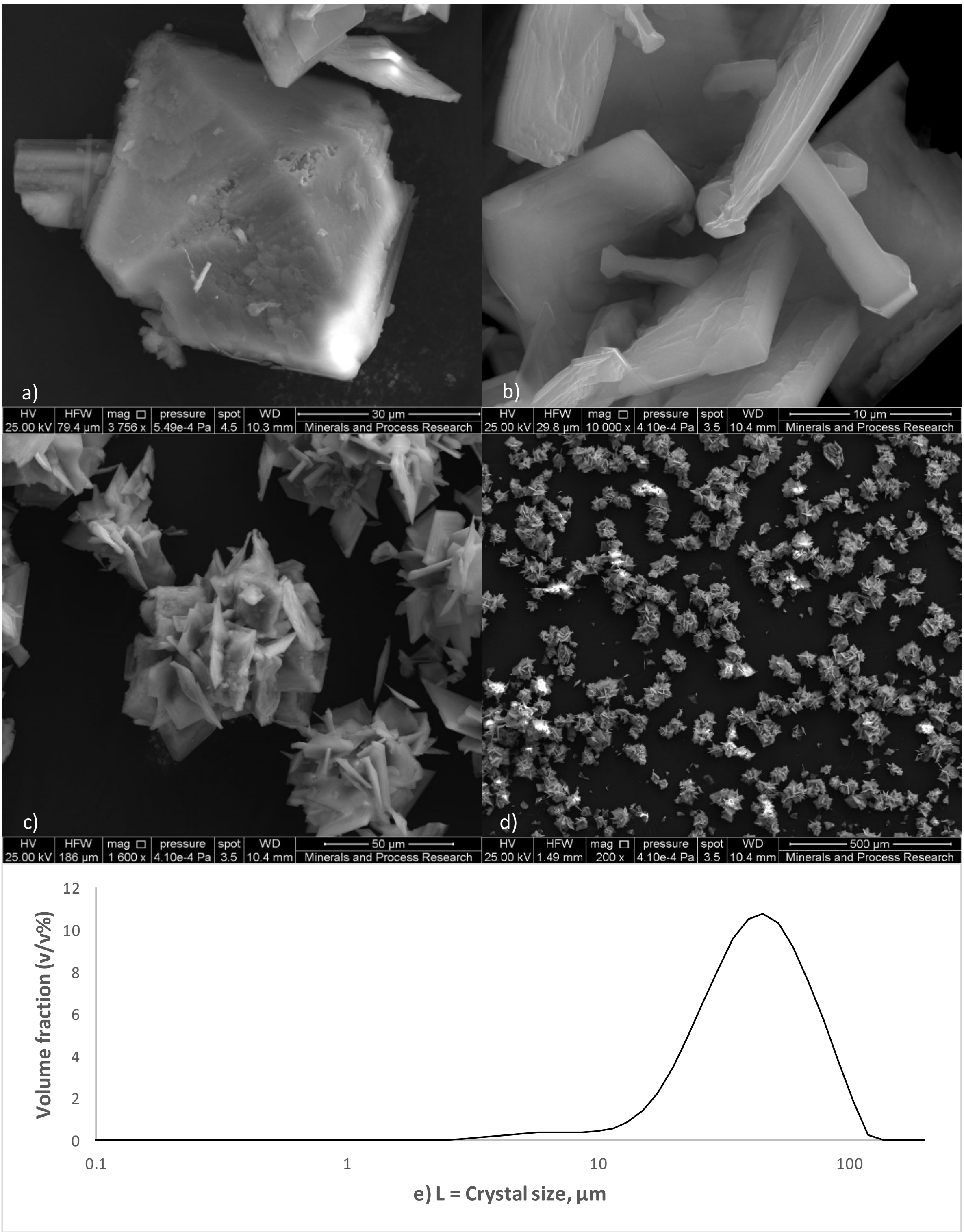

Figure 7.4.5: a) to d) SEM photographs (scales ranging from 30, 10, 50 and 500µm) of diethylenetriammonium hexachlororhodate crystals and e) CSD after 3 hours. Experimental conditions described by experiment 3 in Table 4.2.1

The population density curves in Figure 7.4.6 show a similar trend to Figure 7.4.4 b) with the exception that the population density drops off below the submicron range. This observation indicates that breakage or more likely disruption possibly occurs within this size range. The population density shape in the submicron range shares similarities with halide precipitation as described by Leubner (2009).

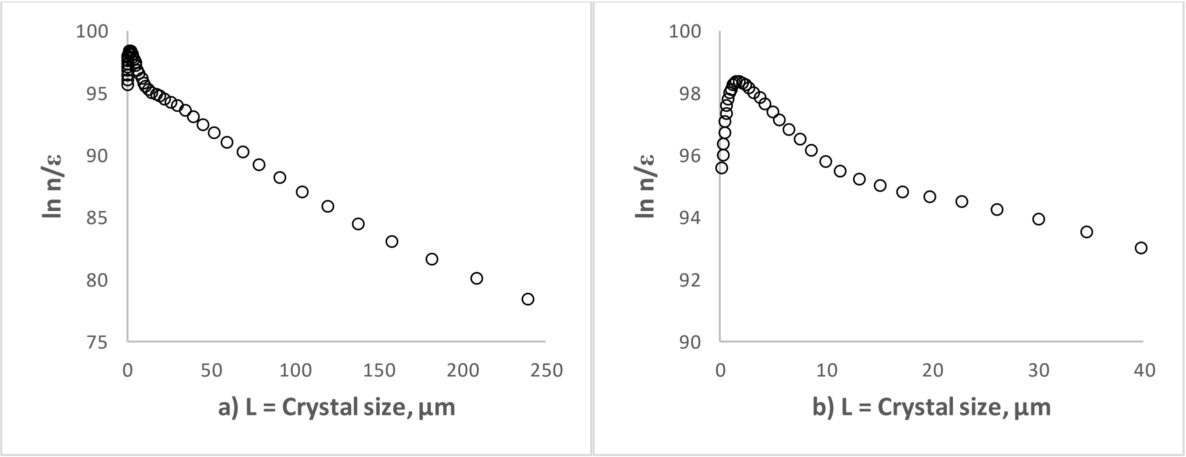

Figure 7.4.6: Experiment 3 in Table 4.2.1 population density versus size after 3 hours: a) normal scale and b) zoomed scale L ∈ [0, 40]

After 4 hours of precipitation, the crystals in Figure 7.4.7 have grown to an L_{43} size of 83µm, approximately 1.9 times the size of the crystals produced at 3 hours in Figure 7.4.5.

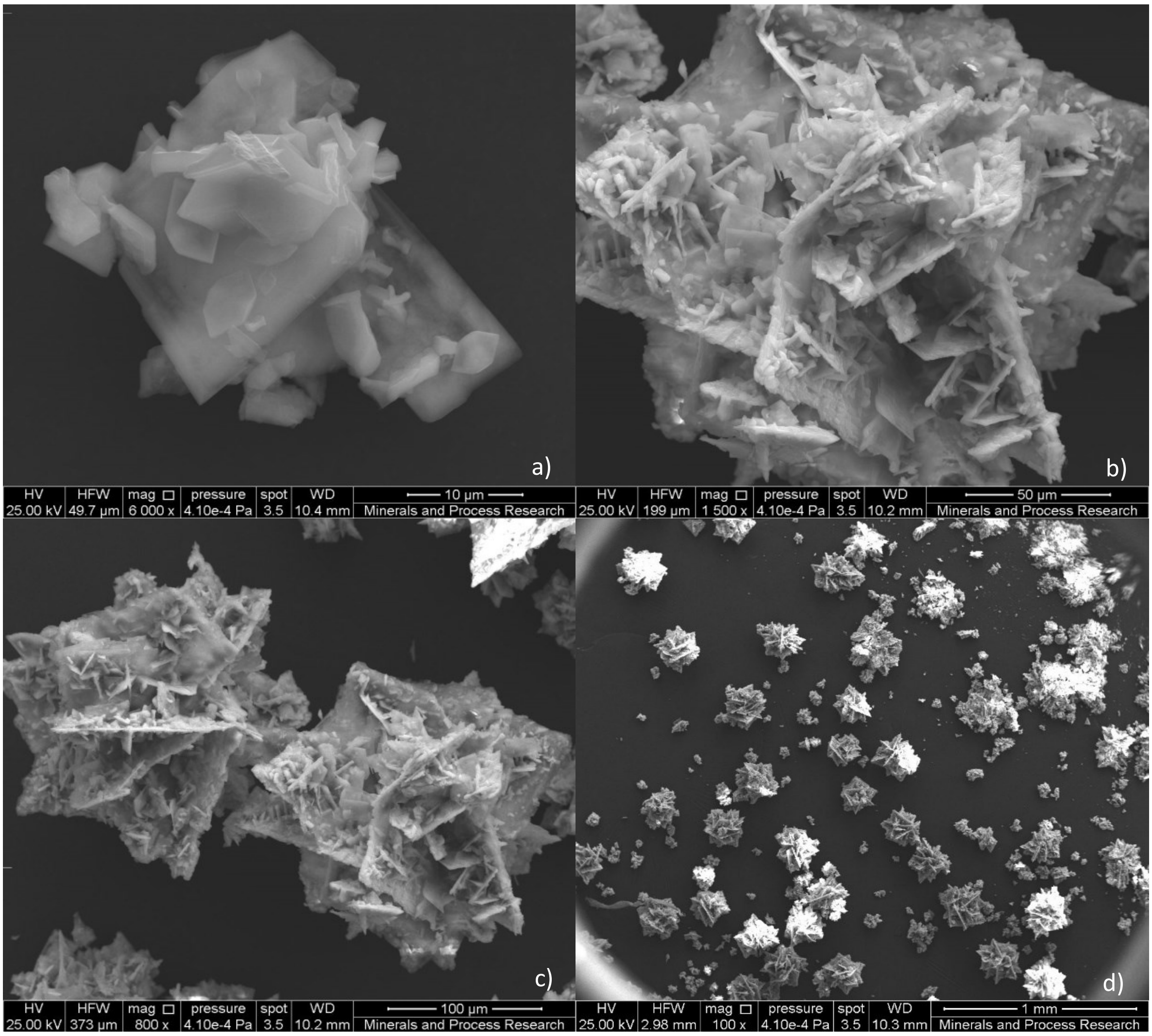

Figure 7.4.7: SEM photographs (scales ranging from 10, 50, 100 and 1000µm) of diethylenetriammonium hexachlororhodate crystals after 4 hours. Experimental conditions described by Experiment 3 in Table 4.2.1

Figure 7.4.7 a) shows that small agglomerates continuously form as the transient progresses, demonstrating that nucleation, growth and agglomeration remain present. The lower magnification SEM photographs show that the square planar structure of the crystals that make up each agglomerate have smaller crystals that are attached to the square faces, especially visible in Figures 7.4.7 b) and c).

Figure 7.4.7 b) and c) show that the number of crystals adhering to the larger surfaces seems to increase over time. This observation validates the assumption that agglomeration rate is affected by the number of crystals in the system through orthokinetic agglomeration, as described in Chapter 3, Section 3.1.3. Figure 7.4.7 d) shows single and agglomerated crystals at low magnification.

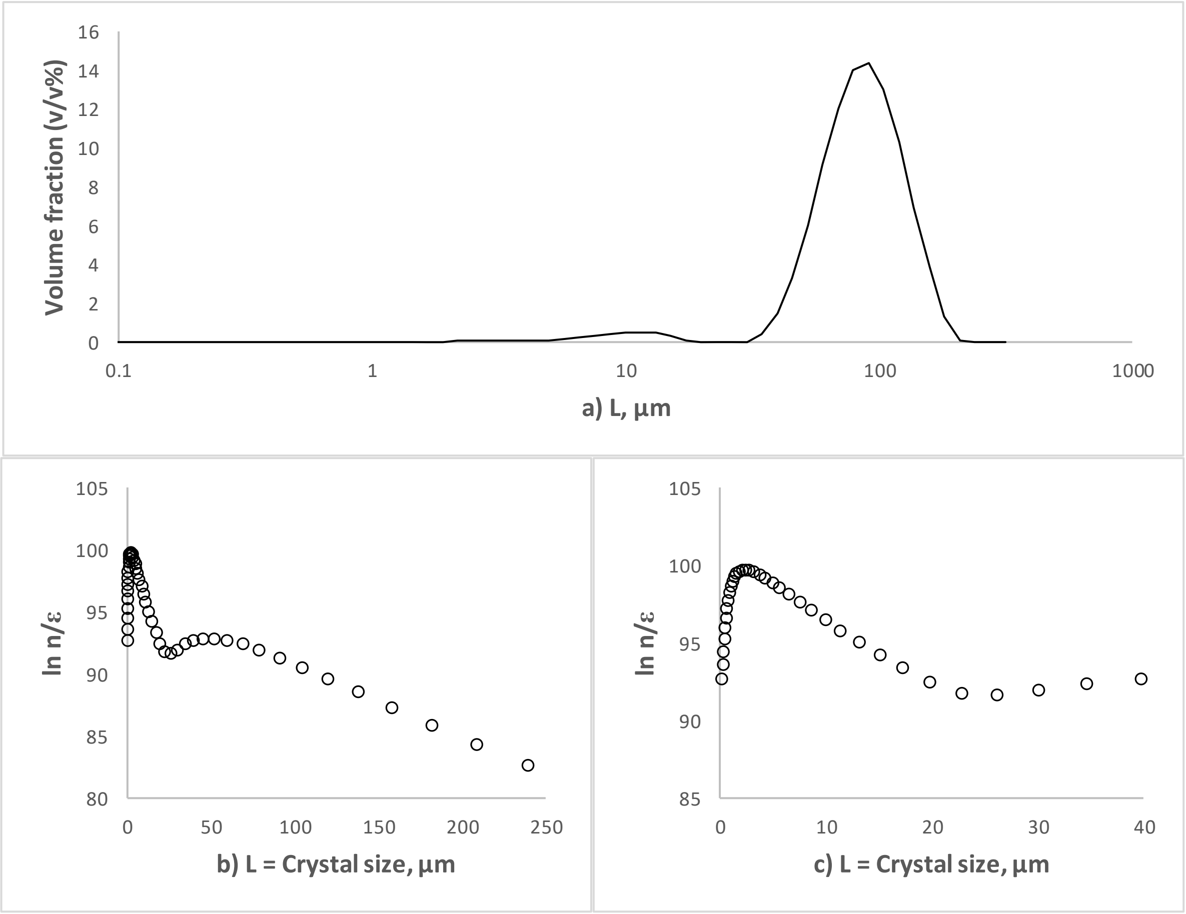

Figure 7.4.8: Experiment 3 in Table 4.2.1 CSD after 4 hours: a) by volume per cent, b) by the logarithm of the population density and c) zoomed population density with L ∈ [0, 40]

In Figure 7.4.8 a) the volume fraction crystal size distribution of the crystals in Figure 7.4.7 shows bimodal behaviour. This remains a characteristic feature and is not likely to be an artefact of the reagent injection system whereby localised nucleation zones around the separated dip-tubes cause two independent nucleation rates. Vicum (2005) performed similar experiments with a barium sulphate system whereby the reagents were added into separate dip-tubes. Bimodal behaviour was not observed in the barium sulphate system, supporting the notion that the separate reagent injection system is not the cause of the bimodal size distribution.

To further elaborate, a comparison of the mixing scales in Chapter 4, Section 4.2, revealed two substantial differences between the barium sulphate system used by Vicum (2005). The first discrepancy was a much slower macromixing time for the barium sulphate system compared to this system. The second discrepancy is related to salt solubility, in that barium sulphate is less soluble than diethylenetriammonium hexachlororhodate (III) by roughly a factor of 100.

One would therefore expect highly localised saturation zones at the dip-tubes in the barium sulphate system relative to this system. The CFD simulations by Vicum (2005) showed highly localised saturation zones around the reagent dip-tubes. It is therefore conceptually feasible that two separate nucleation rates at each localised reactant injection point should be more likely in the barium sulphate system compared to this system.

However, the volume fraction crystal size distributions in Vicum (2005) showed no inclination towards bimodal behaviour. The localised zones were thus averaged out by bulk mixing and the sampled crystal size distributions did not show bimodal behaviour. In another study, by Bałdyga, et al. (1995), involving a semi batch reactor configuration, barium sulphate precipitation through separate reagent dip-tubes also showed no signs of bimodal crystal size distribution behaviour.

Bimodal behaviour was observed for precipitates of diethylenetriammonium hexachlororhodate (III) in a semi batch reactor configuration by Hagemann et al. (2003). Considering that the bimodal behaviour was also observed for the t-mixer PFR configuration in Chapter 6, Section 6.4, it seems reasonable that this mechanism is consistent between the two reactor configurations studied in this work. Thus, the bimodal behaviour of the diethylenetriammonium hexachlororhodate (III) crystal size distribution may be unique to this system, or an artefact of another mechanism yet to be defined.

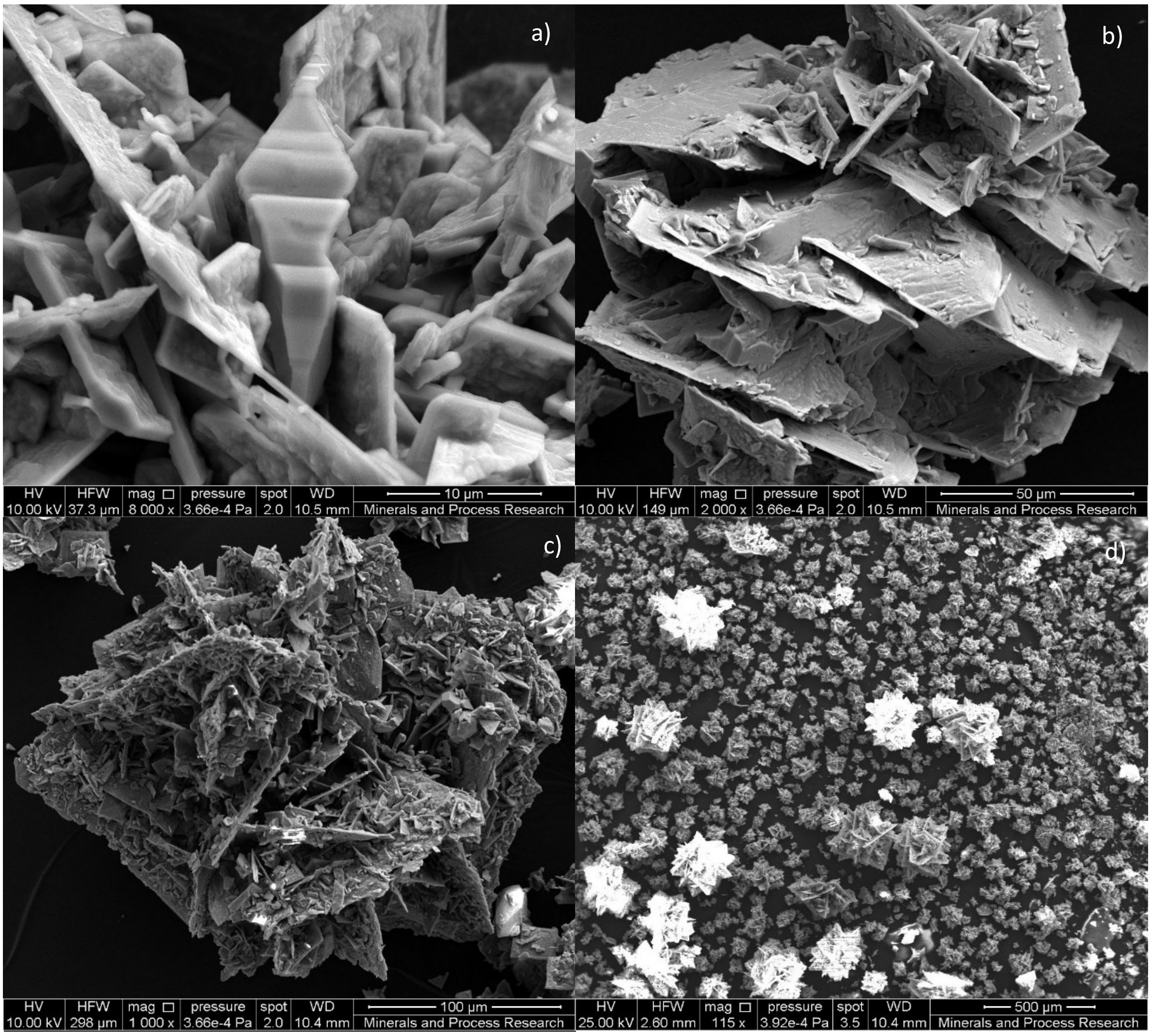

Figure 7.4.9: SEM photographs (scales ranging from 10, 30, 50 and 500μm) of diethylenetriammonium hexachlororhodate crystals after 5 hours. Experimental conditions described by experiment 3 in Table 4.2.1

After 5 hours the crystals in Figure 7.4.9 have grown to an L_{43} size of 95μm and is approximately 1.1 times larger than the crystals in Figure 7.4.7. The crystal size therefore tapers off as time progresses beyond the point where saturation steadies out. The SEM photographs after 5 hours affirm that agglomeration is a prominent feature of this system. Figure 7.4.9 b) indicates that the gaps created by agglomeration are filled in some cases. It is likely that filling of the gaps is mathematically represented by the growth rate expressed in Equation (3.1.27), as opposed to agglomerative growth in Equation (3.1.28). Higher magnification in Figure 7.4.9 a) shows a highly irregular surface that further supports the argument that the fill process is not likely to be due to agglomeration.

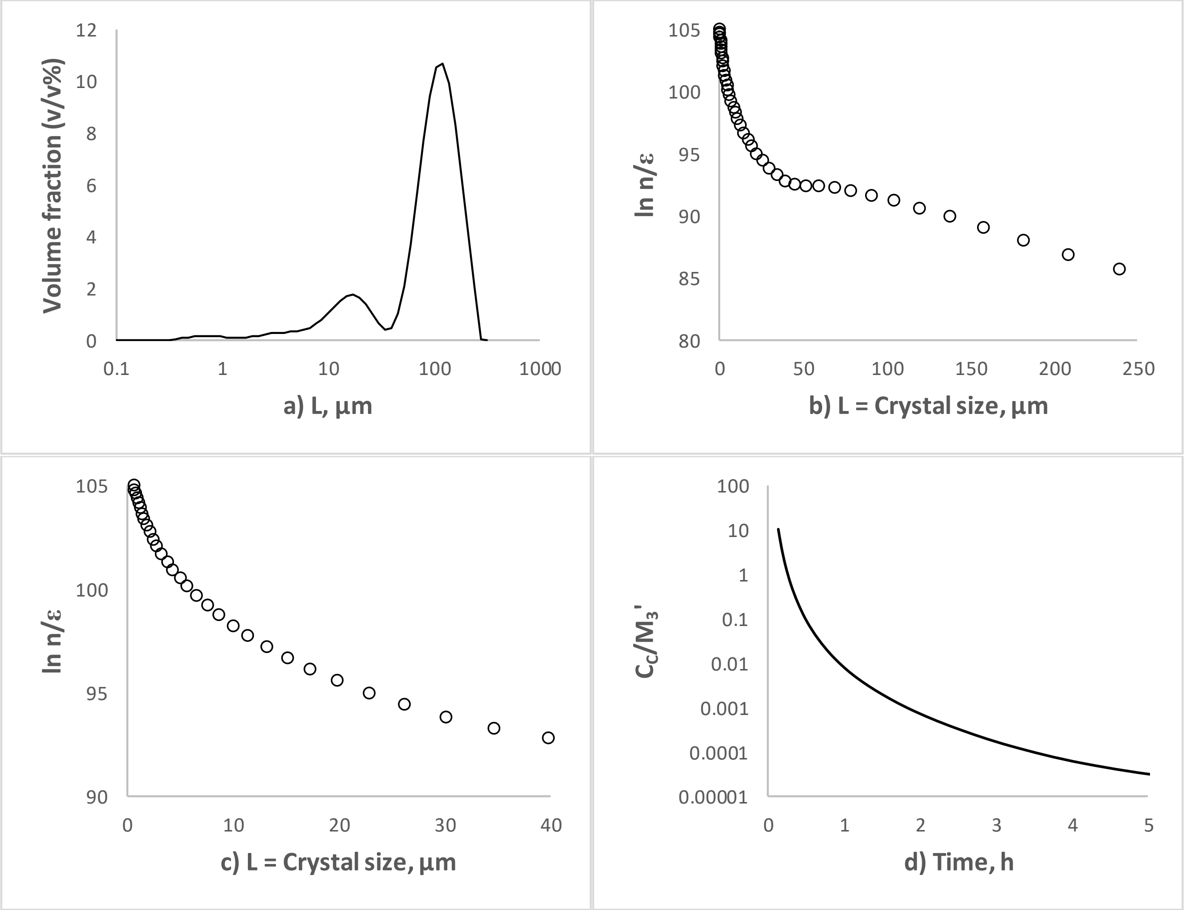

Figure 7.4.10: Experiment 3 in Table 4.2.1 after 5 hours: a) CSD and population density versus size: b) normal scale; c) zoomed scale L ∈ [0, 40]; d) Scaled volume shape factor

The volume per cent and population density size distributions are shown in Figure 7.4.10 a) to c). A bimodal crystal size distribution is apparent in Figure 7.4.10 a). A summary of the mixed lognormal distribution parameters for the crystal size distributions in Figures 7.4.2 to 7.4.10 is given in Table 7.4.1.

Table 7.4.1: Non-linear least squares mixed lognormal parameter estimation results, L_{43} size and scaled third moment (Experiment 3 over the sample period of 1-5h, Table 4.2.1)

Saturation = S	22.2	34.4	39.9	42.1	42.9
Parameter	***t = 1h***	***t = 2h***	***t = 3h***	***t = 4h***	***t = 5h***
m_1	-0.40	0.56	2.77	2.10	2.79
m_2	2.45	3.11	3.72	4.39	4.68
s_1	0.43	1.28	0.74	0.55	1.10
s_2	0.50	0.50	0.45	0.35	0.38
x_1	-0.40	0.56	2.77	2.10	2.79
R^2	0.9999	0.9995	0.9997	0.9999	0.9994
L_{43}, μm	12	24	43	83	95
$M_3' = M_3/\varepsilon$	1.61E+42	3.41E+45	7.61E+46	2.97E+47	5.81E+47

From a comparison between Figure 4.3.3 in Chapter 4 and Figure 7.4.9, it is seen that the crystal structure is not markedly different. Note that the crystals from Figure 4.3.3 were produced at 100°C whereas the crystals in Figures 7.4.1 to 7.4.9 were produced at 60°C. A comparison of the saturation profiles between the CSTR experiments reveals that at 60°C (Experiment 3) saturation settled out at ~43, and at 100°C (Experiment 1) saturation settled out at ~20 (Figure 7.1.3 a)). This suggests that temperature and saturation within the measured range did not affect morphology. This was also observed in the t-mixer PFR arrangement in Chapter 6, Section 6.4, albeit with a potential variation in volume shape factor.

The SEM photographs in Figures 7.4.1 to 7.4.9 show various complex shapes that range between square planar, octahedral and intergrown square plates. The various shapes suggest that the volume shape factor during the transient changes. From the measurements it is not possible to determine the volume shape factor, but it can be inferred from the crystal concentration and third moment time profiles, as was done for the PFR crystals.

A comparison of Figure 7.3.6 b), the third moment of Experiment 3, and the crystal concentration shown in Figure 7.1.3 b), reveals that the graphs possibly have the same shape. However, figure 7.4.10 d) shows that the ratio between the crystal concentration and the scaled third moment monotonically decreases. Thus, Figure 7.4.10 d) indicates that the volume shape factor as per Equation (6.4.2) is not a constant over time in the CSTR configuration.

The bimodal behaviour of the CSD shown in Figure 7.4.10 a) persists through the transient and appears to be a characteristic observation for this system. The population density curve in Figure 7.4.10 b) follows a similar trend, as shown in Figures 7.4.2 c), 7.4.4 c), 7.4.6 b) and 7.4.8 c). The convex shape is indicative of agglomeration and was consistently observed throughout the transient.

In Table 7.2.2, the growth rate supersaturation exponent α was found to be 2.31 for the CSTR configuration and 1.13 for the PFR configuration. This suggests that the growth process for the CSTR falls outside the limits of the BCF and Chernov models and is more in line with polynuclear growth (Jones, 2002). The CSTR growth rate supersaturation exponent may be inflated relative to the PFR configuration due to growth rate enhancement by the presence of microcrystals. Microcrystals are present in all the SEM photographs of crystals produced in the CSTR. Matsuoka & Eguchi (1993) and Matsuoka et al. (1996) report that this mechanism can inflate the growth rate by up to 5 times relative to a system that has no microcrystals.

The nucleation rate supersaturation exponent is the sum of α and β values, while the sum is equal to 2.36. The nucleation rate order is therefore smaller than typical values for highly insoluble systems such as barium sulphate and calcium carbonate that are driven by homogeneous nucleation (Myerson, 2002; Nielsen, 1961). In Chapter 3, Section 31.1.3, the proposed model for nucleation is of the form typically used to describe secondary nucleation. Since the population and mass balance model is in agreement with the measurements, as observed in Sections 6.1 and 6.2, it is likely that the nucleation process is mainly secondary in nature.

An interesting observation is that the agglomerated crystals produced in the continuous reactor configuration have a remarkable resemblance to naturally formed gypsum or barite crystal clusters that form in arid sandy environments under evaporative crystallisation conditions. These crystal clusters are often referred to as desert roses and are found in areas such as the Sahara, Namib and Tunisian deserts (Wikipedia, 2016). Thus, it seems appropriate to classify the crystal appearance of diethylenetriammonium hexachlororhodate (III) precipitated under CSTR conditions as a desert rose.

The SEM photographs in this section compared to Chapter 6, section 6.4, shows that the morphology in a CSTR is vastly different to the morphology produced in a PFR. Morphology of diethylenetriammonium hexachlororhodate (III) salt is therefore affected by reactor configuration but seems to be insensitive to temperature (saturation). Fundamentally the reactor configuration determines the crystal flow patterns as well as the energy intensity of reagent mixing. Therefore, reactor configuration affects the morphology of a system that tends to agglomerate as different designs have different trajectories of the crystals in the flow field.

8. CONCLUSIONS: KINETICS OF DIETHYLENETRIAMMONIUM HEXACHLORORHODATE (III) PRECIPITATION

What follows is a concluding summary of the experimental, and in some cases theoretical, findings from Chapters 2 to 7 in this thesis, bearing in mind the initial objectives of this work. For reference, the initial objectives as listed in Chapter 2, Section 2.3, are given below:

- Derive a mathematical model of the transient precipitation process of diethylenetriammonium hexachlororhodate (III) crystals in a continuous stirred tank reactor configuration.
- Derive a mathematical model of the precipitation process of diethylenetriammonium hexachlororhodate (III) crystals in a t-mixer with a pipe reactor in series configuration.
- Determine if the growth and nucleation kinetics are interchangeable between the two reactor configurations to establish the extent to which mixing scales may have influenced kinetics.
- Determine if the reactor configuration affects crystal morphology.
- Measure the solubility of diethylenetriammonium hexachlororhodate (III) salt since it is an important thermodynamic property that appears in the definition of saturation.
- Measure the viscosity since it is required to calculate the Reynolds number.

Mathematical derivations in Chapter 3 aim to address the first two objectives and are summarised briefly. The PFR mass balance caters for two operating regimes where mixing on the micro- or mesoscale limits conversion at low Reynolds numbers and where equilibrium limits conversion at high Reynolds numbers. The pseudo reaction rate constant or inverse mixing scale in the PFR was modelled through two competing mixing scales. The micromixing scale was empirically related to temperature whereas the mesomixing scale was empirically related to fluid velocity.

Under very low velocity conditions (low Reynolds number) the mesomixing length scale became the dominant factor, and mass transfer in terms of mixing the two reagents was primarily limited by reagent dispersion through disintegration of large eddies. Under moderate velocity conditions (below the point where conversion becomes independent of Reynolds number) where temperature limited the reaction rate, micromixing was deemed the mass transfer limitation through molecular diffusion.

A key assumption in the PFR pseudo reaction rate constant is that particle surface area has a constant effect on reaction rate over the length of the reactor. This assumption decouples the mass balance from the population balance and inherently implies that growth rate is limited by interfacial attachment kinetics, more precisely the kinetics of any of the growth processes listed under iii) to vi) of the list given by Dirksen & Ring (1991) in Section 2.1.2 of Chapter 2. The PFR data fit in Chapter 6 shows evidence that the derived model accounts for both salt conversion and L_{43} size.

From the literature review the objective was to design a CSTR that had negligibly small concentrated reagent injection zones to mitigate the effects that micro- or mesomixing may have on precipitation kinetics, as discussed in Chapter 4. As a result, the CSTR system equilibrated within the resolution of sampling. Solubility and activity coefficient parameters described the bulk aqueous profiles through a transient mass balance using reagent flow, reactor volume, initial concentrations, and temperature as input. Equilibration therefore occurred at the point of injection, suggesting efficient micromixing and rapid dispersion through mesomixing.

Due to the CSTR equilibrating rapidly, an unreactive mass balance was required to define saturation in the CSTR model. Data fitting in Chapter 7 show that this definition of saturation translates to growth and nucleation rates that give good predictions of the L_{43} size through the moment transformed population balance.

In the sections that follow, the last four objectives are covered by providing a summary of the conclusions related to solubility and precipitation kinetics as well as observed differences in crystal morphology.

8.1. EQUILIBRIUM OBSERVATIONS

It was found that the logarithm of the solubility product was proportional to the inverse of temperature through an Arrhenius relationship. The solubility appeared to be affected by the level of oxidation in the system. Under oxidising conditions, using hydrogen peroxide as oxidant, the salt is less soluble compared to non-oxidising conditions.

From the solubility measurements an activity coefficient model was determined. The activity coefficient model shares features from Debye-Hückel theory. The natural logarithm of the activity coefficient was found to be proportional to the root of ionic strength. The activity coefficient was referenced to a value of 1 at 6M hydrochloric acid in solution with no other species present, thus the ionic strength at the reference state is 6. Figure 8.1.1 a) shows the solubility relationship and Figure 8.1.1 b) shows the activity coefficient model for the system within the range of experimental conditions.

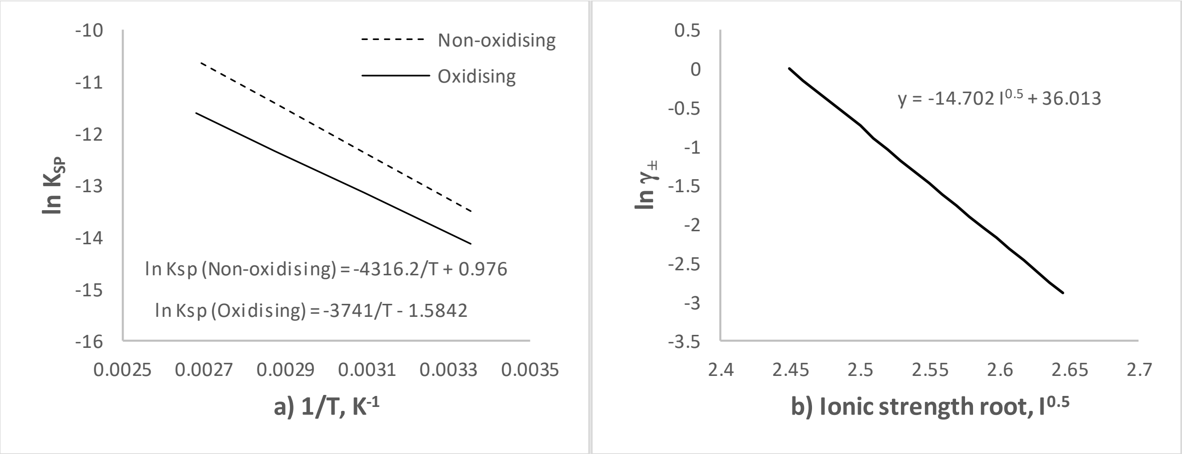

Figure 8.1.1: Diethylenetriammonium hexachlororhodate (III) salt a) solubility and b) activity coefficient

The equilibrium hexachlororhodate (III) concentration data in Figure 5.1.6 a) was manipulated to generate the data as plotted in Figure 8.1.2 a). The purpose of the data manipulation was to extract the heat of crystallisation from the equilibrium concentration data. From the literature the heat of crystallisation is described by Equation (8.1.1) (Mersmann, 2001).

$$\frac{\partial \ln \gamma_\pm C_e}{\partial (1/T)} = -\frac{\Delta H_{CL}}{R} \qquad \textbf{(8.1.1)}$$

Where $\gamma_\pm$ = Mean activity coefficient
C_e = Equilibrium concentration [M]
T = Temperature [K]
ΔH_{CL} = Heat of crystallisation [kJ/mol]
R = Universal gas constant = 0.008314 [kJ/mol.K]

The slope of the data in Figure 8.1.2 a) represents the left-hand side of Equation (8.1.1). The equilibrium concentration in the plot is taken to be the reagent that is not in excess, thus if the initial mol ratio in Figure 8.1.2 b) is above 1, the equilibrium concentration used to extract the heat of crystallisation is taken from the slope of the plot of the hexachlororhodate (III) concentration versus the inverse of temperature. When the initial mol ratio is less than 1, the equilibrium concentration is that of protonated diethylenetriamine. This method gave the best linear relationship as shown in Figure 8.1.2 a).

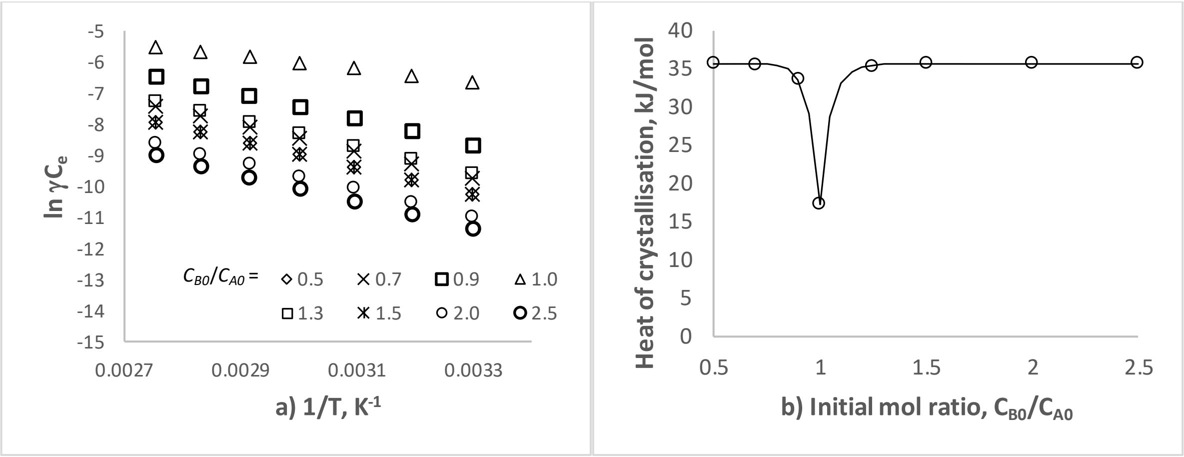

Figure 8.1.2: a) Equilibrium concentration versus temperature plot and b) Heat of crystallisation versus initial reagent molar ratio (C_{A0} = 0.1M for all mol ratios)

The peculiar heat of crystallisation versus initial mol ratio in Figure 8.1.2 b) is due to the ionic strength passing through a minimum at equivalent molar conditions (refer to Figure 5.1.6 b)). Equivalent molar conditions translate to the lowest equilibrium concentrations, therefore the lowest ionic strength and solute activity. Figure 8.1.2 b) demonstrates that the heat of crystallisation is a function of initial mol ratio of the reagents. The expression that best describes this relationship is given in Equation (8.1.2) below.

$$\Delta H_{CL} = \begin{cases} 17.29 + 18.38\left(1 - exp\left[-19.79\left(\frac{C_{B0}}{C_{A0}} - 1\right)\right]\right), & \frac{C_{B0}}{C_{A0}} \geq 1 \\ 17.29 + 18.38\left(1 - exp\left[-19.79\left(\frac{C_{A0}}{C_{B0}} - 1\right)\right]\right), & \frac{C_{B0}}{C_{A0}} < 1 \end{cases} \qquad \textbf{(8.1.2)}$$

The slopes from the data in Figure 8.1.2 a) are tabulated in Table 8.1.1 as a function of initial mol ratio. It is evident that the heat of crystallisation data suggests an energy requirement to precipitate diethylenetriammonium hexachlororhodate (III) salt. The precipitation process therefore appears endothermic. Some systems found in literature that exhibit endothermic behaviour in terms of heat of crystallisation are lithium sulphate (Li_2SO_4 with ΔH_{CL} = 4.8kJ/mol), manganese sulphate ($MnSO_4$ with ΔH_{CL} = 10kJ/mol), sodium iodide (NaI with ΔH_{CL} = 6.7kJ/mol) and sodium bromide (NaBr with ΔH_{CL} = 17.7kJ/mol) (Mersmann, 2001).

Table 8.1.1: Heat of crystallisation data as displayed in Figure 8.1.2 b)

C_{B0}/C_{A0}	*Slope from Figure 8.1.2 a)*	ΔH_{CL}, *KJ/mol*	*R²*
0.5	-4293	35.69	0.999994
0.7	-4271	35.51	0.999970
0.9	-4049	33.66	0.999361
1.0	-2080	17.29	0.999921
1.3	-4251	35.34	0.999960

8.2. CRYSTAL GROWTH AND NUCLEATION KINETICS

In Chapter 3, models were derived to describe conversion and average volume particle size based on the theory and literature presented in Chapter 2. The experimental procedure followed from the theory and literature and the experiments were designed to elucidate nucleation and growth kinetics from a CSTR and a PFR. In Chapters 6 and 7 the growth and nucleation kinetic parameters for diethylenetriammonium hexachlororhodate (III) precipitation were directly estimated through a non-linear least squares routine using concentration profiles and L_{43} size measurements.

It was found that the temperature dependence of the growth, agglomeration and nucleation rates were applicable to both the t-mixer PFR configuration and the CSTR configuration. The temperature dependence parameters that relate to the activation energies of each process are given in Table 8.2.1.

Table 8.2.1: Growth, agglomeration and nucleation activation energy for diethylenetriammonium hexachlororhodate (III) salt in 6M hydrochloric acid

Parameter	*Growth rate*	*Agglomeration rate*	*Nucleation rate**
$B_i = E_{a,i}/R$, K	-23203	-78921	29322
$E_{a,i}$, kJ/mol	-192.9	-656.1	50.9

*Nucleation rate temperature dependence is the product between K_n and K_g => B nucleation = $B_g + B_n$

The growth activation energy indicates that growth through interfacial attachment is exothermic, likewise for growth due to agglomeration. Nucleation appears to be an endothermic process that corresponds to the observed endothermic heat of crystallisation in Table 8.1.1.

To aid interpretation of the remaining parameters of the growth and nucleation rate functions, the differences in morphology and population density-size relationship are first discussed from Chapters 6 and 7, Sections 6.4 and 7.4. Figure 8.2.1 shows the morphology produced in a CSTR in comparison to a PFR. Figure 8.2.2 shows the typical population density curves associated with the crystals in Figure 8.2.1.

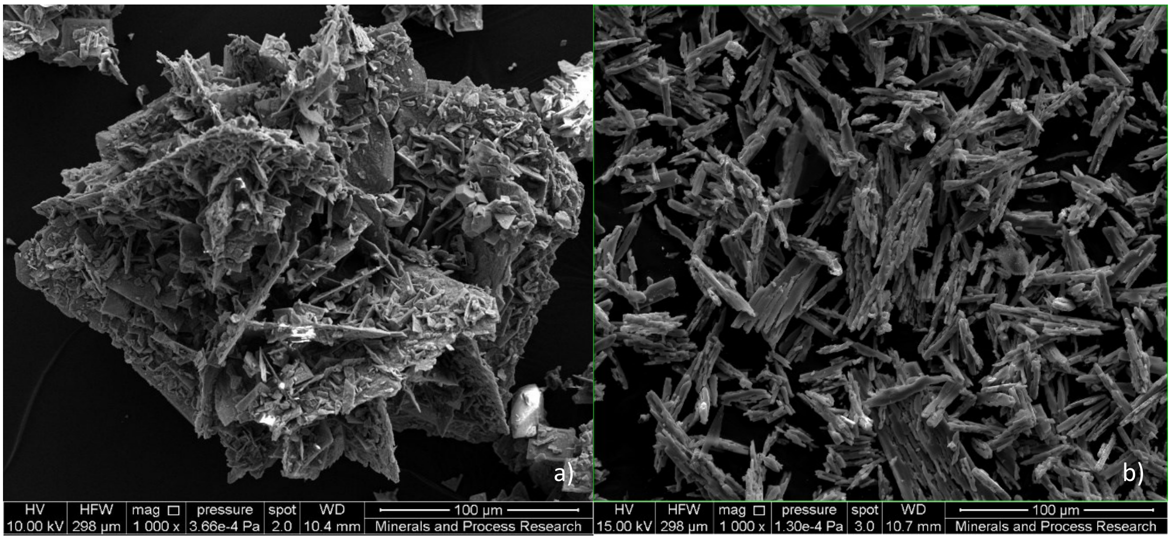

Figure 8.2.1: Typical precipitated crystal morphology at 60°C in a) a CSTR configuration after 5h into the transient at 1h residence time and b) a PFR configuration

In Figure 8.2.1 the crystal structures are clearly different with the CSTR crystals representing a desert rose appearance whereas the PFR crystals represent a feathery, flat and elongated shape. The differences in the shapes are believed to arise due to crystal and aqueous flow patterns specific to each configuration. The PFR crystal flow pattern is linear whereas the CSTR flow pattern has components that are angular, horizontal and vertical, giving rise to a more chaotic crystal flow pattern relative to the PFR. Furthermore, crystal collisions in a CSTR are hypothesised to be at points where different flow patterns intersect whereas in a PFR it is induced by radial aqueous velocity fluctuations.

In Figure 8.2.1 a) the random orientation of crystals during crystal collisions is evident from the overall chaotic crystal agglomerate structure. However, the crystals are symmetric to an extent, suggesting that the chaotic flow patterns inside the CSTR have some degree of consistency. In contrast, the linear elongated shape of the PFR crystals in Figure 8.2.1 b) are indicative of the crystals following in a linear flow path. In both SEM photographs the linking of separate crystals is evident, suggesting that the individual crystals in this system tend to attach and cement to each other by the adhesive characteristics of the aqueous phase through supersaturation.

Figure 8.2.2 illustrates a population density comparison between a CSTR and a PFR configuration. Generally, the population density versus size curves in Chapters 6 and 7, sections 6.4 and 7.4, were convex and indicative of either agglomeration, growth rate dispersion, fines dissolution or classification as per the literature (Myerson, 2002; Mersmann, 2001).

Considering the convex shape of the population density curves in Figure 8.2.2 combined with the observed linking of crystals in the SEM photographs, agglomeration is considered a prominent mechanism in this system. In Chapter 7, Section 7.3, strong evidence was provided to exclude segregation as a mechanism for the convex population density curve, particularly for the CSTR configuration. Likewise, segregation was excluded in the PFR configuration in Chapter 6, Section 6.4, based on a conservative estimate of the sublayer thickness described in Massey (1970). Typically, rounded crystal edges are expected when crystals dissolve. Rounded crystal edges were observed in some of the CSTR SEM photographs, Figures 7.4.1 and 7.4.5, but this was likely caused by sample handling. All other SEM photographs showed sharp crystalline edges and on this basis fines dissolution mechanisms were discounted.

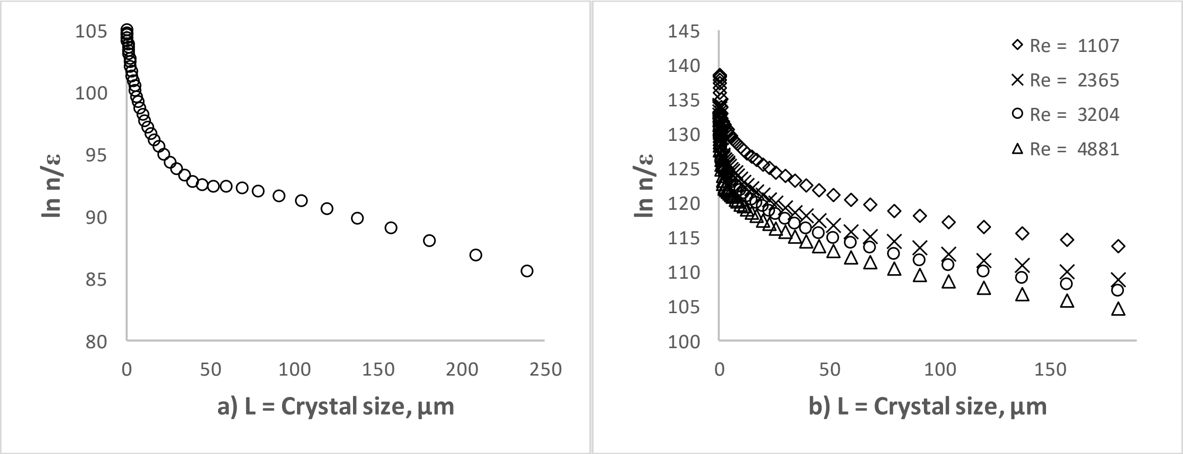

Figure 8.2.2: Typical crystal population density curves at 60°C for a) a CSTR configuration with 1h residence time after 5 hours and b) a PFR configuration at a reactor length of 4.84m

Growth rate dispersion was not formally excluded as the model representing agglomeration in Equation (3.1.13) is like the random fluctuation model of Randolph and White used to describe systems with growth rate dispersion (Myerson, 2002).

Table 8.2.2: Best fit CSTR nucleation and growth parameters from Monte Carlo data fit

Configuration	$\ln A_g$	$\ln A_{ag}$	$\ln A_n$	α	β
PFR	73.44	29.16	15.00	1.13	0.51
CSTR	64.70	41.69	6.35	2.31	0.05

With reference to the above morphology and population density discussion, the remaining growth and nucleation rate parameters are discussed and shown in Table 8.2.2. The frequency constant A_g and the growth rate exponent α in Table 8.2.2 suggest that crystal growth rate through interfacial attachment in a PFR is larger than in a CSTR. By extrapolation, this statement is valid up to a saturation of ~1648, thereafter the CSTR growth rate is larger than the PFR (Equation (8.2.1)). Note that the temperature dependence term cancels as temperature dependence was found to be universal between the two configurations (see Table 8.2.1).

$$\frac{G|_{PFR}}{G|_{CSTR}} = \frac{A_g(S-1)^{\alpha}\big|_{PFR}}{A_g(S-1)^{\alpha}\big|_{CSTR}} = \frac{exp(73.44)(S-1)^{1.13}}{exp(64.7)(S-1)^{2.31}} > 1 \quad <=> \quad S < 1648 \qquad \textbf{(8.2.1)}$$

Potentially the larger growth rate in a PFR configuration may be caused by the linear flow pattern of the crystals relative to a turbulent aqueous front that has a random velocity profile over the diameter of the reactor that averages to the crystal velocity. The random nature of the aqueous velocity profile therefore promotes multiple collisions between a molecule and a crystal. In a CSTR the expectation is that the crystals and the aqueous phase move in flow patterns that are similar and parallel, giving rise to a lower collision rate between molecules and crystals. Aqueous molecules in the PFR configuration therefore collide more frequently with the crystals relative to the CSTR configuration, giving rise to a higher growth rate frequency constant in a PFR as opposed to a CSTR.

In Chapter 6, Equation (6.2.4) illustrated that the parameters A_{ag} and A_n are affected by numeric scaling after data fitting. Therefore, no direct comparison can be made between the agglomerative growth and nucleation frequency constants of the PFR and CSTR configurations based only on the fitted constants. To explain the differences in the agglomeration frequency parameter A_{ag} it is argued that the number of collisions between crystals in a PFR is lower compared to a CSTR due to physically fewer crystals in the PFR volume compared to CSTR volume. The CSTR active volume in all experiments was 2dm^3 compared to 0.094dm^3 at a reactor length of 4.838m, and 0.058dm^3 at a reactor length of 2.954m for the PFR.

Visual comparison of the crystal cluster in a CSTR agglomerate versus a PFR agglomerate illustrates that there are more crystals in the CSTR agglomerate (see Figure 8.2.1). It is therefore expected that the agglomeration rate in a CSTR is larger than in a PFR simply because there are substantially more crystals available for collision, which increases the agglomeration rate as per Equations (3.1.28) and (3.2.24). System supersaturation between PFR and CSTR is believed to be a small contributing factor that increased agglomeration rate in the PFR above that of the CSTR. The experimental saturation ranges between the configurations overlapped, with the highest CSTR saturation being 43 compared to 64 in the PFR. One would therefore expect the saturation contribution to drive the PFR growth rate above that of the CSTR according to Equations (3.1.28) and (3.2.24). However, this was not the case as the number of crystals is orders of magnitude larger than the saturation. Thus, although not directly comparable in Table 8.2.2, it is expected that the agglomerative frequency number A_{ag} is greater in the CSTR configuration relative to the PFR configuration.

Following on from the molecular collision frequency discussion for growth rate in a PFR relative to a CSTR, it is expected that the nucleation rate in a PFR is larger than a CSTR due to more frequent molecular collisions. Typical volume per cent crystal size distributions in Chapters 6 and 7 suggest that the PFR crystal size distribution averages are smaller than the CSTR crystal size distribution averages, indicating that nucleation is more prevalent in the PFR than the CSTR.

By applying the same logic as per Equation (8.2.1), and acknowledging that A_n is not directly comparable, it is found that the PFR nucleation rate is greater than the CSTR nucleation rate at saturation < 1.87E5 and the nucleation frequency constants A_n equal. If the CSTR nucleation frequency constant is greater than the PFR constant by a factor equal to the ratio of the growth frequency constants, i.e. $exp(8.74)$, then the nucleation rate in the CSTR is greater than the PFR at saturation > 2. Taking into consideration that the growth rate frequency constant in the PFR is greater than the CSTR, it is not likely for the nucleation frequency constant of the CSTR to be greater than the PFR if the primary driving force behind these numbers is number of collisions on a molecular level. Therefore, it is expected that the nucleation rate in the PFR, under realistic saturation levels, will always be greater than the CSTR nucleation rate. This finding is in line with a study on benzoic acid precipitation in a CSTR and PFR by Ferguson et al. (2013).

Growth rate supersaturation exponent α is expected to be the same in both reactor configurations, provided the same growth mechanisms apply in each system. The observed differences in this exponent in Table 8.2.2 is believed to be linked to the phenomenon of growth rate enhancement by the presence of sub-micron crystals (Matsuoka & Eguchi, 1993; Matsuoka et al., 1996). The SEM photographs of the CSTR crystals show many instances of small crystals, as opposed to more uniformly sized crystals in the PFR (refer to the SEM photographs in Figures 6.4.1, 6.4.3 and 6.4.5 for the PFR and Figures 7.4.1, 7.4.3, 7.4.5, 7.4.7 and 7.4.9 for the CSTR).

It is reasoned that the CSTR growth rate is enhanced by the formation of sub-micron or nano crystals at the reagent dip-tube outlets that then enhance the growth rate of the crystals in the bulk as they pass by the reagent injection points. This gives rise to an increase in the growth rate supersaturation exponent α relative to the PFR configuration. In the PFR configuration it is argued that the bulk of the nucleation process occurs at the point where the two reagents meet in the t-mixer, thereby affecting growth rate along the length of the PFR to a lesser extent as the crystals move in a plug along the reactor length. Therefore, growth rate enhancement by the presence of sub-micron or nano crystals is less likely to occur in the PFR configuration, resulting in a lower dependency of growth rate on supersaturation.

By the same argument the presence of micro crystals tends to drive secondary nucleation processes thereby causing the CSTR nucleation rate to be more strongly dependent on supersaturation through the exponent ($\gamma = \alpha + \beta$). Note that the growth and nucleation rate supersaturation dependency is substantially dampened by the numeric value of the frequency constants as they are orders of magnitude larger than the supersaturation term contribution. Hence, the reactor configuration is the most significant variable to manipulate crystal growth and nucleation rate in this system under the tested initial PFR saturation range of 2.2 to 64, and the CSTR saturation range of 1 to 43 (see Appendix 9.1 and Figure 7.1.3 a)).

Sections 6.4 and 7.4 in Chapters 6 and 7 showed that morphology is insensitive to operating temperature and Reynolds number but markedly sensitive to reactor configuration as discussed above. To some extent the morphology showed response to saturation levels in the CSTR. From the initial stages in the CSTR precipitation, where saturation was low the crystal shape changed from an irregular surface to square planar and sometimes octahedral shaped crystals at higher saturation. The shape factor, inferred from the ratio of the crystal concentration and the scaled third moment of the population density, showed that it is not a constant in both reactor configurations. Agglomeration was evident throughout and is highlighted in Figures 7.4.1, 7.4.3, 7.4.5 and 7.4.7. It is possible that the shape factor of a crystal is related to the agglomeration conditions within the reactor. In some SEM photographs, Figures 6.4.3 d) and 6.4.5 d), crystal twinning was observed, and this is another form of agglomeration as discussed in Chapter 2.

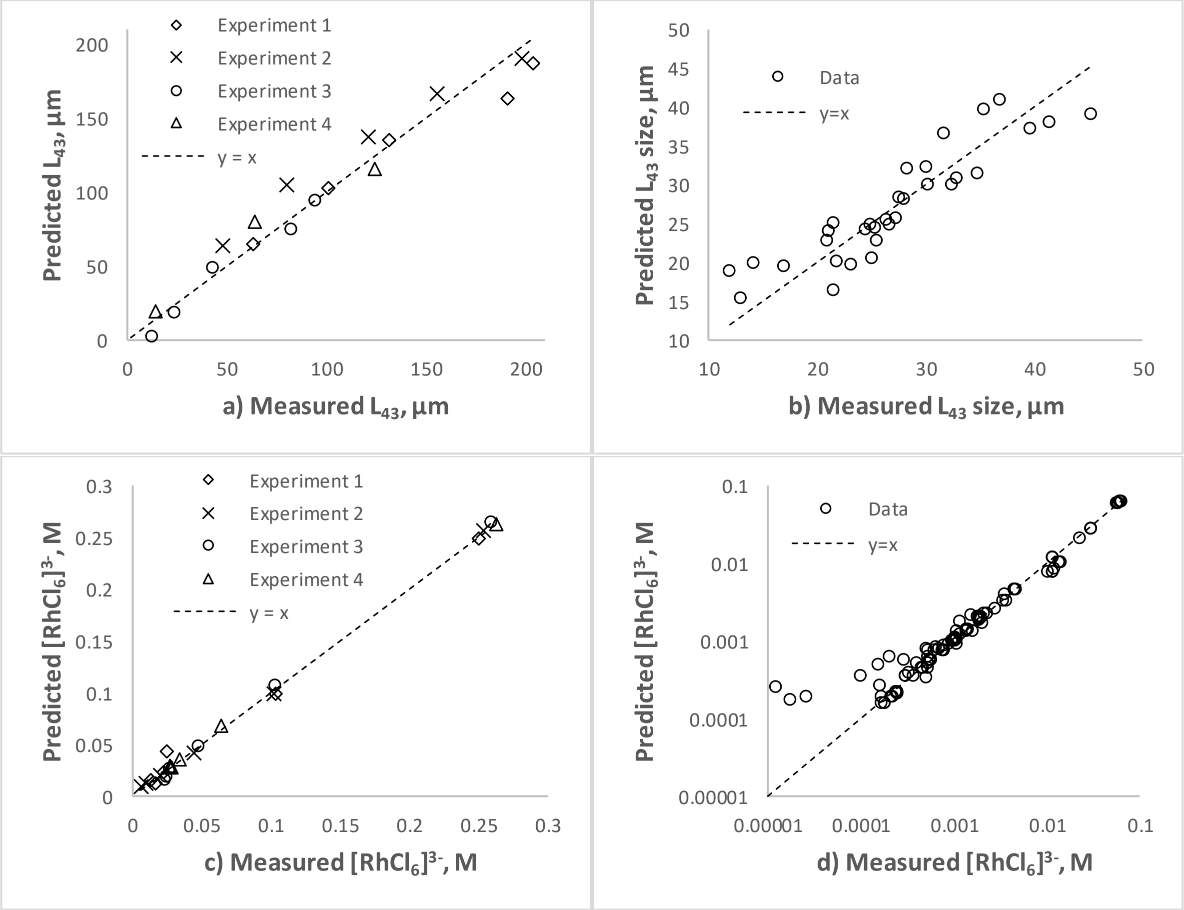

Figure 8.2.3: L_{43} size parity chart for a) CSTR configuration with $R^2 = 0.96$ and b) PFR configuration with $R^2 = 0.82$. Concentration parity chart for c) CSTR configuration with $R^2 = 0.97$ and d) PFR configuration with $R^2 = 0.99$.

The mathematical expressions used to describe the growth through interfacial attachment, growth by agglomeration, and population density at size zero as discussed above gave reasonable predictions of the L_{43} size through the moment transform of the population balance. Likewise, the aqueous concentration profile predictions compared well to the measurements. Therefore, the measured data is well represented by the models, as judged by the coefficient of determination and the parity charts in Figure 8.2.3.

8.3. CONCLUSIONS SUMMARY

Two reactor configurations, namely a CSTR and a t-mixer PFR, were used to determine nucleation and growth rates for diethylenetriammonium hexachlororhodate (III) crystals. The purpose was to eliminate mixing effects on nucleation and growth rates extracted from concentration and volume average crystal size profiles.

From a mixing scale time perspective in the CSTR configuration, the residence time was 30min to 1h compared to a macromixing time of 3.25s and meso- and microscale mixing times < 16ms. In the PFR the residence time varied from 4s to 30s. The short macromixing time in the CSTR relative to the residence time gives a strong argument for a homogenised bulk as Bałdyga & Bourne (1999) have argued. The retention time in the PFR is similar to the macromixing time of the CSTR but changed under certain flow conditions, such that it reached values that were ~8 fold greater than the CSTR macromixing time.

All experiments in the CSTR remained equilibrium-limited and the concentration profiles were adequately represented by a transient equilibrium based model. In comparison the PFR became mesomixing or micromixing limited at very low Reynolds numbers (long residence time) and equilibrium-limited as the residence time approached the macromixing time of the CSTR. Saturation in the CSTR was therefore defined from the assumption that the reactants are inert, thus the calculation represents saturation at the reactant dip-tube outlet. In the PFR, saturation was defined from concentration profiles that were determined from a series reaction pathway whereby either meso- or micromixing could limit reaction. Micro- and mesoscale mixing were represented by a characteristic length scale that was empirically related to temperature for the microscale and fluid velocity for the mesoscale.

From the two different reactor configuration models it was found that temperature dependent kinetic parameters were interchangeable. They are shown in Table 8.2.1. Parameters related to mixing were found to differ between the configurations as given in Table 8.2.2. The different mixing patterns in the reactor configurations are evident in the difference in morphology of the crystals produced in the reactors. The crystals in the PFR configuration appear to collide both in the radial and axial direction with an overall linear flow path giving rise to a feathery flat and elongated crystal cluster. In contrast the crystals in the CSTR configuration collide in a chaotic but consistent pattern giving rise to a desert rose-like crystal cluster.

No evidence of heterogeneous primary nucleation in the form of crystals adhering to the side walls of the reactor or the agitator blades was observed. The experiments were not explicitly designed to distinguish between primary and secondary nucleation mechanisms, therefore excluding one over the other is not justified. However, considering the presence of nucleated crystals in each system combined with the good model fit using a nucleation rate expression typically associated with secondary nucleation, it is likely that the dominating nucleation mechanism is secondary in nature.

In the PFR configuration, nucleation and growth occurred at greater rates in comparison to the CSTR configuration, as inferred from the kinetic parameters in Table 8.2.2. This observation is linked to a much higher mixing intensity achieved in the PFR relative to the CSTR. The crystal agglomeration rate was found to be greater in the CSTR relative to the PFR and this is related to physically more crystals present in the CSTR than in the PFR.

In Table 8.2.2 the PFR growth rate supersaturation exponent was 1.13, suggesting a BCF type growth model. This is indicative of crystal growth from screw dislocations that are limited through either diffusion processes to the crystal surface, or surface integration kinetics. Thus, it is expected that crystal conversion in the PFR configuration is responsive to mixing conditions at the micro- or mesoscale. In comparison the CSTR growth rate supersaturation exponent was 2.31, which is more in line with polynuclear growth. The difference relative to the PFR configuration is believed to be due to growth rate enhancement by the presence of sub-micron or nano crystals, as found by Matsuoka et al. (1996). Furthermore, the growth rate is likely to be limited by interfacial attachment kinetics as opposed to mass transfer as the bulk in the CSTR configuration equilibrates.

Lastly a key finding from this work is the ability to manipulate the crystal morphology by changing reactor configuration. By creating elongated flat crystal structures in the PFR configuration as opposed to a desert rose crystal structure in the CSTR, it may be possible to reduce impurities within the crystal by entraining less mother liquor. This observation provides a basis for future work to investigate the effect of morphology on impurity rejection for this system.

9. REFERENCES

Adekani, M. N., Costa, P. Breugem, W. P. & Brandt, L., 2016. Numerical study of the sedimentation of spheroidal particles. *International Journal of Multiphase Flow,* Volume 87: 16-34.

Aoun, M., Plasari, E., David, R. & Villermaux, J. 1996. Are barium sulphate kinetics sufficiently known for testing precipitation reactor models?. *Chemical Engineering Science,* 51(10): 2449-2458.

Atkins, P. W. 1997. *Physical Chemistry.* 6 ed. Oxford: Oxford University Press.

Aubin, J., Fletcher, D. F. & Xuereb, C. 2004. Modeling turbulent flow in stirred tanks with CFD: the influence of the modeling approach, turbulence model and numerical scheme. *Experimental theremal and Fluid Science,* 28: 431-445.

Bałdyga, J. 1989. Turbulent mixer model with application to homogeneous, instantaneous chemical reactions. *Chemical Engineering Science,* 44(5): 1175-1182.

Bałdyga, J. & Bourne, J. R. 1992. Interactions between mixing on various scales in stirred tank reactors. *Chemical Engineering Science,* 47(8): 1839-1848.

Bałdyga, J. & Bourne, J. R. 1999. *Turbulent Mixing and Chemical Reactions.* New York: John Wiley & Sons, ISBN: 0471981710.

Bałdyga, J., Bourne, J. R. & Hern, S. J. 1997. Interaction between chemical reactions and mixing on various scales. *Chemical Engineering Science,* 52(4): 457-466.

Bałdyga, J., Bourne, J. R. & Walker, B. 1998. Non-isothermal micromixing in turbulent liquids: theory and experiment. *Canadian Journal of Chemical Engineering,* 76: 641-649.

Bałdyga, J., Makowski, Ł. & Orciuch, W. 2007. Double-feed semibatch precipitation: Effects of mixing. *Chemical Engineering Research and Design,* 85(A5): 745-752.

Bałdyga, J., Podgorska, W. & Pohorecki, R. 1995. Mixing-precipitation model with application to double feed semibatch precipitation. *Chemical Engineering Science,* 50(8): 1281-1300.

Beckmann, W. (Ed). 2013. *Crystallization. Basic Concepts and Industrial Applications.* Weinheim: Wiley-VCH.

Boss, C. B. & Fredeen, K. J. 2004. *Concepts, Instrumentation and Techniques in Inductively Coupled Plasma Optical emission Spectrometry,* Shelton: PerkinElmer, Inc..

Brits, B. 2014. *Personal communication: Rh-DETA salt metal content, S2014_165.* Johannesburg(Gauteng): Anglo Technical Solutions.

Burden, R. L. & Faires, D. J. 1993. *Numerical Analysis, 5th Edition.* Boston: Prindle, Weber and Schmidt.

Burnham, R. F., Cox, M. A., Drake, V. A., Grant, R. A., Smith, A. J., Smith, C. S. & Taylor, J. R., 1993. *Internal Report: The Application of Polyamines to the Refining of the Precious Metals.* Sonning: Johnson Matthey Technology Centre, Project 014RM003.

Byron, M. 2015. *The rotation and translation of non-spherical particles in homogeneous isotropic turbulence.* Doctoral Dissertation*,* Berkeley: University of California.

Coleman, T. F. & Li, Y. 1994. On the Convergence of Reflective Newton Methods for Large-Scale Nonlinear Minimization Subject to Bounds. *Mathematical Programming,* 67(2): 189-224.

Coleman, T. F. & Li, Y. 1996. An Interior, Trust Region Approach for Nonlinear Minimization Subject to Bounds. *SIAM Journal on Optimization, 6:* 418-445.

Cowley, A, 2013. *Platinum 2013: Interim Review.* Roysten: Johnson Matthey.

Crozier, W. D. & Grant, R. A. 1992. USA, Patent No. 5165901.

Denisov, E. T., Sarkisov, O. M. & Likhtenshtein, G. I. 2003. *Chemical Kinetics: Fundamentals and New Developments.* Elsevier, ISBN: 978-0-444-50938-3.

Dirksen, J. A. & Ring, T. A. 1991. Fundamentals of crystallization: Kinetic effects on particle size distributions and morphology. *Chemical Engineering Science,* 46(10): 2389-2427.

Falk, L. & Villermaux, J. 1997. Numerical Scale-up and Design of High-Efficiency Mixers for Control and Optimisation of the Yield and Selectivity in Chemical Reactors. *Applied Thermal Engineering,* 17: 845-859.

Fang, J. Z. & Lee, D. J. 2001. Micromixing efficiency in static mixer. *Chemical Engineering Science. 56:* 3797-3802.

Ferguson, S., Morris, G., Hao, H., Barrett, M., Glennon, B. 2013. Characterization of the anti-solvent batch, plug flow and MSMPR crystallization of benzoic acid. *Chemical Engineering Science,* 104: 44-54.

Fortes, A. F., Joseph, D. D. & Lundgren, T. S. 1987. Nonlinear mechanics of fludization of beds of spherical particles. *Journal of Fluid Mechanics,* 177: 467-483.

Fournier, M. C., Falk, L. & Villermaux, J. 1996. A new parallel competing reaction system for assessing micromixing efficiency-experimental approach. *Chemical Engineering Science, .* 51*:* 5053-5064.

Gaines, P. 2010. *ICP-OES Measurement - Trace Analysis Guide: Part 15.* [Online] Available at: http://www.inorganicventures.com/tech/trace-analysis/icp-oes-measurement [Accessed 2010].

Garside, J., Mersmann, A. & Nyvlt, J. 2002. *Measurement of Crystal Growth and Nucleation rates,* 2nd Edition. Rugby: IChemE, ISBN: 0852954492.

Geswindt, T. E, 2013. *Chemical speciation of RhIII complexes in acidic, halide-rich media by means of 103Rh NMR spectroscopy: The importance of speciation in the selective separation and recovery of rhodium*. PhD Dissertation. Stellenbosch: Stellenbosch University.

Ghanem, A., Lemenand, T. & Della Valle, D. 2014. Static mixers: Mechanisms, applications, and charaterization methods - A review. *Chemical Engineering Research and Design,* Volume 92: 205-228.

Hagemann, J. P., Botha, J. J., Lewis, A. E. & Bryson, A. 2003. *Internal Report: The production of rhodium via the DETA route: Report 1.* Johannesburg: Anglo Platinum Management Services (Pty) Ltd.

Jager, J., De Wolf, S. & Kramer, H. J. M. 1991. Estimation of nucleation kinetics from crystal size distribution transients of continuous crystallizer. *Chemical Engineering Science,* 46(3): 807-818.

Javed, K., Mahmud, T. & Zhu, J. 2006. Numerical Simulation of Turbulent Batch Mixing in a Vessel Agitated by a Rushton Turbine. *Chemical Engineering and Processing,* Volume 45: 99-112.

Johnson, N. L., Kotz, S. & Balakrishnan, N. 1994. *Continuous univariate distributions. Vol. 1 - Wiley Series in Probability and Mathematical Statistics: Applied Probability and Statistics,* 2nd Edition. New York: John Wiley & Sons, ISBN 978-0-471-58495-7.

Jolly, W. L. 1984. *Modern Inorganic Chemistry.* Michigan: McGraw-Hill.

Jones, A. G. 2002. *Crystallization Process Systems.* Oxford: Butterworth Heinemann, ISBN 0 7506 5520 8.

Jung, W.-M., Kang, S. H., Kim, W.-S. & Choi, C. K. 2010. Precipitation of calcium carbonate particles by gas-liquid reaction: Morphology and size distribution of particles in Couette-Taylor and stirred tank reactors. *Journal of Crystal Growth,* 312: 3331-3339.

Kenney, J. F. & Keeping, E. S. 1951. *Mathematics of Statistics, Pt. 2.* 2nd Edition. Princeton, NJ: Van Nostrand.

Ku, H. H. 1966. Notes on the Use of Porpagation of Error Formulas. *Journal of Research of the National Bureau of Standards - C. Engineering and Instrumentation,* 70C(4): 263-274.

Lagarias, J. C., Reeds, J. A., Wright, M. H. & Wright, P. E. 1998. Convergence Properties of the Nelder-Mead Simplex Method in Low Dimensions. *SIAM Journal of Optimization,* 9(1): 112-147.

Leubner, I. H. 2009. *Precision Crystallization: Theory and Practice of Controlling Crystal Size.* Boca Raton: CRC Press.

Levenspiel, O. 1999. *Chemical Reaction Engineering.* 3rd ed. New York: John Wiley & Sons.

Lide, D. R. 2007. *CRC Handbook of Chemistry and Physics.* 88th ed. s.l.:Taylor & Francis.

Lindenberg, C., Schöll, J., Vicum, L., Mazzotti, M., Brozio, J. 2008. Experimental characterization and multi-scale modelling of mixing in static mixers. *Chemical Engineering Science, 63:* 4135-4149.

Makaryan, I. A., Sedov, I. V. & Savchenko, V. I. 2015. Platinum Group Metal-Catalysed Carbonylation as the Basis of Alternative Gas-To-Liquids Processes. *Johnson Matthey Technology Review* 59*:* 14-25.

Malvern Instruments Ltd., 2007. *Mastersizer 2000 User Manual.* 1 ed. Worcestershire: Malvern.

Massey, B. S. 1970. *Mechanics of Fludis.* London: Van Nostrand Reinhold Company Ltd.

Matsuoka, M. & Eguchi, N. 1993. Growth of m-chloronitrobenzene crystals in the presenece of microcrystals. *Journal of Physics D: Applied Physics,* 26*:* 162-167.

Matsuoka, M., Kamada, T. & Takiyama, H., 1996. Growth rate enhancement of potash alum crystals by microcrystals. *Journal of Crystal Growth,* 158*:* 322-327.

Mersmann, A. 2001. *Crystallization Technology Handbook, 2nd Edition.* New York: Marcel Dekker, Inc.

Myerson, A. S. 2002. *Handbook of Industrial Crystallization, 2nd Endition.* Boston: Butterworth-Heinemann, ISBN: 0750670126.

Nielsen, A. E. 1961. Homogeneous Nucleation in Barium Sulfate Precipitation. *Acta Chemica Scandinavica No. 2:* 441-442.

Nienow, A. W. 1997. On impeller circulation and mixing effectiveness in the turbulent flow regime. *Chemical Engineering Science,* 52(15): 2557-2565.

Perry, R. H. & Green, D. W. 1998. *Perry's Chemical Engineers' Handbook, 8th Edition.* New York: McGraw-Hill, ISBN: 0071601503.

Pitzer, S. 1993. Thermodynamics of natural and industrial waters. *The Journal of Chemical Thermodynamics,* January, 25(1): 7-26.

Ramkrishna, D. 2000. *Population Balances: Theory and Applications to Particulate Systems in Engineering.* San Diego: Academic Press, ISBN: 0125769709.

Randolph, A. D. & Larson, M. A. 1971. *Theory of Particulate Processes: Analysis and techniques of Continuous Crystallization.* s.l.:Elsevier Inc.

Shampine, L. F. & Reichelt, M. W. 1997. The MATLAB ODE Suite. *SIAM Journal on Scientific Computing,* 18: 1-22.

Shampine, L. F., Reichelt, M. W. & Kierzenka, J. A. 1999. Solving Index-1 DAEs in MATLAB and Simulink. *SIAM Review,* 41: 538-552.

Söhnel, O. & Garside, J. 1992. *Precipitation: Basic Principles and Industrial Applications.* Michigan: Butterworth-Heinemann.

Sowul, L. & Epstein, M. A. F. 1981. Crystallization kinetics of sucrose in a CMSMPR evaporative crystallizer. *Industrial and Engineering Chemistry Process Design and Development,* 29(2): 197-203.

Spanier, J. & Oldham, K. B. 1987. The Error Function erf(x) and its Complement erfc(x). In *An Atlas Of Functions.* Washington DC: Hemisphere: 385-393.

Sposito, G. 1994. *Chemical Equilibria and Kinetics in Soils.* New York: Oxford University Press, Inc., ISBN 0-19-507564-1.

Surender, V. & Rao, K. K. 1993. Growth and habit modifcation of sodium chlorate crystals. *Bulletin of Material Science,* 16(2): 155-158.

Tavare, N. S. 1986. Crystallization kinetics from transients of an MSMPR crystallizer. *The Canadian Journal of Chemical Engineering,* 64(5): 752-758.

Timm, D. C. & Larson, M. A. 1968. Effect of nucleation kinetics on the dynamic behavior of a continuous crystallizer. *American Institute of Chemical Engineers,* 14(3): 452-457.

Torbacke, M. & Rasmuson, C. 2001. Influence of different scales of mixing in reaction crystallisation. *Chemical Engineering Science,* 56(7): 2459-2473.

Vicum, L. 2005. *Investigation of the influence of turbulent mixing on precipitation processes carried out in stirred tank reactors, PhD dissertation,* Zurich: ETH.

Villermaux, J., Falk, L., Fournier, M. C. & Detrez, C. 1992. Use of parallel competing reactions to characterize micromixing efficiency. *A.I.Ch.E. Symposium Series,* 286(88): 6-10.

Vining, G. 1998. *Statistical Methods for Engineers.* London: Brooks & Cole.

Weisstein, E. W. 2016. *Log Normal Distribution.* [Online] Available at: http://mathworld.wolfram.com/LogNormalDistribution.html.

Wikipedia, 2016. *Desert rose (crystal).* [Online] Available at: https://en.wikipedia.org/wike/Desrt_rose_(crystal).

Wilcox, R. R. 2003. *Applying Contemporary Statistical Techniques.* Los Angeles: Elsevier Inc.

Wright, M. 2007. *An Introduction to Aqueous Electrolyte Solutions.* Chichester: John Wiley & Sons, Ltd.

Zauner, R. & Jones, A. G. 2000. Determination of nucleation, growth, agglomeration and disruption kinetics from experimental precipitation data: the calcium oxalate system. *Chemical Engineering Science,* 55: 4219-4232.

Zauner, R. & Jones, A. G. 2002. On the influence of mixing on crystal precipitation processes - application of the segregated feed model. *Chemical Engineering Science 57:* 821-831.

10. APPENDIX

10.1. PFR CONFIGURATION INLET ACTIVITY AND SATURATION

Table 10.1.1: Initial reagent concentrations (A = $RhCl_6^{3-}$, B = $DETA.3H^{3+}$) and saturation in the t-mixer PFR experiments

Test	x, m	T, °C	$C_A\|_{x=0}$, M	$C_B\|_{x=0}$, M	K_{SP}, M^2 Equation (3.1.9)	$\gamma_{\pm}\|_{x=0}$ Equation (3.1.8)	$S\|_{x=0}$ Equation (3.2.22)
1	4.84	30	4.95E-03	2.18E-02	1.739E-06	0.698	7.0
2	4.84	30	4.95E-03	2.18E-02	1.739E-06	0.698	7.0
3	4.84	30	4.95E-03	2.18E-02	1.739E-06	0.698	7.0
4	4.84	30	4.95E-03	2.18E-02	1.739E-06	0.698	7.0
5	4.84	30	4.97E-03	2.17E-02	1.739E-06	0.699	7.0
6	4.84	30	4.97E-03	2.17E-02	1.739E-06	0.699	7.0
7	4.84	30	4.97E-03	2.17E-02	1.739E-06	0.699	7.0
8	4.84	35	4.99E-03	2.18E-02	2.191E-06	0.698	6.3
9	4.84	35	4.99E-03	2.18E-02	2.191E-06	0.698	6.3
10	4.84	35	4.99E-03	2.18E-02	2.191E-06	0.698	6.3
11	4.84	20	4.97E-03	2.19E-02	1.070E-06	0.697	8.9
12	4.84	20	4.97E-03	2.19E-02	1.070E-06	0.697	8.9
13	4.84	20	4.97E-03	2.19E-02	1.070E-06	0.697	8.9
14	4.84	38	4.99E-03	2.18E-02	2.508E-06	0.698	5.9
15	4.84	37	4.99E-03	2.18E-02	2.399E-06	0.698	6.0
16	4.84	38	4.99E-03	2.18E-02	2.508E-06	0.698	5.9
17	4.84	50	4.99E-03	2.18E-02	4.199E-06	0.698	4.5
18	4.84	50	4.99E-03	2.18E-02	4.199E-06	0.698	4.5
19	4.84	50	4.99E-03	2.18E-02	4.199E-06	0.698	4.5
20	4.84	47	4.94E-03	4.95E-03	3.705E-06	0.875	2.5
21	4.84	51	4.94E-03	4.95E-03	4.375E-06	0.875	2.3
22	4.84	52	4.94E-03	4.95E-03	4.558E-06	0.875	2.2
23	4.84	47	4.92E-03	4.96E-03	3.705E-06	0.875	2.5
24	4.84	45	4.92E-03	4.96E-03	3.404E-06	0.875	2.6
25	4.84	45	4.92E-03	4.96E-03	3.404E-06	0.875	2.6
26	4.84	30	4.92E-03	4.96E-03	1.739E-06	0.875	3.7
27	4.84	30	4.92E-03	4.96E-03	1.739E-06	0.875	3.7
28	4.84	30	4.92E-03	4.96E-03	1.739E-06	0.875	3.7
29	4.84	44	4.92E-03	4.96E-03	3.261E-06	0.875	2.7
30	4.84	45	4.92E-03	4.96E-03	3.404E-06	0.875	2.6
31	4.84	43	4.92E-03	4.96E-03	3.124E-06	0.875	2.7
32	2.95	33	1.47E-01	9.27E-02	2.000E-06	0.045	53.8
33	2.95	34	1.47E-01	9.27E-02	2.094E-06	0.045	52.5
34	2.95	34	1.47E-01	9.27E-02	2.094E-06	0.045	52.5
35	2.95	54	1.47E-01	9.27E-02	4.943E-06	0.045	32.6
36	2.95	53	1.47E-01	9.27E-02	4.747E-06	0.045	33.4
37	2.95	54	1.47E-01	9.27E-02	4.943E-06	0.045	32.6
38	2.95	40	9.27E-02	1.46E-01	2.741E-06	0.045	42.0
39	2.95	40	9.27E-02	1.46E-01	2.741E-06	0.045	42.0
40	2.95	40	9.27E-02	1.46E-01	2.741E-06	0.045	42.0

Test	x, m	T, °C	$C_A\|_{x=0}$, M	$C_B\|_{x=0}$, M	K_{SP}, M^2 Equation (3.1.9)	$\gamma_{\pm}\|_{x=0}$ Equation (3.1.8)	$S\|_{x=0}$ Equation (3.2.22)
41	2.95	40	1.18E-01	1.21E-01	2.741E-06	0.045	64.0
42	2.95	40	1.18E-01	1.21E-01	2.741E-06	0.045	64.0
43	2.95	40	1.18E-01	1.21E-01	2.741E-06	0.045	64.0
44	2.95	70	1.21E-01	1.18E-01	9.145E-06	0.045	27.8
45	2.95	70	1.21E-01	1.18E-01	9.145E-06	0.045	27.8
46	2.95	70	1.21E-01	1.18E-01	9.145E-06	0.045	27.8
47	2.95	70	1.18E-01	1.21E-01	9.145E-06	0.045	33.9
48	2.95	70	1.18E-01	1.21E-01	9.145E-06	0.045	33.9
49	2.95	70	1.18E-01	1.21E-01	9.145E-06	0.045	33.9
50	2.95	55	1.21E-01	1.18E-01	5.146E-06	0.045	41.0
51	2.95	55	1.18E-01	1.21E-01	5.146E-06	0.045	46.3
52	2.95	65	1.05E-02	9.88E-03	7.593E-06	0.760	3.5
53	2.95	65	1.05E-02	9.88E-03	7.593E-06	0.760	3.5
54	2.95	65	1.05E-02	9.88E-03	7.593E-06	0.760	3.5
55	2.95	30	1.03E-02	1.01E-02	1.739E-06	0.760	7.5
56	2.95	30	1.03E-02	1.01E-02	1.739E-06	0.760	7.5
57	2.95	30	1.03E-02	1.01E-02	1.739E-06	0.760	7.5
58	2.95	30	6.92E-03	1.34E-02	1.739E-06	0.761	6.9
59	2.95	30	6.92E-03	1.34E-02	1.739E-06	0.761	6.9
60	2.95	30	6.92E-03	1.34E-02	1.739E-06	0.761	6.9
61	2.95	50	6.96E-03	1.33E-02	4.199E-06	0.761	4.4
62	2.95	50	6.96E-03	1.33E-02	4.199E-06	0.761	4.4
63	2.95	50	6.96E-03	1.33E-02	4.199E-06	0.761	4.4
64	2.95	30	1.05E-02	1.48E-01	1.739E-06	0.126	12.0
65	2.95	50	1.06E-02	1.45E-01	4.199E-06	0.129	7.8
66	2.95	40	1.06E-02	1.45E-01	2.741E-06	0.129	9.7
67	2.95	40	1.06E-02	1.45E-01	2.741E-06	0.129	9.7
68	2.95	40	1.06E-02	1.45E-01	2.741E-06	0.129	9.7
69	2.95	60	1.11E-02	1.39E-01	6.269E-06	0.139	6.5
70	2.95	60	1.06E-02	1.45E-01	6.269E-06	0.129	6.4
71	2.95	60	1.05E-02	1.47E-01	6.269E-06	0.127	6.3
72	2.95	60	1.04E-02	1.48E-01	6.269E-06	0.125	6.3
73	2.95	40	1.11E-02	1.39E-01	2.741E-06	0.139	9.9
74	2.95	40	1.06E-02	1.45E-01	2.741E-06	0.129	9.7
75	2.95	40	1.05E-02	1.47E-01	2.741E-06	0.127	9.6
76	2.95	40	1.04E-02	1.48E-01	2.741E-06	0.125	9.5
77	2.95	50	1.11E-02	1.39E-01	4.199E-06	0.139	8.0
78	2.95	50	1.06E-02	1.45E-01	4.199E-06	0.129	7.8
79	2.95	50	1.05E-02	1.47E-01	4.199E-06	0.127	7.7
80	2.95	50	1.04E-02	1.48E-01	4.199E-06	0.125	7.7
81	2.95	60	1.11E-02	1.39E-01	6.269E-06	0.139	6.5
82	2.95	60	1.06E-02	1.45E-01	6.269E-06	0.129	6.4
83	2.95	60	1.05E-02	1.47E-01	6.269E-06	0.127	6.3
84	2.95	60	1.04E-02	1.48E-01	6.269E-06	0.125	6.3

Test	x, m	T, °C	$C_A\|_{x=0}$, M	$C_B\|_{x=0}$, M	K_{SP}, M^2 Equation (3.1.9)	$\gamma_\pm\|_{x=0}$ Equation (3.1.8)	$S\|_{x=0}$ Equation (3.2.22)
85	2.95	70	1.11E-02	1.39E-01	9.145E-06	0.139	5.3
86	2.95	70	1.06E-02	1.45E-01	9.145E-06	0.129	5.2
87	2.95	70	1.05E-02	1.47E-01	9.145E-06	0.127	5.2
88	2.95	70	1.04E-02	1.48E-01	9.145E-06	0.125	5.2
89	4.84	40	8.65E-03	1.25E-01	2.741E-06	0.172	9.1
90	4.84	40	8.15E-03	1.34E-01	2.741E-06	0.154	8.7
91	4.84	40	8.03E-03	1.36E-01	2.741E-06	0.150	8.6
92	4.84	40	7.92E-03	1.38E-01	2.741E-06	0.147	8.4
93	4.84	50	8.65E-03	1.25E-01	4.199E-06	0.172	7.3
94	4.84	50	8.15E-03	1.34E-01	4.199E-06	0.154	7.0
95	4.84	50	8.03E-03	1.36E-01	4.199E-06	0.150	6.9
96	4.84	50	7.92E-03	1.38E-01	4.199E-06	0.147	6.8
97	4.84	60	8.65E-03	1.25E-01	6.269E-06	0.172	6.0
98	4.84	60	8.15E-03	1.34E-01	6.269E-06	0.154	5.7
99	4.84	60	8.03E-03	1.36E-01	6.269E-06	0.150	5.6
100	4.84	60	7.92E-03	1.38E-01	6.269E-06	0.147	5.6
101	4.84	70	8.65E-03	1.25E-01	9.145E-06	0.172	4.9
102	4.84	70	8.15E-03	1.34E-01	9.145E-06	0.154	4.7
103	4.84	70	8.03E-03	1.36E-01	9.145E-06	0.150	4.7
104	4.84	70	7.92E-03	1.38E-01	9.145E-06	0.147	4.6

10.2. AGGREGATION AND DISRUPTION MODEL JUSTIFICATION

In this section the model proposed in Equation (3.1.13) is justified by population density flux over a particle surface. The diagram below depicts the concept from a Lagrangian frame of reference. Note that the following derivation is for a system where particles aggregate due to diffusion and convection.

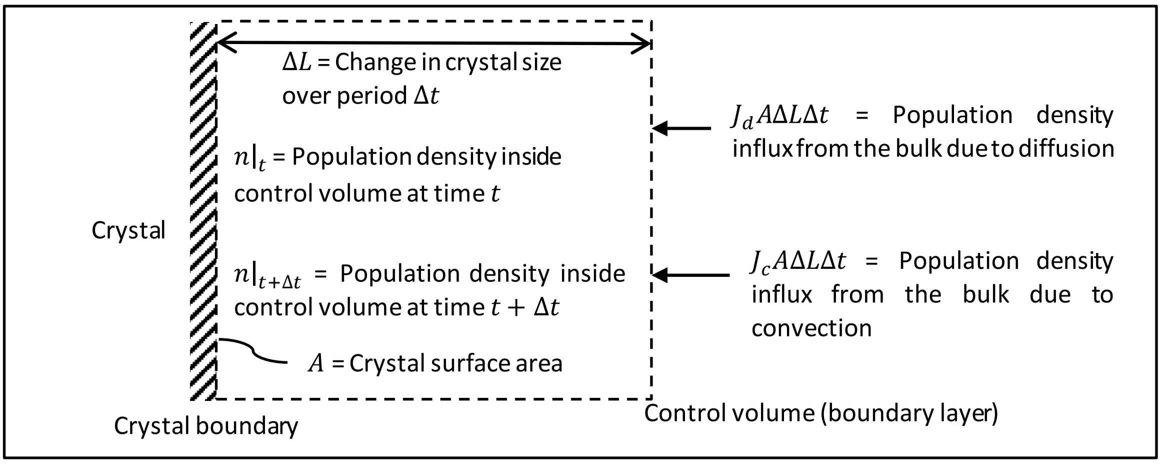

Figure 10.2.1: Control volume concept for crystal enlargement due to convection and diffusion

Equation (10.2.1) is derived through the principle of accumulation is equal to influx less outflux depicted in Figure 10.2.1.

$$n|_t A\Delta L - n|_{t+\Delta t} A\Delta L = J_d A\Delta t + J_c A\Delta t \qquad \textbf{(10.2.1)}$$

Where n = Population density [#/µm.m^3]
J_d = Population density flux due to diffusion [#/µm.m^3.m^2.h]

J_c = Population density flux due to convection [#/µm.m^3.m^2.h]
A = Crystal surface area [m^2]
t = Time [h]
Δt = Infinitesimal change in time [h]
L = Crystal size [µm]
ΔL = Infinitesimal change in crystal size [µm]

From Fick's first law described in Atkins (1997), diffusive flux is the product of the diffusion coefficient and the intrinsic property gradient with respect to length. In this example length refers to the crystal size. The diffusion coefficient is assumed to be the product between the crystal growth rate due to interfacial attachment, growth due to agglomeration, and the time available for agglomeration (residence time). Equation (10.2.2) incorporates the above assumption regarding the diffusion coefficient and expands the diffusive flux term.

$$J_d = GG_a\tau\frac{n|_L - n|_{L+\Delta L}}{\Delta L} \qquad \textbf{(10.2.2)}$$

In Equation (10.2.3) the convective flux term expansion assumes that the convection velocity is represented by the growth through interfacial attachment.

$$J_c = G(n|_L - n|_{L+\Delta L}) \qquad \textbf{(10.2.3)}$$

By inserting Equations (10.2.2) and (10.2.3) into Equation (10.2.1), dividing by $A\Delta L\Delta t$ and taking the limit as $\Delta L, \Delta t \to 0$, Equation (10.2.4) emerges.

$$\frac{\partial n}{\partial t} = \frac{\partial}{\partial L}\left[G_a\tau\left(G\frac{\partial n}{\partial L} + \frac{n}{\tau}\right)\right] = R_{ag} \qquad \textbf{(10.2.4)}$$

10.3. LOGNORMAL POPULATION DENSITY DERIVATION

Let $\phi(L)$ be the differential form of the volume fraction cumulative size distribution (volume fraction density distribution). Let n be the population density as defined in Garside et al. (2002), Jones (2002) and Mersmann (2001). The standard definition of the population density is that it is the number of particles or crystals per size class per unit volume of suspension. Jones (2002) amongst many other sources defines the third moment of the population density function as the volume of crystals per volume of suspension. Furthermore, a common assumption is a constant volume shape factor that translates to the factor cancelling out when calculating the volume fraction, as shown in Equation (10.3.1),

$$\phi(L) = \frac{d}{dL}\left(\frac{\int_0^L nl^3 dl}{\int_0^\infty nl^3 dl}\right) = \frac{nL^3}{\int_0^\infty nl^3 dl} = \frac{nL^3}{M_3} \qquad \textbf{(10.3.1)}$$

Where $\phi(L)$ = Volume fraction density distribution as a function of size L [µm^{-1}]
n = Population density function [#/µm.dm^3]
M_3 = Third moment of the population density (volume of particles per volume of suspension) [#.µm^3/dm^3]

If the relationship of the volume fraction distribution is known, Equation (10.3.1) can be rearranged such that the population density is the argument. Under the premise that the volume fraction distribution is a mixed lognormal distribution, the population density function is likely to be represented by Equation (10.3.2).

$$\begin{aligned} &Let\ \ \phi(L) = \frac{1}{L}\sum_{i=1}^{p}\frac{x_i}{\sqrt{2\pi}s_i}exp\left(-\frac{(\ln L - m_i)^2}{2s_i^2}\right) \\ &\therefore n = \frac{M_3\phi(L)}{L^3} = \frac{M_3}{L^4}\sum_{i=1}^{p}\frac{x_i}{\sqrt{2\pi}s_i}exp\left(-\frac{(\ln L - m_i)^2}{2s_i^2}\right) \end{aligned} \qquad \textbf{(10.3.2)}$$

Where m_i = Location parameter of the ith lognormal distribution
s = Spread parameter of the ith lognormal distribution
L = Crystal size [μm]
x_i = Contribution of the ith lognormal distribution ($\sum_{i=1}^{p} x_i = 1$ and $0 \leq x_i \leq 1$)

10.4. AVERAGE CRYSTAL SIZE FOR T-MIXER PFR EXPERIMENTS

The crystal size distributions for the test 73 to 104 in Table 4.4.1 are tabulated in Table 10.4.1. All the measured cumulative volume fraction distributions by Malvern Mastersizer are described by a mixed lognormal distribution. The location and spread parameters of the distribution as well as the distribution weighting are determined through non-linear regression and are tabulated Table 3.4.2. Equation (10.4.1) shows the mixed lognormal distribution that is applied to the data.

$$\phi(L)=\frac{1}{L}\sum_{i=1}^{2}\frac{x_i}{\sqrt{2\pi}s_i}exp\left(-\frac{(\ln L-m_i)^2}{2s_i^2}\right) \quad \& \; x_1+x_2=1$$
$$\therefore \Phi(L)=\int_0^L \phi(L')\,dL'=\frac{1}{2}\left[1+x_1 erf\left(\frac{\ln L-m_1}{\sqrt{2}s_1}\right)+(1-x_1)erf\left(\frac{\ln L-m_2}{\sqrt{2}s_2}\right)\right] \qquad \textbf{(10.4.1)}$$

The location, spread and distribution contribution fraction parameters in Equation (10.4.1) are determined by non-linear least squares. The average particle size L_{43} is calculated from the identity in Equation (4.3.5). For a mixed lognormal distribution consisting of two component distributions, the identity reduces to Equation (10.4.2). Table 10.4.1 shows the fitted parameters for the test results in Tables 10.4.2 to 10.4.5 and the associated L_{43} size as calculated from Equation (10.4.2).

$$L_{43}=\int_0^\infty \phi(L)\,LdL = x_1 exp\left(m_1+\frac{s_1^2}{2}\right)+(1-x_1)exp\left(m_2+\frac{s_2^2}{2}\right) \qquad \textbf{(10.4.2)}$$

Tables 10.4.2 to 10.4.5 give the raw data of the cumulative crystal size distributions for the crystals produced in Tests 73 to 104.

Table 10.4.1: Plug flow reactor product crystal size distribution mixed lognormal parameters

Test	R^2	x_1	m_1	s_1	m_2	s_2	L_{43}, M
73	0.9997	0.1163	0.821	1.523	2.680	0.670	17.0
74	0.9997	0.0547	-0.663	0.020	2.458	0.701	14.1
75	0.9999	0.0761	-0.544	0.352	2.321	0.690	12.0
76	0.9998	0.0703	-0.520	0.379	2.406	0.668	12.9
77	0.9999	0.0444	-0.526	0.358	3.011	0.796	26.7
78	0.9999	0.0373	-0.452	0.434	3.015	0.719	25.4
79	0.9999	0.0372	-0.452	0.418	2.975	0.722	24.5
80	0.9998	0.0348	-0.441	0.431	3.017	0.686	25.0
81	0.9997	0.0364	-0.501	0.383	3.230	0.843	34.8
82	0.9999	0.0333	-0.455	0.432	3.253	0.742	32.9
83	0.9999	0.0328	-0.453	0.437	3.251	0.721	32.4
84	1.0000	0.0324	-0.392	0.502	3.222	0.664	30.3
85	0.9998	0.0349	-0.482	0.381	3.234	0.858	35.4
86	0.9999	0.0038	0.769	0.163	3.542	0.744	45.3
87	0.9999	0.0027	-0.454	0.436	3.477	0.706	41.4
88	0.9998	0.0306	0.028	1.030	3.485	0.669	39.6

Test	R^2	x_1	m_1	s_1	m_2	s_2	L_{43}, M
89	0.9998	0.0580	-0.251	0.708	2.902	0.770	23.1
90	0.9996	0.1121	0.809	1.390	3.039	0.740	25.0
91	0.9996	0.0995	0.387	1.226	2.902	0.742	21.9
92	0.9996	0.1032	0.430	1.275	2.901	0.723	21.5
93	0.9999	0.0393	-0.578	0.297	2.795	0.797	21.6
94	0.9998	0.0455	-0.442	0.429	2.945	0.828	25.6
95	0.9998	0.0508	-0.482	0.390	2.782	0.785	20.9
96	0.9998	0.0528	-0.420	0.462	2.808	0.763	21.0
97	0.9997	0.0500	-0.504	0.364	2.994	0.896	28.4
98	0.9998	0.0481	-0.485	0.387	3.019	0.849	28.0
99	0.9998	0.0517	-0.461	0.418	3.010	0.837	27.3
100	0.9997	0.0576	-0.363	0.565	3.029	0.777	26.4
101	0.9994	0.0343	-0.512	0.335	3.239	0.896	36.8
102	0.9998	0.0421	-0.466	0.390	3.137	0.850	31.7
103	0.9998	0.0439	-0.462	0.395	3.098	0.836	30.1
104	0.9999	0.0492	-0.390	0.480	3.048	0.796	27.5

Table 10.4.2: Plug flow reactor cumulative volume per cent crystal size distributions for Test 73 - 80

Size, µm	*Test 73*	*Test 74*	*Test 75*	*Test 76*	*Test 77*	*Test 78*	*Test 79*	*Test 80*
0.26	0.00	0.00	0.00	0.00	0.00	0.00	0.00	0.00
0.30	0.02	0.01	0.01	0.01	0.02	0.01	0.01	0.01
0.34	0.16	0.24	0.32	0.28	0.17	0.13	0.11	0.11
0.39	0.52	0.71	0.93	0.82	0.53	0.39	0.37	0.34
0.45	1.07	1.41	1.80	1.60	1.02	0.76	0.73	0.68
0.51	1.75	2.26	2.86	2.54	1.60	1.20	1.17	1.09
0.59	2.49	3.18	3.99	3.55	2.23	1.68	1.66	1.53
0.68	3.21	4.06	5.07	4.52	2.85	2.15	2.14	1.97
0.78	3.84	4.82	6.01	5.35	3.40	2.58	2.57	2.37
0.89	4.34	5.40	6.73	5.99	3.84	2.92	2.93	2.70
1.02	4.69	5.79	7.22	6.42	4.17	3.18	3.20	2.95
1.17	4.90	6.01	7.50	6.67	4.38	3.35	3.38	3.12
1.35	5.02	6.12	7.67	6.80	4.51	3.45	3.50	3.23
1.55	5.11	6.20	7.81	6.90	4.60	3.52	3.58	3.32
1.78	5.21	6.30	8.01	7.04	4.67	3.58	3.66	3.39
2.04	5.38	6.50	8.37	7.29	4.77	3.67	3.74	3.47
2.34	5.66	6.86	8.99	7.75	4.89	3.77	3.85	3.55
2.69	6.13	7.50	9.99	8.51	5.06	3.92	3.99	3.64
3.09	6.84	8.49	11.47	9.67	5.32	4.13	4.21	3.75
3.55	7.89	9.97	13.56	11.34	5.73	4.45	4.55	3.95
4.07	9.37	12.05	16.35	13.65	6.35	4.94	5.09	4.29
4.68	11.39	14.84	19.91	16.68	7.29	5.70	5.94	4.88
5.37	14.05	18.41	24.30	20.52	8.66	6.82	7.20	5.85
6.17	17.46	22.84	29.49	25.21	10.55	8.43	9.01	7.32
7.08	21.65	28.09	35.43	30.73	13.06	10.65	11.46	9.44

Size, µm	*Test 73*	*Test 74*	*Test 75*	*Test 76*	*Test 77*	*Test 78*	*Test 79*	*Test 80*
8.13	26.65	34.12	41.99	37.00	16.27	13.58	14.67	12.33
9.33	32.40	40.77	48.98	43.88	20.20	17.30	18.68	16.05
10.72	38.80	47.86	56.18	51.17	24.83	21.86	23.50	20.67
12.30	45.67	55.15	63.32	58.63	30.09	27.21	29.07	26.13
14.13	52.82	62.39	70.17	65.98	35.87	33.28	35.30	32.36
16.22	59.99	69.32	76.50	72.95	42.01	39.93	42.02	39.20
18.62	66.97	75.73	82.13	79.32	48.36	46.97	49.05	46.47
21.38	73.53	81.47	86.96	84.89	54.74	54.17	56.17	53.93
24.55	79.49	86.40	90.93	89.54	61.00	61.31	63.17	61.35
28.18	84.73	90.49	94.04	93.23	67.01	68.15	69.86	68.49
32.36	89.14	93.73	96.36	95.98	72.67	74.51	76.05	75.13
37.15	92.70	96.16	97.97	97.88	77.90	80.22	81.60	81.11
42.66	95.43	97.88	99.01	99.07	82.62	85.20	86.41	86.29
48.98	97.39	98.99	99.60	99.73	86.80	89.39	90.44	90.60
56.23	98.70	99.64	99.90	99.99	90.41	92.79	93.67	94.01
64.57	99.48	99.98	99.99	100.00	93.41	95.44	96.14	96.56
74.13	99.90	100.00	100.00	100.00	95.82	97.40	97.92	98.33
85.11	99.99	100.00	100.00	100.00	97.64	98.74	99.08	99.46
97.72	100.00	100.00	100.00	100.00	98.90	99.63	99.84	99.96
112.20	100.00	100.00	100.00	100.00	99.73	99.94	100.00	100.00
128.82	100.00	100.00	100.00	100.00	100.00	100.00	100.00	100.00
147.91	100.00	100.00	100.00	100.00	100.00	100.00	100.00	100.00
169.82	100.00	100.00	100.00	100.00	100.00	100.00	100.00	100.00
194.98	100.00	100.00	100.00	100.00	100.00	100.00	100.00	100.00
223.87	100.00	100.00	100.00	100.00	100.00	100.00	100.00	100.00
257.04	100.00	100.00	100.00	100.00	100.00	100.00	100.00	100.00
295.12	100.00	100.00	100.00	100.00	100.00	100.00	100.00	100.00
338.84	100.00	100.00	100.00	100.00	100.00	100.00	100.00	100.00
389.05	100.00	100.00	100.00	100.00	100.00	100.00	100.00	100.00
446.68	100.00	100.00	100.00	100.00	100.00	100.00	100.00	100.00
512.86	100.00	100.00	100.00	100.00	100.00	100.00	100.00	100.00
588.84	100.00	100.00	100.00	100.00	100.00	100.00	100.00	100.00

Table 10.4.3: Plug flow reactor cumulative volume per cent crystal size distributions for Test 81 - 88

Size, µm	*Test 81*	*Test 82*	*Test 83*	*Test 84*	*Test 85*	*Test 86*	*Test 87*	*Test 88*
0.26	0.00	0.00	0.00	0.00	0.00	0.00	0.00	0.00
0.30	0.01	0.01	0.01	0.01	0.01	0.00	0.00	0.00
0.34	0.13	0.11	0.11	0.09	0.10	0.00	0.00	0.01
0.39	0.40	0.34	0.34	0.30	0.34	0.00	0.00	0.16
0.45	0.80	0.68	0.67	0.61	0.70	0.00	0.00	0.38
0.51	1.26	1.08	1.07	0.98	1.14	0.00	0.00	0.65
0.59	1.77	1.52	1.49	1.37	1.62	0.00	0.00	0.93
0.68	2.26	1.94	1.90	1.76	2.10	0.00	0.00	1.21
0.78	2.69	2.31	2.27	2.10	2.52	0.00	0.00	1.46

Size, µm	***Test 81***	***Test 82***	***Test 83***	***Test 84***	***Test 85***	***Test 86***	***Test 87***	***Test 88***
0.89	3.04	2.62	2.56	2.37	2.88	0.00	0.00	1.66
1.02	3.30	2.83	2.77	2.57	3.14	0.00	0.00	1.80
1.17	3.46	2.98	2.91	2.71	3.32	0.00	0.00	1.89
1.35	3.56	3.07	3.01	2.80	3.43	0.00	0.00	1.95
1.55	3.63	3.15	3.09	2.88	3.52	0.00	0.00	2.01
1.78	3.70	3.23	3.18	2.98	3.59	0.07	0.02	2.09
2.04	3.77	3.33	3.29	3.08	3.67	0.15	0.10	2.18
2.34	3.87	3.45	3.42	3.20	3.77	0.26	0.19	2.30
2.69	4.01	3.59	3.57	3.32	3.92	0.38	0.29	2.43
3.09	4.21	3.74	3.71	3.43	4.13	0.52	0.38	2.55
3.55	4.51	3.93	3.87	3.54	4.45	0.66	0.47	2.67
4.07	4.97	4.17	4.05	3.67	4.94	0.81	0.55	2.79
4.68	5.65	4.51	4.31	3.87	5.66	0.98	0.67	2.91
5.37	6.65	5.03	4.73	4.23	6.70	1.20	0.85	3.08
6.17	8.03	5.84	5.42	4.85	8.13	1.51	1.18	3.37
7.08	9.89	7.04	6.50	5.88	10.02	2.01	1.74	3.85
8.13	12.28	8.79	8.14	7.47	12.43	2.79	2.66	4.65
9.33	15.26	11.20	10.48	9.78	15.40	3.99	4.05	5.90
10.72	18.86	14.40	13.65	12.94	18.97	5.74	6.05	7.72
12.30	23.04	18.45	17.72	17.04	23.11	8.18	8.79	10.26
14.13	27.78	23.37	22.71	22.13	27.80	11.45	12.36	13.61
16.22	33.00	29.09	28.55	28.16	32.97	15.60	16.81	17.85
18.62	38.59	35.46	35.10	35.01	38.51	20.64	22.16	22.99
21.38	44.43	42.30	42.13	42.48	44.31	26.50	28.32	28.99
24.55	50.41	49.35	49.38	50.31	50.23	33.03	35.17	35.74
28.18	56.39	56.38	56.60	58.18	56.16	40.01	42.50	43.06
32.36	62.26	63.15	63.55	65.80	61.96	47.20	50.06	50.71
37.15	67.92	69.51	70.05	72.88	67.55	54.37	57.61	58.43
42.66	73.30	75.33	75.99	79.21	72.83	61.30	64.89	65.96
48.98	78.33	80.55	81.29	84.66	77.76	67.86	71.69	73.03
56.23	82.94	85.15	85.91	89.17	82.29	73.94	77.88	79.44
64.57	87.08	89.12	89.83	92.75	86.38	79.46	83.32	85.02
74.13	90.70	92.46	93.07	95.47	89.99	84.38	87.96	89.68
85.11	93.74	95.15	95.63	97.43	93.06	88.62	91.78	93.39
97.72	96.15	97.20	97.53	98.74	95.55	92.13	94.76	96.15
112.20	97.92	98.63	98.81	99.52	97.42	94.87	96.94	98.05
128.82	99.07	99.53	99.58	99.91	98.70	96.85	98.41	99.21
147.91	99.71	99.91	99.91	100.00	99.46	98.14	99.28	99.81
169.82	99.95	100.00	100.00	100.00	99.85	98.89	99.73	100.00
194.98	100.00	100.00	100.00	100.00	99.98	99.27	99.92	100.00
223.87	100.00	100.00	100.00	100.00	100.00	99.43	100.00	100.00
257.04	100.00	100.00	100.00	100.00	100.00	99.51	100.00	100.00
295.12	100.00	100.00	100.00	100.00	100.00	99.56	100.00	100.00
338.84	100.00	100.00	100.00	100.00	100.00	99.63	100.00	100.00

Size, µm	*Test 81*	*Test 82*	*Test 83*	*Test 84*	*Test 85*	*Test 86*	*Test 87*	*Test 88*
389.05	100.00	100.00	100.00	100.00	100.00	99.72	100.00	100.00
446.68	100.00	100.00	100.00	100.00	100.00	99.83	100.00	100.00
512.86	100.00	100.00	100.00	100.00	100.00	99.93	100.00	100.00
588.84	100.00	100.00	100.00	100.00	100.00	99.99	100.00	100.00

Table 10.4.4: Plug flow reactor cumulative volume per cent crystal size distributions for Test 89 - 96

Size, µm	*Test 89*	*Test 90*	*Test 91*	*Test 92*	*Test 93*	*Test 94*	*Test 95*	*Test 96*
0.26	0.00	0.00	0.00	0.00	0.00	0.00	0.00	0.00
0.30	0.02	0.02	0.02	0.01	0.01	0.01	0.02	0.02
0.34	0.17	0.16	0.19	0.24	0.14	0.14	0.18	0.17
0.39	0.50	0.47	0.57	0.64	0.47	0.44	0.54	0.52
0.45	0.98	0.93	1.10	1.20	0.94	0.88	1.06	1.01
0.51	1.55	1.48	1.73	1.86	1.53	1.41	1.68	1.61
0.59	2.17	2.08	2.43	2.57	2.17	2.00	2.36	2.26
0.68	2.79	2.68	3.12	3.26	2.80	2.58	3.03	2.92
0.78	3.35	3.24	3.76	3.89	3.35	3.12	3.65	3.51
0.89	3.81	3.70	4.29	4.40	3.78	3.57	4.17	4.01
1.02	4.15	4.06	4.70	4.77	4.08	3.91	4.57	4.39
1.17	4.39	4.31	4.98	5.02	4.26	4.14	4.84	4.65
1.35	4.54	4.49	5.18	5.18	4.36	4.29	5.01	4.82
1.55	4.66	4.63	5.33	5.31	4.41	4.40	5.12	4.95
1.78	4.79	4.79	5.50	5.46	4.46	4.50	5.23	5.08
2.04	4.98	4.99	5.73	5.68	4.53	4.64	5.38	5.25
2.34	5.26	5.29	6.06	6.02	4.66	4.85	5.61	5.51
2.69	5.67	5.71	6.55	6.51	4.91	5.18	5.98	5.90
3.09	6.26	6.29	7.23	7.19	5.37	5.69	6.57	6.49
3.55	7.07	7.07	8.17	8.11	6.12	6.43	7.47	7.33
4.07	8.15	8.10	9.41	9.32	7.28	7.49	8.75	8.52
4.68	9.59	9.43	11.03	10.88	8.97	8.93	10.52	10.13
5.37	11.46	11.11	13.08	12.85	11.28	10.82	12.85	12.25
6.17	13.82	13.22	15.62	15.32	14.29	13.22	15.81	14.97
7.08	16.75	15.80	18.70	18.33	18.02	16.17	19.42	18.32
8.13	20.30	18.91	22.36	21.95	22.46	19.69	23.68	22.36
9.33	24.50	22.58	26.61	26.19	27.53	23.76	28.55	27.07
10.72	29.33	26.84	31.44	31.05	33.14	28.39	33.98	32.41
12.30	34.75	31.67	36.81	36.51	39.14	33.49	39.84	38.30
14.13	40.66	37.04	42.63	42.47	45.40	39.01	46.03	44.60
16.22	46.94	42.86	48.82	48.83	51.75	44.83	52.40	51.17
18.62	53.44	49.05	55.22	55.43	58.07	50.87	58.80	57.82
21.38	59.97	55.47	61.69	62.09	64.21	56.98	65.08	64.38
24.55	66.38	61.94	68.05	68.61	70.07	63.04	71.09	70.66
28.18	72.49	68.31	74.12	74.80	75.54	68.92	76.71	76.50
32.36	78.14	74.37	79.73	80.47	80.54	74.48	81.81	81.76
37.15	83.21	79.97	84.74	85.49	84.99	79.61	86.30	86.36

Size, µm	*Test 89*	*Test 90*	*Test 91*	*Test 92*	*Test 93*	*Test 94*	*Test 95*	*Test 96*
42.66	87.61	84.96	89.04	89.74	88.85	84.22	90.11	90.23
48.98	91.29	89.23	92.57	93.17	92.07	88.24	93.22	93.36
56.23	94.23	92.72	95.31	95.80	94.67	91.63	95.66	95.79
64.57	96.47	95.44	97.32	97.68	96.66	94.39	97.45	97.55
74.13	98.07	97.42	98.69	98.91	98.11	96.52	98.69	98.76
85.11	99.11	98.76	99.50	99.61	99.07	98.08	99.46	99.50
97.72	99.72	99.55	99.92	99.95	99.66	99.12	99.91	99.92
112.20	99.94	99.93	100.00	100.00	99.92	99.73	100.00	100.00
128.82	100.00	100.00	100.00	100.00	100.00	99.95	100.00	100.00
147.91	100.00	100.00	100.00	100.00	100.00	100.00	100.00	100.00
169.82	100.00	100.00	100.00	100.00	100.00	100.00	100.00	100.00
194.98	100.00	100.00	100.00	100.00	100.00	100.00	100.00	100.00
223.87	100.00	100.00	100.00	100.00	100.00	100.00	100.00	100.00
257.04	100.00	100.00	100.00	100.00	100.00	100.00	100.00	100.00
295.12	100.00	100.00	100.00	100.00	100.00	100.00	100.00	100.00
338.84	100.00	100.00	100.00	100.00	100.00	100.00	100.00	100.00
389.05	100.00	100.00	100.00	100.00	100.00	100.00	100.00	100.00
446.68	100.00	100.00	100.00	100.00	100.00	100.00	100.00	100.00
512.86	100.00	100.00	100.00	100.00	100.00	100.00	100.00	100.00
588.84	100.00	100.00	100.00	100.00	100.00	100.00	100.00	100.00

Table 10.4.5: Plug flow reactor cumulative volume per cent crystal size distributions for Test 97 - 104

Size, µm	*Test 97*	*Test 98*	*Test 99*	*Test 100*	*Test 101*	*Test 102*	*Test 103*	*Test 104*
0.26	0.00	0.00	0.00	0.00	0.00	0.00	0.00	0.00
0.30	0.02	0.02	0.02	0.02	0.01	0.01	0.01	0.01
0.34	0.18	0.16	0.18	0.20	0.09	0.12	0.13	0.13
0.39	0.55	0.51	0.54	0.57	0.34	0.41	0.43	0.44
0.45	1.07	1.01	1.05	1.09	0.71	0.83	0.86	0.88
0.51	1.71	1.60	1.67	1.71	1.16	1.34	1.39	1.42
0.59	2.41	2.25	2.34	2.38	1.65	1.90	1.96	2.02
0.68	3.10	2.90	3.00	3.04	2.15	2.45	2.54	2.60
0.78	3.73	3.48	3.61	3.63	2.60	2.96	3.07	3.14
0.89	4.26	3.96	4.11	4.12	2.99	3.39	3.51	3.60
1.02	4.67	4.33	4.49	4.48	3.29	3.73	3.86	3.95
1.17	4.96	4.59	4.76	4.73	3.52	3.98	4.11	4.21
1.35	5.16	4.76	4.93	4.89	3.68	4.15	4.29	4.40
1.55	5.31	4.87	5.06	5.00	3.80	4.28	4.43	4.54
1.78	5.45	4.98	5.18	5.11	3.89	4.39	4.54	4.69
2.04	5.61	5.10	5.31	5.25	3.97	4.50	4.66	4.85
2.34	5.82	5.26	5.50	5.43	4.04	4.62	4.79	5.05
2.69	6.12	5.50	5.76	5.70	4.11	4.78	4.96	5.30
3.09	6.58	5.88	6.17	6.09	4.23	5.01	5.21	5.64
3.55	7.27	6.46	6.77	6.65	4.46	5.37	5.60	6.12
4.07	8.27	7.31	7.65	7.44	4.87	5.95	6.22	6.80

Size, µm	***Test 97***	***Test 98***	***Test 99***	***Test 100***	***Test 101***	***Test 102***	***Test 103***	***Test 104***
4.68	9.66	8.53	8.89	8.53	5.57	6.82	7.14	7.77
5.37	11.52	10.18	10.55	9.99	6.65	8.08	8.46	9.10
6.17	13.90	12.35	12.70	11.89	8.20	9.81	10.26	10.89
7.08	16.82	15.05	15.39	14.30	10.29	12.07	12.60	13.21
8.13	20.30	18.34	18.65	17.28	12.96	14.91	15.54	16.15
9.33	24.30	22.18	22.47	20.87	16.21	18.32	19.08	19.73
10.72	28.77	26.56	26.83	25.08	20.02	22.32	23.21	23.99
12.30	33.63	31.42	31.69	29.89	24.32	26.85	27.89	28.89
14.13	38.79	36.69	36.98	35.27	29.04	31.85	33.07	34.36
16.22	44.16	42.27	42.61	41.12	34.08	37.24	38.63	40.29
18.62	49.64	48.06	48.47	47.34	39.34	42.92	44.49	46.54
21.38	55.15	53.95	54.45	53.78	44.74	48.77	50.50	52.95
24.55	60.60	59.84	60.43	60.27	50.18	54.68	56.54	59.34
28.18	65.92	65.59	66.28	66.64	55.60	60.54	62.48	65.56
32.36	71.02	71.12	71.87	72.73	60.94	66.22	68.20	71.44
37.15	75.86	76.31	77.11	78.37	66.15	71.65	73.60	76.88
42.66	80.37	81.08	81.89	83.43	71.21	76.74	78.61	81.79
48.98	84.51	85.36	86.14	87.83	76.08	81.43	83.16	86.11
56.23	88.22	89.12	89.83	91.50	80.71	85.66	87.20	89.81
64.57	91.46	92.30	92.91	94.44	85.04	89.39	90.70	92.89
74.13	94.20	94.90	95.38	96.67	88.97	92.58	93.63	95.36
85.11	96.40	96.91	97.27	98.25	92.39	95.19	95.97	97.24
97.72	98.06	98.38	98.61	99.26	95.21	97.20	97.73	98.58
112.20	99.16	99.32	99.44	99.85	97.34	98.61	98.93	99.43
128.82	99.81	99.85	99.89	100.00	98.77	99.48	99.64	99.88
147.91	100.00	100.00	100.00	100.00	99.59	99.87	99.93	100.00
169.82	100.00	100.00	100.00	100.00	99.92	100.00	100.00	100.00
194.98	100.00	100.00	100.00	100.00	100.00	100.00	100.00	100.00
223.87	100.00	100.00	100.00	100.00	100.00	100.00	100.00	100.00
257.04	100.00	100.00	100.00	100.00	100.00	100.00	100.00	100.00
295.12	100.00	100.00	100.00	100.00	100.00	100.00	100.00	100.00
338.84	100.00	100.00	100.00	100.00	100.00	100.00	100.00	100.00
389.05	100.00	100.00	100.00	100.00	100.00	100.00	100.00	100.00
446.68	100.00	100.00	100.00	100.00	100.00	100.00	100.00	100.00
512.86	100.00	100.00	100.00	100.00	100.00	100.00	100.00	100.00
588.84	100.00	100.00	100.00	100.00	100.00	100.00	100.00	100.00

10.5. ABBREVIATIONS AND TERMS

BCF - Burton, Cabrera and Frank growth model based on growth from screw dislocations.

Calcination - The process of burning rhodium-DETA salt in an oxygen atmosphere. The major reaction is the combustion of organic materials and the oxidation of rhodium.

CFD - Computational fluid dynamics.

CSD - Crystal size distribution. This term refers to the mass or volume portion of crystals in a precipitated product that are smaller than a certain size (usually in units of micrometres).

CSTR - Continuous stirred tank reactor.

DETA or DE - Diethylenetriamine or $(NH)C_2H_4(N)C_2H_4(NH)$. Protonated DETA refers to $(NH_2)C_2H_4(NH)C_2H_4(NH_2)^{3+}$ or DETA.3H^{3+} unless otherwise stated.

Diethylenetriammonium hexachloroirridate - Refers to the salt $[IrCl_6][(NH_2)C_2H_4(NH)\ C_2H_4(NH_2)]$.

Diethylenetriammonium hexachlororhodate - Refers to the salt $[RhCl_6][(NH_2)C_2H_4(NH)\ C_2H_4(NH_2)]$.

Diethylenetriammonium hexachlororuthenate - Refers to the salt $[RuCl_6][(NH_2)C_2H_4(NH)\ C_2H_4(NH_2)]$.

ICP-OES - Inductively coupled plasma optical emission spectrometry. A method used to analyse metal ion concentration in solution.

JMTC - Johnson-Matthey Technology Centre.

Macromixing - Mixing occurring on the scale of the vessel.

Mesomixing - Mixing that occurs on a length scale between that of the molecular scale and the vessel scale.

Micromixing - Mixing occurring on the molecular scale.

Model variance - Spread of measured data about the model of the data.

MSMPR - Mixed suspension mixed product removal reactor.

ODE - Ordinary differential equation.

PFR - Plug flow reactor.

PGM - Platinum group metals (Platinum, palladium, rhodium, ruthenium, iridium, osmium, gold)

PMR - Anglo Platinum's Precious Metal Refinery in Rustenburg, North-West Province, South-Africa.

Precipitation agent - Chemical used to induce precipitation. In this thesis it refers to DETA.

Purity - Desired metal mass divided by product mass; impurity refers to the mass of undesired metal divided by product in units of parts per million by mass.

p-value - Calculated Type I error probability. Used in statistical hypothesis testing.

Recovery - Term used to describe the ratio of pure metal output divided by metal input into a separation process. Synonyms in context of this work are yield, percent precipitation and conversion.

Reduction - The burning of rhodium(III)oxide (calcinate) in a mixture of hydrogen and nitrogen atmosphere to form metallic rhodium.

Rh - Rhodium. When Rh implies hexachlororhodate (III) anion it is specified in the text.

SEM - Scanning electron microscopy or microscope.

SFM - Segregated feed model.

Sponge - Grainy, sand-like solid i.e. rhodium sponge is rhodium metal in grain form.

Type I error - The chance of rejecting a hypothesis when it is true.

10.6. NOTATION

α	Mol ratio of protonated diethylenetriamine to hexachlororhodate (III); or growth rate supersaturation exponent; or growth rate exponent, unless otherwise specified.
a	Agitation energy dissipation and mesomixing constant.
A_0	Intercept of concentration product versus temperature intercept versus the root of the ionic strength.
$A_{0,AC}$	Activity coefficient frequency number.
$A_{0,SP}$	Solubility product frequency number.
A_1	Slope of concentration product versus temperature intercept versus the root of the ionic strength.
A_{bs}	Scale constant.
A_c	Pipe cross sectional area.
A_g	Growth rate frequency constant.
A_{ag}	Agglomeration growth rate frequency constant.
A_{IP}	Ion pairing rate constant frequency number.
A_{m0}	Mass transfer rate frequency parameter.
A_{m1}	Mass transfer rate constant 1st order slope parameter.
A_{m2}	Mass transfer rate constant 2nd order slope parameter.
A_n	Primary nucleation frequency constant.
$\hat{A}_p$	Specific particle area.
A_Q	Intercept of the concentration product versus temperature.
A_T	Total crystal area per volume suspension.
B	Decay constant in exponential distribution.
β	Population density at size zero supersaturation exponent.
B_g	Growth rate activation energy divided by the gas constant.
B_{ag}	Agglomeration growth rate activation energy divided by the gas constant.

B_{IP}	Ion pairing rate constant activation energy divided by the gas constant.
B_n	Primary nucleation activation energy divided by the gas constant.
b_s	Segregation spread.
B_{SP}	Solubility product activation energy divided by the gas constant.
C, *[]*	Elemental or specie concentration. Subscripts e and eq refers to equilibrium concentration. Subscripts A, B, C… refer to specie. Subscript 0 refer to initial or feed. Superscript ref refer to reference concentration. Note that in chemical reactions *[]* refers to a complexed compound i.e. rhodium complexes with 6 chloro ligands to form $[RhCl_6]^{3-}$.
D	Pipe reactor diameter.
D_{AB}	Diffusivity of paired Rh-DETA ions in 6M HCl.
D_i	Agitator impeller diameter.
D_p	Reactor discharge pipe diameter.
E_a	Activation energy.
ε	Moment scaling constant or loacal energy dissipation rate
F	Age function.
h	Mass transfer coefficient.
ϕ	Volume fraction density distribution.
Φ	Cumulative volume fraction distribution.
f	Size segregation function.
G	Crystal growth rate due to surface integration of paired ions.
ΔH_{CL}	Heat of crystallisation.
$\gamma_{\pm}$	Activity coefficient.
G_a	Crystal growth rate due to agglomeration.
η_i	Kinematic viscosity of the ith stream.
ΔH_{CL}	Heat of crystallisation.
I	Ionic strength.
IC	Initial conditions.
K_1	Background ionic strength in MSMPR or lumped constant in Equations (7.3.5) and (7.3.6)
K_2	Lumped constant in Equations (7.3.5) and (6.3.7)
K_{bs}	Decay constant.
K_g	Growth rate constant.
K_{ag}	Agglomeration growth rate constant.
K_{IP}	Ion pairing rate constant.
K_{m3}	Lumped crystal concentration constant.
K_{mt}	Mass transfer reaction rate constant.
K_n	Nucleation rate constant.
K_r	Reaction rate constant.
K_{SP}	Solubility product.
K_v	Volume shape factor.
L	Crystal size.

L_{32}	Average size defined by the ratio of the third moment divided by the second moment (Sauter mean size).
L_{43}	Average size defined by the ratio of the fourth moment divided by the third moment.
L_{max}	Maximum size integration limit.
m	Location parameter of the lognormal distribution or Reynolds number exponent.
m_{bs}	Location parameter for K_{bs}.
M_i	Population density moment. Subscript i refers to the ith moment.
M_T	Total crystal mass per suspension volume.
n	Population density or maximum count or Schmidt number exponent.
n_0	Initial population density at crystal size zero.
n_{0i}	ith Nucleated population density.
n_{out}	Population density in discharge stream.
N_P	Agitator power number.
N_q	Flow number.
N_T	Total number of crystals per unit suspension volume. This variable is equal to the zeroth moment, M_0.
N	Agitator angular velocity.
η	Kinematic viscosity.
OF	Objective function.
R	Universal gas constant.
R^2	Coefficient of determination.
r_A	Reaction rate.
R_{ag}	Crystal agglomeration rate.
ρ_c	Crystal density.
Re	Reynolds number.
R_{eq}	Mol reacted of a specie at equilibrium.
s	Spread parameter of the lognormal distribution.
S	Saturation ratio.
s_{bs}	Spread parameter for K_{bs}.
Sc	Schmidt number.
SD	Standard deviation.
Sh	Sherwood number.
SS	Sum of squared errors.
SSE	Sum of squared errors.
T	Temperature.
t	Time.
τ	Residence time.
τ_a	Time required for agglomeration.
τ_{micro}	Micromixing time.
τ_{meso}	Mesomixing time.
τ_{macro}	Macromixing time.

t_m	Discreet time at a measurement.
t_{ss}	Time required to attain steady state.
u	Fluid or pulp velocity or local fluid velocity near dip-tube.
u_p	Fluid velocity inside dip-tube.
u_c	Crystal plug velocity.
v_i	Volumetric flow rate. Subscript i refers to i^{th} stream.
y_i	Volume fraction of the i^{th} stream.
V_r	Reactor working volume.
$WSSE$	Weighted sum of squared errors.
x	Reactor length or distribution fraction of a mixed lognormal distribution.
X_A	Hexachlororhodate (III) conversion.
X_{Ae}	Equilibrium hexachlororhodate (III) conversion.
X_{Am}	Measured hexachlororhodate (III) conversion.
x_r	Maximum reactor length.
ψ_i	i^{th} Moment of the segregated discharge stream.
z_i	Charge of the i^{th} ion.